

## DOCTOR OF PHILOSOPHY

### Investigating plasmonic based fibre optic sensing as a battery diagnostic technique

Gardner, Christopher

*Award date:*  
2024

*Awarding institution:*  
Coventry University

[Link to publication](#)

#### **General rights**

Copyright and moral rights for the publications made accessible in the public portal are retained by the authors and/or other copyright owners and it is a condition of accessing publications that users recognise and abide by the legal requirements associated with these rights.

- Users may download and print one copy of this thesis for personal non-commercial research or study
- This thesis cannot be reproduced or quoted extensively from without first obtaining permission from the copyright holder(s)
- You may not further distribute the material or use it for any profit-making activity or commercial gain
- You may freely distribute the URL identifying the publication in the public portal

#### **Take down policy**

If you believe that this document breaches copyright please contact us providing details, and we will remove access to the work immediately and investigate your claim.

# Investigating plasmonic based fibre optic sensing as a battery diagnostic technique



**Coventry**  
University

By

Christopher Gardner

PhD

December 2023

# Investigating plasmonic based fibre optic sensing as a battery diagnostic technique

A thesis submitted in partial fulfilment of the University's requirements for Degree of Doctor of Philosophy

December 2023



In collaboration with the project industrial partner, Insplorion AB.



## **Certificate of Ethical Approval**

Applicant: Christopher Gardner  
Project Title: Investigating plasmonic based fibre optic sensing as a battery diagnostic technique

This is to certify that the above named applicant has completed the Coventry University Ethical Approval process and their project has been confirmed and approved as Medium Risk

Date of approval: 14 Nov 2023  
Project Reference Number: P166376

# Acknowledgments

This project was supported by the excellent academic team in the Centre for Advanced Low Carbon Propulsion Systems (C-ALPS) in Coventry University. Help and support was provided by many of the staff and my colleagues at the centre which I am very grateful for; I would like to note the support of my supervisory team, Joe Fleming, Rohit Bhagat, Alexander Roberts and in particular my director of studies Tazdin Amietszajew, for their highly knowledgeable input and the considerable time they provided, without which this project would not have been possible.

This project was co-funded by Insplorion AB, who provided the sensing platform for the project. Staff at the business provided considerable support to me throughout the project, in particular my industrial supervisor Elin Langhammer provided invaluable expertise and ongoing support.

A wide variety of literature was consulted throughout the project, the extent of which is largely covered by the Bibliography in this document. The Conferences I attended throughout my PhD, Future Propulsion Conference 2022 and 2023, Swiss Battery Days 2022 and the Electrochemical Society 244<sup>th</sup> Conference 2023, were also excellent sources of information and highly insightful.

A final acknowledgement, and the most significant one, for the patience of my friends and family, particularly my wife Maria and son Adrian, while I worked on this project.

## Externally reviewed work completed during project

The following three papers have been published from the content of this thesis:

C. Gardner, E. Langhammer, W. Du, D.J.L. Brett, P.R. Shearing, A.J. Roberts, T. Amietszajew, In-Situ Li-ion Pouch Cell Diagnostics Utilising Plasmonic Based Optical Fibre Sensors, *Sensors*. 22 (2022) 738. <https://doi.org/10.3390/s22030738>.

C. Gardner, E. Langhammer, A.J. Roberts, T. Amietszajew, Plasmonic based fibre optic detection and electrochemical identification of phase transitions in NMC111/graphite lithium-ion pouch cells, *J. Energy Storage*. 63 (2023) 107105. <https://doi.org/10.1016/J.EST.2023.107105>.

C. Gardner, E. Langhammer, V. Marsic, J. Fleming, A.J. Roberts, T. Amietszajew, Novel Li-Ion Battery Diagnostics; Detection Of Redox Peaks Utilising Plasmonic Fibre Optic Sensors And Evaluation Of Interference On Cell Function, *Batteries & Supercaps* (2024), e202400079. <https://doi.org/10.1002/batt.202400079>.

Work from this thesis was also presented at the following conferences:

- Future Propulsion Conference 2022, Solihull, U.K.
- Swiss Battery Days 2022, Dübendorf, Switzerland
- 244th Electrochemical Society Conference 2023, Gothenburg, Sweden

## Copyright

This material in this thesis is available for reproduction under a Creative Commons 4.0 License; however where material in this document has been reproduced from other referenced sources including publications and Insplorion AB, permission must be sought from those parties to reproduce their material.

# Contents

1.	Introduction .....	18
1.1.	Abstract .....	18
1.2.	Objectives .....	18
1.3.	Thesis Overview .....	18
2.	Literature Review .....	20
2.1.	Lithium-ion batteries .....	20
2.1.1.	Rechargeable battery market background .....	20
2.1.2.	Lithium-ion battery properties and competitors.....	24
2.1.3.	Battery cell designs .....	27
2.1.4.	Li-ion battery electrode material structures and phase transitions .....	31
2.1.5.	Li-ion cell working mechanisms .....	35
2.1.6.	Cell kinetics/ thermodynamics .....	37
2.1.7.	Lithium-ion diffusion.....	41
2.1.8.	Limitations, ageing mechanisms and failure modes.....	42
2.1.9.	Potential developments in lithium-ion batteries.....	44
2.2.	Current battery diagnostic techniques.....	46
2.2.1.	Common non-invasive battery diagnostic methods.....	46
2.2.2.	Laboratory battery diagnostic techniques .....	52
2.2.3.	<i>In situ</i> and <i>in operando</i> battery diagnostics method .....	53
2.3.	Fibre optics .....	55
2.3.1.	The use of fibre optics for battery diagnostics .....	55
2.3.2.	Plasmonic/Nanoplasmonic sensing .....	60
2.3.3.	The use of SPR in energy storage devices.....	64
2.4.	The potential benefits of utilising SPR in lithium-ion batteries.....	67
2.5.	Hypotheses .....	68
3.	Methodology.....	69
3.1.	Plasmonic sensor technology .....	69
3.2.	Fibres in Electrolyte experiment setup.....	72
3.2.1.	Electrolyte exposure over time.....	72
3.2.2.	Changing concentrations of electrolyte.....	73
3.3.	Cell making .....	74
3.3.1.	Reference cells assembly .....	74
3.3.2.	Manufacture of cells with one and two sensor fibres .....	78
3.3.3.	Manufacture of cells with reference electrode .....	83

3.4.	Cell and optical sensors characterisation and cycling .....	85
3.4.1.	Test setup and formation cycling.....	85
3.4.2.	Cell characterisation .....	88
3.4.3.	Cell cycling and testing.....	92
3.4.4.	Impact of temperature and pressure on optical signal .....	97
3.5.	Forced Lithium Plating testing .....	99
3.5.1.	Open cell .....	99
3.5.2.	Lithium plating in pouch cells .....	101
3.6.	Materials analysis .....	107
3.6.1.	X-ray tomographic imaging of cell .....	107
3.6.2.	Cell teardown.....	107
3.6.3.	Lithium presence testing .....	109
3.6.4.	SEM and EDX.....	109
4.	Results and Discussion .....	110
4.1.	Sensor and Cell Characterisation.....	110
4.1.1.	Fibres response to Li-ion battery electrolyte.....	111
4.1.2.	Baseline cell characterisation .....	113
4.1.3.	Evaluation of impact of sensor presence on cell .....	118
4.1.4.	X-ray tomographic images of sensor in cell.....	131
4.2.	Optical signal correlation with cell cycling .....	132
4.2.1.	Formation and initial cycling optical data.....	132
4.2.2.	Fibre optic sensor performance over repeated cycling.....	139
4.2.3.	Effect of temperature, pressure and impact on optical signal .....	144
4.3.	Optical response to different cell phenomena and insight into underlying mechanisms	148
4.3.1.	GITT test.....	149
4.3.2.	IC analysis and phase transitions.....	151
4.3.3.	Cyclic Voltammetry analysis .....	156
4.3.4.	Urban Profile cycling .....	159
4.3.5.	Optical signal behaviour at different charge rates .....	160
4.4.	Lithium plating detection with optical sensor.....	163
4.4.1.	Open cell forced lithium plating .....	163
4.4.2.	Identifying forced lithium plating in pouch cells .....	165
4.4.3.	Forced lithium plating cycles optical data analysis.....	171
5.	Conclusions .....	172
6.	Further Work.....	174
7.	References .....	175

8.	Appendices.....	189
8.1.	Appendix A- Specification and order of glovebox optical pass through .....	189
8.2.	Appendix B- Formation step settings.....	190
8.3.	Appendix C- Galvanostatic cycling with constant voltage step settings .....	191
8.4.	Appendix D- Galvanostatic Intermittent Titration Technique test settings.....	192
8.5.	Appendix E- Cyclic Voltammetry test settings .....	193
8.6.	Appendix F- Electrochemical Impedance Spectroscopy test settings.....	194
8.7.	Appendix G- Urban Profile discharge cycle .....	195
8.8.	Appendix H- Forced lithium plating at room temperature settings .....	201
8.9.	Appendix I- Forced lithium plating on reference cells at 0°C.....	202
8.10.	Appendix J- Forced lithium plating on cells in copper jigs at 0°C.....	203
8.11.	Appendix K- Typical cell safety settings .....	204
8.12.	Appendix L- Battery cell information .....	205
8.13.	Appendix M- Copyright approvals for 3 <sup>rd</sup> party figures utilised.....	206

## List of Figures

Figure 2-1- a) Projections for EV fleet numbers [13]- significant growth can be seen across the global market, although there is a wide range in future volume predictions, b) Projections for installed battery stationary energy storage [13].	23
Figure 2-2- Comparison of specific power and specific energy of Li-ion batteries compared to other electrical energy storage technologies [22] Acronyms: SMES (superconducting magnetic energy storage), VRB (vanadium redox battery), ZnBr (zinc-bromine battery), NaS (sodium-sulphur), TES (thermal energy storage)	26
Figure 2-3- Image of a simple pouch cell and internals	28
Figure 2-4- Images of layered (a), spinel (b), olivine (c) and tavorite (d) crystal structures, and e) Typical discharge profiles for a selection of chemistries [29]	33
Figure 2-5- Incremental (or differential) capacity (IC) versus cell voltage for NMC111, NMC622 and NMC811 cathodes versus graphite electrodes [51]	34
Figure 2-6- Cyclic voltammogram of a carbon/Li cell cycled at $2 \mu\text{V s}^{-1}$ [62]	35
Figure 2-7- schematic example of a charging/ discharging lithium-ion galvanic cell [64]	36
Figure 2-8- Charge and discharge profiles of new Li-ion NMC cells at C/25, showing both cell operational voltage and OCV against state of charge [68]	37
Figure 2-9- Degradation modes in lithium-ion cells [78]	42
Figure 2-10- Relationship between a) phase diagram of material 'M' being lithiated, b) Gibbs free energy, c) voltage curve, d) voltage curve with e) IC and f) DV plots [67]	48
Figure 2-11 - An example equivalent circuit of a single electrode and expected impedance response at different frequencies	49
Figure 2-12- Typical cell equivalent circuit model and idealised Nyquist impedance plot relating to each circuit feature. $R_{HF}$ represents the initial electrolyte diffusion resistance, $R_1$ and $R_1$ are the respective electrode charge transfer resistances and $W$ is the Warburg element [105]	50
Figure 2-13 - Graphical representation of model training steps for data driven machine learning	51
Figure 2-14 - A summary of some SOH and SOC estimation methods [108]	51
Figure 2-15- Schematic of thermistor element inserted inside a pouch cell and cylindrical cell [118]	54
Figure 2-16- Sketches of different fibre-optic SPR configurations, including a fibre with a Tilted Fibre Bragg grating (TFBG) incorporated inside it in (g) [142]	57
Figure 2-17- Constant current charge (a) and discharge (b) of a LFP-lithium half-cell and associated ATR light signal attenuation, (C) and (d) respectively [127]	59
Figure 2-18-Sketch of Kretschmann-Raether configuration prism with totally internally reflected incident light and a surface plasmon wave on the surface, this is an example of a biotechnology sensing application [142]	61
Figure 2-19- Evanescent wave (EW) produced at the surface of fibre optic waveguide due to totally internally reflected light couples with the surface plasmon wave (SPW) in a thin metallic layer on the fibre optic waveguide when the propagation constants match	62
Figure 2-20- a) CV response of a supercapacitor, i) and iii) showing polarised states and ii) showing neutral state b) SPR signal response of P-polarised input [18]	65
Figure 3-1- Annotated picture of the optical fibre plasmonic sensor	69
Figure 3-2- a) SPR fibre sensor and pigtail fibre being placed in fusion splicer, b) SPR sensor fibre and pigtail fused with splice protector added	71
Figure 3-3- Three neck flask containing a SPR fibre optic sensor	72
Figure 3-4- Optical set up utilising optical pass through to carry out experiments inside glovebox, a) shows optical unit controlled by laptops and patchcords connecting OU to FCPC connectors on	

glovebox passthrough, b) shows patchcords connecting passthrough inside the glovebox to pigtailed and optical sensor .....	73
Figure 3-5- a) Cell stack and b) electrolyte used in the manufacture of all cells in this study .....	75
Figure 3-6- Sealing machine used to make initial seals on pouch cell, the metal bar is heated to 180°C and then dropped onto the edge of the pouch cell that requires sealing, a) sealing machine with controls, b) zoomed in image of sealing bar .....	75
Figure 3-7- a) a cell inside the vacuum sealing machine ready for the final seal, b) sealing machine closed during the sealing process, and c) a fully sealed cell after completion of the sealing process.	77
Figure 3-8- Sealed cells in acrylic compression jigs on oven shelf, jigs with brass blocks for tab contact and potentiostat connection .....	78
Figure 3-9- Pouch cell material with fibre sealed through edge filled with water and leak tested, a) filling the sealed pouch material (only open at the top) with water, b) leaving the water filled pouch material in cups to observe if any leakage occurred .....	79
Figure 3-10- Methods tested to remove polyamide from ends of sensor fibre to allow fusion splicing to pigtailed, a) KOH etching method, b) burning method using simple lighter .....	80
Figure 3-11- Plasmonic based fibre optic sensor fibres introduced through the centre of cell stacks, adjacent to an electrode.....	80
Figure 3-12- a) Fibre and stack in pouch material before sealing and b) after top and bottom edges sealed .....	81
Figure 3-13- A cell with fibre sensor incorporated before final seal under vacuum takes place .....	82
Figure 3-14- a) Assembled cells with integrated fibre optic sensor and b) cell dimensions (mm).....	82
Figure 3-15- Cell with fibre sensors in jigs, connected to optical patch cables, potentiostat and thermocouples.....	83
Figure 3-16- a) A lithium reference electrode being placed in formed cell inside a glovebox, b) preparing to mix the resin, c) the inserted and sealed electrode in a cell, d) a 3 electrode cell connected to a potentiostat .....	85
Figure 3-17- Schematic of test setup, cell with two fibre sensors connected to OU and potentiostat	86
Figure 3-18- Cells in chamber connected to potentiostat channels and OU multiplexor, thermocouples can also be seen .....	87
Figure 3-19- a) and b) Three reference cells (no fibre sensors) in an chamber with thermocouples attached to each cell, c) thermocouple control device, d) oven temperature settings .....	89
Figure 3-20- a) Cells in copper jigs and b) cells in acrylic jigs, with thermocouples (green and white cables) .....	97
Figure 3-21- Brass block weights incrementally added on top of jigs, to observe pressure impact on optical signal, a) 12 blocks totalling 744g on cell, b) 21 blocks totalling 1302g on cell.....	98
Figure 3-22- a) Open cell being placed into glovebox entry chamber, b) Open cell inside glovebox, c) Open cell with lithium electrode and electrolyte added, d) Open cell connected to potentiostat with 4-wire setup .....	100
Figure 3-23- a) Prepared copper plates, b) cell being placed in jig, c) two cells in jigs with copper plates acting as heat sinks (inside binder chamber, with thermocouples, optical sensors and potentiostat cables) .....	104
Figure 3-24- X-ray instrumentation (Nikon XTH 225, Nikon Metrology, UK) with sample cell, a) complete unit including shielding, b) zoomed in image of scanner and cell sample in holder .....	107
Figure 3-25- a) after cutting the other 3 edges of the cell off the top edge of the cell with the tabs is cut with plastic scissors, b) the cell is peeled apart, c) the separator is unwrapped and d) the electrodes are separated. ....	108
Figure 4-1- Sensor reading in electrolyte over time in enclosed space outside glovebox, a) sensor one, and b) sensor two .....	111

Figure 4-2- Plasmonic sensor optical reading change as lithium salt (LiPF <sub>6</sub> ) is added to solvent, experiment carried out inside an argon atmosphere glovebox. ....	112
Figure 4-3- The light extinction at different wavelengths plotted against increasing Lithium salt concentration.....	113
Figure 4-4- Formation cycle of three reference cells, capacity-voltage profile.....	114
Figure 4-5- Waterfall test cell characterisation on reference cells, from C/5 to 3C charge rates.....	115
Figure 4-6- Pouch cell surface temperatures recorded during C/5 (280mAh) cycling in 25°C ambient .....	116
Figure 4-7- a) temperature of one cell at different charge rates and D/5 (top), b) temperature of multiple cells .....	117
Figure 4-8- EIS testing of the reference cells in the charged and discharged states after 10 cycles..	118
Figure 4-9- Formation cycles capacity-voltage profiles of three cells with one fibre sensor in each and three cells without fibres, for comparison .....	119
Figure 4-10- Coulombic efficiencies of cells with one fibre optic sensor compared a reference cell	120
Figure 4-11- a) Autopsied cell with sensor fibre, opened after 50 cycles, b) SEM image of discoloured region on electrode at x73 magnification c) SEM image at x566 magnification (enlarged section of figure b).....	121
Figure 4-12- Formation cycle capacity-voltage profile comparison for reference cells and cells with two fibre optic sensors .....	122
Figure 4-13- a) Cycling carried out on 3 cells with two sensors in, with coulombic efficiencies for each cycle (the cycles with efficiencies that deviate significantly from the mean are due to the testing being stopped and started) b) Comparison of coulombic efficiencies of the cells with two sensors to a reference cell cycled at C/5 for 150 cycles, shown at higher resolution. ....	123
Figure 4-14- Cycling carried out on 3 cells with two sensors in with discharge capacities for each cycle, compared to two reference cells without fibres. The discharge capacities in the purple dashed circle deviate from the trend due to stopping and restarting the cycling, to carry out other testing including higher C rate (C/2 and C/3) cycling, CV and GITT- all other cycles for the cells carried out galvanostatically at C/5.....	124
Figure 4-15- EIS response comparison for reference and fibre cells in a) fully discharged state and b) fully charged state.....	125
Figure 4-16- Equivalent Circuit Model EIS data fitting, a) ECM consisting of inductor (L), resistors (R), constant phase elements (Q) and Warburg diffusion coefficient (W), b) Fitted ECM plot overlaid onto EIS data for reference cell 1 and fibre cell 1, both in median positions of respective groupings in Figure 4-15. ....	126
Figure 4-17- SEM images of anode from cell cycled for over 150 cycles with fibre optic sensors inside. Lithium salt deposits can be seen in blue circles. a) shows section of electrode at 300 magnification, line of lithium salt deposit can be seen where the fibre was previously. b) 3000x magnification of area of electrode that had visible deposits, where fibre had been. c) 3000x magnification of area of electrode without visible deposits, where fibre had not been present. ....	128
Figure 4-18- EDX analysis of section graphite anode from cycled cell with fibre sensors, including deposit in region of fibres. a) SEM image of region- profile could be indicative of poorly mixed carbon black b) Carbon, oxygen, fluorine and potassium detected by EDX c) Second SEM image of region d) Carbon, oxygen, fluorine and potassium distribution as detected by EDX spectrum analysis of region in blue box in image c). ....	129
Figure 4-19- SEM images of cathode adjacent to sensor, at 300× (a) and 3000× (b) magnification..	130
Figure 4-20- EDX mapping of cathode area in Figure 4-16 b).....	131
Figure 4-21- a), b) X-ray of fibre in cell and c) cell stack X-ray side profile (5mm width).....	131

Figure 4-22- Formation cycle optical spectra data from fibres adjacent to a) anode and b) cathode .....	133
Figure 4-23- Formation cycle data with 725nm wavelength optical data from fibres adjacent to anode and cathode .....	134
Figure 4-24- First 10 galvanostatic cycles (C/5) after formation cycles with 725nm optical signals from a sensor on a) the anode side and b) the cathode side of the cell .....	135
Figure 4-25- Optical spectra of fibre adjacent to anode during 6 <sup>th</sup> and 7 <sup>th</sup> galvanostatic cycles (C/5) of cell after formation, with indicative inverted voltage plot in background.....	136
Figure 4-26- a) 725nm wavelength optical signal and voltage profile during 6 <sup>th</sup> and 7 <sup>th</sup> galvanostatic cycles (C/5) after formation, with corresponding electrode voltages at that stage of cycling for the b) cathode and c) anode .....	137
Figure 4-27- a) Optical signal light spectra for the 6 <sup>th</sup> and 7 <sup>th</sup> galvanostatic cycles (C/5) after formation, with the indicative inverted voltage profile in the background, and b) the same signals showing specifically the 725nm wavelength .....	138
Figure 4-28- a) Light extinction of the fibre optic signal of the sensor adjacent to the anode over 50 cycles of galvanostatic cycling (C/5) and b) A section of that cycling showing the behaviour of the signal when the cell was at rest.....	139
Figure 4-29-Optical signal strength at 725nm for optical fibres adjacent to an anode and cathode electrode during galvanostatic cycling (C/5) .....	140
Figure 4-30- Microscope photographs of the a) middle and b) edge of the sensing region of an unused plasmonic based fibre optic sensor, at approximately 10x magnification. ....	141
Figure 4-31- SEM images of the sensing region of an unused plasmonic based fibre optic sensor, at magnifications of a) 66x, b) 170x and c) 381x. ....	142
Figure 4-32- SEM images of sensing region of a sensor from the initial batch of sensors, after being adjacent to the anode of a cell galvanostatically cycled for 50 cycles,at a) 100x magnification and b) and c) at 400x magnification.....	143
Figure 4-33- a) Photograph of used cathode side (top) and anode side (bottom) fibre sensors prepared for SEM analysis, b) SEM analysis of cathode side fibre sensing region at 582x magnification, c) SEM analysis of anode side fibre sensing region at 582x magnification .....	144
Figure 4-34- Response of optical fibre signals to temperature change while cell is at rest, a) anode side fibre optical spectrum with indicative inverted temperature change (from 25°C to 35°C), b) anode side fibre signal at 725nm wavelength during 25°C to 35°C temperature change, c) cathode side fibre signal at 725nm wavelength during 25°C to 35°C temperature change, d) optical signal of reference fibre in oven during 25°C to 35°C temperature change, e) anode side fibre signal at 725nm wavelength during 35C to 15°C temperature change, f) cathode side fibre signal at 725nm wavelength during 35°C to 15°C temperature change .....	146
Figure 4-35- Cell cycled at C/5 at 3 different temperatures, with corresponding optical response ..	147
Figure 4-36- fibre optic 725nm wavelength signal change due to physical disturbance .....	147
Figure 4-37- 725nm wavelength optical signal from a) anode side and b) cathode side of a cell during pressure testing .....	148
Figure 4-38- GITT testing time-voltage profile and optical response at different wavelengths.....	149
Figure 4-39- Cell voltage and OU response over two GITT cycles. The IR drop regions on the first GITT pulse are indicatively identified, along with the voltage values that can be used in diffusion coefficient calculations. The difference between the pulsed voltage and relaxed voltage is described as the overpotential and includes elements such as the electrical resistance IR drop, and kinetic steps such as adsorption, mass transfer and charge transfer [180]. .....	150
Figure 4-40- Time- Voltage (T-V) and IC plots (solid blue line is charge, dotted red line is discharge) on NMC111 cell with graphite anode and Lithium reference electrode cycles at 280mA (C/5); a) Full T-V	

plot, b) Full cell IC plot, c) Cathode Time-Voltage plot, d) Cathode IC Plot, e) Anode T-V Plot, f) Anode IC Plot .....	152
Figure 4-41- a) Cell voltage and anode side sensor optical response (lux) over time, b) Full cell IC plot and differentiated optical signal plot during charge, c) Full cell IC plot and differentiated optical signal plot during discharge .....	154
Figure 4-42- a) Cell voltage and cathode side sensor optical response (lux) over time, b) Full cell IC plot and differentiated optical signal plot during charge, c) Full cell IC plot and differentiated optical signal plot during discharge .....	154
Figure 4-43- a) Anode side differentiated optical signal, with lesser filtering, and full cell IC plot, b) Anode side differentiated optical signal, with lesser filtering, and anode voltage data IC plot.....	156
Figure 4-44- Cyclic voltammetry plots at scan rates of a) 0.1mV/s and b) 0.05mV/s .....	157
Figure 4-45- Voltage- current cyclic voltammetry plots for a cell with two fibre optic sensors, one adjacent to an anode and one adjacent to a cathode, at a scan rate of 0.05mVs <sup>-1</sup> . On both graphs only one voltage-current cycle is shown representatively, while a) includes the optical response of optical sensor adjacent to the anode over two CV cycles and b) includes the optical response of optical sensor adjacent to the cathode over two CV cycles. Here we can see how the optical signal follows the cycle profile including the redox peak. The green dashed arrows show apparently corresponding inflections between the CV cycling profile and optical signal, including redox peaks. The green dashed circle shows an apparently anomalous response, possibly due to a disturbance of the system.....	158
Figure 4-46- a) Three cycles of partial charge and discharge with discharge according to UP cycling, anode side sensor optical signal and cell voltage, b) Zoomed in focus on urban profile discharge section of 2 <sup>nd</sup> cycle .....	159
Figure 4-47- Figure of optical signal and cell SOC during urban profile cycling discharge .....	160
Figure 4-48- a) Cells at 0°C, charged at 3C and discharged at D/20 for 3 cycles, with corresponding anode side sensor optical signal and cell voltage, b) Same cycling data showing SOC profile instead of voltage.....	162
Figure 4-49- Open cell charged at C/5, showing voltage profile of cell and optical signal at the 725nm wavelength.....	163
Figure 4-50- Pictures of open cell materials after forced lithium plating and dendrite formation, a) The graphite in the electrolyte delaminated from copper substrate, b) Fibre optic sensor blackened, c) Material deposits in electrolyte, d) Additional picture showing damage to fibre optic sensor .....	164
Figure 4-51- Cells cycled at 25°C ambient, a) Cell cycled at C/5 charge and C/20 discharge for 5 cycles, b) Cell cycled at 1.5C charge and C/20 discharge for 5 cycles, c) IC analysis of first cycle from Figure a, d) IC analysis of first cycle from Figure b .....	165
Figure 4-52- Cells cycled at 0°C ambient, a) Cell cycled at C/40 charge and C/20 discharge for 3 cycles, b) Cell cycled at C/2 charge and C/20 discharge for 5 cycles, c) IC analysis of first cycle from Figure a, d) IC analysis of second cycle from Figure b .....	166
Figure 4-53- Graphite counter electrode voltage, on further C/2 charge and C/20 discharge cycling. ....	167
Figure 4-54- a) anode from torndown cell with visible lithium plating (left), b) reaction to water indicating lithium presence.....	168
Figure 4-55- Copper plate cells with C/2 charge and C/20 discharge, a) Time versus voltage plot of 5 cycles and b) IC plot of the first cycle .....	168
Figure 4-56- a) Cell surface temperature of cells in acrylic jigs, b) Cell surface temperature of cells in copper jigs, c) Comparison of formation cycles of cells in acrylic and copper jigs, d) Comparison of EIS of cells in acrylic jigs and copper jigs at same early stage of life in discharged state, e) Comparison of EIS of cells in acrylic jigs and copper jigs at same early stage of life in charged state.....	170

Figure 4-57- Cell at 0°C cycled at C/2 charge and then C/20 discharge, a) showing 10 cycles and b) zoomed in on 3 cycles, with the voltage profile and optical signal response from anode side fibres at 725nm ..... 171

## List of Tables

Table 2-1- Market share of rechargeable battery cells in portable electronic devices in 2005 (millions of cells sold) [12] .....	20
Table 2-2- Lithium-ion battery types in passenger electric vehicles, 2017 snapshot [8].....	21
Table 2-3 Comparison of lithium-ion battery and competing traditional battery technologies pros and cons [8].....	25
Table 2-4- Characteristics of four types of batteries common in portable electronic devices [17] .....	26
Table 2-5- A variety of electrolyte additives and their properties [38] .....	30
Table 2-6- Typical intercalation cathode compounds and their characteristics [29] .....	31
Table 2-7- Comparison of some of the common use cases and properties for ATR, SPP and LSPR measurement techniques .....	63
Table 3-1- Cell formation cycling procedure.....	86
Table 3-2- Table showing c-rate, current and current density values for the cells used in this study .	88
Table 3-3- First ten galvanostatic cell cycles followed by EIS testing in discharged and charged states .....	89
Table 3-4- Cell characterisation ‘waterfall test’ settings .....	90
Table 3-5- Overview of cells assembled and testing carried out.....	92
Table 3-6- GITT test profile .....	94
Table 3-7- Cyclic voltammetry test profiles. ....	95
Table 3-8- EIS procedure, EIS carried out in cell discharged and charged states. ....	95
Table 3-9- Cell cycling with urban profile cycle on discharge .....	96
Table 3-10- Cell cycling at different temperatures to observe impact of temperature on signal.....	97
Table 3-11- Table of weight added to and removed from cell .....	98
Table 3-12- Open cell cycling parameters.....	100
Table 3-13- Forced lithium plating testing carried out at 25°C.....	101
Table 3-14- Forced lithium plating cycling of reference cells .....	102
Table 3-15- Cells in copper plates forced lithium plating cycling. ....	105
Table 3-16- Cycling for forced lithium plating on cells with fibre sensors in acrylic jigs, at 0°C.....	106
Table 4-1- Equivalent c-rates, currents and charge densities for cells .....	113
Table 4-2- Iteratively calculated ECM element values (BioLogic EC-Labs software), according to the ECM model and fitting shown in Figure 4-16. ....	126

## List of Abbreviations

SOH- State of Health

SOC- State of Charge

OCV- Open Circuit Voltage

ICA- Incremental Capacity Analysis

DVA- Differential Voltage Analysis

Li-ion- Lithium ion

Na-ion- Sodium ion

NMC- Lithium Nickel Manganese Cobalt Oxide

NCA- Lithium Nickel Cobalt Aluminium Oxide

LFP- Lithium Iron Phosphate Oxide

LCO- Lithium Cobalt Oxide

Ni-Cd- Nickel Cadmium

Ni-MH- Nickel Metal Hydride

C-rate- Charge rate

FTIR- Fourier Transform Infrared

ATR- Attenuated Total Reflection

PS- Plasmonic Sensing

NPS- Nanoplasmonic sensing

LSPR- Localised Surface Plasmon Resonance

SPR- Surface Plasmon Polariton

EW- Evanescent Wave

OU- Optical Unit

FO- Fibre Optic

SMF- Single Mode Fibre

MMF- Multi Mode Fibre

MOF- Micro-structured optical fibre

LOD- Limit of Detection

FOM- Figure of Merit

FP- Fabry- Perot

FOEWS- Fibre Optic Evanescent Wave Sensor

FBG- Fibre Bragg Grating

TFBG- Tilted Fibre Bragg Grating

IRE- Internally Reflective Element

LDPE- Low Density Polyethylene

FC/PC connector- Fixed Connection Physical Contact fibre connector

BMS- Battery Management System

SEM- Scanning Electron Microscopy

EDX- Energy Dispersive X-ray Analysis

TEM- Transmission Electron Microscopy

XRF- X-ray fluorescence

EQCM- Electrochemical Quartz Crystal Microbalance

GITT- Galvanostatic Intermittent Titration Technique

EIS- Electrochemical Impedance Spectroscopy

RE- Reference Electrode

PED- Portable Electronic Device

EV- Electric Vehicle

eVTOL- Electric Vertical Take Off and Landing

PED- Portable Electronic Device

LLI- Loss of lithium inventory

LAM<sub>PE</sub>- Loss of active positive electrode material

LAM<sub>NE</sub>- Loss of active negative electrode material

SEI- Solid electrolyte interface

CEI- Cathode Electrolyte Interface

RC circuit- Resistance Capacitor Circuit

EECM- Electrical Equivalent Circuit Model

# 1. Introduction

## 1.1. Abstract

This study demonstrates for the first time the application of plasmonic based fibre optic sensors inside Lithium-ion pouch cells. The study shows the successful integration of the sensor platform into battery cells, acquisition of diagnostic data in-situ and in real time, correlation of data to battery internal process phenomena and demonstration of negligible impact of the sensor presence on battery cell function. This study demonstrates the potential of plasmonic based fibre optic sensors as a battery cell diagnostic technique and can also be considered within the wider field of fibre optic based battery diagnostics.

## 1.2. Objectives

To integrate the plasmonic based fibre optic sensors inside Lithium-ion pouch cells for the first time.

To interrogate the optical data collected and investigate correlation with battery cell state, to ascertain if there is potential value as a battery diagnostic tool.

To investigate different cell phenomena and the sensing platform's sensitivity to them.

To investigate the impact of the sensor on the battery performance and the robustness of the sensor to the cell environment.

To assist in developing the sensor design and the manufacturing and assembly techniques.

To investigate and hypothesise upon the sensor measurement mechanisms within the cell.

## 1.3. Thesis Overview

This study investigates the novel use of plasmonic based fibre optic sensors as a battery diagnostic technique, and demonstrates the potential of this technique to take data from directly inside battery cells via optical fibres and correlate this data to cell state and cell events.

Plasmonic sensing, most notably used in bio-technology, measures changes in the refractive index of the adjacent substance via attenuation of the internally reflected light signal [1–5]. The technology presents itself as a technology with numerous advantages applicable to lithium-ion battery cells, namely the potential for *in situ* and continuous monitoring of electrochemical activity (Li-ion diffusion at the electrode surface), the compact size, flexibility, chemical robustness, resistance to electrical and electromagnetic interference, low cost of sensors and remote operating capability [3]. The ability of the plasmonic based fibre optic sensors to 'look inside' the cell potentially offers an unprecedented view into internal cell phenomena.

The benefits and hence motivation of developing an *in situ* real time battery diagnostic technique can be envisaged. Cell processes down to the level of ion diffusion kinetics and electrode lithiation could be observed. Increased State of Charge (SOC) or State of Health (SOH) measurement accuracy could be utilised by the Battery Management System (BMS) to allow the battery to be run closer to its charge and discharge limits, allowing battery sizing to be closer to what is required for a given application, resulting in battery cost and weight savings. Battery charge profile impacts on batteries could be better understood, allowing further reduction of the recharge times by developing more optimised fast-charge regimes. Second life applications could also be better enabled, as a key challenge around

retired batteries is developing a reliable and efficient method of measuring the current State of Health. This could be of particular benefit in the EV industry as predictions of up to 120GWh of retired batteries with up to 80% capacity remaining by 2028 gives an idea of the scale of the second life reuse potential [6]. Similarly real time detection of cell events such as phase transitions or lithium-plating could have important research and production applications, such cell failure detection for safety considerations. Ultimately, while there are challenges that will be discussed further, it is not inconceivable to develop a battery pack diagnostics system that is entirely based on optical fibres.

This work investigates for the first time the application of the plasmonic sensing method inside Li-ion cells and demonstrates the potential for providing additional diagnostics data that can be used for cell research, cell characterisation, improved state measurement and support of production applications. In this study we report correlation between the sensor optical signal and cell state of charge, differing optical data obtained from both the anode and cathode side of the cells and detection of cell phase transition events including the use of reference electrodes, incremental capacity analysis and cyclic voltammetry. In addition substantial data is gathered confirming the presence of the sensor has negligible impact on the cell performance over repeated cell cycling, along with subsequent cell teardowns and Scanning Electron Microscopy (SEM) and Energy Dispersive X-ray (EDX) materials analysis. The cell mechanisms and kinetics that the optical sensors are responding to are further analysed by observing the optical response to Galvanostatic Intermittent Titration Technique (GITT) testing and the redox events during cyclic voltammetry. Forced lithium plating testing is also carried out and the optical response analysed, to analyse the optical response to this event and consider if such failure modes can be detected in real time by these sensors.

Fundamentally the hypothesis being tested in this study is that plasmonic based fibre optic sensors can be agnostically implemented inside lithium-ion cells and will provide data from inside the cell that correlates to cell state and electrochemical events, via measurement of internal material composition changes. In testing this hypothesis we explore the use of this novel sensing technology inside Li-ion pouch cells, which opens up the possibility of a new cell diagnostic and research tool able to obtain data from directly inside unmodified commercial standard cells.

## 2. Literature Review

### 2.1. Lithium-ion batteries

#### 2.1.1. Rechargeable battery market background

The rechargeable lithium-ion battery was first invented in the 1970's by Stanley Whittingham, with a functional and commercially viable version developed in 1976 utilising lithium/ aluminium and titanium di-sulphide electrodes [7], the achieved battery potential of approximately 2V was greater than many batteries of the time. Jürgen Otto Besenhard, Samar Basu and Rachid Yazami subsequently all contributed to the proposal, demonstration and development of using graphite as an anode in which lithium-ions could reversibly intercalate [8]. John Goodenough further developed this design by using a lithium-oxide instead of a metal sulphide cathode, discovering that lithium cobalt oxide almost doubled the voltage (to 3.9V) and energy density of the battery as well as having the additional benefit of being safer and less reactive than pure lithium [9]. Akira Yoshino subsequently utilised a petroleum coke anode which he found to have a longer cycling life than natural graphite which was decayed by the electrolyte. This series of developments resulted in a high potential, highly reversible battery with good safety and lifecycle characteristics and set the foundations for the modern lithium-ion battery.

In the 1980's Japanese companies had been looking for energy dense and rechargeable battery solutions to complement the development of portable electronic devices such as video cameras and phones, and the developed lithium-ion battery technology presented a solution that met these requirements and led to Sony first commercialising Lithium-ion batteries in 1991 [10]. Li-ion batteries subsequently gained an increasing share in portable electronic devices such as smartphones and laptops, such that they have displaced Ni-Cd batteries as the market leader[11]. The table below shows how by 2005 lithium-ion batteries had grown to dominate the portable electronic device market.

Table 2-1- Market share of rechargeable battery cells in portable electronic devices in 2005 (millions of cells sold) [12]

Application	Cell type				
	Ni-Cd	Ni-MH	Cylindrical Li-Ion	Prismatic Li-Ion	Pouch Li-Ion
Mobile phone		50		898.16	125.85
Notebook		22	422.68	16.34	2.50
Movie	2	4	67.98	11.91	
Digital camera		56	18.88	48.17	0.94
Power tools	575	53	20.14	0.08	
Audio	80	35	6.99	31.02	45.63
Games				26.82	14.4
Consumer	45	300			
Cordless phones	190	83			
Others	330	178	22.854	28.98	14.42

Lithium-ion batteries today have three primary market segments as well as further niche applications. These areas can be broadly described as the aforementioned portable consumer electronic devices, automotive electric vehicles and grid energy storage [8]. In addition there are numerous niche applications for lithium-ion batteries. An example is that Li-ion batteries are used to power electrical systems for aerospace, such as in the Boeing 787, where weight is a significant cost factor [11] and other highly specialised devices such as satellites and medical instruments [8]. There are other developing areas such as the electric vertical take-off and landing (eVTOL) sector, small planes, trains and boats [13,14].

Portable electronics have typically grown in their complexity and power demands, such as the transition from simple mobile phones to smartphones, while there has simultaneously been a desire to make the devices smaller for consumers. Both of these trends have increased the value of the lithium-ion battery's superior energy density. The trend of smaller and more powerful devices like smartphones, laptops, smartwatches etc. shows no sign of abating, while the growth potential of the market is still large, e.g. only 33% of the world's population currently has a smartphone. More specifically still lithium cobalt oxide (LCO) batteries currently dominate this market due to having the highest specific energy density of the common lithium battery materials, however as this battery type approaches its theoretical limits it is expected improved lithium nickel manganese cobalt (NMC) batteries will gain increasing market share, as the energy densities improve and with the added benefit of longer lifecycle [8].

Lithium-ion batteries have gained significant traction and have massive potential in the transport sector, particularly automotive. Two of the bestselling electric cars, the Tesla Model S and the Nissan Leaf, both use Li-ion batteries as their primary energy source [11]. In the first quarter of 2023 the Tesla Model Y became the best-selling car in the world over the quarter; the vehicle can contain both NCA and LFP battery chemistries, while the newly developed 4680 cell contains NMC 811 cathode chemistry. Table 2-2 demonstrates the dominance of Lithium-ion batteries in the EV market in 2017, NMC is the most commonly used chemistry while since then LFP (LiFePO<sub>4</sub>) has become increasingly common [15].

Table 2-2- Lithium-ion battery types in passenger electric vehicles, 2017 snapshot [8]

Manufacturer	Name	Battery Chemistry	Capacity (kWh)	E-engine Power (kW)	Vehicle Weight (kg)	Battery Pack share in weight (%)
Tesla	Model S 75D	NCA	75	245	2108	24
	Model S 90D	NCA	90	311	2240	25
	Model S 100D	NCA	102	451	2390	25
	Model S P100D	NCA	102	567	2234	26
General Motors	Chevrolet Bolt	NMC	60	149	1624	27
Volkswagen	e-Golf	NMC	35.8	100	1605	22
	e-Up	NMC	18.7	60	1139	20
Nissan	Leaf	NMC	30	80	1516	20
Hyundai	Ioniq	NMC	28	88	1420	20

<b>Ford</b>	Focus	NMC	33.5	107	1651	20
<b>Fiat</b>	500e	NMC	24	83	1352	19
<b>BMW</b>	I3	NMC	33	127	1343	24
<b>Daimler</b>	Mercedes B-Class	NCA	36	132	1725	17
	Smart Fortwo	NMC	18	60	995	16
<b>Kia</b>	Soul	NMC	27	82	1554	18
<b>Renault</b>	Zoe	NMC	41	68	1480	26
<b>BYD</b>	E6	LFP	82	89	2420	29
<b>Mitsubishi</b>	i-MiEV	NMC	16	49	1170	19

Figure 2-1 demonstrates the rate of growth of the global EV car market over the period of 2010 to 2017, from less than 100,000 EV cars on the road in 2010 to over 3 million in 2017, to around 30 million in 2022 [16]; while projections for future fleet numbers range from 100m to 900m EV's by 2040 [13]. The use of lithium-ion batteries in EV's has had a massive impact on the production of lithium-ion batteries which had previously been dominated by portable electronic devices, 120GWh of lithium-ion batteries were produced in 2017 of which 70GWh were for electric vehicles. Similarly going forward EVs are projected to demand 90 – 95% of total production of Li-ion batteries by 2030 respectively, compared with about 55% today. Considerations such as the rate the batteries can be charged and cost are currently regarded as obstacles to increased adoption [17], and as a consequence a lot of research is going into these areas, increased production volumes are also expected to improve the cost position [13].

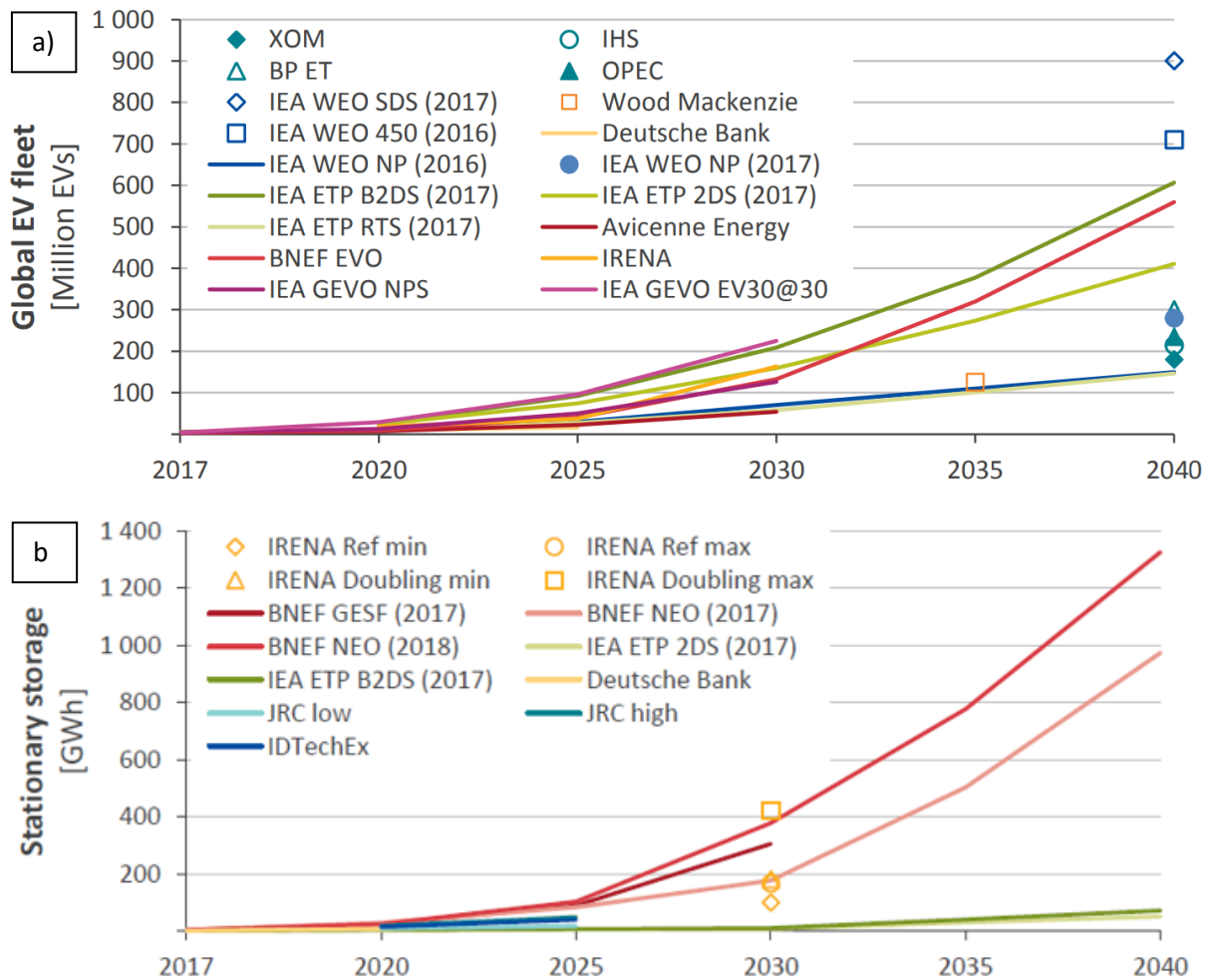


Figure 2-1- a) Projections for EV fleet numbers [13]- significant growth can be seen across the global market, although there is a wide range in future volume predictions, b) Projections for installed battery stationary energy storage [13].

Lithium-ion batteries can also be used to balance out energy supply and demand in the grid, particularly from renewable energy sources with inconsistent levels of power production such as wind energy, in order to help move towards a greener and more sustainable energy system. [18]. Tesla and PG&E recently began construction of a lithium-ion battery energy storage system in California that will become the largest in the world with 730 megawatt hours of capacity, with further potential to upgrade to 1.2-gigawatt-hours in the future- enough to power every home in San Francisco for six hours. [19]. The development of micro-grids could provide further application for lithium-ion batteries. These are localised grids that are not connected to the national grid, with potential use cases for the 13% of the world’s population that do not have access to electricity, remote locations and potentially part of a transition to a more decentralised supply of renewable energy sources [20].

Increasing automotive requirement for lithium-ion batteries due to EV has the potential to dovetail with energy storage needs, through the utilisation of ‘used’ EV batteries in ‘second life’ energy storage applications. Due to the customer requirements in automotive applications, such as long range and good recharge times, after a certain level of degradation the battery will no longer be fit for purpose. Li-ion batteries typically have to be retired from EV use while still preserving 70% - 80% of their initial capacity [21]. Potentially other applications can be found for which the retired EV batteries may still be suitable, such as energy storage systems, mobile battery charging stations and frequency response services. Reusing electric vehicle batteries once they have been retired from the automotive

application is recognised as one of the possible solutions to reducing electric vehicle costs and increasing the viability and adoption of electric vehicles. Current estimations predict that there will be 120Gwh of retired EV batteries by 2028 [6]. Currently the market penetration for using lithium-ion batteries for stationary electrical energy storage is low, around 6.5 GWh installed in 2017, but some projections estimate there could be an installed capacity of up to 1000 GWh by 2040.

There is some contention about lithium-ion batteries being an effective solution for grid energy storage however, as one of the key lithium-ion battery advantages of high energy density is not generally of great significance in this application. Other forms of energy storage such as for example pumped hydro energy storage, which dominates grid energy storage capacity with an installed capacity of 127–129 GW in 2012, representing more than 99% of worldwide bulk storage capacity in 2012 [22], and other battery types may be more suitable in some cases of this application [23]. There are a variety of electrical energy storage technologies that can be utilised for stationary energy storage, included mechanical devices such as pumped storage hydropower and compressed air, electrochemical devices including secondary batteries and flow batteries, electrical devices such as capacitors and superconducting magnets, chemical devices such as hydrogen fuel cell technologies and thermal heat storage [22]. Nonetheless the installed Li-ion battery power capacity for stationary energy storage continues to grow and is projected to continue to do so [13].

In summary, lithium-ion batteries have grown to dominate the portable electronics market, a market which continues to grow. In addition huge new markets in the form of electric vehicles and stationary energy storage have opened up for the technology [16], as well as promising niche applications. Analysts predict base case estimations of 4700GWh Li-ion battery capacity demand in 2030 across mobility, stationary energy storage and portable electronic devices [24]. While projections differ widely the current consensus is the market for lithium-ion batteries will grow hugely over the coming decade [13].

### 2.1.2. Lithium-ion battery properties and competitors

Lithium-ion batteries have dominated the rechargeable galvanic cell market over the past two decades. This is due to the properties of lithium including low mass-density, high theoretical capacity and highly negative reduction potential of lithium (-3.04V compared to a standard hydrogen electrode) making them well suited to applications where high power density and recharging is required [10]. Large negative reduction potential allows greater power to be produced due to power delivery being a squared relationship to voltage [23], while high power density is crucial in many application such as mobile phones, laptops, cars and potentially even aircraft [25].

Key existing and established competitor rechargeable battery technologies include lead-acid, nickel metal hydride and nickel cadmium, however current Li-ion batteries have a number of advantages over these competing rechargeable battery options; some of the pros and cons of these technologies are summarised in Table 2-3.

Table 2-3 Comparison of lithium-ion battery and competing traditional battery technologies pros and cons [8]

Battery Type	Pros	Cons
<b>Lead-acid</b>	<ul style="list-style-type: none"> <li>Relatively low initial cost</li> <li>Abundant cheap materials</li> <li>Low- self discharge rate</li> <li>No memory effect</li> <li>Mature Technology</li> <li>Proven recycling efficiency</li> </ul>	<ul style="list-style-type: none"> <li>Modest specific energy</li> <li>Short cycle life</li> <li>Sensitive to temperature</li> <li>Long charging time</li> <li>Limited reliability</li> <li>Safety; gas release and lead content</li> <li>High operating and maintenance requirements</li> </ul>
<b>Li-ion</b>	<ul style="list-style-type: none"> <li>Superior specific energy</li> <li>High efficiency</li> <li>Long calendar and cycle life</li> <li>Satisfactory operating temp. window</li> <li>Low operating and maintenance requirements</li> <li>High reliability</li> <li>Diverse range of chemistries</li> <li>Ecologically friendly chemistries available</li> </ul>	<ul style="list-style-type: none"> <li>Safety concerns, such as thermal runaway</li> <li>High initial cost</li> <li>Materials bottleneck, lithium and cobalt</li> <li>Currently weak recovery and recycling schemes</li> <li>Advance BMS required</li> </ul>
<b>NiMH</b>	<ul style="list-style-type: none"> <li>Moderate initial cost</li> <li>Moderate specific energy and power requirements</li> <li>Relatively fast recharge</li> <li>Satisfactory operating temp. window</li> <li>High reliability</li> <li>Good safety record</li> <li>Ecologically friendly materials</li> </ul>	<ul style="list-style-type: none"> <li>High self-discharge rate</li> <li>Slight memory effect</li> <li>Relatively short life cycle</li> <li>Currently weak recovery and recycling schemes</li> </ul>
<b>NiCd</b>	<ul style="list-style-type: none"> <li>Relatively low initial cost</li> <li>Outstanding calendar and cycle life</li> <li>Mature technology</li> <li>High reliability</li> <li>Low operating and maintenance requirements</li> <li>Reasonable self-discharge rate</li> <li>Good safety record</li> <li>Extensive operating temperature range</li> <li>Relatively fast recharge</li> </ul>	<ul style="list-style-type: none"> <li>Modest specific energy and power</li> <li>Memory effect</li> <li>Hazardous cadmium</li> <li>Relatively low efficiency</li> </ul>

Li-ion battery cells can deliver a potential of typically around 3.6 Volts nominal, 3 times higher than technologies such as Ni-Cd or Ni-MH. Li-ion batteries have no memory effect, a process where repeated partial discharge/charge cycles can cause a battery to ‘remember’ a lower capacity- an advantage over both Ni-Cd and Ni-MH, which display this effect. Li-ion batteries also have low self-discharge rate of around 1.5-2% per month. They do not contain toxic cadmium, which makes them easier to dispose of than Ni-Cd batteries- although nickel and cobalt also have adverse health effects. Li-ion batteries are also comparatively low maintenance, and do not require scheduled cycling to maintain their battery life. Lithium-ion batteries also have superior coulombic efficiency, typically 99% when charged to moderate current and temperature, compared to typically 90% for lead acid and 70-90% for nickel based batteries [11].

The high specific and volumetric densities of lithium-ion batteries, typically cited at 100-265 Wh/kg and 250-670 Wh/L [11], are crucial in many applications. Further to this, lithium-ion batteries also exhibit high specific power. Not only are the lithium-ion battery specific power and specific energy properties superior to other rechargeable batteries, the combination of the properties hits achieves a good balance for many applications when compared to other comparable electrical energy storage systems. Figure 2-2 compares these properties of Li-ion batteries to other comparable energy storage technologies.

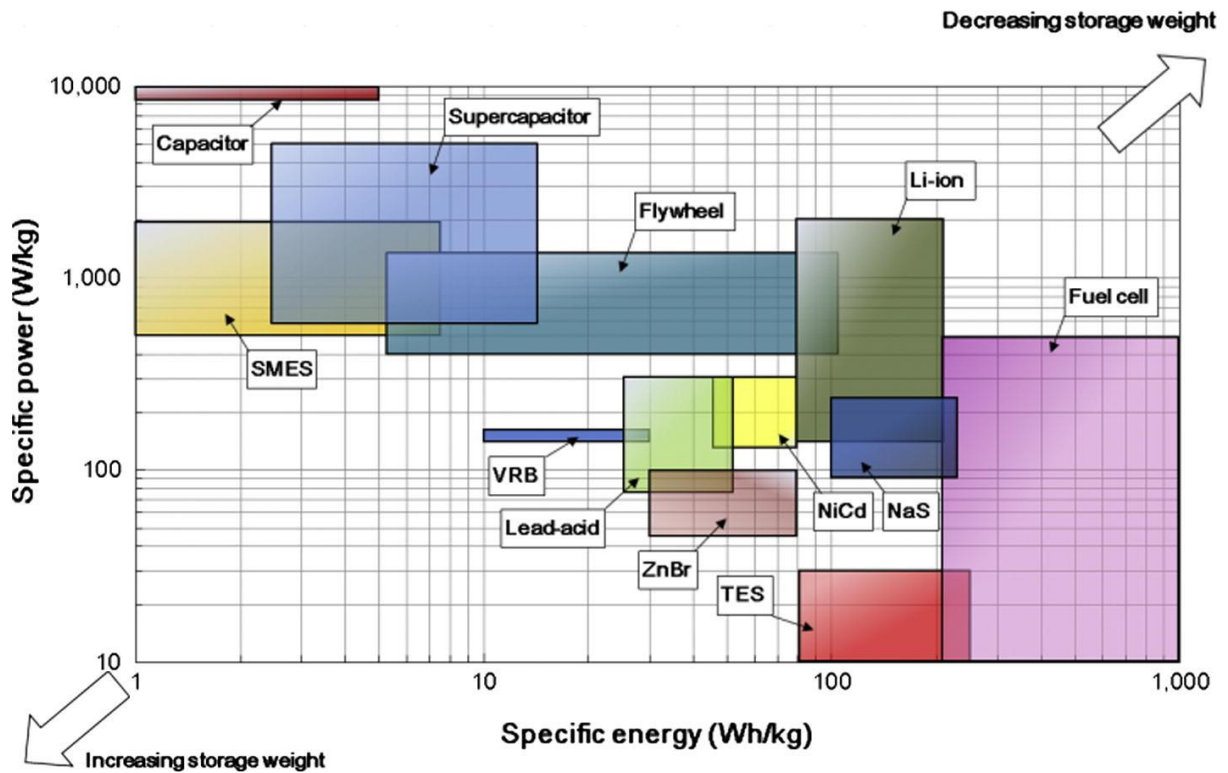


Figure 2-2- Comparison of specific power and specific energy of Li-ion batteries compared to other electrical energy storage technologies [22] Acronyms: SMES (superconducting magnetic energy storage), VRB (vanadium redox battery), ZnBr (zinc-bromine battery), NaS (sodium-sulphur), TES (thermal energy storage)

A summary of a variety of key metrics that demonstrate the superiority of lithium-ion batteries when compared to the established rechargeable battery competitors is given in Table 2-4.

Table 2-4- Characteristics of four types of batteries common in portable electronic devices [17]

Characteristics	Lead-acid battery	Ni-Cd battery	Ni-MH battery	Li-ion battery
Gravimetric energy density (Wh/ Kg)	30-50	40-60	60-120	170-250
Volumetric energy density (Wh/ L)	60-110	150-190	140-300	350-700
Battery voltage (V)	2.0	1.2	1.2	3.7
Cycle life (to 80% of the initial capacity)	300	1500	1000	500-2000
Self-discharge per month (%)	5	20	30	<10
Fast charging time (h)	8-16	1	1-4	1 or less
In use since	Late 1800s	1950	1990	1991
Toxicity	High	High	Low	Low
Overcharge tolerance	High	Moderate	Low	Low
Operating temperature range (°C)	-20 to 60	-40 to 60	-20 to 60	-20 to 60

In summary, lithium-ion batteries are superior to their current competitors in most characteristics. The primary drawback to the lithium-ion battery is cost, at typically \$300kWh<sup>-1</sup> for portable electronic device batteries it is the most expensive, compared to \$90kWh<sup>-1</sup> for lead-acid batteries. Nickel

Cadmium and Nickel Manganese fall between the two, with Nickel Cadmium being cheaper [27]. Regarding the use of lithium-ion batteries for EV's and stationary energy storage, cost is currently regarded as one of the significant barriers to increasing adoption, however studies have projected that the cost per unit of power will drop rapidly as technological advancements are made and production increases- from €500 – 800/ kWh at up to 10GWh hour cumulative deployment, to potentially €200 – 300/ kWh at 1000GWh cumulative deployment [13].

Ultimately Li-ion battery chemistry has some fundamental advantages. Lithium has the lowest reduction potential of any element ( $-3.04V_{SHE}$ ), which therefore entails that Li-ion cells have the highest possible potential. Lithium has the third smallest atomic weight allowing high gravimetric ( $0.534\text{ g/cm}^3$ ) and volumetric capacity and power density ( $3.86\text{Ah/g}$ ) [28]. Lithium also has one of the smallest ionic radii of any single charged ion which is crucial for mobility and electrode intercalation, particularly given that for battery power performance ionic diffusion in the solid electrodes is often the rate-limiting factor [29]. Despite the intrinsic advantages of Li-ion chemistry there are a diverse range of factors and disciplines that go into the optimisation of battery cell and pack performance for a given application; at their inception in 1991 Li-ion batteries could achieve specific energy of  $100\text{ Wh/kg}$  at a cost of approximately  $\$1000/\text{kWh}$ , in 2023 these figures have increased to  $350\text{ Wh/kg}$  ( $800\text{ Wh/L}$ ) at a cost of approximately  $\$200/\text{kWh}$ , with short-term targets in excess of  $400\text{ Wh/kg}$  ( $1100\text{ Wh/L}$ ) [30].

### 2.1.3. Battery cell designs

The modern established Lithium-ion battery cell's composition typically consists of a lithium metal oxide compound cathode with a layered, spinel or olivine structure, which can release lithium ions from its structure. The anode is typically graphite, into which lithium-ions can intercalate through diffusion and electrons can conduct through. An organic electrolyte allows the ionic movement of lithium ions, containing a mixture of organic carbonates, salts and additives. A microporous polymer separator prevents the cathode and anode layers from touching and short circuiting while allowing the electrolyte and ions to pass through, and copper or aluminium current collectors are used to allow current to pass through the circuit from the cathode to anode and *vice versa* [17]. These battery cell elements in a pouch cell structure are shown in Figure 2-3. Binders are also an essential part of the cell, required to fix the anode and cathode material to the current collectors, although they do not play a role in the electrochemical reaction [12].

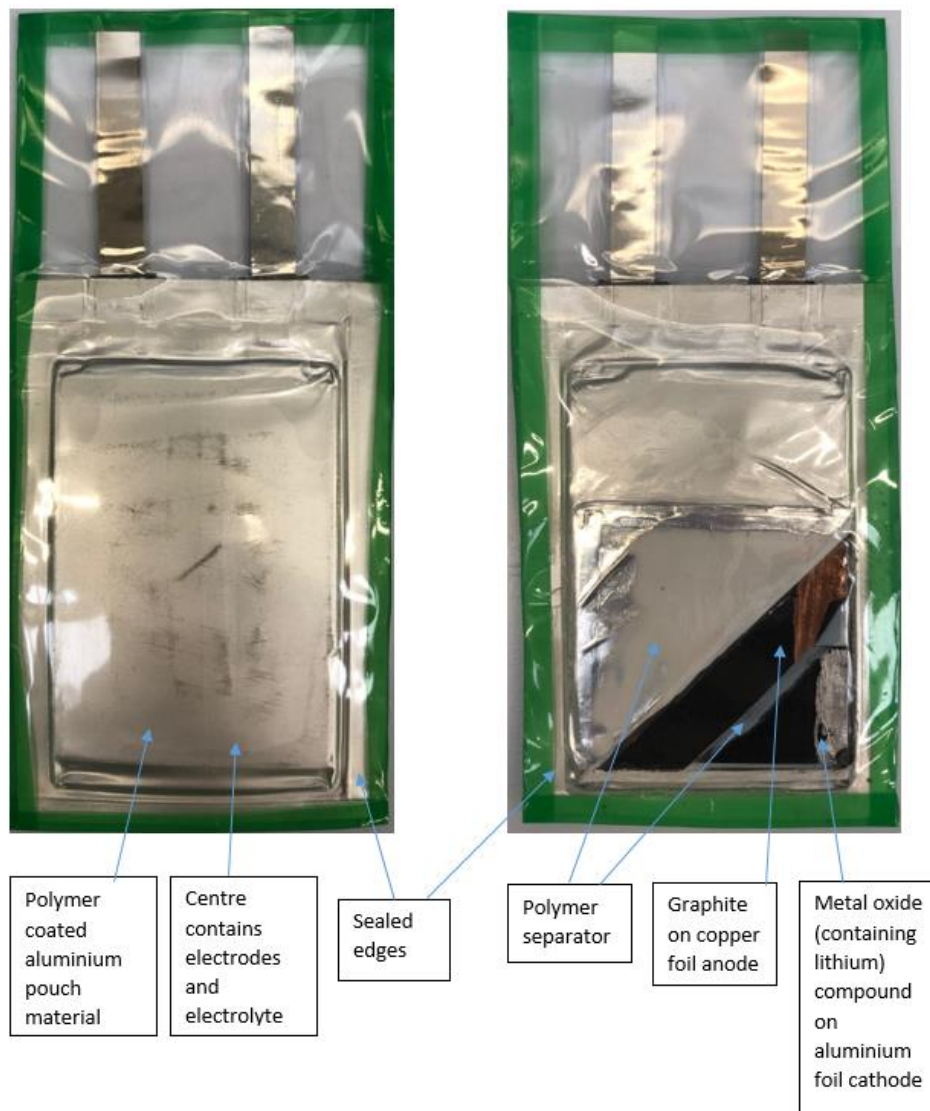


Figure 2-3- Image of a simple pouch cell and internals

Lithium-ion battery cells are typically found in four types; cylindrical, prismatic, pouch and coin cells. They usually consist of multiple electrode layers (a stack), with the exception of coin cells which tend to be single layer; in a cylindrical cell the electrodes are wound into a coil, in a pouch cell the electrodes are stacked flat, while in a prismatic cell the electrode tend to be stack and rolled but can sometimes be flat. The coin cell is a flexible cell design that is easy to make in low quantities as it can be assembled manually, it has a compact design but can swell when charged quickly with no safety vent- for applications requiring a large energy supply it would be a very inefficient choice due to the quantity required and ratio of casing to active electrode material. The cylindrical cell has good mechanical stability due the cylindrical shape which withstands internal pressure, it has good cycling ability, a long calendar life and is economical, but is heavy and has low packaging density due to space cavities. The prismatic cell improves space utilisation but it can be more expensive to manufacture than cylindrical cells in a higher volume industrialised process and less efficient in terms of thermal management, some swelling normally occurs and a firm enclosure is required for compression. Pouch cells are a simple, lightweight and flexible design solution, where the internals are encased in laminated pouch

material, the cells use space very efficiently, they do not have a rigid casing and can swell significantly however (8-10%) and are susceptible to heat and humidity [31].

A further cell design typically used in research and to investigate the electrochemical properties of battery cell materials is the Swagelok cell. They can be a two electrode style, where the electrode being studied is known as the working electrode and the other electrode is known as the counter-electrode. In cases where the counter electrode properties vary with current and so do not allow deconvolution of the properties of the working electrode from the overall cell, a three electrode design can be adopted where a reference electrode is introduced. The reference electrode should maintain a stable voltage that is not influenced by current, allowing the separation of the measurements of the working and counter electrode [32].

In terms of the cell component materials, the Li-ion cell anode must be a material which allows for reversible intercalation and de-intercalation. To allow this the material must be crystalline, there must be empty sites in the lattice in the form of isolated vacancies and electronic and ionic conductivity must be possible. Graphite has become the established anode material of choice in the lithium-ion battery, which has 2D layer vacancies in the layers held together by Van der Waals forces, allowing ionic movement and free electrons that can conduct electricity [9]. The anode is typically made of micro-particles of carbon (usually graphite) bound to a copper (typically) or aluminium current collector with a chemically inert binder, typically styrene-butadiene-rubber [12]. The practice of adding a small percentage of silicon to the graphite anode is also becoming a more common technique to increase its specific and volumetric capacity [33,34].

The cathode is typically a host structure that allows the release of the Li-ions from the lattice and movement of electrons[12]. There are various factors at play when considering the optimum cathode compound, including energy density, discharge profile, cost and safety depending on the requirements of the application. The typical material compounds used for Li-ion cell cathodes will be discussed in more detail in the following section. As well as the compound composition, particle morphology also plays a role in the capability of the cathode. The binder on the cathode must also be oxidation-resistant due to the unstable oxidising environment at the cathode, as well as chemically inert. Common cathode binders are polyvinylidene fluoride (PVDF) and acrylate-type copolymer (ACM) [12], while the cathode substrate is usually aluminium current collector.

Electrolyte in a battery cell acts as an ionic conductor allowing the lithium-ions to move between the electrodes, while being non-conductive for electrons. While there is extensive research into solid electrolytes, currently liquid electrolyte is much more common in lithium-ion batteries, the liquid electrolyte must seep into the porous electrodes such that they transfer lithium-ions smoothly between the liquid and solid phase interface. The standard electrolyte used today, first developed in the 1990's, is a liquid electrolyte with  $\text{LiPF}_6$  in carbonate solvents, such as propylene carbonate (PC). Other carbonate solvents used for the lithium salts include ethylene carbonate (EC), propylene carbonate (PC), dimethyl carbonate (DMC), ethyl methyl carbonate (EMC) and diethyl carbonate (DEC) [12].

A vital part of the cell is the formation of a passive layer called the solid electrolyte interface (SEI), the SEI layer provides a crucial role in the cell function, as it prevents the electrons in the anode coming into contact with and reacting with the electrolyte [35]. The SEI layer is formed during charging and discharging of the cell as some of the lithium ions react with the surface of the anode at the electrolyte interface; typically 10% of initial cell capacity is lost to SEI layer formation during the first cycle [36]. Initial cell cycling (formation cycling) is slow to ensure an effective SEI layer formation [37], SEI layers with a good structure and low electronic conductivity leads to very good negative electrode stability over long-term aging and at elevated temperatures. Additives play a crucial role in helping effective

SEI layer creation, and many additives have been experimented with. Vinylene carbonate is the most common example of an organic additive that has been shown to produce excellent results [35].

Additives are dissolved into the electrolyte to provide characteristics such as encouraging SEI growth and preventing SEI layer and graphite exfoliation, these are known as ‘functional electrolytes’ [12]. For example the additive 1,3,2-dioxathiolane-2,2-dioxide (DTD) was shown by Ming *et al.* to prevent SEI and graphite anode exfoliation at 4wt% or higher, while significant exfoliation occurred at only 1wt % [38]. The effect of such an additive is it to allow natural graphite to be used in the anode, rather than the more robust petroleum coke used in early lithium-ion batteries [9]. Another example is cyclohexylbenzene (CHB), at higher voltages it generates hydrogen gas which activates the current interrupt device and safety vent to prevent to prevent overcharge and serious safety issues [12]. Additives can further provide a number of improvements including improved cyclability, higher coulomb efficiency, improved reversible intercalation, higher voltage, improved stability and lower resistance, examples are detailed in Table 2-5 [38]. Also it should be noted that a cathode-electrolyte interface (CEI) layer forms on a Li-ion battery cell cathode. However the CEI layer is generally much less well understood than the SEI layer, partly this is because it’s role in battery cell function is not considered as significant as the SEI layer, it is also sensitive to electron beam and x-ray radiation and reacts with air and moisture [39]. The CEI layer thickness varies depending on chemistry, electrolyte and cell ageing, but is typically in the order of 10’s of nm, considered to possibly be slightly thicker than the SEI layer [167].

Table 2-5- A variety of electrolyte additives and their properties [38]

Electrolyte	Additives	Performance
1.0 M LiClO <sub>4</sub> in FEC/PC/EC (1/3.5/3.5, v/v/v)	Fluoroethylene carbonate	Improved cyclability
1.0M LiAsF <sub>6</sub> in EC-DMC (1:1, v/v)	5wt% Vinylene carbonate (VC)	Higher CE
1.0M LiClO <sub>4</sub> in EC/DEC (1:1, v/v)	2wt% VC + 0.5wt% SL	Higher CE
1.0M LiPF <sub>6</sub> in EC/PC/EMC (1:1:3, v/v/v)	1wt% Butyl sultone (BS)	Improved cyclability
1.0M LiBF <sub>4</sub> in PC/EC/EMC (1:1:3, v/v/v)	1-5mol % LiBOB	Improved cyclability
1.0M LiPF <sub>6</sub> in PC/DMC (1:1, v/v)	3,5-bis(trifluoromethyl) benzenboronic acid (BA)	Reversible intercalation
1.0M LiClO <sub>4</sub> in PC	10-20% VES	Reversible intercalation
1.0M LiPF <sub>6</sub> in PC/EMC (1:1, v/v)	PyrSO <sub>3</sub> , Me <sub>3</sub> NSO <sub>3</sub> , Et <sub>3</sub> NSO <sub>3</sub>	Reversible cyclability
1.0M LiTFSI/TMHATFSI	20 vol% Cl-EC	4V LIBs
1.0M LiClO <sub>4</sub> in EC/DEC (1:1, v/v)	K <sub>2</sub> CO <sub>3</sub> , KClO <sub>4</sub> , K <sub>2</sub> SO <sub>3</sub>	Higher CE
1.0M LiPF <sub>6</sub> in PC/ EC (1:1, v/v)	1,3,2-dioxathiolane-2,2-dioxide and its derivatives (cyclic sulfates)	Reversible Higher CE
1.0M LiPF <sub>6</sub> in PC-EMC (1:1, w/w)	Prop-1-ene-1,3-sultone	Reversible performance
Concentrated LiN(SO <sub>2</sub> CF <sub>3</sub> ) <sub>2</sub> in PC	Ca(N(SO <sub>2</sub> CF <sub>3</sub> ) <sub>2</sub> ) <sub>2</sub>	Reversible intercalation
1.0M LiPF <sub>6</sub> in EC/EMC/TMP (1:2:3, v/v/v)	0.5 M NaTFSA, or KTFSA	Higher CE

<b>1.0M LiPF<sub>6</sub> in EC/EMC (1/2, v/v)</b>	1-3% TMSP	Improved stability
<b>1.0M LiPF<sub>6</sub> in PC/DEC (1/1, v/v)</b>	1.5% 2(5H)-furanone	Lower resistance
<b>M LiClO<sub>4</sub> in EC/DEC (1:1, v/v)</b>	20 mass% TMP, PF-3DM, PF-3M, TFEP, or TEP	Variable performance

In general there are two primary methods to improve the energy density of a lithium-ion cell, one is to enrich the Li content using Li-rich cathodes to increase the charge density, and the other is to increase the output voltage by using high-voltage cathodes. The cathode must provide a structure to ensure reversibility of the reaction, with consideration to the thermodynamic and kinetic factors. The output voltage must also be within the electrochemical window of the electrolyte to suppress the decomposition of the electrolyte and parasitic reactions at the electrolyte- electrode interfaces. Adjustments in electrolytes and electrolyte additives can also be used to adjust the electrochemical window of the electrolyte[40]. In most lithium-ion battery applications, with the exception of stationary energy storage, there is a further challenge to maximise the volumetric energy density and power delivery, while mitigating the resulting safety issues [12]. In this respect battery diagnostics, which will be discussed later, plays a vital role as part of battery management system in monitoring the battery state and any potential issues.

#### 2.1.4. Li-ion battery electrode material structures and phase transitions

There are a variety of lithium compounds that are used on the cathode side of the cell, the most commonly utilised compounds and their properties will be discussed further here, an example of some typical compounds are given in the Table 2-6 [29].

Table 2-6- Typical intercalation cathode compounds and their characteristics [29]

Crystal structure	Compound	Specific capacity (mAhg <sup>-1</sup> ) (theoretical/ experimental/ typical)	Volumetric capacity (mAhcm <sup>-3</sup> ) (theoretical/ experimental/ typical)	Average voltage (V)	Level of development
<b>Layered</b>	LiTiS <sub>2</sub>	225/ 210	697	1.9	Commercialised
	LiCoO <sub>2</sub>	274/ 148/ 145	1363/ 550	3.8	Commercialised
	LiNiO <sub>2</sub>	275/ 150	1280	3.8	Research
	LLiMnO <sub>2</sub>	285/ 140	1148	3.3	Research
	LiNi <sub>0.33</sub> Mn <sub>0.33</sub> Co <sub>0.33</sub> O <sub>2</sub>	280/ 160/ 170	1333/ 600	3.7	Commercialised
	LiNi <sub>0.8</sub> Co <sub>0.15</sub> Al <sub>0.05</sub> O <sub>2</sub>	279/ 199/ 200	1284/ 700	3.7	Commercialised
	Li <sub>2</sub> MnO <sub>3</sub>	458/ 180	1708	3.8	Research
<b>Spinel</b>	Li <sub>2</sub> Mn <sub>2</sub> O <sub>4</sub>	148/ 120	596	4.1	Commercialised
	LiCo <sub>2</sub> O <sub>4</sub>	142/ 84	704	4.0	Research
<b>Olivine</b>	LiFePO <sub>4</sub>	170/ 165	589	3.4	Commercialised
	LiMnPO <sub>4</sub>	171/ 168	567	3.8	Research
	LiCoPO <sub>4</sub>	167/ 125	510	4.2	Research
<b>Tavorite</b>	LiFeSO <sub>4</sub> F	151/ 120	487	3.7	Research
	LiVPO <sub>4</sub> F	156/ 129	484	4.2	Research

The cathode materials are intercalation compounds, they create a structure which can store the lithium-ions and allow Li-ions to be removed from the structure reversibly. The typical compound types are lithium metal oxides (such as  $\text{LiN}_{1/3}\text{M}_{1/3}\text{C}_{1/3}\text{O}_2$ , or NMC, containing  $\text{O}_2$ ) and lithium-polyanion compounds (such as  $\text{LiFePO}_4$ , or LFP, containing the  $\text{PO}_4$  polyanion). Solid metal lithium electrodes are also a high priority research area [41], while another experimental research area involves using the metal chalcogenide Li-S in lithium-sulphur batteries [42]. These intercalation compounds can be further categorised by their crystal structures, such as layered, spinel, olivine, and tavorite [29]; these structures are graphically illustrated in Figure 2-4.

The different structures of the cathode compounds contributes to the differing properties of battery cells. Layered intercalation compounds (LIC) such as such as LCO (ie.  $\text{LiCoO}_2$ ), NCA (ie.  $\text{LiNi}_{0.85}\text{Co}_{0.1}\text{Al}_{0.05}\text{O}_2$ ) and in particular NMC (such as  $\text{LiN}_{1/3}\text{M}_{1/3}\text{C}_{1/3}\text{O}_2$  - NMC111) [43] play a significant role in commercial applications such as electric vehicles due to the relatively high volumetric and gravimetric energy densities, high operating voltages and naturally good electronic conductivity. Polyanion oxide olivine structure LFP (ie.  $\text{LiFePO}_4$ ) is also popular due to high thermal stability and better safety, relatively flat voltage charge profile, good conductivity when carbon coated and lower cost more abundant materials [8,29,44].

The different material compounds and structures also result in different phase transition behaviour during charge and discharge, that is to say the re-ordering of the material structure as the Li-ions intercalate/ deintercalate from it. Phase transitions have an important practical impact on the cell charge and discharge profile, during phase transitions the cell voltage will change less per unit of charge [45] and a more consistent voltage and power output across the battery state of charge is generally desirable. The discharge profiles for a selection of cathode chemistries of different material structures are shown in Figure 2-4.

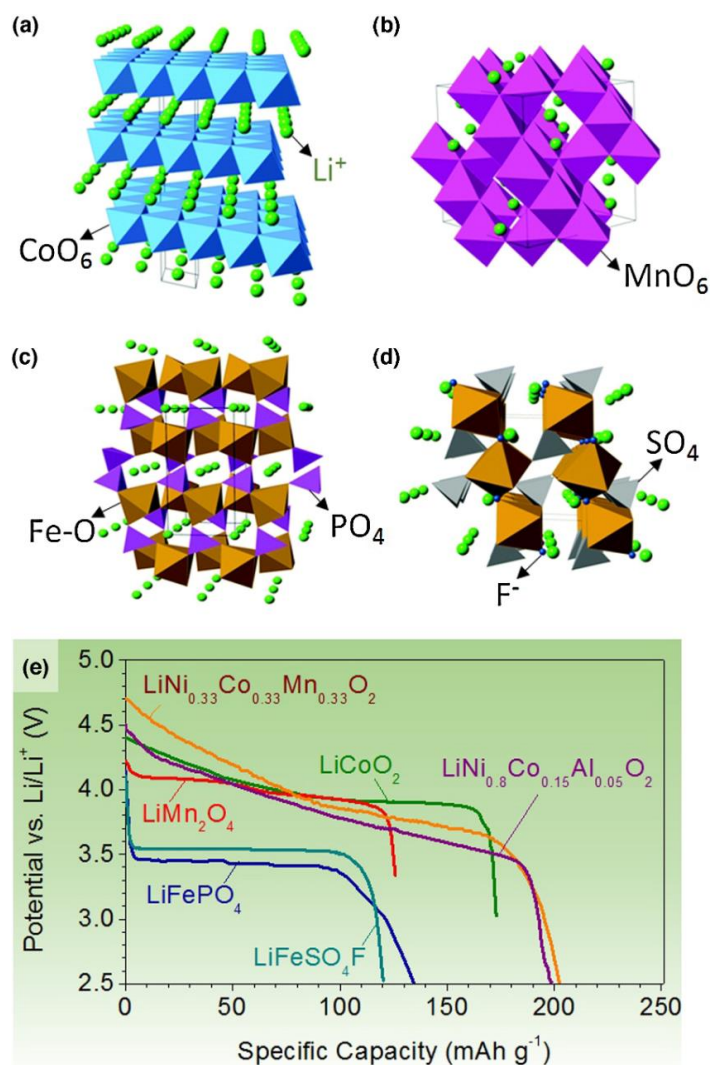


Figure 2-4- Images of layered (a), spinel (b), olivine (c) and tavorite (d) crystal structures, and (e) Typical discharge profiles for a selection of chemistries [29]

Phase transition behaviour can vary significantly between different electrode chemistries. For example, NMC111 is a transition metal oxide layered intercalation cathode that stores Li-ions between the lattice layers in octahedral sites [29,46]. During deintercalation of Li-ions when charging the cell the charge compensation mechanism is understood to be oxidation of the  $\text{Ni}^{2+}$  ions to  $\text{Ni}^{3+}$  and  $\text{Ni}^{4+}$  [47–49]. As the transition metal elements are oxidised during cell charging the Jahn-Teller effect leads to distortion of the octahedral structures within the lattice [50]. As can be seen in Figure 2-5, while NMC111 normally undergoes two clear detectable phase changes under full cell IC analysis, NMC811 undergoes a third at approximately 4.1V [51].

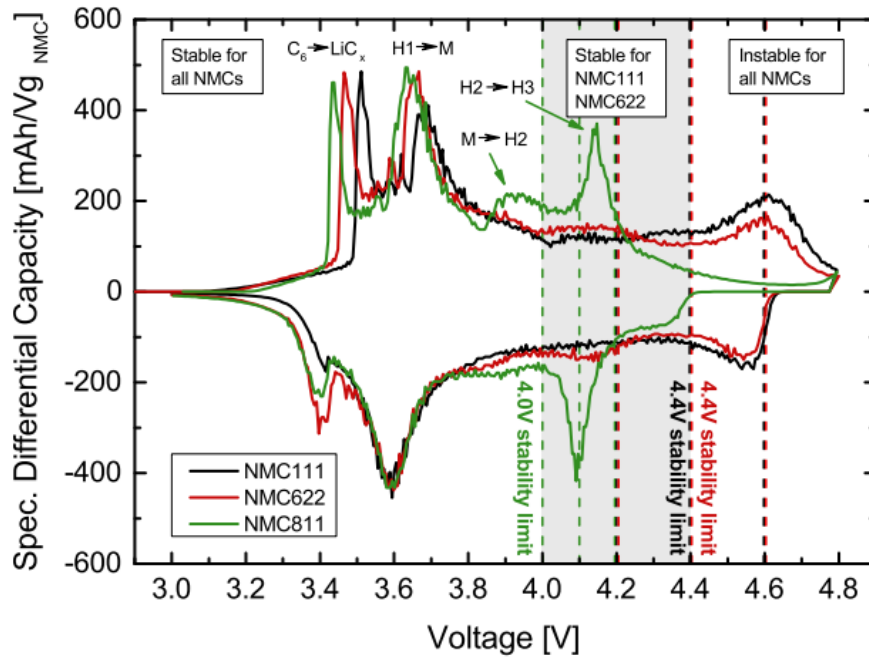


Figure 2-5- Incremental (or differential) capacity (IC) versus cell voltage for NMC111, NMC622 and NMC811 cathodes versus graphite electrodes [51]

While the cell voltage is determined primarily by the cathode voltage once the anode has undergone initial lithiation on the first charge cycle, we can also note that the counter-electrode has a significant impact on the full cell phase change behaviour. Studies have shown that an IC plot of a ‘half-cell’ of NMC111 versus lithium, also shows a possible initial phase change peak that is much less obvious and almost merges into the second peak [52]. We can also compare NMC versus graphite IC plots to LFP versus graphite IC plots. In IC plots for an LFP versus graphite cells studies have identified five peaks, three of which are distinct and two of which are more subtle, across the voltage range of 3.1 to 3.45V [53].

The graphite anode also undergoes structural changes during charge as lithium ions intercalates into it, from delithiated carbon through to fully lithiated  $\text{LiC}_6$  [54–59]. The argument has been made that graphite can go through up to 6 phases as it is lithiated from  $\text{Li}_0\text{C}_{12}$  to  $\text{LiC}_{12}$ , with some temperature dependency on the nature of the phases and when the transitions occur [60]. Once lithitated following initial charge the anode voltage drops from around 2V vs lithium to 0.2V in a NMC versus graphite cell ([61]). During subsequent charge and discharge the anode voltage then changes relatively little (between 0.1V to 0.2V versus lithium) compared to the cathode voltage change. As such the graphite anode impact on overall cell voltage is minimal, while playing a vital role in the cell function by hosting the Li-ions. In Figure 2-6 the graphite phase transitions in a lithium-graphite cell are detected via the peaks in a cyclic voltammetry plot [62].

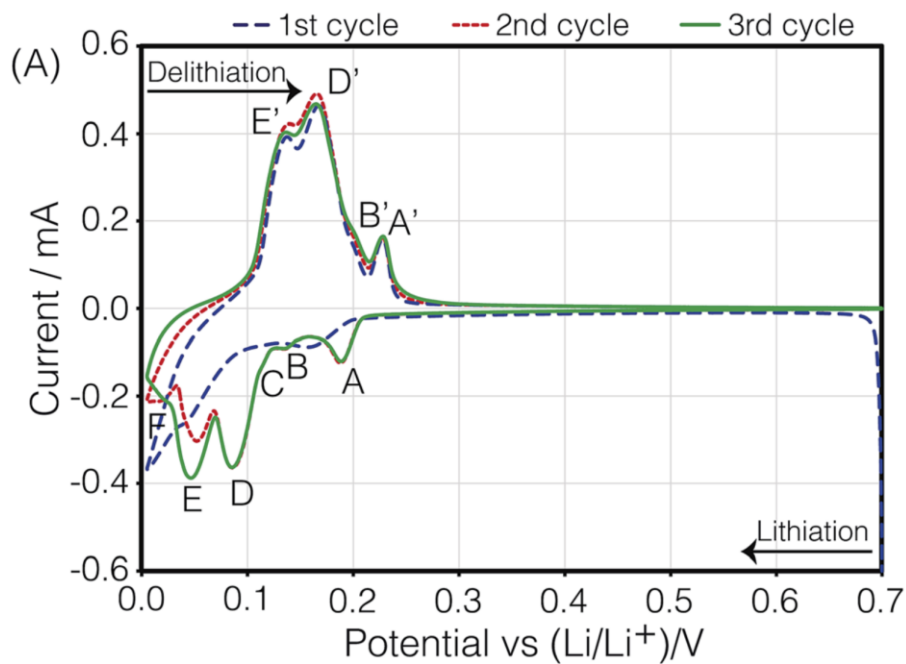


Figure 2-6- Cyclic voltammogram of a carbon/Li cell cycled at  $2 \mu\text{V s}^{-1}$  [62]

Secondary anode materials are currently standard in Li-ion batteries due to challenges such as dendrites formed by pure lithium that can cause short circuiting and cycle life issues [29].

### 2.1.5. Li-ion cell working mechanisms

The lithium-ion battery is a galvanic cell that is charged by applying a voltage to it that forces the oxidation of lithium atoms at the cathode. The applied voltage forces the free electrons to be transferred from the cathode to the anode via the current collectors and circuit, while the lithium ions, attracted by the electrons, flow through the electrolyte to the anode and intercalate there. Once the charging voltage is disconnected and a circuit applied from the anode current collector to the cathode current collector the lithium ions flow back to the cathode, where they are more thermodynamically stable, attracting the electrons which flow back through the circuit as they cannot pass through the non-conductive electrolyte, generating electricity in the circuit [63].

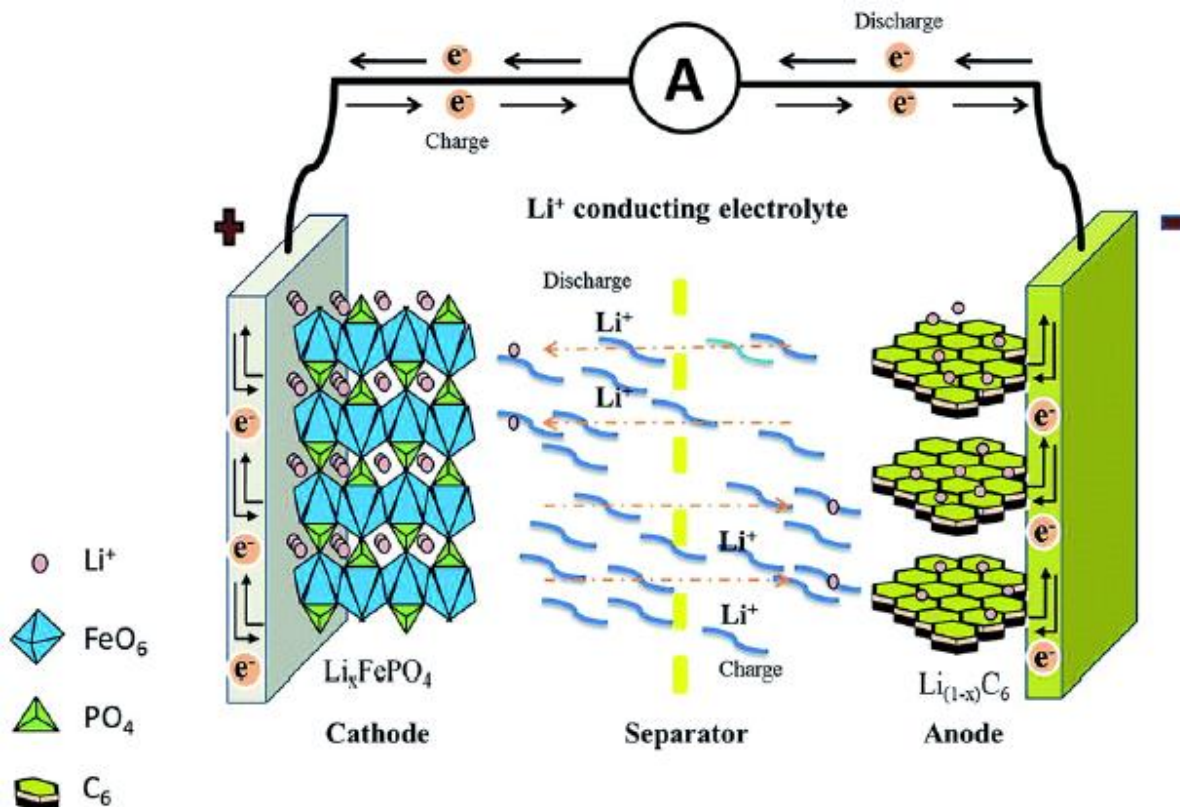


Figure 2-7- schematic example of a charging/ discharging lithium-ion galvanic cell [64]

Galvanic cells, through which faradaic current spontaneously flows on the connection of the electrodes via a conductor, are employed to convert chemical to electrical energy in a huge variety of applications. Variations can include non-rechargeable, rechargeable and fuel cells. The electrolytic cell works in the reverse direction, in which a voltage greater than the open circuit potential of the cell causes a chemical reaction [63].

Although current is predominately produced through faradaic process in galvanic cells such as lithium-ion based cells, non-faradaic processes also occur as the electrode-solution interface changes through processes such as adsorption, double layer capacitance, SEI layer formation and other incidental chemical reactions. These processes can also produce transient currents as well as impacting the properties of the cell [63]. Faradaic processes are best described as the completion of redox reactions at the electrode where both the reactants and products come from or go to a phase material outside and in contact with the electrode. While non-faradaic processes are any other type of reaction in which charge is stored, including irreversible reactions and redox reactions where charge does not leave the electrode [65]. In a reversible electrode reaction, the mass transfer is the limiting factor in charge transfer and the reactions that occur are very rapid. In a faradaic process the surface concentrations of the species involved are related to the electrode potential by the Nernst form equation. The modes of mass transfer are migration under the gradient of an electric field/ potential, diffusion under the gradient of a chemical potential and natural convection caused by density gradients or forced convection [63].

The typical voltage range of a Li-ion cell with lithium metal oxide cathode and carbon anode is 2.5 to 4.2 V, with a nominal voltage of approximately 3.6V. The voltage of the cell varies with the cell state of charge, at full charge the cell is at its peak voltage, this voltage drops rapidly after the first 30% or

so of discharge, then plateauing at the 'nominal' voltage of the cell for most of the cycle, before finally dropping again rapidly to the minimum voltage after about 80% discharge. At lower state of charge and voltage the battery kinetics, or ability to push the ions from cathode to anode, are affected, with the time for the battery to reach an equilibrium state after charge or discharge being increased [66]. The relationship between charge and open circuit voltage (OCV) also changes with battery temperature and ageing, although such effects in a Li-ion battery with carbon anode are minimal [67]. The graph in Figure 2-8 gives an example of a change in a Li-ion NMC cell operational voltage and OCV with state of charge. Note the operational voltage is the voltage measured at the terminals when the battery is in operation, while the OCV is the voltage of the unconnected cell, the difference between the values being known as overvoltage [68].

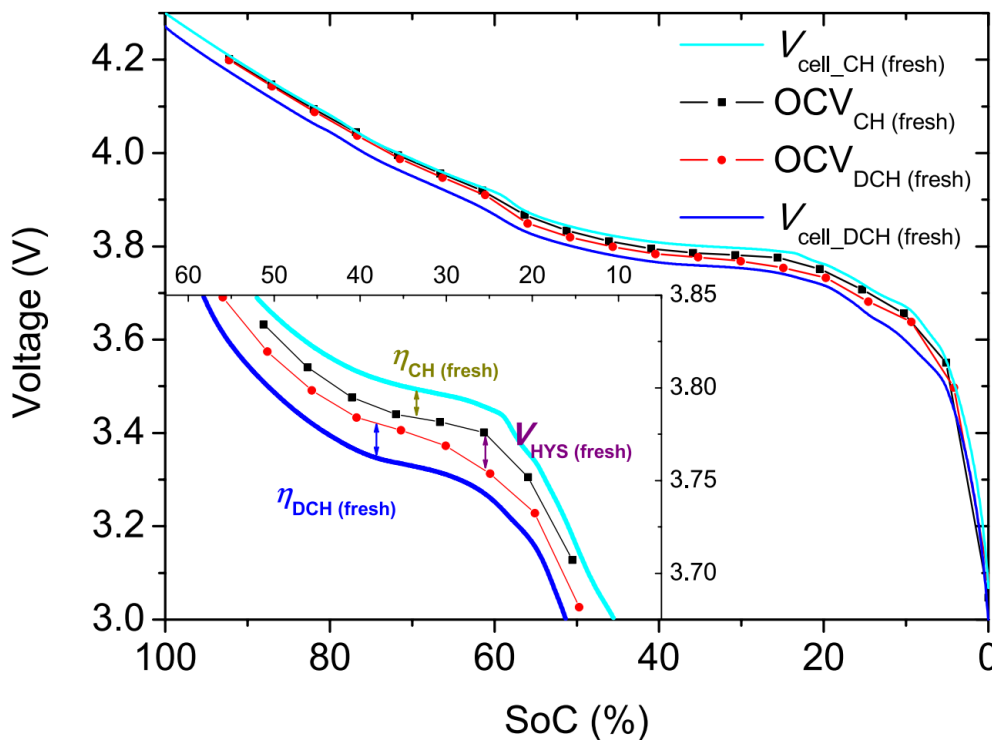


Figure 2-8- Charge and discharge profiles of new Li-ion NMC cells at C/25, showing both cell operational voltage and OCV against state of charge [68]

State of Charge (SOC) and State of Health (SOH) are two key characteristics when defining a battery's current state. The SOC of a battery cell is best defined as the remaining exchangeable lithium-ions in a cell as a proportion of the total at a low rate of exchange, at a given point in the cell's life - this equates to the proportion of remaining capacity under specified conditions. This should not be confused with remaining capacity under nominal conditions, as the conditions of the cell can dramatically affect the remaining capacity. The remaining number of intercalation sites also cannot be used as a measure because in practice the full number of sites are not utilised [67]. The SOH of a battery is a measure of its capacity at that point in its life compared to its capacity when new.

### 2.1.6. Cell kinetics/ thermodynamics

There are many processes within a typical Li-ion cell that contribute to the overall cell kinetics. The electric field generated in a battery cell is crucial to the operation of the cell, during the charge process this is generated by applying a voltage to the cell which forces electrons to the cathode and

subsequently creates an electrostatic force that attracts the positively charge lithium ions. During cell discharge the potential is created by the greater stability of the Li-ions in the metal oxide, encouraging the discharge of Li-ions from the anode to cathode. The relationship between migratory flux and electric field is given in Equation 1. However in a Li-ion cell the solvent between the electrodes is typically flooded with background electrolyte (such as LiPF<sub>6</sub>) of at least 0.1M concentration, typically at least 100 times the concentration of the reactant, which supplies sufficient background ions to maintain electroneutrality within the solution. As such the migratory effects of the electric field within the electrolyte solution are negligible in the bulk of the solution and are confined to the consequently compressed double layer [69].

$$j_m \propto -u[B] \frac{\partial \phi}{\partial x} \quad (1)$$

Where:

- $j_m$  is the migratory flux
- $u$  is the ionic mobility of the ionic species
- $[B]$  is the concentration of the ionic species
- $\frac{\partial \phi}{\partial x}$  is the electric field strength

The current density at the electrode surface can be related to the materials, surroundings and potential difference between the electrode and electrolyte via the Butler-Volmer equation; this equation takes into account the activation overpotential, which is the energy required to start the reaction (the charge transfer). The equation is based around a simple redox reaction where both reduction and oxidation happens at the electrode surface, and has a term for both the oxidation and reduction directions of the reaction. The proportion of the potential that lowers the energy barrier, by changing the Fermi level, to allow the reaction to proceed is represented by the charge transfer coefficient ( $\alpha$ ); in a completely reversible reaction which proceeds entirely via electron transfer (no chemical steps) then  $\alpha$  is equal to 0.5 and the Butler-Volmer equation reduces to the Nernst equation, which will be discussed subsequently [69].

$$j = j_a + j_c$$

Where:

- $j$  is net current density
- $j_a$  is anodic current density
- $j_c$  is cathodic current density

Expanded to:

$$j = j_0 \cdot \left\{ \exp \left[ \frac{\alpha_a z F}{RT} \right] (E - E_{eq}) - \exp \left[ \frac{\alpha_c z F}{RT} \right] (E - E_{eq}) \right\}$$

Where:

- $j_0$  is the exchange current density, this is when the reaction is at equilibrium and the current flowing in both directions is balanced such that no net current flows.
- $\alpha_a$  is the anodic charge transfer coefficient (oxidation as metal ions dissolve into electrolyte)
- $\alpha_c$  is the cathodic charge transfer coefficient (reduction)
- $z$  is number of electrons involved in the electrode reaction
- $F$  is Faraday's constant ( $9.9 \times 10^4 \text{ C} \cdot \text{mol}^{-1}$ )
- $R$  is the universal gas constant ( $8.314 \text{ J} \cdot \text{K}^{-1} \cdot \text{mol}^{-1}$ )
- $T$  is the temperature of the system (K)
- $E$  is the applied potential
- $E_{eq}$  is the equilibrium potential

In a reversible battery cell we therefore can assume that the potential applied to the cell adjusts the reaction quotient (the ratio of products to reactants) in the electrolyte at the surface of the electrode according to the Nernst equation ((2). When the potential exceeds the equilibrium potential the reaction favours the products and the ratio of products to reactants increases, and *vice versa* when the potential is less than the equilibrium potential. In this way applying a potential to the electrode leads to a change in the product and reactant ratio in the electrolyte at the surface of the electrode, this change in concentration then drives diffusion from the bulk of the electrolyte solution.

$$E = E^0 + \left(\frac{RT}{nF}\right) \ln \frac{[ox]}{[red]} \quad (2)$$

Where:

- $E$  is the applied voltage
- $E^0$  is the equilibrium voltage
- $R$  is the universal gas constant ( $8.314 \text{ J} \cdot \text{K}^{-1} \cdot \text{mol}^{-1}$ )
- $T$  is the temperature of the system (K)
- $n$  is the number of moles of electrons transferred
- $F$  is Faraday's constant ( $9.9 \times 10^4 \text{ C} \cdot \text{mol}^{-1}$ )
- $[ox]$  is the concentration of the oxidised product
- $[red]$  is the concentration of the reduced reactant

Cell kinetic processes include ionic diffusion of the lithium-ions through the electrode bulk material, the charge transfer process of the ions passing across the electrode- electrolyte boundary, the diffusion resistance of the Li-ions through the electrolyte solution and the resistance through the separator membrane. The charge transfer process is in itself a multi-step process, involving the desolvation of the  $\text{Li}^+$  ion from the liquid electrolyte, diffusion of the ion through the SEI layer and then addition of an electron to form a lithium molecule [70]. The charge transfer process begins in a reversible reaction when the voltage is sufficient to achieve the activation energy to instigate the

charge transfer, in an irreversible reaction additional 'overpotential' is required in addition to the activation energy to instigate the reaction. Additionally, a Helmholtz double layer is formed at the surface of the electrodes, caused due to the net charge at the electrode surface in non-steady state conditions, which has a capacitive effect. As such equivalent circuit models can be used to model a cell behaviour [71]; a simple example of model representing an electrode and electrolyte interface is typically a resistor in series with a resistor and capacitor in parallel (such as that shown in

Figure 2-11)- the parallel resistor and capacitor represent the capacitance of the Helmholtz double layer and the charge transfer resistance across the boundary layer, while the series resistor represents resistance of the ions passing through the electrolyte.

A diffusion layer (or Nernst layer) forms in the electrolyte when the electrochemical reaction is taking place, this is caused due to the consumption of reactants in the electrolyte at the electrode surface which causes a gradient in product concentration to be created between the electrolyte at the electrode surface and the bulk electrolyte. This gradient drives diffusion of the Li-ions in the electrolyte, and the diffusion layer will grow over time- in theory the diffusion layer can continue to grow but in practice natural convection normally limits it's depth [69,72]. Diffusion tends to be the driving force of Li-ion movement in the bulk of the solution in the absence of migratory flux (due to the high concentrations of background electrolyte).

For cells in typical conditions with electrodes of thickness in the order of millimetres the Nernst diffusion layer thickness can grow to approximately 0.5mm. Fick's law states that the number of moles of material diffusing through a unit area in one second is:

$$j_B = -D_B \frac{\partial[B]}{\partial x} \quad (3)$$

Where:

- $j_B$  is the diffusional flux, or number of moles of species B diffusing through a unit area per second
- $[B]$  is the concentration of species B
- $x$  is the distance from the electrode surface
- $D_B$  is the diffusion coefficient for the given species.

This therefore tells us that flux of the species to the electrode surface should increase when the diffusion layer concentration difference over depth gradient is greater [69].

Additionally, the magnitude of current given by an electrochemical reaction is defined by:

$$i = AFj \quad (4)$$

Where:

- $F$  is the Faraday constant (96485 Cmol<sup>-1</sup>)
- $A$  is the electrode area (cm<sup>2</sup>)
- $J$  is the flux of the reactant species reaching the electrode surface (moles cm<sup>-2</sup>s<sup>-1</sup>)

Combining Equation 3 and Equation 4, and assuming a linear diffusion layer gradient, we can say that:

$$i = \frac{D_B F A ([B]_{bulk} - [B]_o)}{\delta_d} \quad (5)$$

Where:

- $[B]_{bulk}$  is the concentration of species B in the electrolyte bulk
- $[B]_o$  is the concentration of species B at the electrode surface

That is to say that the current generated, which is a result of the species reacting at the surface, is therefore proportional to the gradient of the diffusion layer for a given species when diffusion transport is the rate-limiting factor. The amount of reactants in the electrolyte at the electrode surface depends on the electrode potential, at high electrode potentials reactants rapidly undergo redox reactions and so  $[B]_o$  tends to zero [69].

The slowest step in the reaction processes is known as the 'rate-limiting step', this step acts as the 'bottleneck' which dominates the electrochemical response. For example, if the slowest step is the transport of molecules through the electrode bulk to the surface, the reaction is described as 'mass transport limited'. The rate limiting step in a Li-ion cell varies depending on the cell composition and conditions, however it is typically the lithium migration through the electrode bulk material at higher voltages and in warmer conditions [70], and the charge transfer resistance involving the de-solvation of the Li-ions from the electrolyte and transport of Li-ions through the SEI layer at lower voltages and in colder conditions [73]. The activation energy required to transport the Li-ions across the SEI or CEI layer is dependent on the composition of the layers, which can be influenced by the electrolyte solvent, ionic salt and additives used [70].

### 2.1.7. Lithium-ion diffusion

As noted in previous sections, lithium-ion movement in the electrolyte is caused by diffusion and convection, as well as the fundamental migratory effect of electric potential difference induced in the cell [69]. As such, it is complicated to model the flow of Li-ions in electrolyte, however if a cell has minimum agitation and a fairly controlled temperature then the convection effects can be minimised, if the electrolyte has sufficient quantity of ions the migration due to the electric potential is also negligible, while the reaction quotient at the electrode surface can be modelled using the Nernst equation and the profile of Li-ion reactants approaching the surface can be modelled using Fick's law.

Additionally the rate of diffusion of the Li-ions in the electrodes can be considered. Typically in Li-ion cells in a metal oxide versus graphite configuration, the graphite is recognised as being the rate limiting electrode with the slower diffusion rate, in which a high charging rate risks causing lithium plating on the graphite anode surface [74]. By extension the Li-ions will not diffuse linearly into the electrode, the Li-ion concentration will build up at the surface of the electrode and then diffuse into the bulk material over time; this is something that is particularly observable in GITT tests, where voltage spikes after the initial voltage pulse and then relaxes during the rest period, this allows the diffusion coefficient to be calculated through GITT testing. Diffusion coefficients can be influenced by material structure and temperature [75].

Measuring the change in Li-ion concentrations in different locations in the electrolyte and electrode through physical measurements is a challenging task due to the nanometer resolution variations and the fact that a measurement process risks disturbing the natural behaviour. An interesting study into this area has been carried out using a lithium versus graphite half-cell with an optical window at the base of the graphite to carry out Fourier transform infrared spectroscopy (FTIR) and attenuated total reflection (ATR) optical measurements. The IR measurements could be correlated to lithium concentration, and it was found that higher charge rates had a greater impact on Li-ion concentration variation due to the ion-transport limitations [76]. FTIR techniques have also shown the change in solvents in the electrolyte as the Li-ions intercalate into a graphite anode [77].

### 2.1.8. Limitations, ageing mechanisms and failure modes

Limitations and failure modes of batteries can be considered at different physical size scales. At the atomic level; the electrical potential of the electrode materials, the speed with which ions can diffuse and transfer charge are key factors. At the nano to microscale; SEI growth, lithium plating and mechanical degradation of the electrodes can all contribute to cell degradation. At the cell level; inhomogeneous temperature, current and charge distribution can cause mechanical strains and create failure points within the cell. At the battery pack level; cooling, cell balancing and management are required to minimise premature failure within a particular cell or group of cells [17].

The causes of battery cell failure can be both operational and environmental. Key causes of failure include the reactions that occur in the cell over time, high temperature, the cell being charged to high voltage or SOC, high current loads, low temperatures during operation or charging, formation of corrosive substances and the changing stoichiometry of the cell as parasitic reactions occur, mechanical stresses in the cell due to temperature and charge inhomogeneity or the battery reaching a very low voltage or SOC. These can in turn contribute to a host of degradation mechanisms, including continued SEI growth, SEI decomposition, electrolyte decomposition, binder decomposition, graphite exfoliation, structural disordering, lithium plating/ dendrite formation, loss of electric contact, electrode particle cracking, transition metal dissolution and corrosion of current collectors [78]. Figure 2-9 visually displays a range of cell degradation mechanisms.

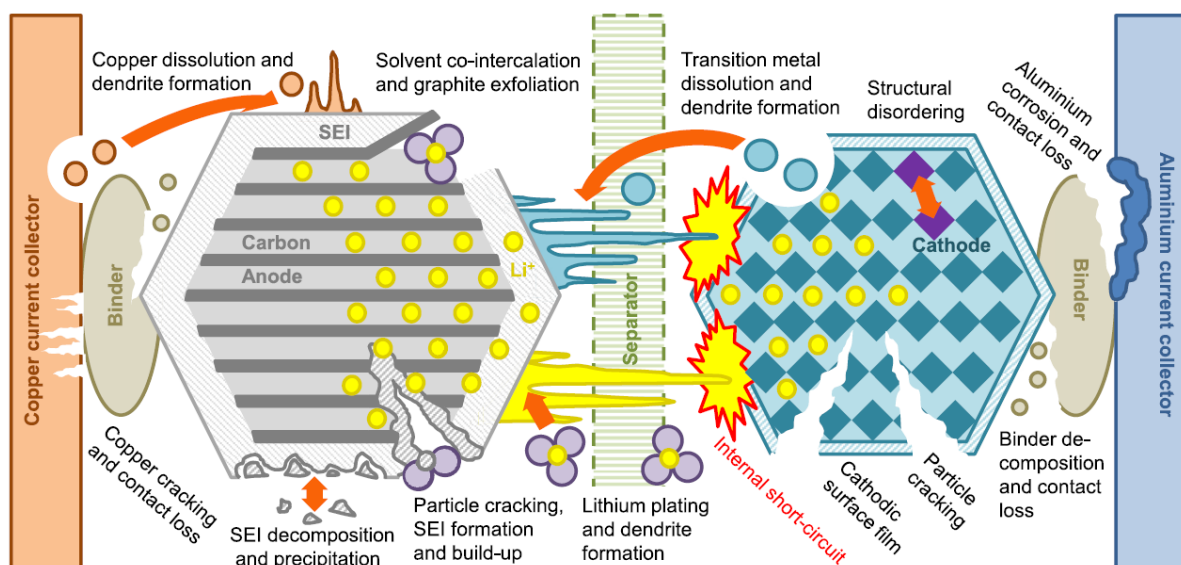


Figure 2-9- Degradation modes in lithium-ion cells [78]

Despite the complex interplay of factors that can lead to battery cell degradation, the measurable and physical effects can be classed in three general groups, namely loss of lithium inventory (LLI), loss of active positive electrode material (LAM<sub>PE</sub>) and loss of active negative electrode material (LAM<sub>NE</sub>). LLI causes capacity fade due to loss of lithium ions which are no longer available for cycling due to loss in SEI layer growth, decomposition reactions, lithium plating and dendrite formation etc. LAM<sub>NE</sub> causes capacity and power fade through loss of intercalation sites due to particle cracking, loss of electrical contact and blocking of active sites. LAM<sub>NE</sub> also causes capacity and power fade through loss of lithium insertion material due to structural disordering, particle cracking or loss of electrical contact [78].

At the extreme end of the consequences of cell degradation is catastrophic failure, usually triggered by thermal runaway in which rising cell temperature become self-sustaining via SEI decomposition, electrolyte decomposition, melting separator, complete short-circuit, metal oxide decomposition and releasing oxygen, lithium melting and combustion [79]. Events such as short circuiting or prolonged overcharge can set this process in motion, which ultimately causes the cell to burst into flames due to the reaction of the freed oxygen with lithium. An event such as short circuiting could occur due to battery penetration from an external body or dendrite growth. [8]

The negative electrode/electrolyte interface plays a critical role in some aspects of cell degradation. Excessive SEI growth induces a capacity loss over time due to LLI, while the active surface area degradation and increase in charge transfer resistance increases cell impedance and reduces the power capability of the electrode. In the worst case the reduction of charge rate capability may lead to local lithium plating during cycling, further increasing rate of capacity reduction through LLI and LAM<sub>NE</sub> [35]. An SEI layer that is susceptible to corrosion by the electrolyte leads to exfoliation of the SEI layer and graphite anode, while electrons in the carbon can then react with the electrolyte leading to LLI. As such, the electrolyte and additives used must ensure good SEI stability [12].

The electrode/electrolyte interface can be affected by high SOC and/or elevated temperatures inducing parasitic reactions at the anode surface resulting in electrolyte decomposition. This results in an increase of cell impedance and potentially slow gas evolution, which can cause a pressure build up in the cell. Again, appropriate choice of active materials and electrolyte and effective cell design have a significant impact on the longevity of the cell [35].

These material characteristics and risks result in conservative limitations to lithium-ion battery recharge times. Range anxiety and recharge times (compared to combustion engine vehicles) are issues typically cited as being amongst primary issues hindering greater adoption. However, the high currents needed for a fast rate of charge typically reduce energy efficiency and cause the battery to lose capacity and power more rapidly, shortening its useful life. Fast charging can accelerate many failure modes by inducing higher temperatures and a more uneven temperature gradient, including causing more rapid electrolyte decomposition and SEI growth. Fast charging can also cause lithium plating and dendrite growth [17], another potentially catastrophic failure mode. As such, careful consideration and monitoring of these aspects is crucial to enhanced cell performance and Li-ion technology development.

A particular failure mode to consider is lithium-plating, this failure mechanism tends to be extremely detrimental to cell capacity and function and also poses safety risk in the form of lithium dendrites that can lead to a short circuit; although it has been observed lithium deposition tends to take mossy form at lower currents and dendritic form at higher currents [80]. Lithium plating is generally caused by an imbalance in the cell, such that more lithium-ions are being forced into the anode than the anode can accommodate, or because the lithium ions are being forced into the anode faster than they

can intercalate into the bulk material [81]. The latter failure mechanism is exacerbated at low temperatures, which slows the movement and intercalation rate of Li-ions in the graphite anode material [82] and by anything that impedes the charge transfer rate at the anode surface such as excessive SEI layer growth[81]. Inhomogeneous current or potential distribution in the cell, caused by such things defects, uneven surfaces and uneven electrode wetting, also increase the risk of localised lithium plating [83]. Lithium plating has also been observed to occur preferentially at the edge of the anodes [84]. A further challenge to consider with lithium-plating is that it is difficult to detect its onset in real time, while experimental techniques utilising IC analysis [81,85], three electrode systems, acoustic detection and EIS have shown the capability to do this [86]. Diagnostics methods that can effectively detect li-plating in real time could provide valuable information, not least in safety respects.

### 2.1.9. Potential developments in lithium-ion batteries

There is a variety of research avenues focused on improving lithium-ion batteries, encompassing everything from the composition of the anode, electrode, and electrolyte to removing the anode altogether and looking at improvements at the cell, module and pack level. In terms of cell technology there are many pioneering technologies under research such as sodium-ion batteries, iron batteries, redox flow batteries, solid state, silicon and carbon blend anode, sulphur anode, graphene anodes, anode free dual salt electrolyte batteries, amongst others [8,10,22,34,41,87–95].

New electrode materials with better chemistry that consequently have higher energy densities, higher charge rate capabilities, improved cycling performances and greater safety are being studied to improve key limitations in current lithium-ion batteries [96]. Currently anodes are typically graphite with energy densities of approximately 372 mAh/g [34], generally twice the energy density of common cathodes. Further to this next-generation anode materials, such as lithium metal or silicon-graphite mixes, have the potential for even greater energy density than carbon. As a result the bottleneck for improved energy density in the current common lithium-ion cell relates more to the metal oxide cathode [40].

While an increase in energy density of the anode will still benefit the overall battery energy density, a more pertinent aspect to improving anode energy density is arguably the potential to increase charging rates- that is at high SOC the resistance to charging is increased as fewer intercalation sites are available in the anode for the lithium-ions [97]. Two potential secondary anode material technologies for increasing the intercalation site density are graphene anodes [93] and silicon anodes [34]. Mixing part silicon into graphite anodes to increase specific capacity is an active and promising research area, with silicon having an approximately ten times greater specific capacity than graphite; however a significant challenge is that greater expansion and contraction of the silicon leads to mechanical cyclic stresses and this cause the silicon to lose capacity much more rapidly than graphite [98].

Lithium metal anode batteries are a technology that also has the potential for much higher energy densities. They were first pioneered in the 1970's, but have little utilisation due to safety concerns caused by lithium dendrite growth issues causing short circuiting. Research work into overcoming these issues is ongoing with options such as solid electrolytes or coated separators to block the dendrites, nanofibers to force the lithium to plate more evenly or additives to make the SEI layer more mechanically strong and flexible to stress and deformation [99]. Solid-state batteries, such as a metal oxide cathode, solid electrolyte and lithium anode configuration, potentially offer a higher energy density and a safer solution; however they currently suffer from issues including dendritic growth, maintaining a good contact between the electrolyte and electrodes (requires high pressure), lifecycle

longevity due to cracking and breaking contact during cycling and a complicated manufacturing process [100].

Another potential next generation lithium-ion battery proposal is an anode free lithium metal cell with dual-salt Lithium difluorooxalatoborate (LiDFOB)/ Lithium tetrafluoroborate (LiBF<sub>4</sub>) liquid electrolyte. In this design the lithium morphology formed in the salts is suitable for the storage of the active charge transfer lithium atoms/ ions. The cell has an energy density of 360 Wh/ kg and 1000Wh/ l, which is a substantial improvement on the current Li-ion typical range of 120 to 220 Wh kg<sup>-1</sup> [10]. In addition, the manufacturing methods required for the pouch cell form of this battery can be carried over from existing pouch cell designs. The primary issue facing the cell at the moment is the longevity. Initial research work into producing a viable cell established a lifecycle of sustaining 80% capacity over 90 cycles utilising 0.6M LiDFOB and 0.6M LiBF dual salt electrolyte [41], this is compared to a typically recognised requirement of 800- 1000 lifecycles in industrial applications. Further cell improvements, namely utilising higher concentration dual-salt 2M LiDFOB and 1.4M LiBF electrolyte and maintaining a higher pressure on the cells, have resulted in a lifecycle increase to 200 cycles in initial testing [101].

A further experimental technology is lithium-sulfur batteries, which has the potential to provide excellent gravimetric energy density, low cost and safety compared to lithium-ion batteries [92]. A further advantage is sulphur is a cheap and plentiful substance with minimal environmental impact. In this cell the lithium and sulphur react to produce polysulfides (sulphur compounds containing lithium) which allow the transfer of energy, and the lithium shuttles between the lithium metal anode and Sulphur (S) / Lithium Sulphide (Li<sub>2</sub>S) cathode. The technology has challenges including volume expansion of the cathode and loss of active material during cycling leading to short life span, but could have potential applications in aerospace and large vehicles such as lorries [91].

Sodium-ion (Na-ion) batteries are a promising complementary alternative to Li-ion ion batteries [95]. The raw material for sodium is typically an order of magnitude cheaper to produce than lithium, it is significantly more abundant and relatively easy to exploit, so it has significant cost, quantity and supply chain advantages [102]. In addition Na-ion can also be safer due to lower operating voltages, use of different electrolytes that operate at lower voltages and additives that help prevent fire, while also having the advantage of having a similar chemistry to Li-ion [95]. Na-ion batteries have the lower energy density than Li-ion due to lower operating voltage, while the primary challenge is the necessity to develop a suitable anode to accommodate the Na-ion ions which are larger and so do not intercalate into the anode as easily [95].

The diversity of future cell chemistries poses challenges not only to manufacturing, but also diagnostics. Diagnostics techniques will be discussed in a subsequent section, but the above point underlines the importance of cell chemistry-neutral tools and methodologies, that can address challenges across various types of batteries. Such ability is highly sought and would be a highly valued, if successfully developed.

## 2.2. Current battery diagnostic techniques

Battery cells degrade over time as a result of various factors relating to the way the cell is cycled and rested, the external environmental conditions and the material composition and design of the cell [35]. Variable reduction in cell capacity depending on the conditions necessitates that any system utilising lithium-ion cells must be able to diagnose the cell at a given point in time to understand how much energy can be stored and power provided [78]. In addition to that failure modes such as lithium plating and overheating carry safety concerns, and so ideally diagnostics methods would be able to detect these failure modes as quickly as possible to allow a mitigating response to them. Robust diagnostic systems are therefore crucial to the effective operation and safety of battery cells and packs, while also providing essential research and development data. In the following section existing battery diagnostic techniques are discussed.

### 2.2.1. Common non-invasive battery diagnostic methods

The most commonly applied battery diagnostics techniques are non-invasive testing methods that externally measure battery voltage, current and temperature. These techniques can generally be utilised *in operando* and without impact to the battery cells, and hence are typically utilised to diagnose the ongoing state of a batteries being used in commercial and production applications. This includes methods such as capacity testing, coulomb counting, open circuit voltage and electrochemical spectroscopy.

Capacity testing requires fully charging the battery followed by cycling the cell with highly accurate coulomb counting equipment to effectively quantify the input electric charge. However, the cell performance is highly sensitive to variables such as the charge rate, profile and temperature, so models and capacity testing in different scenarios can be applied to attempt to account for the cell performance in different conditions. In real-life operation the conditions can vary significantly and the battery may degrade in different ways over time- these factors significantly reduce the accuracy of the developed model in estimating capacity, SOH and SOC over time. A further consideration is that the process of carrying out extensive characterisation testing is usually time consuming and consumes some of the cell capacity [67].

Coulomb counting, the process by which the charge input and output from a battery is recorded, is an established and common diagnostic method in battery management systems. While specialist coulomb counting equipment is highly accurate, the low cost current sensors that are typically used in commercial applications are susceptible to drift over time, this error compounds the fact that it is a predominantly open-loop technique. Developed coulomb counting techniques that utilise carefully developed models and dynamically re-calibrate over time have still been shown to develop state of charge estimation errors of approximately 3%, even with relatively benign loading profiles [103].

Open circuit voltage (OCV) is assumed to be directly impacted by the different degradation modes in cells, namely LLI, LAMNE and LAMPE, and as such can be used to measure these effects. Birkl *et al.* carried out experimental work to align different battery cell setups and induced failure modes to the corresponding OCV readings, creating an algorithm to identify the nature and extent of a given degradation mode from the OCV reading [78]. The OCV curve is influenced by the structure and phase changes of the electrode material which varies from cell to cell and needs to be calibrated for each cell type and make; material phase transition stages are associated with a much smaller change in voltage per unit increase in cell charge. Due to the differing OCV gradients throughout the

charge/discharge cycle sensitive measurements are required at certain points in the cycle to get a good resolution. Changes in temperature can have a slight impact on the OCV curve, while the battery degradation over time can have a significant impact on it, so the initial calibration at the start of life would reduce in accuracy throughout the battery cell life. The OCV characterisation techniques are a trade-off between time and accuracy, as running them at a slower rate and allowing time for battery kinetics to reach equilibrium between SOC step changes improves accuracy but can be much more time consuming [67]. The information that can be gained from OCV measurements tends to be more qualitative in nature.

The most common method for measuring the OCV vs. SOC curve is based on the galvanostatic intermittent titration technique (GITT), where the cell's SOC is systematically adjusted with a controlled current, while allowing long periods of relaxation before measuring voltage to equilibrium to be reached and the effect of battery kinetics negated. A similar method using voltage as the control parameter rather than current can also be utilised, called potentiostatic intermittent titration technique, while GITT is generally more popular [67].

The technique of electrochemical voltage spectroscopy (EVS) tests further builds on the OCV methodology. EVS testing involves differentiating the voltage and state of charge curve to be able to identify small changes in the OCV reading. Changes in the EVS reading can be related to degradation modes in the battery, as loss of active material (LAM), loss of lithium inventory (LLI), ohmic and faradic changes tend to result in specific changes to the EVS readings. However, while EVS curves can qualitatively indicate the nature and extent of the degradation mode that is occurring, they cannot do so with quantitative accuracy without extensive testing of a given cell in the relevant conditions. Figure 2-10 demonstrates how OCV changes with phase changes in the battery, and how incremental capacity ( $IC = dQ/dV$ ) and differential voltage ( $DV = dV/dQ$ ) plots highlight phase transitions [67].

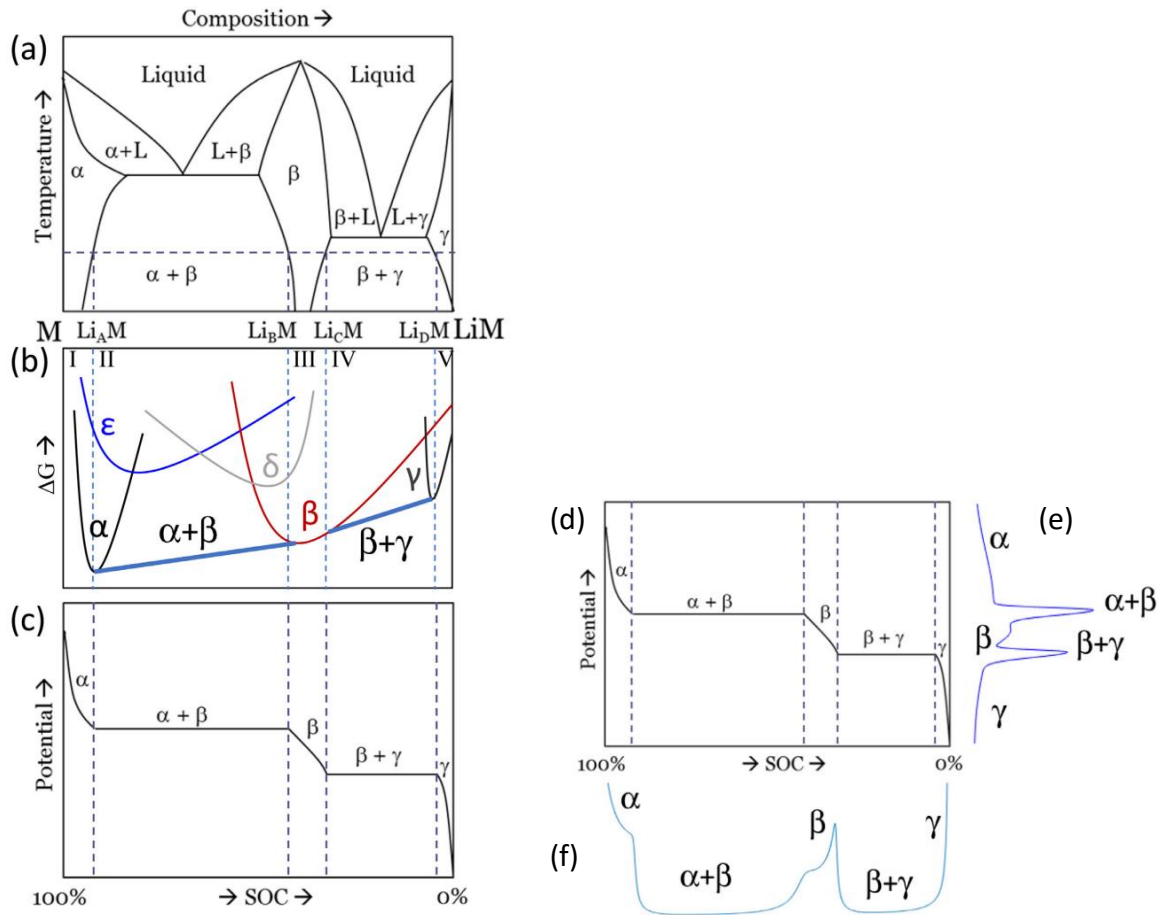


Figure 2-10- Relationship between a) phase diagram of material 'M' being lithiated, b) Gibbs free energy, c) voltage curve, d) voltage curve with e) IC and f) DV plots [67]

Impedance of the cell, which accounts for the resistance of the cell including both the electrical and ionic (movement of ions through electrolyte and into electrode) components and the reactance in the cell (capacitive and inductive effects), can be estimated from the voltage drop across the cell at a given current or current response at an applied voltage. The impedance of the cell is dependent on a number factors- such as material composition, electrolyte composition and concentration, SOC, temperature, current magnitude, pressure, ageing effects such as degradation of cell structure, SEI and parasitic reactions. Techniques used for impedance measurements include pulse power tests, electrochemical impedance spectroscopy and pulsed multisine signal tests. These techniques can be used to model resistance as a function of state of charge and as a battery ages, allowing estimation of state of charge and state of health. Typically an exhaustive amount of testing is required to model the battery comprehensively in all of the potential use cases and environments. It is also a computationally demanding technique, which takes both time and significant resources to deploy.

Electrochemical Impedance Spectroscopy is a technique in which an alternating current (AC) is applied across a range of frequencies to cells at a particular state of charge. As the current is alternating the mean cell SOC does not deviate from the SOC at the start of the experiment, but will imperceptibly oscillate about that value according to the frequency and amplitude of the AC. Due to small size of the

perturbation of the EIS signal on the battery state, EIS is regarded as a steady state test [104]. Responses to different mechanisms of the cell behaviour can be observed at different frequencies, such as double layer capacitance, charge transfer resistance and diffusion coefficients.

We have shown previously that a cell can be modelled as an equivalent circuit of resistors and capacitors. Further to this we know that the impedance values of a resistor and capacitor respectively are:

$$Z_R = R \quad (6)$$

$$Z_C = \frac{1}{\omega C} \quad (7)$$

Where:

$\omega$  = frequency of signal oscillation

C= capacitance value

Considering a simple cell electrode model as shown in Figure 2-11, we can say that at very low frequency the capacitive resistance is very high and so the resistance of the system effectively becomes ( $R_0 + R_1$ ), while at very high frequency the capacitive resistance becomes negligible and so the resistance of the system effectively becomes ( $R_0$ ). In this way, in this simple example, we would be able to identify the electrolyte diffusion resistance ( $R_0$ ) and the charge transfer resistance ( $R_1$ ). An equivalent circuit diagram and Nyquist plot of the expected impedance response is shown in Figure 2-11.

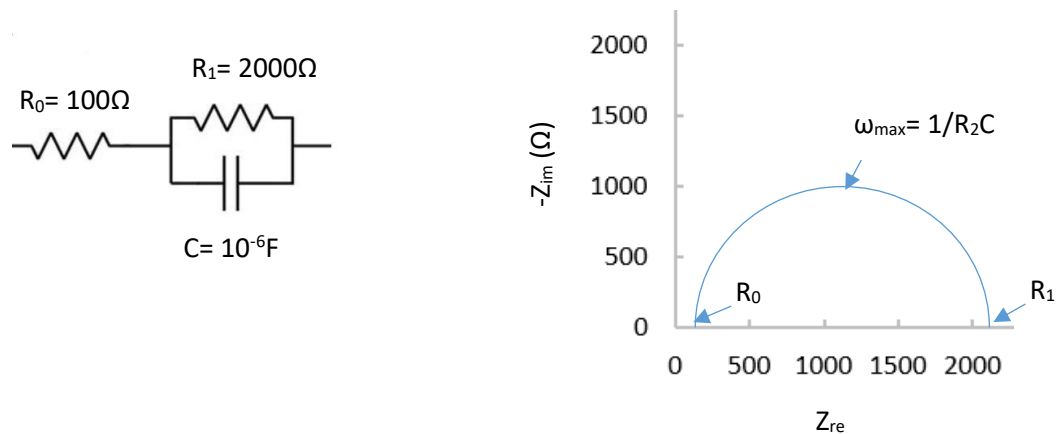


Figure 2-11 - An example equivalent circuit of a single electrode and expected impedance response at different frequencies

In a full cell the mechanisms are more complicated, including having two electrodes, which leads to the typical Nyquist impedance plot shown in Figure 2-12 [105]. Note that all impedance Nyquist plots should be isotropic, that is to say the same scale and length on both axis. Each RC circuit corresponds to a semi-circle in the Nyquist plot, corresponding to an electrode, while the 'tail' is known as the Warburg element which models the diffusion resistance in the electrolyte diffusion layer [105].

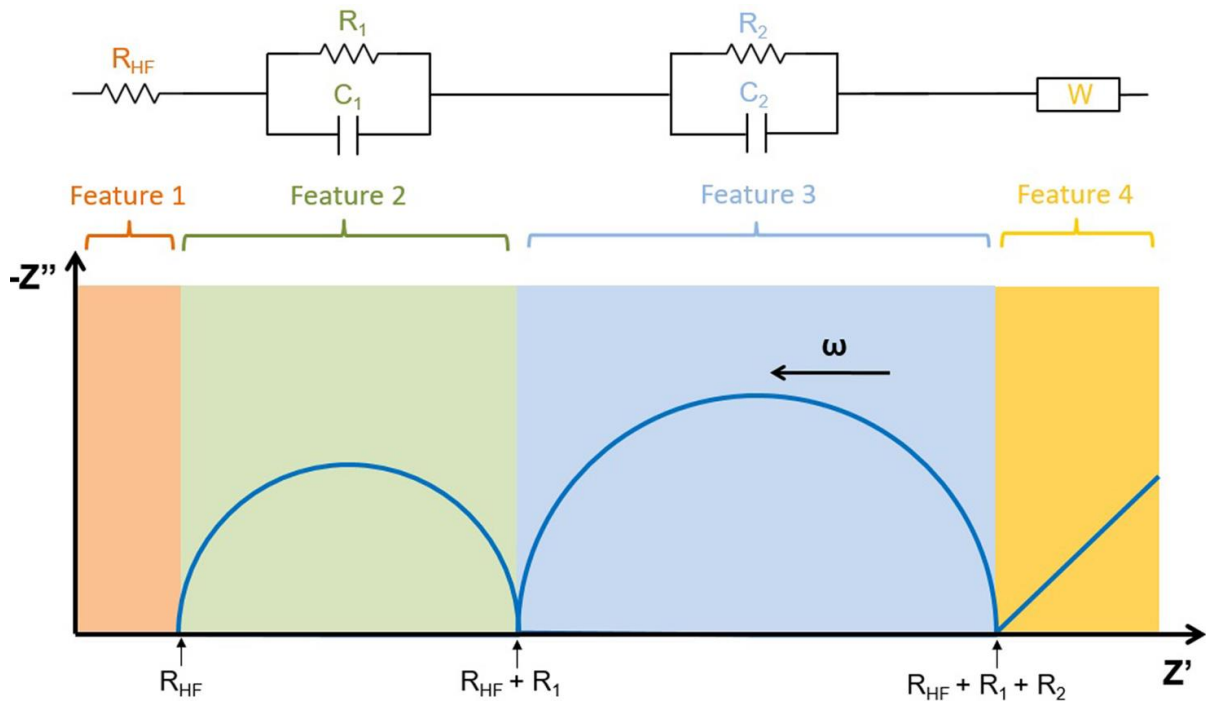


Figure 2-12- Typical cell equivalent circuit model and idealised Nyquist impedance plot relating to each circuit feature.  $R_{HF}$  represents the initial electrolyte diffusion resistance,  $R_1$  and  $R_2$  are the respective electrode charge transfer resistances and  $W$  is the Warburg element [105]

Apart from cell characterisation, EIS can also be used as a cell diagnostic technique. Impedance measurements can be used to indicate SEI layer formation, state of charge, state of health [106] and lithium plating [107]. However care has to be taken with interpretation of EIS results, as ultimately an equivalent circuit can be developed to fit almost anything so the representative circuit should be grounded in an understanding of the mechanism of the particular cell. The results of EIS are often applied relatively for a given cell, and may not carry across well between different cells even if they are similar.

A variety of empirical and semi-empirical models have been developed for battery state and performance monitoring, but are generally hindered by the impracticalities of developing a universally fitting model and relying on external battery measurements that can have inaccuracy and drift over time. In the case of all battery management/ monitoring systems that rely on OCV, operational voltage and delivered charge, the accuracy deteriorates over time with internal losses and cell degradation [68].

Electrical Equivalent Circuit Models (EECM) have been developed to model battery behaviour, with popular models including the Randles model and the 2RC model [108]. One approach in SOC estimation is to select what is expected to be a suitable model based on understating of the electrochemical system and experience [108]. The battery is then tested to define the parameters of the model, however as a battery's properties dynamically vary with life it is then additionally required to apply some kind of statistical filter to account for the changing parameters over battery life, a popular tool for this is the Kalman Filter or Extended Kalman filter [108]. The model based method can be applied to both SOC and SOH estimation, while both of these methods need to accommodate the challenge of the dynamically changing behaviour of a battery over its life which can vary greatly depending on the usage conditions [109].

Data driven methods are another heavily researched and applied methodology for both SOC and SOH estimation. This method essentially collects data for the external cell parameters that can be measured- temperature, voltage, current- over time while simultaneously measuring SOC and SOH values with highly accurate equipment, and then conducting an exhaustive amount of testing with machine learning to develop a model which can correlate the externally measured values to cell state [108]. A graphical representation of this process for SOC is shown in Figure 2-13. This process allows a battery ‘digital twin’ to be created, which is simulating the state of the real battery it is taking data from [110]. Additionally, increasing capabilities and proliferation of artificial intelligence (AI) opens up the possibility of incorporating AI into the machine learning and digital twin models [111]. Challenges with this methodology include the significant amount of data required to characterise a cell, combined with variability between cells of even nominally the same composition and the dynamically changing composition and state of a battery cell in varied and unpredictable usage conditions.

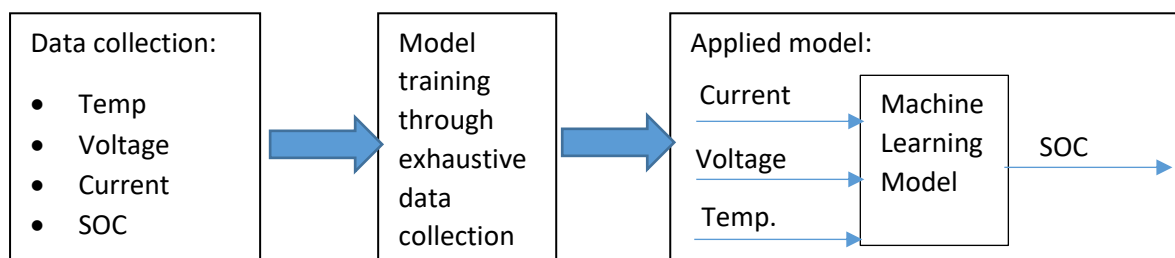


Figure 2-13 - Graphical representation of model training steps for data driven machine learning

A summary of some SOC and SOH estimation methods is given in Figure 2-14, categorised by ‘online’ methods which can be run while the battery is in operation, and ‘offline’ methods which must be run when the battery is at rest (due to requiring certain measurements) [108]. Listed here are the coulomb counting, model-based, data driven, OCV and differential analysis methods (such as IC analysis) already discussed. Additionally there are some advanced sensor based detection methods which will be discussed further in the following sections.

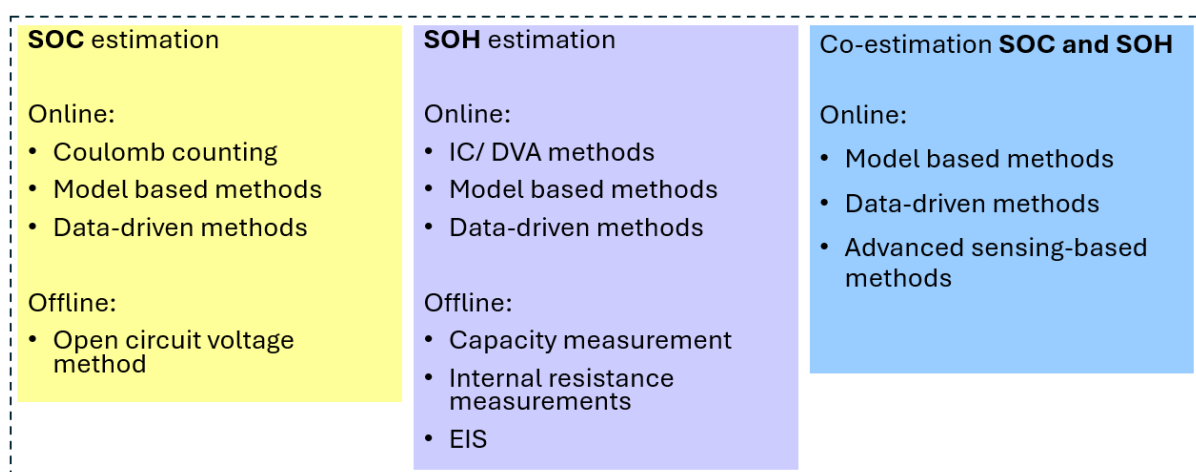


Figure 2-14 - A summary of some SOH and SOC estimation methods [108]

### 2.2.2. Laboratory battery diagnostic techniques

*In operando* investigations of lithium-ion battery internal processes have also proven to be extremely insightful and can provide invaluable information into cell and active material composition and function. A drawback of many of the techniques is the need for electrochemical setups that are compatible with the applied technique and not necessarily reflective of production batteries. Additionally a number of the *in situ* measurement techniques can be performed on production-like cells, but it may not be possible to deploy the test equipment in the application environment [112]. This section will give an overview of some of the insightful real time and physical cell diagnostics techniques that are available, while noting where these techniques are not suitable to be used on a production cell or an *in operando* cell.

The scanning electron microscope (SEM) and X-ray microanalysis can be utilised to create magnified images which reveal microscopic-scale information on the composition, size, shape, crystallography, and other physical and chemical properties of a battery cell material specimen [113]. X-ray techniques enables us to obtain information about the crystallographic structure in an electrode and changes as the electrochemical reactions take place. This technique generally requires the battery to have no casing, leaving it vulnerable to air and moisture contamination, or a transparent 'window' in the battery casing of clear material. A synchrotron high energy x-ray diffraction device can be used to take readings from normal battery cells without requiring casing modification providing excellent insight into physical structure and internal behaviour of a production cell [114], although it is difficult to use this equipment in an operational environment. Similarly Interference Scattering on an LCO electrode has been utilised as a cell characterisation technique, by setting up a half cell with a glass window on the side of the active LCO electrode, allowing the dielectric properties of the sample material to be determined which corresponds to the lithium content and local electronic structure. This experimental setup demonstrated the ability to detect phase transitions in the active material, via a corresponding change in the light intensity [115].

Transmission electron microscopy (TEM) enables the monitoring of lattice changes and electron and ion related phenomena in electrodes. Ex-situ the technique can observe the electrode state at specific points in time, but it is difficult to observe non-equilibrium states. *In situ* TEM allows observation of the lithiation kinetics and structure evolution throughout, including non-equilibrium states [96]. *In situ* TEM requires a cell that is able to fit in a very small in vacuum area, therefore a nano-battery with electrodes, current collectors and electrolyte that remains stable under vacuum is required. Once the constraints of the setup are overcome the technique is capable of providing valuable information, such as the structure of an electrode and flow of ions. For example high resolution TEM images of an Fe<sub>3</sub>O<sub>4</sub> single crystal have shown the spinel and rock-salt phases during in situ Lithium intercalation, and TEM electron energy loss spectra mapping of Ni<sup>2+</sup>(green) and Li<sup>+</sup> + Ni<sup>0</sup>(red) in a lithiated NiO nanosheet at high-rate discharge [96].

Scanning ion conductance microscopy is another technique that can be used to measure ionic currents and to map surface topography, this technique allows characterisation of active material profile and ionic current flow, providing fascinating insights [116]. This technique does require the electrodes to be exposed and housed in an inert argon environment which can significantly change the system in question, so is best used for obtaining specific insights into active materials.

We can further consider a variety of established and developing destructive lithium-ion battery testing techniques available, delivering a variety of valuable information but with the obvious drawback that they cannot be used *in operando* and the cell is no longer of use. For physical analysis of the electrode

surface from a torn down cell scanning probe microscopy can be used, which involves the deflection of a cantilever with a sharp (micro or nanoscale) tip to examine surface profile and roughness, this allows volume changes or the formation of the SEI layer to be measured and visualised. Nano-indentation can also be used to determine mechanical properties at the electrode surface, while voltage techniques can be applied to study the surface potential and topographic changes as a function of voltage.

Various spectroscopy techniques can be applied to visible electrode surfaces. Raman spectroscopy can be utilised to identify chemical bonds and structure through the measurement of monochromatic light reflection, absorption and scattering. Fourier transform infrared spectroscopy, through measurement of the absorption of infrared light, can similarly identify molecular bonds, bonding mechanisms and quantities. X-ray fluorescence (XRF), also known as energy dispersive x-ray (EDX), a technique that utilises the application of x-rays to excite the source and then measures the generated secondary x-rays, can be utilised on an exposed electrode to determine the elemental composition of the sample (although the technique cannot detect very small atoms such as lithium). Optical microscopy can also be used to observe the colour change of lithiated graphite, which can be a measure of the battery's state of charge. While all of these techniques can provide useful information about the battery, they again require significant modifications of the system under evaluation, such as a glass window in the casing of the cell [114] or full teardown of the cell; however the use of optical fibres in a battery cell does open up the possibility of a 'laboratory on fibre approach' to use such techniques inside relatively unmodified production type cells with fibre optic sensors, although this is not currently common.

Another novel technique that has been utilised to measure  $\text{Li}_2\text{S}$  dissolution and deposition is that of an electrochemical quartz crystal microbalance (EQCM). The EQCM was placed in an open cell and coated with a sulfur-carbon cathode, with the anode being lithium foil. The change in the mass of the cathode was detected via the changing vibration frequency of the EQCM. This technique does require an open cell setup and the high sensitivity of the EQCM to different processes can make it difficult to decouple the information [117]. Simple visual analysis can also be carried out on dismantled cells. A graphite anode will visually appear black, while lithium plating will result in a silvery hue created on the surface. As such lithium plating of the anode can be visually identified and the size and strength of colour of the silvery areas on the anode surface is proportional to the level of lithiation [66]. The aforementioned techniques in this section provide a variety of cell analysis possibilities offering different insights into the cell and different sets of data in laboratory conditions or through destructive testing, but do not currently offer the possibility of measuring both *in situ* and *in operando* production cells, which will be covered in the following section.

### 2.2.3. *In situ* and *in operando* battery diagnostics method

Diagnostic methods that can directly monitor the internal processes of a battery have the potential to provide valuable information such as more accurate current state readings and optimising battery charging profiles [97]. Such methods will be referred to as *in situ*. As discussed in the previous sections, currently established *in operando* battery diagnostic techniques involve taking external readings to diagnose the battery state. Where methods exist for analysing internal battery processes *in operando*, they often involve heavily modified cells in laboratory conditions or substantial testing equipment that could not be deployed in a production application environment [112]. The following section will discuss some early research into *in operando* and *in situ* battery diagnostic methods requiring simple and non-invasive sensing techniques.

Effective use of a thermistor element inside a pouch cell and automotive grade cylindrical cell has been recently demonstrated [118], the schematic for which can be seen in Figure 2-15. Negative Temperature Coefficient (NTC) thermistor elements were deposited on polyamide Kapton substrate, subsequently covered with a 1  $\mu\text{m}$  thick Parylene C layer to protect it, as stability is a particular concern for *in situ* sensors due to the corrosive environment. The resulting experimental work demonstrated high fidelity internal temperature readings that closely correlated with the lower surface temperature measurements. Further analysis also demonstrated the integrated thermistor did not have a significant impact on the performance of the cell, and that the sensor remained stable over a period of three months. The acquisition of internal cell data is a significant aid for battery modelling, and opens up the possibility for optimisation of battery management systems (BMS) and cell operation based on more accurate cell information than is provided by external measurements.

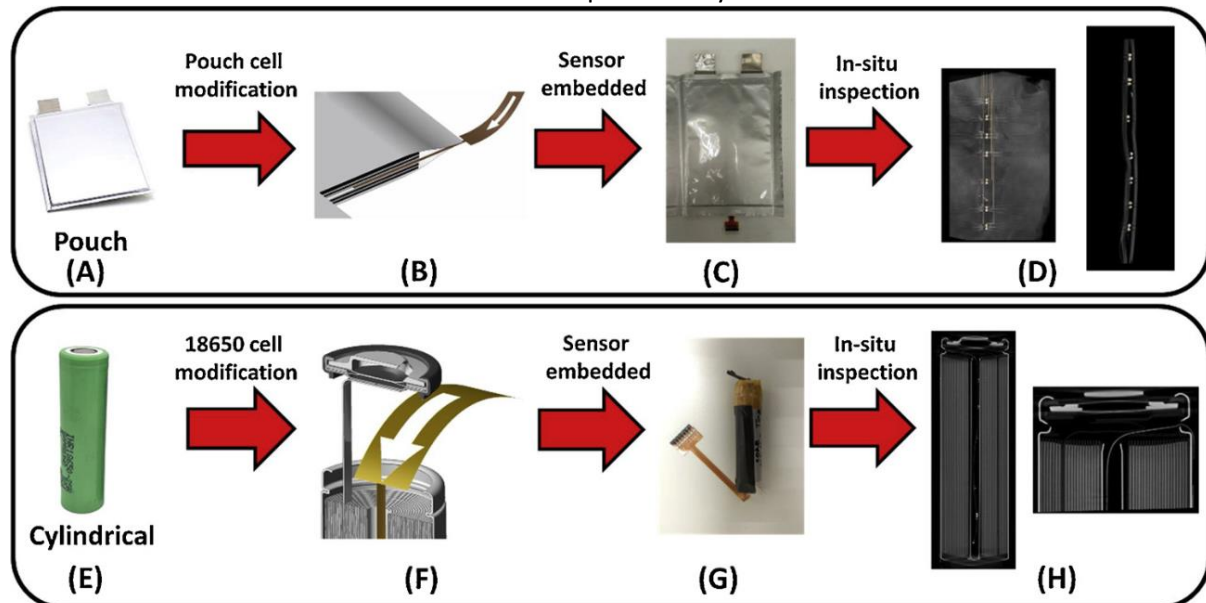


Figure 2-15- Schematic of thermistor element inserted inside a pouch cell and cylindrical cell [118]

On the electrochemical analysis side, typical two-electrode lithium-ion cells only allow the voltage difference between the two electrodes to be measured, as such it is not possible to measure the individual voltages and changes of the electrodes. A third stable fixed reference electrode (RE) makes this possible. A challenge with reference electrode is implementing them in such a way that they do not substantially affect the battery function and get good results, they can require different electrolyte to be used, be positioned too far from the working counter electrode to get good results or require damaging cell modifications [119]. The choice of RE material is also significant, e.g. it has been noted that a lithium metal electrode reference voltage can change with current density due to polarisation within the metal, while  $\text{Li}_4\text{Ti}_5\text{O}_{12}$  (LTO) and  $\text{LiFePO}_4$  (LFP) are much more stable across a wider range of current density [120]. The reference electrode will be placed outside the main current path such that it is minimally affected by the passage of current and polarisation is minimised [32].

It has been demonstrated that a RE setup able to determine the working and counter electrode profiles of a cell can be implemented while having minimum impact on the voltage discharge profile when compared to an unmodified commercial cell. A 'patch' lithium reference electrode and a 'wire' lithium reference electrode were both evaluated, with the wire setup cell demonstrating minimal deviation in discharge profile from that of an unmodified commercial cell at a charge rate of  $C/10$  and  $40^\circ\text{C}$  environment. A pouch cell was chosen for the experiment due to the pouch cell design and manufacturing process being relatively accommodating to modifications. This experimental work

demonstrated working and counter electrode potential information being obtained from a commercial pouch cell [119].

Acoustic detection is another interesting real-time diagnostic technique that has shown the potential to detect physical defects in cells, which in turn can be associated with cell ageing and state of health [121]. The technique has also been demonstrated to be able to detect short circuiting events in a cell [122], SEI/ CEI layer formation [123], lithium plating and gas generation [124].

Use of a lithium metal reference electrode and FBG temperature sensor in an 18650 commercial cell was also demonstrated and used to optimise the speed of the fast charging profile [97]. The aim was to charge the cell as fast as possible, while not exceeding the manufacturer's internal cell safety temperature of 60°C (at which electrolyte decomposition is accelerated and there is increased risk of thermal runaway) nor allowing the anode voltage to drop below 0.05V (at 0V lithium plating becomes favourable). A charge rate of 2.2C (6.6A) was found to hit the 60°C temperature limit and <0.05V anode limit, as measured by the FBG and RE electrode respectively. Nonetheless the results suggested a charge rate of 2C (6A) was acceptable up to 80% SOC, which is 6.7 times faster than the manufacturer recommended limit. The impacts of such a charge profile on the lifespan and SOH of the battery cell should also be considered, as must the impact of the sensors- FBG have been shown to have a negligible impact on cell performance [125] while as discussed above a RE can have some impact. Nonetheless these results indicate the considerable potential for battery optimisation through superior data collection via *in situ* and *in operando* production cell diagnostics.

## 2.3. Fibre optics

### 2.3.1. The use of fibre optics for battery diagnostics

There have been numerous studies [126–131] utilising fibre optic (FO) sensors in battery cells, as has been touched on briefly in the previous section, with the recognition that their small diameter (typically 100µm) makes them well suited for such attempts. Key properties that make fibre optics suitable for *in situ* battery cell measurements include minimal electromagnetic interference, low weight, tolerance to chemical environments and inertness, being electrically insulating, capability to monitor in real time and capability to receive and process multiple signals simultaneously (multiplexing) [127]. Additionally the remote operating capability of fibre optics is a key advantage, a consequence of their ability to transport high quality light signals over a variety of distances; this can be seen in the variety of fibre optics uses from 1m long sensing devices to 550m long multimode transmission fibres.

Total internal reflection is utilised to guide the light along the length of the fibre, as such the core of the fibre optical waveguide is often doped with germanium or other high refractive index materials to create a higher refractive index than the cladding and ensure total internal reflection [127]. Single mode FO sensors taking measurements at one point, quasi-distributed measure at multiple discrete points and fully distributed measure along the length of the fibre using temporal and spatial resolution techniques [132]. The use of optical fibres encompasses various techniques, such as FBG's, colorimetry and evanescent wave signals. This section will give a brief synopsis of the research work that has been carried out in this field, while the mechanisms behind the focus of this study, plasmonic sensing, are discussed further in Section 2.3.2.

A popular technique with which a fibre optic waveguide can be used to measure temperature and strain involves the inscribing of a Fibre Bragg Grating (FBG). FBG is a periodic inscribed 'grating' in the

fibre optic core that reflects particular wavelengths of light and transmits others. As a fibre heats up and expands, the periods between the gratings increase, affecting reflected wavelengths [126], similarly when under strain the periods between the gratings change. Consequently changes in temperature and strain can be measured through a corresponding change in the reflected Bragg wavelength as the distance between the grating changes and refractive index of the silica fibre changes. The Bragg wavelength is a function of refractive index and the period of the grates, as set out in Equation 8.

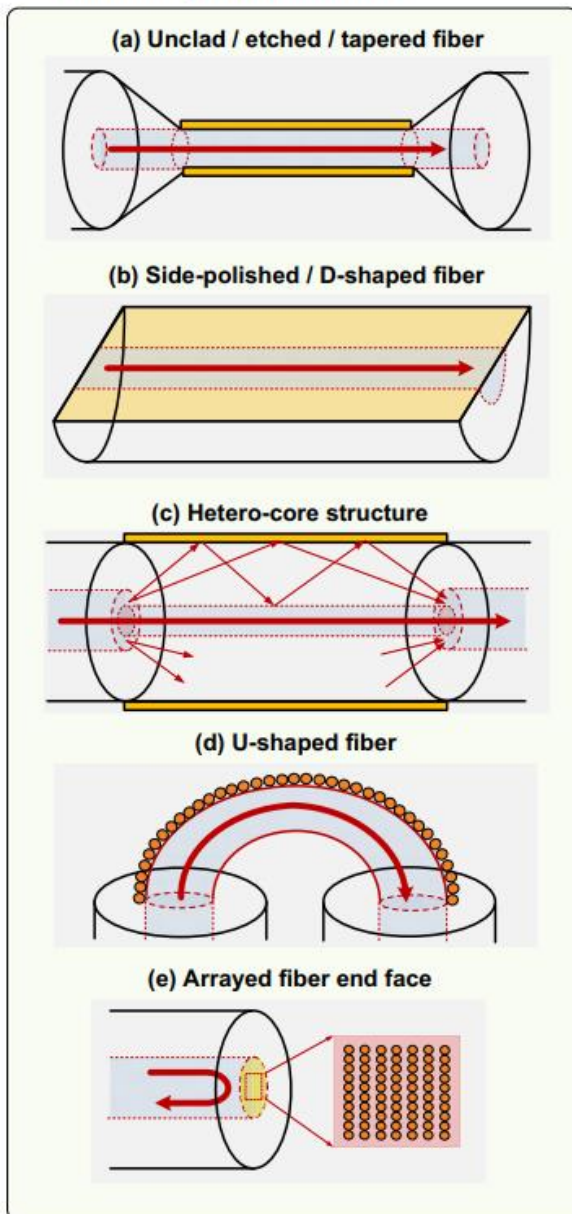
$$F_{Bragg} = 2n\Lambda \quad (8)$$

Where:

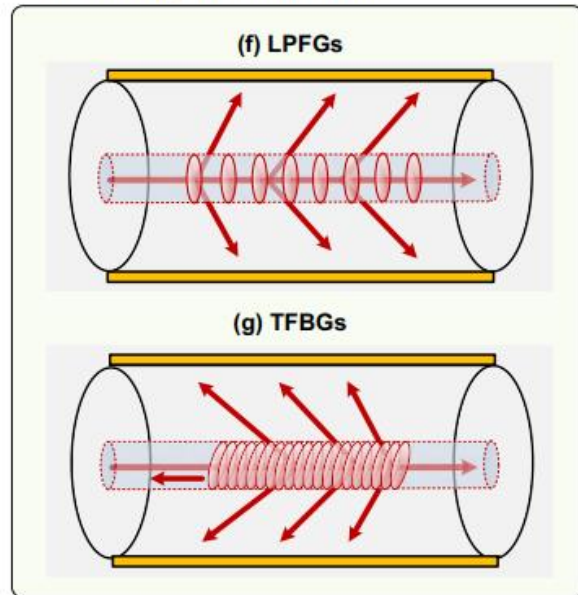
- $F_{Bragg}$  is the Bragg wavelength
- $n$  is the refractive index
- $\Lambda$  is the period of the grates

Fibre Bragg Gratings (FBG's) and the similar methodology of Tilted Fibre Bragg Gratings (TFBG's) are generally the subject of significant research and application inside Li-ion cells, the high sensitivity of these devices to temperature and strain and the ability to place them inside cells with minimal impact on the cell performance [133] allows the possibility to detect a variety of cell processes. A variety of studies have been carried out utilising these sensors for temperature and strain measurements in cells [97,134–136], identifying phase changes and diffusion rates through strain measurements [137,138], SEI layer formation detection [139] and even SOC estimation via strain measurement [140]. Notably FBG sensors can also be used for current sensing [141], either utilising methodologies that exploit the Faraday effect or indirectly through the use of a current transformer and piezoelectric element. Figure 2-16 gives a diagrammatical representation of different fibre-optic SPR configurations, including an example with a Tilted Fibre Bragg grating [142].

### I. Geometry-modified fibers



### II. Grating-assisted fibers



### III. Specialty fibers

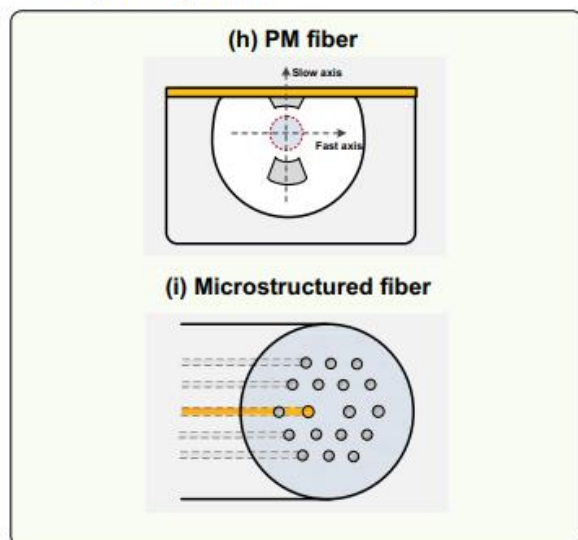


Figure 2-16- Sketches of different fibre-optic SPR configurations, including a fibre with a Tilted Fibre Bragg grating (TFBG) incorporated inside it in (g) [142]

Use of two FBG sensor simultaneously, with one mechanically adhered to the sample of study and one free to move, can allow the deconvolution of temperature and strain data. An example of a setup in which two FBG sensors were attached to the anode electrode inside a battery pouch cell was evaluated by Ragahvan *et al.* [128], the fibres were fixed in place using a styrene-butadiene-rubber binder, selected for its compatibility with battery materials. The setup involved placing one FBG sensor in a tube to allow it to move freely while the other was fixed to the electrode surface. The fibres were sealed in the pouch material with a protective heat seal film around the fibre [128]. A variety of cell cycling profiles and drive cycling was carried out, and a clear correlation was observed between the FBG wavelength and the charge capacity; this correlation is attributed to the volume expansion of the electrode as Li-ions diffuse into it, resulting in the FBG measuring a change in strain. In this experimental setup and testing regime the results demonstrated that the FBG signal was able to measure SOC to within 2.5% accuracy, and was also able to predict the cell capacity up to 10 cycles ahead with less than 2% error. Three US patents relating to inserting fibre optics sensors into battery

cells have been published in 2019-2020 with Ragahavan *et al.* listed as the inventors, namely patents US 10446886 B2, US 2020000681 A1 and US 10777855 B2, research lead by the Paulo Alto Research Centre.

Another technique that has been utilised with fibre optic waveguides is attenuated total reflection (ATR), also known as a fibre optic evanescent wave sensor (FOEWS) [143]. ATR is a technique whereby light, usually broadband light or infra-red (IR), is shone into an internally reflective element (IRE) with a high refractive index. An evanescent wave is formed at the interface boundary as a consequence of the internally reflected light, that is to say an energy field with no net flow, which extends into the analyte. In regions of the spectrum where the sample absorbs energy, according to the normal vibration modes of the analyte particles (stretching, rocking, scissoring and bending) the evanescent wave will be attenuated. The attenuated beam returns to the IRE, then exits the opposite end and is directed to a spectrometer detector. The IRE is typically a crystal material such as silica, germanium or diamond- as fibre optic waveguides are silica they are a suitable material for this technique. The internally reflective element can be pressed against the sample, and light attenuation will occur at wavelengths absorbed by the sample material, while good contact and contact pressure is required [145].

This principle is easily transferred to a fibre optic waveguide. Total internal reflection is utilised to guide the light along the length of the fibre, as such the core of the fibre optical waveguide is often doped with germanium or other high refractive index materials to create a higher refractive index than the cladding and ensure total internal reflection [127]. There are therefore two components in the fibre optic waveguide, the internally reflected light through the core and the evanescent wave at the core-cladding boundary. The evanescent wave does not normally extend beyond the cladding due to its short range and so does not interact with the surrounding medium, however the cladding can be removed at the point of interest so the interaction will occur and allow measurement there.

Evanescent wave based sensors have been shown to give promising initial results in terms of correlating the light signal with battery SOC, with one study showing an accuracy of around 14% and good sensitivity throughout the charge cycle [129]. The 850nm wavelength light was found to get the best sensitivity, although issues were encountered with noise being created due to temperature and the equipment setup. Another recent study was carried out utilising an evanescent wave fibre optic sensor in a lithium iron phosphate (LFP)- lithium Swagelok cell, adjacent to the cathode [127]. The polymer coating was removed from the silica fibre optic waveguide in the measurement region placed adjacent to the cathode. Constant current charge and discharge and cyclic voltammetry were applied and a clear correlation between the cell state of charge and light signal attenuation were found. The constant current charge showed a steady increase in light attenuation as the cell was charged, and *vice versa* during discharge, as shown in Figure 2-17. Additionally cyclic voltammetry testing also identified a distinct light attenuation response to cell charge and discharge [127].

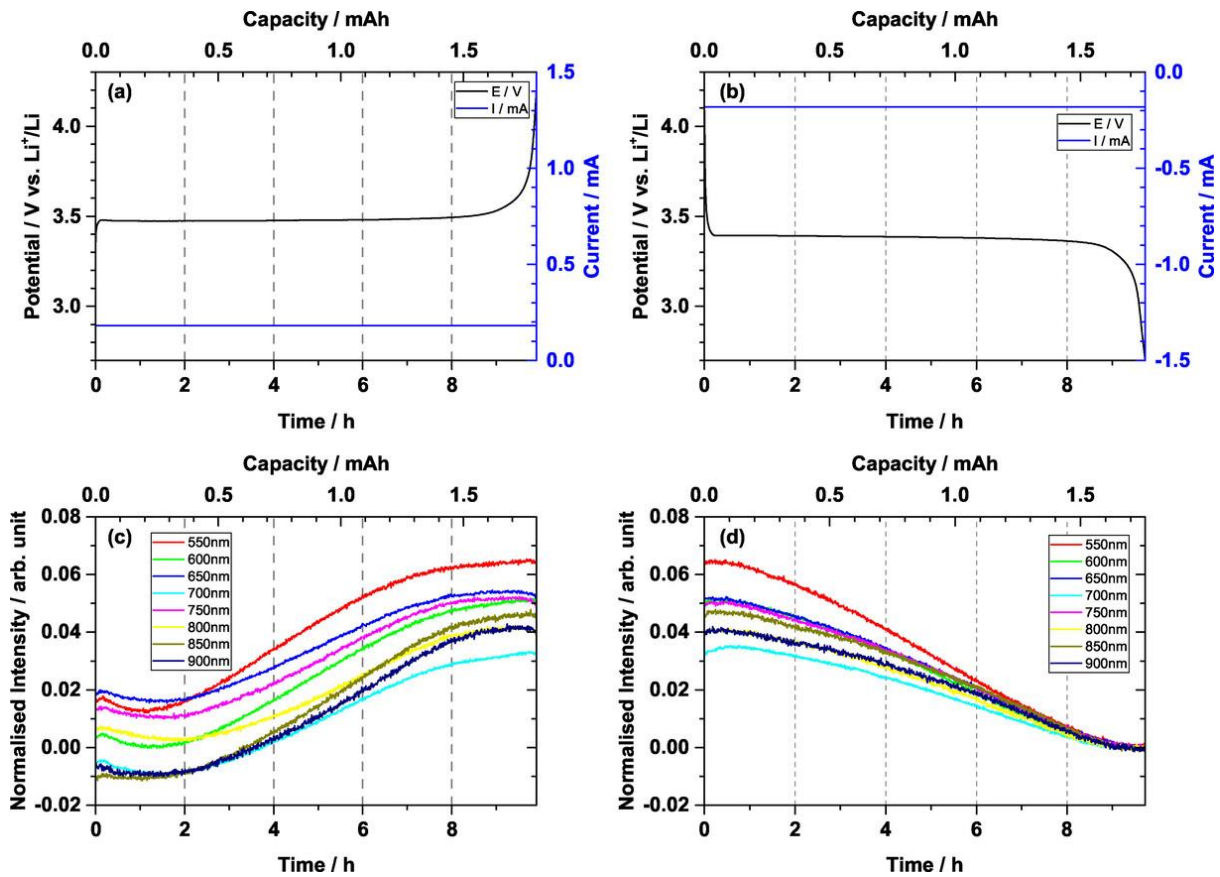


Figure 2-17- Constant current charge (a) and discharge (b) of a LFP-lithium half-cell and associated ATR light signal attenuation, (C) and (d) respectively [127]

These results show a clear potential for ATR to provide real time SOC battery cell information, and doing so by taking data from directly inside the cell rather than utilising external current, voltage or temperature information. The exact mechanism by which the correlation occurs is hypothesised to be related to Li-ion concentration but this theory still needs to be tested further, therefore it is necessary to consider that the effect may be different in different cell designs or with different battery chemistries. Additional FOEWS studies have also demonstrated optical signal correlation to cell charge and discharge [146–148] and graphite lithiation [149][150][151]. Lithium-ion concentration measurements have been demonstrated with FOEWS and Fourier-transform infrared spectroscopy (FTIR) [76], demonstrating the clear potential of the technique as a research and diagnostic tool.

Studies have also demonstrated that carbon anodes change in both reflectivity [130] and colour [131] as they are charged and discharged, such that these properties can be correlated to SOC of the cell. Marie *et al.* showed in a study utilising *in situ* colorimetry that when plotting the red, blue and green colour components of a carbon anode in a half-cell, the red component showed a consistent change with SOC, particularly from 30-100% SOC [56]. The potential to estimate SOC through visual changes in the anode provides a further potential use case for optical fibres in batteries, and the possibility to take this information directly from inside a production cell.

Recently, additional studies have further demonstrated the potential to de-convolute temperature, pressure and strain effects inside a battery using a combination of fibre optic sensors. A single-mode optical fibre with FBG (SMF-FBG) and micro-structured optical fibre with FBG (MOF-FBG) were placed inside a battery cell simultaneously by Huang *et al.* As noted previously the FBG refractive index and grating period are both affected by temperature, pressure and strain; in this experiment Huang *et al.*

experimentally eliminated the strain variable and then used the two optical fibres with different responses to pressure and temperature to create a solvable simultaneous equation allowing the deconvolution of temperature and pressure effects [139]. Huang *et al.* then utilised three fibre optic calorimeters to determine the heat energy change inside a coin cell and the heat loss from the cell to the environment, one inside the cell, one on the surface and one in the external environment. At a charge rate of C/10 the rate of heat generation and loss calculated using the optical calorimeters very closely matched the results determined using both the techniques of isothermal calorimetry and by calculation of battery power loss by measuring and integrating the change in current and voltage over a cycle. This study further made some interesting observations, notably of which at 1C charge rate the ratio of heat generated in the battery to heat lost was greater than for C/10 charge rate [139]. This is consistent with overheating experienced during fast charging [17] and arguably demonstrates the battery cell was not sufficiently effective at transferring heat to its environment. A further observation of note was a peak denoting an increase in pressure in the first cycle only, which the team attributed to gas release during initial SEI layer formation.

Other optical techniques which have been noted in the literature as having potential in battery cells are fluorescence based sensors and Fabry-Perot (FP) interferometers [152]. Fluorescent based sensors have been used to measure cell temperature, for oxygen measurement [143] and to track ionic transport in electrolyte and electrode structures [153]. FP sensors have external cavities that are impacted by strain and temperature, changes to the cavity properties result in changing phase difference in two light waves projected through the fibre, which can be measured. Rayleigh scattering via fibre optic sensors has also been utilised to take electrode strain measurements [154]. Another novel technique has recently been patented in European Patent 'EP 3 517 938 B1', in which a material in a section of the optical fibre cladding is designed to dissolve in the presence of hydrofluoric acid, in this way the optical signal is modified in proportion to the quantity of hydrofluoric acid in the battery cell via modification of the cladding. Further to this, FO sensing techniques have been used to measure CO<sub>2</sub> content; this can potentially be utilised in battery cells, in which CO<sub>2</sub> is as a product of SEI formation and electrolyte decomposition so concentration could be correlated to battery ageing for SOH estimation [132].

Fibre optic sensors enable a 'lab on fibre' [155] approach, in that the optical measurement equipment can be remote to the optical sensor location at or inside the sample of interest; this enables aforementioned spectroscopy techniques such as Rayleigh and Raman scattering to be carried out in difficult to access locations, such as inside a cell. Further to this some fibre optic techniques make it possible to spatially resolve measurements along varying lengths of the fibre [156], known as Distributed Optical Fibre Sensors [143]. An example of a fibre optic setup allowing multiple point sensors on the same fibre optic is quasi-distributed sensing, this approach utilising multiplexing techniques to deconvolute data from several measurement points [152]. The studies discussed in this section are only a selection of numerous studies into the use of optical fibres to measure properties in battery cells. The field is attracting a lot of research and shows clear promise as an *in operando* and *in situ* battery measurement technique, with the other notable advantages of the low cost of the fibres, non-interference in cell function and non-interference in cell design.

### 2.3.2. Plasmonic/Nanoplasmonic sensing

Surface plasmon resonance (SPR) can typically refer to two sensing mechanisms, one involving surface plasmon polaritons (SPP)/ surface plasmon waves (SPW) along metal surfaces and the other involving three dimensional resonance in metal particles known as localised surface plasmon resonance (LSPR) [142]. The term surface plasmon wave can be used interchangeably with SPP. In addition it is noted the term nanoplasmonic sensing (NPS) can also be used to refer to both SPW and LSPR [3]. A brief introduction to the mechanism behind both techniques, SPP/ SPW and LSPR, will be given here.

In the context of SPR, plasma refers to the free moving electrons that can be found in a metal lattice, while polaritons refer to the interactions of EM waves with these electrons exciting resonant wave modes; the term “plasmonics” has been coined to describe the study of metallic and metallodielectric nanostructures and plasmons [1]. The surface plasmon waves can be visualised as a wave moving along the surface of a ‘sea’ of electrons, with a resonant frequency determined by factors such as the metal used and the refractive index of the adjacent analyte. The typical setup for inducing surface plasmon waves for the purpose of measurement is that of the Kretschmann-Raether configuration, whereby a thin metal film is deposited on an optical prism, as shown in Figure 2-18.

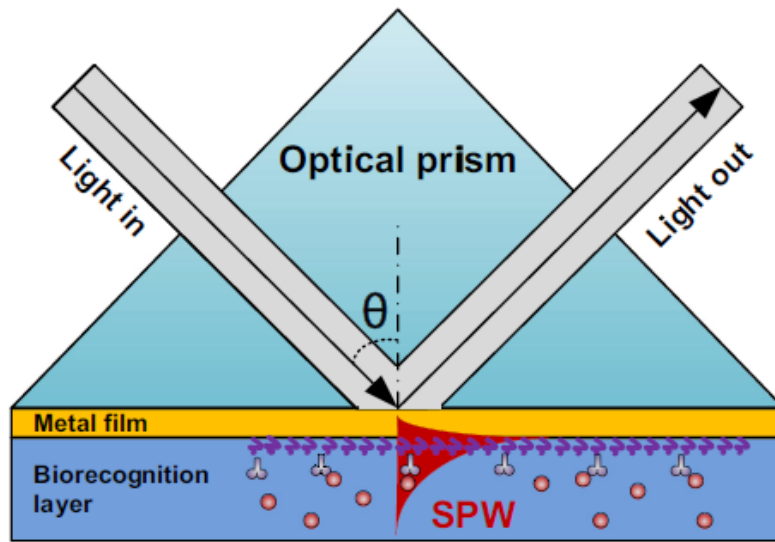


Figure 2-18-Sketch of Kretschmann-Raether configuration prism with totally internally reflected incident light and a surface plasmon wave on the surface, this is an example of a biotechnology sensing application [142]

This approach is easily transferable to fibre optic waveguides by depositing a thin metal film on the waveguide surface, typically gold or silver. Incident light is beamed onto the glass-metal interface at an angle greater than critical to cause total internal reflection. This creates an evanescent wave along the glass metal interface which can excite a SPW on the opposite metal to surrounding medium interface. The polarisation of the light must also be perpendicular to the surface (transverse magnetic polarisation) to excite the SPW wave [142]. Figure 2-19 shows a typical fibre optic waveguide with EW due to totally internally reflected light; the figure then shows that with the addition of a thin metallic layer SPW waves can be created, the evanescent wave ‘couples’ with the thin metallic nanolayer when the propagation constants match, creating a surface plasmon wave.

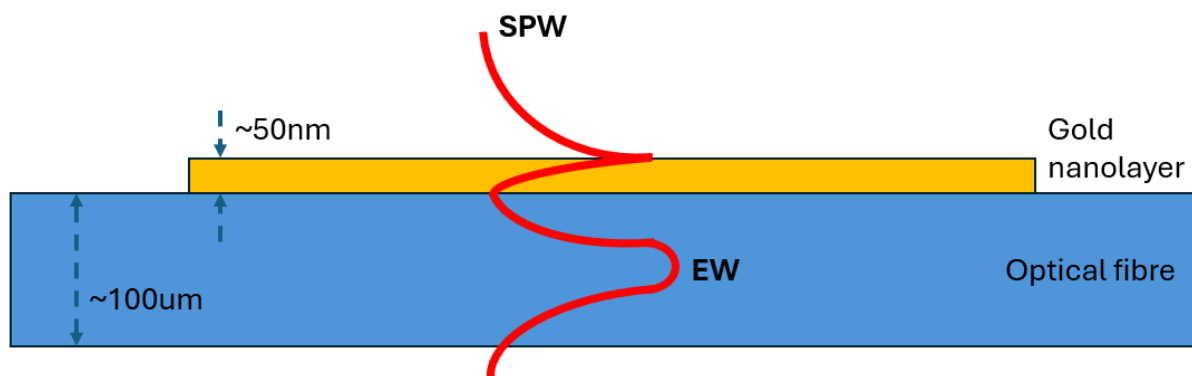


Figure 2-19- Evanescent wave (EW) produced at the surface of fibre optic waveguide due to totally internally reflected light couples with the surface plasmon wave (SPW) in a thin metallic layer on the fibre optic waveguide when the propagation constants match.

While the Kretschmann-Raether configuration is the most commonly used approach to generate SPW excitation other mechanisms that can be utilised to generate this coupling include providing surface rugosity, a grating structure or Otto prism configurations- as a transverse light wave incident directly on a smooth metallic surface cannot excite the longitudinal surface plasmon wave [1].

In terms of utilising this technique for measurement, this is done by placing the metal film adjacent to the analyte. The SPW natural oscillation frequency and propagation constant along the metal-analyte interface depends on the permittivities/ refractive index of the metal film and the surrounding medium. This means that a change in analyte permittivity, such as density fluctuation, thickness changes and molecular adsorption leads to a change in the propagation constant of the SPW. In turn the parallel component of the light wave, determined by angle and wavelength, required to produce an evanescent wave with the propagation that matches and excites the SPW changes. As the light waves that excite the SPW are matched by a transfer of power from the light beam, this can be measured through a decrease in power, of the reflected light, at those wavelengths (light attenuation) in the beam. There are three typical measurement methods; angular interrogation which utilises monochromatic light and measurement of incidence angles, spectral interrogation using a fixed incidence angle and broadband light and measurement of absorption at different wavelengths, and the relative phase shift of TE and TM light as a function of incidence angle or wavelength.

The other SPR technique, LSPR, employs a slightly different mechanism. LSPR is generated by light waves trapped within conductive nanoparticles with dimensions smaller than the wavelength of light, leading to an optical phenomenon. The optical phenomenon is a result of the interaction between the incident light and the electrons in the conductive band of the metallic atoms. This leads to collective oscillation of the particle's conduction electrons with a resonant frequency that depends on multiple factors such as the composition, size, geometry, dielectric environment and particle-to-particle separation of the nanoparticles (NPs) [142]. Again the light wavelengths that cause the excitation are attenuated (due to absorption and scattering of the light), which can be measured, and a change in analyte conditions according to the aforementioned factors leads to a different NP resonant frequency and a different frequency of light being attenuated.

Commonly used materials for NPs are noble metals such as gold or silver, which exhibit LSPR in the visible region of the light spectrum and low losses due to interband electron excitations in that wavelength region [3]. Noble metals provide the best evidence of SPPs due to possession of a high density of electrons that are free to move [1]. The stable and inert nature of the metals is also an advantage [3]. The signal detection method involves, for example, transmitting broadband light to NPs on a substrate such as an optical fibre or dispersed in liquids, the light extinction of the reflected or

transmitted light at different wavelengths can then be measured. LSPR has a smaller sensing penetration depth than SPP [157] meaning the measurement captures a shallower, closer to the surface volume of the analyte.

SPR integrated with fibre optics can be used to create sensors for chemical and biochemical applications. The phenomenon of surface plasmon resonance (SPR) was first exploited in sensing in 1983 [2]. Later on fibre optic SPR sensors were clearly recognised for their properties of high sensitivity, simple structure, small size, ability to place in inaccessible places using fibre optics and their capacity in terms of real-time analysis [1]. SPR has numerous advantages as a diagnostic method. The technology can be applied flexibly to very different material systems, the necessary hardware is relatively simple and there is high local sensitivity at the nano-scale. The fibre optic probes are non-invasive with minimal impact on the studied processes (in contrast to for example electrons, X-rays or scanning probes), which is a key attribute in being able to diagnose cells *in situ* and *in operando* in real world applications. The sensors can be operated in a very wide range of environments, including vacuum, liquids, very low to high temperatures and harsh chemical environments. This opens the application to not only the automotive industry, but also military, space and other extreme scenarios. Valuable real time information can be obtained from widely varying environments with a relatively simple and fast experimental setup [3], however the optical interrogator unit can be more costly (thousands of pounds) while this does depend on some degree to the nature of optical interrogator unit required for the case and can potentially be simplified.

There are a number of key performance metrics for plasmonic sensors. Sensitivity represents the change in the signal (amplitude, wavelength peak change) as a ratio of the change in the measurand. Accuracy defines how closely correlated the signal change is to the measurand change. Repeatability defines how reproducible the results are. Limit of detection (LOD) represents the lowest concentration of analyte that can be detected. Figure of merit (FOM) is a metric that allows more relevant comparison of different sensor configurations, as it accounts for both bandwidth of the measured resonance (full width at half maximum of wave peak) and the shift in the resonance (sensitivity), based on the principle a narrow defined resonance is easier to measure than a broad one [142]. Table 2-7 summarises a few of the use cases and properties of ATR, SPP and LSPR and their performances for comparison.

Table 2-7- Comparison of some of the common use cases and properties for ATR, SPP and LSPR measurement techniques

Properties	Attenuated total reflection	Surface plasmon polaritons	Localised surface plasmon resonance
Typical use cases	Determining material types in a substance.	Biochemical detection- antigens, antibodies, enzymes, proteins etc.  Detecting presence of gases.	Biochemical detection- antigens, antibodies, enzymes, proteins etc.  Swelling, diffusion, phase transitions, corrosion. [142]  Adsorbent molecules on surface, such as gases. [3]
Analyte property detected	Natural frequency modes of molecules of substances present.	Refractive index of analyte/ dielectric field.	Refractive index of analyte/ dielectric field.

<b>Sensing depth/ distance</b>	Typical range from 0.2µm to 3.0µm [158]	Typically 200nm or more at optical frequencies depending partly on sensor design and analyte [157]	Typically 'tens' of nanometers (circa 20 to 40nm) [157]
<b>Limit of detection</b>	Typical 1700ppm for a macro-ATR instrument [159]	Examples: 10ng/ml Staphylococcal enterotoxin B, 0.09 µg/ml peanut allergens, ppb for TNT vapours [142]	Examples: 2 pg/ml prostate specific antigen, Cymbidium mosaic virus 48/pg/ml, 10ppm ammonia [142]
<b>Refractometric sensitivity</b>	N/A	Typically in range of 1300 to 11800 nm/RIU [142]	Typically in range of 49 to 650 nm/RIU [142] [160]

The discussed sensitivity and figure of merit properties of SPR sensors depend to an extent on sensor design and in some cases can be further enhanced by thin layers of certain porous dielectric coatings, such as ZNO or SiO<sub>2</sub>, which can also act to protect and insulate the metal film [5].

A drawback of SPR technology which it is necessary to be cognisant of is the lack of specificity of the readout signal [3], which is potentially problematic in the context of trying to determine accurate lithium-ion battery diagnostic information. In addition electricity cannot be allowed to flow through the metallic film or it will disrupt the signal, therefore a robust protective film that can withstand the chemical environment in the cell and insulate the sensor is necessary.

In terms of future advances in the technology, the development of ordered nanostructures and photonic crystals has opened up new possibilities and opportunities. Although nanoparticles are not new, new tools allowing them to be engineered into ordered and complex architectures at nanoscale have helped to discover and understand new phenomena. The concept of highly integrated optical devices with structural elements smaller than the light wavelength has become a possibility [1].

### 2.3.3. The use of SPR in energy storage devices

To date there are no papers available showing research into diagnosing lithium-ion battery state with SPR. In 2018 the first documented paper was published regarding the utilisation of plasmonic sensing in an energy storage device [18], with the authors affirmation that there were no established diagnostic devices able to 'look inside' energy storage devices and monitor their state of charge in real time. The study investigated and demonstrated diagnosis of the SOC of a supercapacitor using SPR and provides a baseline of relevant good practice, while requiring adaptation to lithium-ion technology. In the described experiment a Tilted Fibre Bragg Grating (TFBG) has also been integrated into the fibre sensor. The Bragg resonance is unaffected in wavelength and power by the external medium hence it can be correlated with temperature and used to deconvolute the temperature effects from the plasmonic resonance (SPR) reading used to determine changes in the surrounding medium composition [142].

In the study normal voltammetry tests, galvanostatic charge/ discharge tests and high voltage hold tests were carried out and the optical results compared to the cell state as measured by potentiostat equipment; the results demonstrated a clear correlation between the SPR readings and the supercapacitor state of charge. In the three different test cases the correlation found was R<sup>2</sup>= 100%

and repeatability= 97.5%,  $R^2= 97.2\%$  and repeatability= 95.8% and  $R^2= 96.4\%$  and repeatability= 94.7% respectively, the correlation between the supercapacitor SOC and optical response is attributed to the movement of the cations and anions in the supercapacitor electrolyte. On the basis of these results this is a highly promising finding and very encouraging for the potential of NPS as an energy storage diagnostic method [18]. The graphs in Figure 2-20 give an overview of the resulting signal obtained by Lao *et al.* The oscillating nature of the signal is caused by the TFBG resonances [142]. The change in the light wavelength intensity associated with the SPR SPP can be found in the light blue 1560nm region, while the reflection intensity change due to the TFBG temperature associated change can be calibrated in the 1615nm light orange region which is unaffected by the surrounding material permittivity.

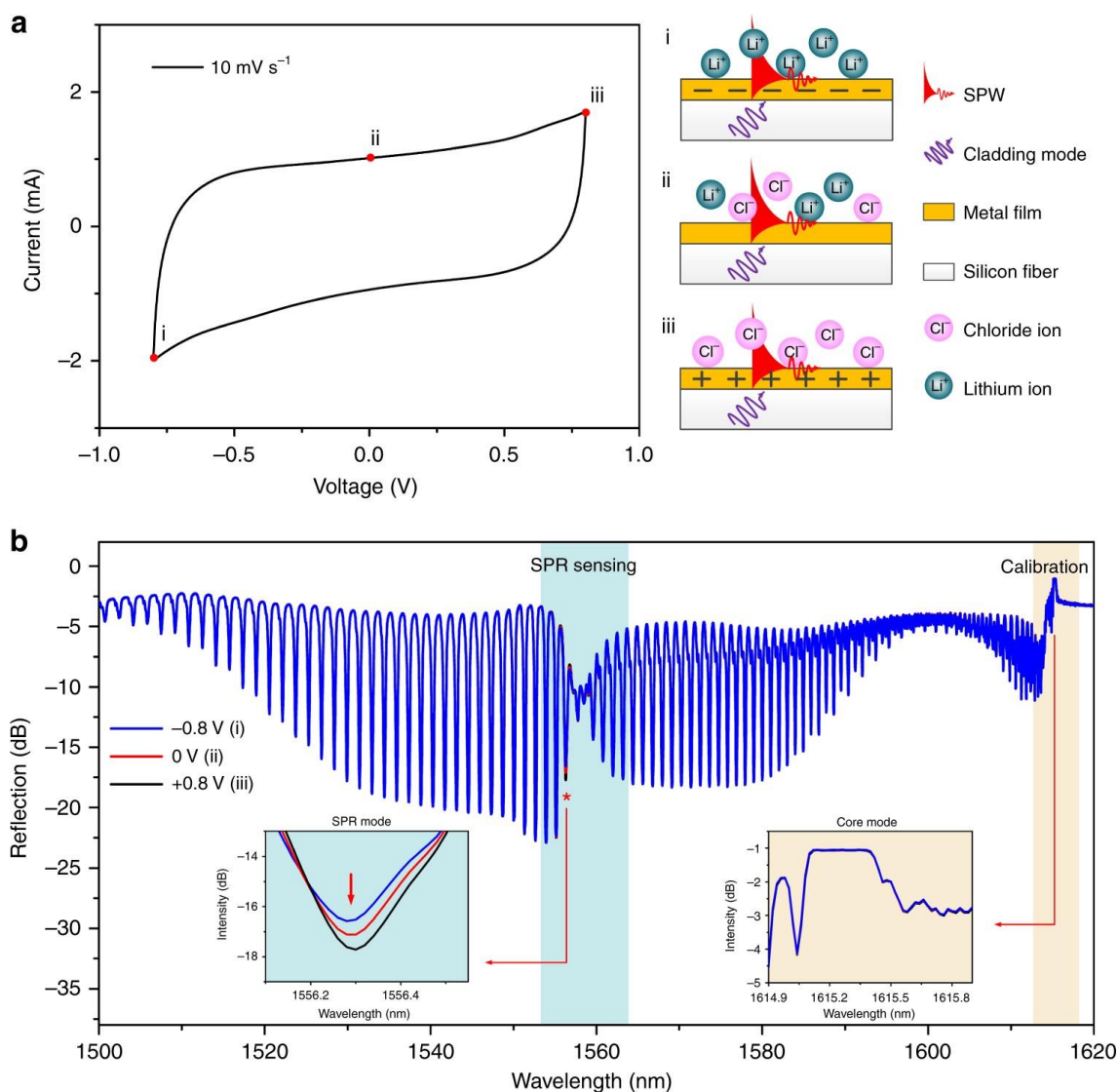


Figure 2-20- a) CV response of a supercapacitor, i) and iii) showing polarised states and ii) showing neutral state b) SPR signal response of P-polarised input [18]

A further study has been carried out utilising both an SPR and an LSPR probe in a supercapacitor, the relatively much less temperature sensitive LSPR probe (which also has a much more localised dielectric sensitivity) is placed adjacent to the electrode surface to measure capacitance via ion-aggregation, while the SPR probe is used in this case for temperature sensitivity [161]. The researchers demonstrated in their results a linear correlation between the optical response and the supercapacitor SOC, and that the capacitance increased with temperature.

More recently a study utilised a SPR and TFBG based sensor in a ZN-MNO<sub>2</sub> aqueous battery, by placing the sensor at the surface of the MNO<sub>2</sub> cathode the researchers were able to demonstrate a clear correlation between the cell charge and discharge and the optical signal intensity [162]. Through analysis of this optical data the two stage intercalation mechanisms of the H<sup>+</sup>/Zn<sup>2+</sup> ions at the electrode-electrolyte interface could be seen. This study is a clear demonstration of the potential of SPR optical techniques to provide insight into cell kinetics.

## 2.4. The potential benefits of utilising SPR in lithium-ion batteries

Current battery management systems rely on monitoring external parameters such as voltage and current to diagnose battery state and ensure safe battery operation, with the limitations of such techniques usually resulting in battery overdesign and inefficient use of capacity [163]. While techniques exist to observe internal battery processes they require either modified cells or substantial testing equipment not suitable for an application environment [112]. Although there are techniques available to non-invasively study Li-ion cell internal processes, these are still in an early research stage with promising but limited information collected so far [97] [139]. Lao *et al* who through their experimentation in 2018 were the first to demonstrate the use of plasmonic based sensing in an energy storage device, a supercapacitor, affirm that there are currently no other diagnostic devices able to 'look inside' energy storage devices and monitor their state of charge in real time [18].

Plasmonic sensing presents itself as a technology with numerous advantages that are equally advantageous to application in lithium-ion batteries, namely the potential for *in situ* and continuous monitoring of electrochemical activity, the compact size, flexible shape, chemical robustness, low cost of sensors and remote operating capability. The silica fibres are also electrically insulating and are not affected by electromagnetic or radiofrequency interference [152]. More accurate diagnostic technique would allow the battery sizing to be closer to what is required, resulting in more optimised application, and the charging and discharging to be closer to the allowable limit with less required safety margin. Battery charge profile impacts on batteries could be better understood, allowing further reduction of the recharge times by developing more optimised fast-charge regimes. Improving battery management through superior diagnostics can also benefit reliability and lifespan [129]. Finally, second life applications could also be better enabled, as key challenge around retired batteries is developing a reliable and efficient method of measuring the current State of Health. This could be of particular benefit in the EV industry in which 120GWh of retired batteries with up to 80% capacity remaining are expected by 2028 [6].

The Battery Management System, crucial in managing cell activity in battery modules and packs through voltage and current controls, relies on cell data to ensure safe operation, e.g. by avoiding overcharge [8]. The potential for plasmonic sensing to provide real time data, or a periodic reference for the BMS to re-calibrate according to the current state, coupled with superior accuracy by taking measurements from inside the cell, opens up the possibility for the BMS to significantly optimise the use of the battery cells with reduced error and better safety margins. While there are challenges in integrating fibre optics into cells, it has been noted that it is common practice to integrate fibres into composite structures such as pressure vessels, and that the cost of an optical-based BMS could be comparable to an electrical one, particularly given that the scale up of greater number of fibres in cells leads to limited additional cost due to multiplexing [155]. While the cost of the optical interrogator unit can be expensive (hundreds or thousands of pounds), it could be possible to 'plug-in' the optical sensors to an optical interrogator so you do not need one per application, or to build a very simple and cheap system with a light emitting diode and photo diode operating at a specific wavelength for a specific application (instead of a more complex and expensive broadband light detector). A further interesting consideration is that with the array of fibre optic based sensors that are available and their capability to measure temperature, strain and even current, it is not inconceivable that it is possible to develop an entirely fibre optic based rather than an electrically based battery diagnostic system.

With the growing uptake and complexity of Li-ion battery systems, superior diagnostics can have a range of benefits including research insights, improved safety, battery use optimisation and supporting application such as second life uses and the 'battery passport' concept [164]. Being able to obtain real time data from directly inside the battery cell opens up new insights and research possibilities, and with greater refinement potentially could offer superior state diagnostics. Safety is always a crucial consideration and a technology capable of diagnosing for example lithium plating before battery failure becomes catastrophic, or allowing a faster response to it, would be very valuable- especially given the dangerous, self-propagating and difficult to mitigate challenge of thermal runaway and battery fires. In terms of second life applications it is considered that EV battery packs are no longer suitable for use in an EV once they drop to 80% capacity, the pack nonetheless has substantial capacity and capability remaining which could be used in another application; however there are significant challenges around diagnosing the state of the battery and its safety, as the degradation it has undergone can vary greatly depending on the history of its usage [165]. Diagnostics that are capable of evaluating battery state of health can therefore play a key role in supporting second life applications and the proposal to develop battery passports to facilitate this [166].

## 2.5. Hypotheses

Review of the plasmonic based fibre optic sensor technology and battery cell properties and working mechanisms leads to the following three primary hypotheses to be tested by this study:

**Hypothesis 1:** That the changes in the chemical and materials environment of the cell during changes in cell state will be detectable via the plasmonic fibre optic based sensor.

**Hypothesis 2:** That the movement of lithium during cell charge and discharge will lead to a refractive index change that will be detectable via the plasmonic fibre optic based sensor.

**Hypothesis 3:** That the plasmonic fibre optic based sensors are sufficiently small and chemically inert that they will not impact the operation of the cell.

## 3. Methodology

### 3.1. Plasmonic sensor technology

The optical measurements in the experimentation are carried out utilising plasmonic sensor fibres and an optical unit transmitter and receiver device (Insplorion AB, Göteborg, Sweden). The fibres used are optical fibres with a 50mm sensing region coated in a thin gold film, the fibre design is illustrated in Figure 3-1. The sensing region and rest of the fibre have polymer coatings to protect it from corrosion within the battery and improve mechanical robustness. The manufacturer estimates the sensing depth of the sensor as 200nm, with exponentially decreasing sensitivity to this depth. Notably the SEI layer thicknesses of an NMC versus graphite cell varies but can be estimated to be 10nm or less on the anode and cathode in the initial stages of cell life, while possibly being slightly thicker on the cathode than the anode [167], as such the sensor placed at the surface should detect through the SEI region and into the electrode boundary layer beneath.

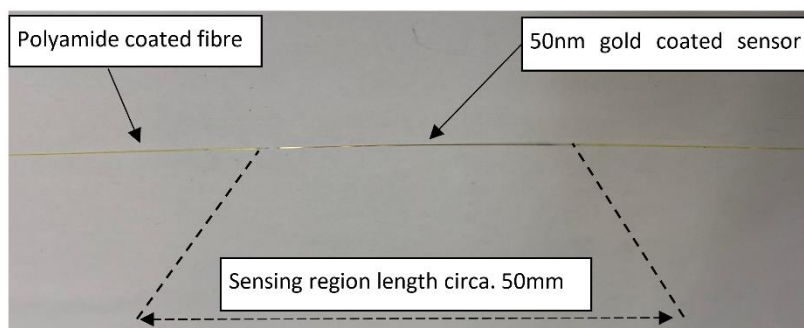


Figure 3-1- Annotated picture of the optical fibre plasmonic sensor

The optical unit consists of a broadband light emitter and an optical spectrometer receiver, the sensor fibre is used in transmission mode - transmitter at one end and the receiver at the other. The sensor fibre is fusion spliced to optical fibre 'pigtailed' connected to the optical unit via FC/PC connectors. As described previously in more detail in the Section 2.3.2 the SPR technique couples the refractive index of the analyte to light attenuation of the optical fibre signal, via the surface plasmon resonance of the metallic coating and the evanescent field created by the internally reflected light signal [168].

In this study we are testing if changes in battery state can be detected by an internally placed SPR optical fibre sensor, ie. if changes in battery state lead to changes in internal material refractive index properties that can be detected by the sensor. Potential material state changes that could be detectable include lithium concentration change at the electrode during charge and discharge, SEI layer formation, lithium plating and the creation of additional products through parasitic reactions.

The optical unit (OU) used includes software for control of the optical unit settings and data capture (Insplorion AB, Göteborg, Sweden). The optical equipment measures the light intensity in counts, where each count is equal to 375000  $\mu\text{W}$  per ms of integration time, as such a normalised reading in which the count value is divided by integration time gives a value of 375000  $\mu\text{W}$  per count- however in general the relative change in light intensity is utilised rather than the absolute values. The integration time and number of measurement averages taken per measurement are selected to ensure an accurate reading without saturating the optical receiver, the OU is unable to differentiate light intensity above 60,000 counts. The sampling rate typically varies between once every 60s and 120s depending on the length and nature of the test, to ensure sufficient resolution.

In order to connect the SPR sensor to the sensor to the optical equipment, it is necessary to fusion splice each end of the SPR sensor to 'pigtail' fibres so they can be connected to standard optical connections; pigtail fibres are acrylic coated fibre optic fibres with an FC/PC optical connection on the end. Ideally the fibres being fused should be the same diameter, in this case there is a slight discrepancy because the SPR fibre has been made with 90 micrometer core diameter optical fibre, whilst the closest standard pigtail optical fibre diameter found to be readily available is 100 micrometers (SQS) and 105 micrometres (Thorlabs, New Jersey, United States), this discrepancy is evaluated by Insporion AB to have minimal impact on the signal. The fibre optic cables that then connect the 'pigtails' to the optical unit are low hydroxyl multimode Ø105 µm silica fibre cores (Thorlabs, New Jersey, United States).

Before the fibres can be fusion spliced the ends of the fibres must be prepared, this involved stripping the coatings from the fibres and then cutting the ends of the fibres to ensure a clean, smooth and perpendicular end surface. The pigtail fibres are coated in acrylic which can be stripped away with strippers. The SPR fibres have been coated in polyimide at our recommendation, to give them corrosion resistance inside the battery, however removing the polyimide is a more difficult process. Initially 1M potassium hydroxide (KOH) in ethanol solution was mixed with de-ionised water at a ratio of 400g ethanol solution to 100g de-ionised water and heated to approx. 70 degrees Celsius, and the ends of the fibres were left inside the solution for 30 minutes as per the Dupont Kapton (polyimide) etching instructions. This method worked but was complicated by the preparation involved, risk of damaging sensors and facility layout; as such a method of 'burning' the polyimide at the end of the fibre for a couple of seconds and then cleaning it away with ethanol wipes was subsequently adopted. Once the ends of the fibres have been cleaned and the optical fibre exposed, the end of the fibre is cut to ready the end surface for fusion, using a high precision optical fibre cutting tool. Finally the SPR fibre and pigtail prepared ends can be placed inside the optical fusion splicer (70S+, Fujikura, Tokyo, Japan), locked into position and the fusion process can be initiated- this step is shown in Figure 3-2.

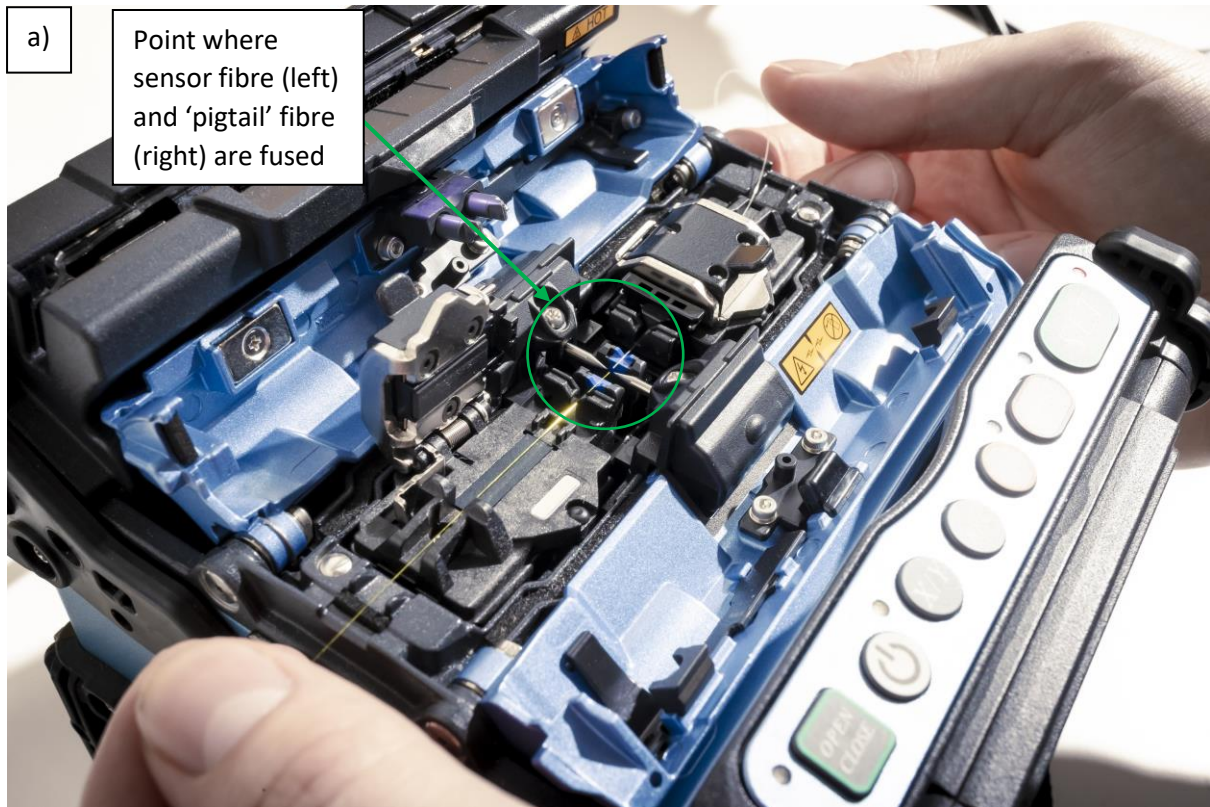


Figure 3-2- a) SPR fibre sensor and pigtail fibre being placed in fusion splicer, b) SPR sensor fibre and pigtail fused with splice protector added

Splice protectors are placed over the spliced fibre ends in order to protect them from the atmosphere (embrittlement) and provide mechanical strength. The spliced SPR sensor and pigtails can then be connected to the optical unit via 'patch cables' (Thorlabs) which have FC/PC connectors at one end to connect to the pigtail FC/PC connectors, and SMA connectors at the other end to connect to the optical unit.

## 3.2. Fibres in Electrolyte experiment setup

### 3.2.1. Electrolyte exposure over time

The spectrometer connected to the optical sensor emits broadband light across the wavelengths 400nm to 1000nm, a range selected for compatibility with the receiver and the plasmonic sensor [169]. In order to identify which wavelengths from the range may be of particular interest and most likely to exhibit a plasmonic response inside a battery cell the sensor has been tested in battery cell electrolyte. The electrolyte is added to the flask inside an argon atmosphere glovebox, to avoid reaction with atmospheric gases and moisture. The glovebox used throughout this study is argon filled, with slight positive pressure, that maintains O<sub>2</sub> and H<sub>2</sub>O at below 1ppm through a monitoring and filtration system (MBraun, Garching, Germany).

Plasmonic optical fibre sensors were initially placed in battery cell electrolyte in an attempt to identify the plasmonic response to the solution and the effect of extended exposure to electrolyte. A 3-neck round bottom flask was used with two optical fibre sensors placed into the flask through the side necks, as shown in Figure 3-3. Bungs were placed in each side neck to hold the fibres in place and seal the vessel. The fibre sensor ends were then spliced to pigtail fibres with FC/PC connectors using the fusion splicing equipment, to allow the sensors to be connected to the optical unit via fibre optic cables.



*Figure 3-3- Three neck flask containing a SPR fibre optic sensor*

A reference reading in air was taken first, subsequently the vessel was then placed inside an argon atmosphere glovebox where electrolyte was poured into the vessel with a pipette through the central neck. 15ml of 1M Lithium hexafluorophosphate (LiPF<sub>6</sub>) in Ethylene Carbonate/ Ethyl Methyl Carbonate (EC/EMC - 3/7 v/v) +2% weight Vinylene Carbonate (VC) electrolyte was added, submerging the sensor regions of the fibres. The flask was then removed from the glovebox, the sensors were plugged into the optical unit and the spectra readings were recorded; this procedure enabled an optical response

comparison between the electrolyte and an air reference. Optical readings of the electrolyte were taken at weekly intervals over a number of weeks, to see how the signal changed over time.

### 3.2.2. Changing concentrations of electrolyte

Subsequently an experiment was designed to measure the fibre optic response to changing concentrations of electrolyte, to do this it was necessary to connect the optical sensors to the OU while still inside the glovebox, then to add pure organic solvent with increasing molar concentrations of lithium hexafluorophosphate ( $\text{LiPF}_6$ ) salt, commonly used in battery electrolytes. To allow the fibre optic cables from the optical unit to be put inside the glove box it was necessary to obtain a 'pass through' for the optical fibres into the glovebox that would maintain the sealed atmosphere. Putting the entire optical unit in the glovebox was not an option because of the size of the unit, because it needed an electrical power source and because the argon atmosphere causes electrical equipment to fail quickly.

The fibre pass through for the glovebox was ordered to fit inside the glovebox entry ports flanges. Four suppliers were contacted about supplying this part, ThorLabs, SQS, Vacom and FiberTech Optica. Thorlabs provide a single port per flange part, all three of the other suppliers showed interest in producing a custom part, but SQS were the fastest to develop a design that met the specifications and provided a quote substantially cheaper than the ThorLabs equivalent. The specification of the part ordered from SQS, as well as the additional mating sleeves, patchcords and pigtailed, can be found in Appendix A. This fibre pass through flange, with FC/PC connectors, allows the optical unit to be connected to a sensor inside the glovebox as per the setup in Figure 3-4.

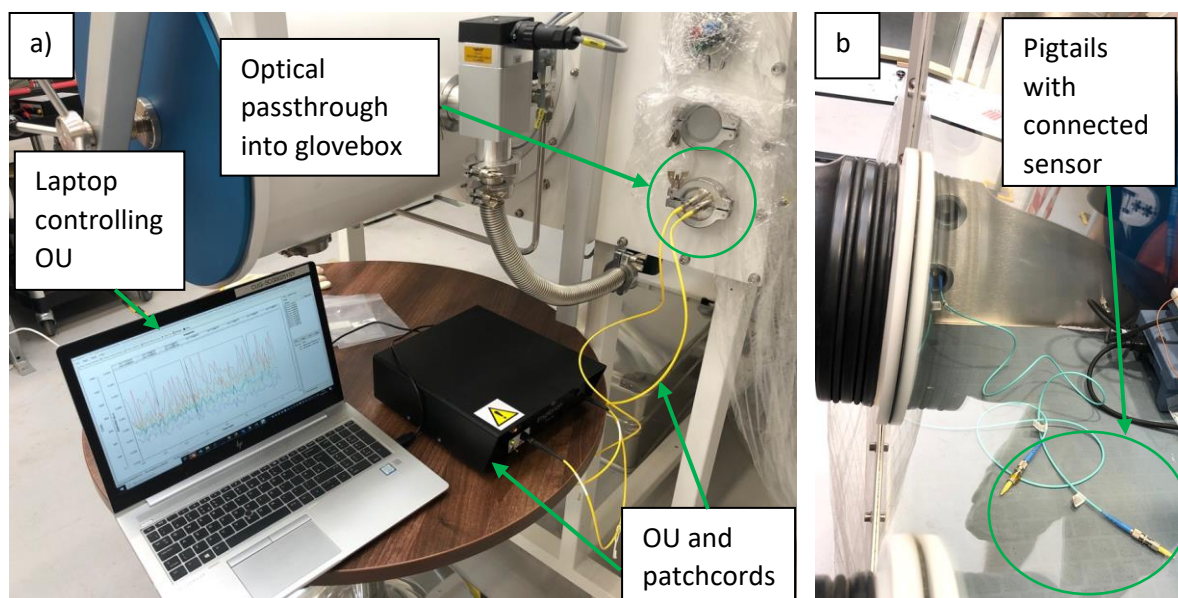


Figure 3-4- Optical set up utilising optical pass through to carry out experiments inside glovebox, a) shows optical unit controlled by laptops and patchcords connecting OU to FCPC connectors on glovebox passthrough, b) shows patchcords connecting passthrough inside the glovebox to pigtailed and optical sensor

A plasmonic based fibre optic sensor was tested connected to the optical unit outside glovebox, and then transferred into the glovebox and tested through the pass through inside the glovebox. The results show that the sensor signal was not significantly impacted by using the pass through, with the software integration time selection only changing from 0.532 seconds outside the glovebox to 0.603

seconds inside the glovebox, indicating only a small light attenuation, and the profile of the signal seemed unaffected.

The installed fibre pass through then allowed experiments with optical sensors to be carried out inside the glovebox. To de-convolute the impact of the lithium salt on the OU response from that of the organic solvent itself, an empty 3-neck round bottom flask with an optical sensor inside was placed inside a glovebox, where pure organic solvent (Dimethyl carbonate- DMC) was first added to the flask to obtain a solvent only optical response. Subsequently lithium salt electrolyte (1M LiPF<sub>6</sub> in EC/EMC (3/7 v/v)) was incrementally added in multiple steps up to 0.5 molar concentration of LiPF<sub>6</sub>, to observe how the signal changes in relation to increasing lithium salt concentration.

### 3.3. Cell making

#### 3.3.1. Reference cells assembly

The cell electrodes used for the experiments throughout this study were electrodes of the composition lithium nickel manganese cobalt oxide (LiNiMnCoO<sub>2</sub>, NMC 111) on an aluminium substrate for the cathode and graphite on a copper substrate for the anode, at a loading of 2 mAh cm<sup>-2</sup>. By mass the cathode material mix was 94% NMC, 3% C65 (carbon black) and 3% polyvinylidene fluoride (PVdF), and the anode material mix was 94% graphite, 3% C65 (carbon black), 1.5% carboxymethyl cellulose (CMC) and 1.5% Styrene-Butadiene Rubber (SBR). The cathode thickness is 116µm with a 21µm thick current collector, and the anode thickness is 108µm with a 9µm thick current collector. The electrode areas are approximately 52mm by 77mm, and a stack of electrodes for a cell is composed of 11 anodes and 10 cathodes divided by and wrapped in a thin polymer separator (16µm Trilayer Microporous membrane), the pouch cells weigh 29.4g +/- 0.2g when dry (no electrolyte). The tabs of the anodes and cathodes respectively are spot welded together to form the negative and positive terminals of the cell. This batch of cell stacks are used for all cells in this study for consistency, and the same electrolyte in the same quantity, 8.6ml of 1M LiPF<sub>6</sub> in EC/EMC (3/7 v/v), is also used in all cells. A picture of a cell stack and the electrolyte used are shown in Figure 3-5, while additional information about the cell is provided in Appendix L.

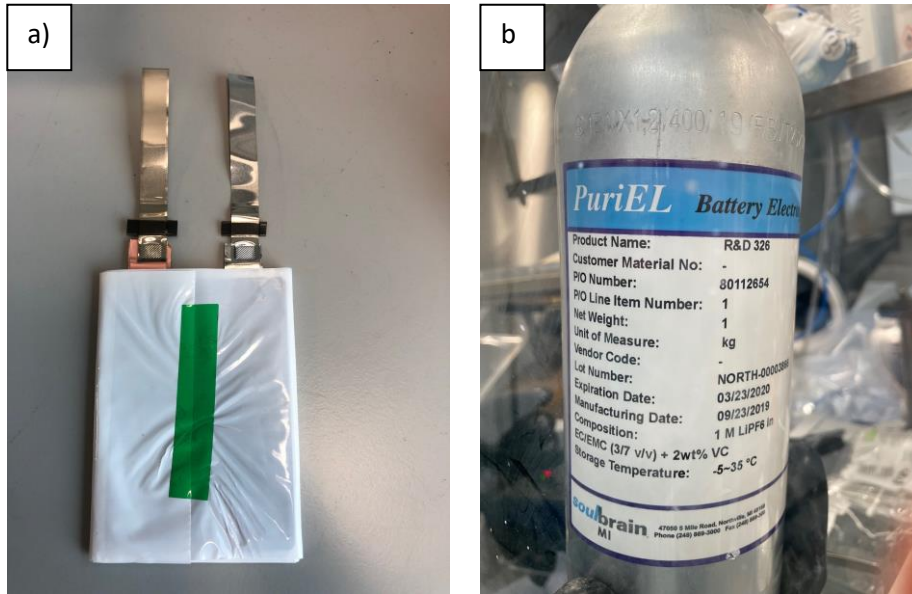


Figure 3-5- a) Cell stack and b) electrolyte used in the manufacture of all cells in this study

A number of 'reference' cells without any additional sensors included were manufactured according to a standard pouch cell manufacturing process. The cell stacks are placed inside formed flexible aluminium pouch material which is 158 microns thick (itself coated in a polymer to make it non-conductive); the pouch material is formed and cut to align with the electrode stack and have enough space around the stack for sealing, with special attention given to the alignment with the hot-melt glue on the electrode tabs. The pouch material is folded over the stack which creates a seal on one side, and then the top and bottom edges of the pouch are sealed with a sealing machine (MSK-140, MTI Corporation, California, United States) that applies a metal sealing bar heated to 180°C and with significant force (the weight of the bar and weight connected to bar). Following this sealing process only one long edge of the cell remains unsealed.

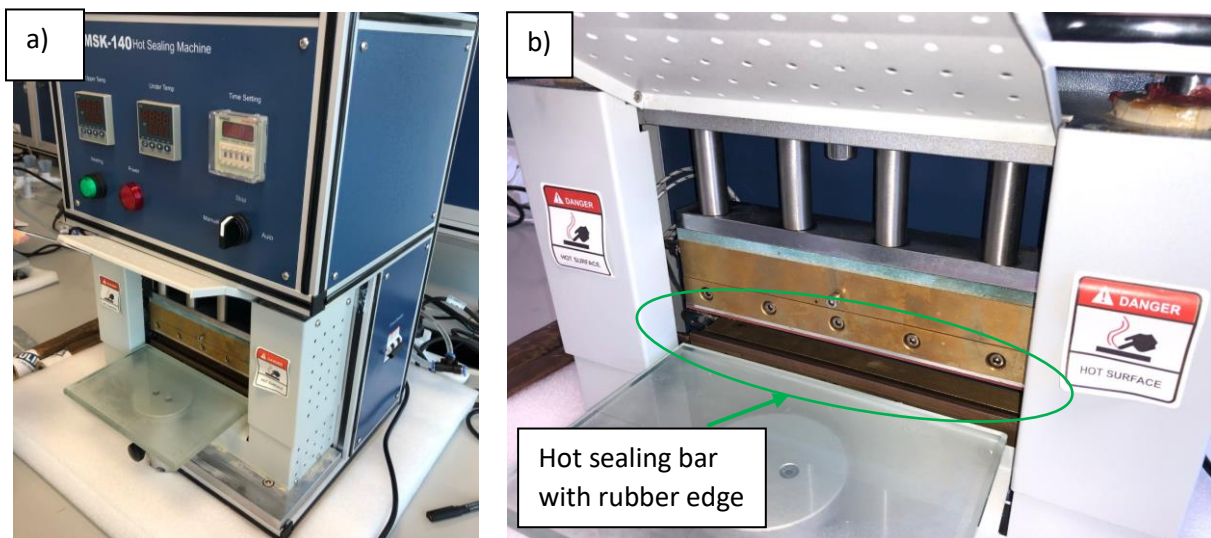


Figure 3-6- Sealing machine used to make initial seals on pouch cell, the metal bar is heated to 180°C and then dropped onto the edge of the pouch cell that requires sealing, a) sealing machine with controls, b) zoomed in image of sealing bar

The cell is then transferred to an argon atmosphere glovebox for the electrolyte to be added (inert atmosphere is required so the electrolyte does not react or pose a health risk) and final seal made. Before this is done the cells are heated to approximately 80°C in an oven to dry them out, before being placed in vacuum in one of the glovebox entry chambers for around 12 hours to remove moisture. Once inside the glovebox 8.6ml of 1M LiPF<sub>6</sub> in EC/EMC (3/7 v/v) electrolyte is added to the cell with a pipette, the capacity of the pipette used is 5ml, so the electrolyte is added in two batches of 4.3ml. The cells are left for 30 minutes after each 4.3ml electrolyte addition to allow the electrolyte to soak into the electrodes and more uniformly distribute around the cell. The cells are then placed inside a vacuum sealing machine inside the glovebox, the machine achieves a pressure of -69mbar (relative) to suck the air out of the cell before the final seal. Finally the final seal of the cell takes place in the vacuum sealing machine, via a metal sealing bars above and below the pouch material, heated to 180°C. The vacuum sealing machine can be seen in Figure 3-7.

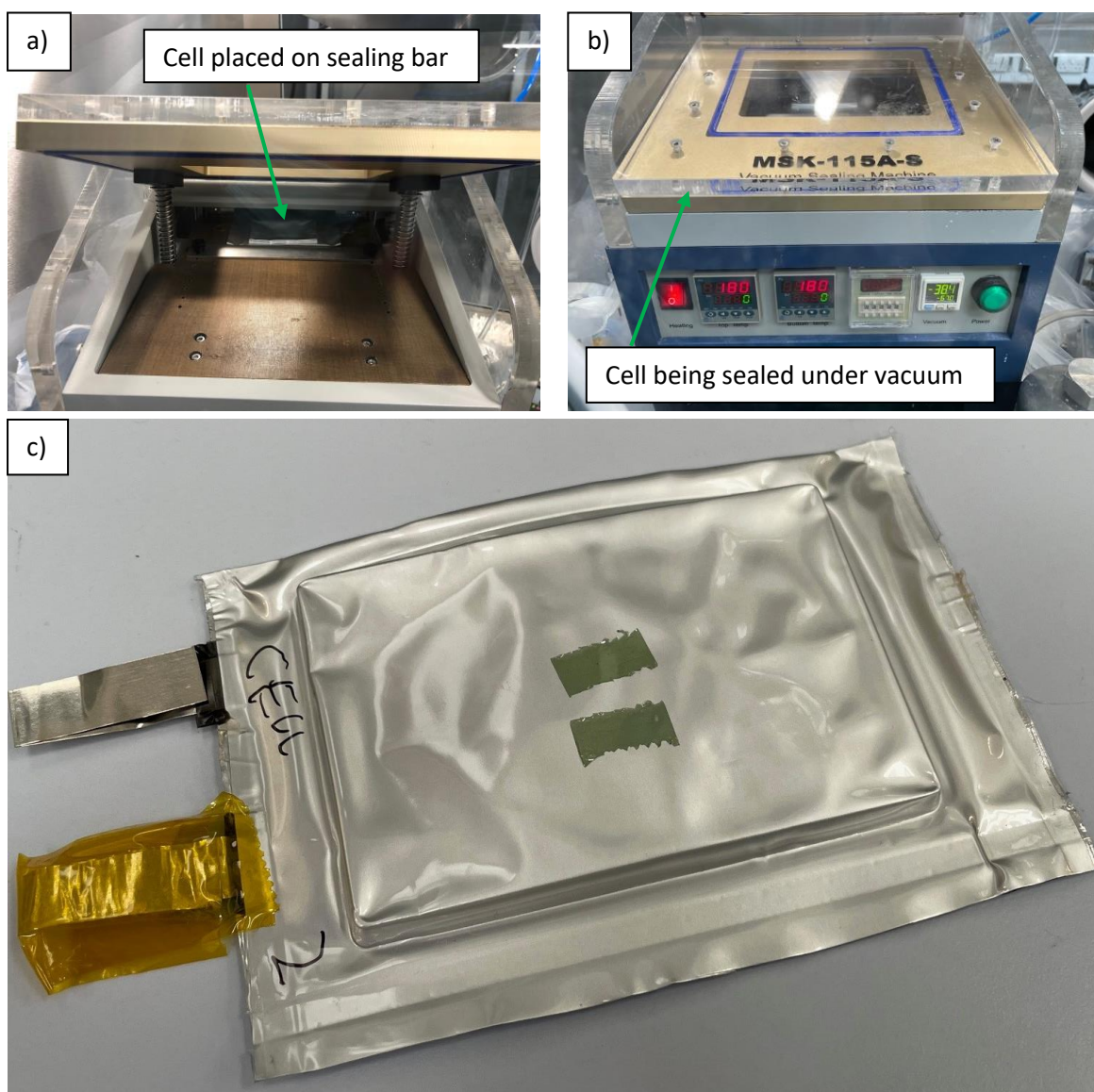


Figure 3-7- a) a cell inside the vacuum sealing machine ready for the final seal, b) sealing machine closed during the sealing process, and c) a fully sealed cell after completion of the sealing process

Once assembled, the cells are placed inside jigs to secure them, keep them under compression so there is no expansion due to gas produced during cycling, and provide convenient connection points to connect the electrode tabs to the potentiostat current cables and measurement cables. The cell is placed on the acrylic bottom panel of the jig, and the two electrodes are clamped with brass blocks. A layer of foam is then placed on top of the cell and the upper jig panel is placed on the foam and then clamped down onto the lower panel with four bolts. A gentle pressure is placed on the top panel and the bolts are mostly hand tightened, before providing a final turn to the bolt nuts with a polymer coated spanner. The cells must be left for at least 12 hours before formation cycle for the electrolyte to fully soak into the electrodes, but not more than 48 hours or the electrolyte can start dissolving and pitting the copper anode. Pictures of a full cell in a jig and connected to a potentiostat are shown in Figure 3-8.

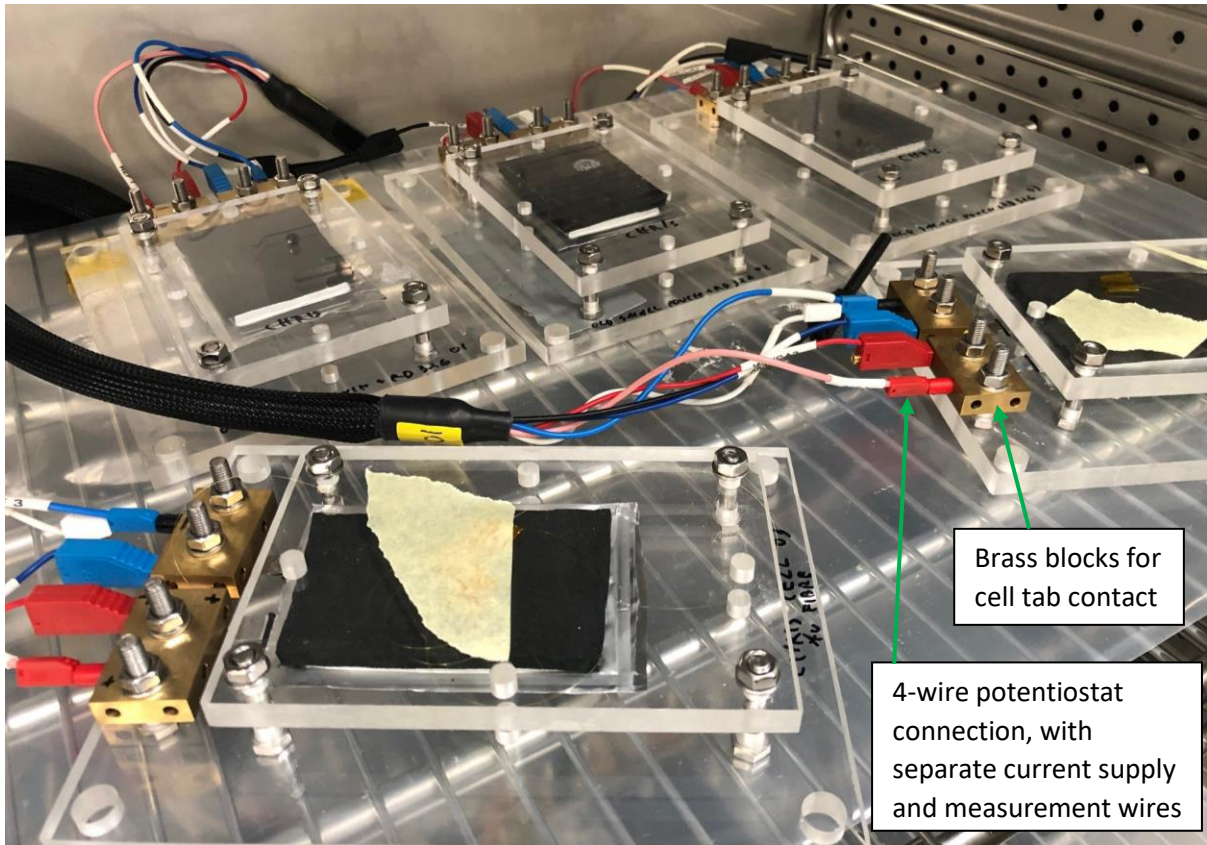


Figure 3-8- Sealed cells in acrylic compression jigs on oven shelf, jigs with brass blocks for tab contact and potentiostat connection

### 3.3.2. Manufacture of cells with one and two sensor fibres

In terms of sensor in cell testing, pouch cell technology is selected for this experimentation for its relatively flexible manufacturing process conducive to accommodating sensors; a method has been developed to reproducibly manufacture pouch cells with fibre optic sensors inside. Before manufacturing cells with the sensors inside different elements of the manufacturing processes were tested. One element that required testing was the process of sealing a sensor inside the pouch material, it was necessary to check that the sealing did not damage the fibre and that the seal did not leak at the point where the fibre passed through it. In order to do this fibres were initially sealed in empty pouch material and then leak tested by filling them with water, leaving them for several days and looking for a leak as can be seen in Figure 3-9. Additional glue (Enhanced Sulfurized Polymer Resin Material with 3 Layers Lamination, Hot Melt Adhesive Polymer Tape, MTI Corporation) was placed at the point that the fibre passed through the seal to fill any gaps and act as a sealant.

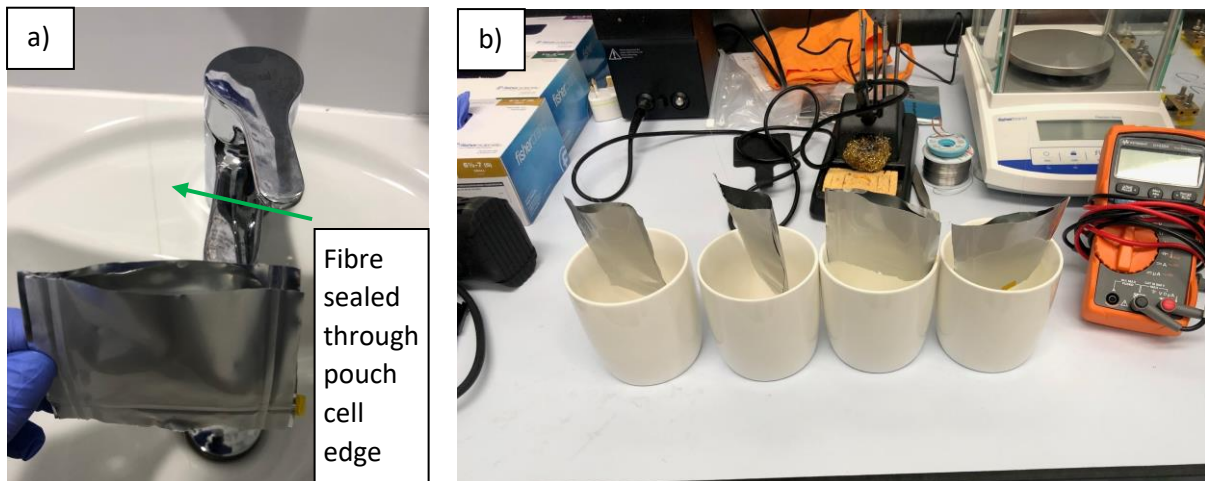


Figure 3-9- Pouch cell material with fibre sealed through edge filled with water and leak tested, a) filling the sealed pouch material (only open at the top) with water, b) leaving the water filled pouch material in cups to observe if any leakage occurred

Additionally the process of splicing the sensor fibres to the pigtail fibres also had to be tested, requiring the polyamide at the ends of the fibres to be removed as discussed previously, while considering this in the context of sensors that have already been incorporated into the cell. Initially 1M potassium hydroxide (KOH) in ethanol solution was mixed with de-ionised water at a ratio of 400g ethanol solution to 100g de-ionised water and heated to approximately 70°C, and the ends of the fibres were left inside the solution for 30 minutes as per the Dupont Kapton (polyamide) etching instructions. This method worked but required considerable care and preparation, as well as different facilities, it would also have been difficult to apply this method to fully manufactured cells with incorporated fibre sensors. Consequently a method of ‘burning’ the polyamide at the end of the fibre for approximately five seconds with a yellow flame and then cleaning it away with ethanol wipes was adopted. This process is not always successful first time and the fibre can break on removal of the polyamide coating due to its brittleness, as such the request was made to Insplorion to increase the length of the fibre sensors to one metre to ensure an excess of material in the event of needing to repeat the process. Figure 3-10 shows the KOH etching process and the removal of the polyamide via the use of a yellow flame.

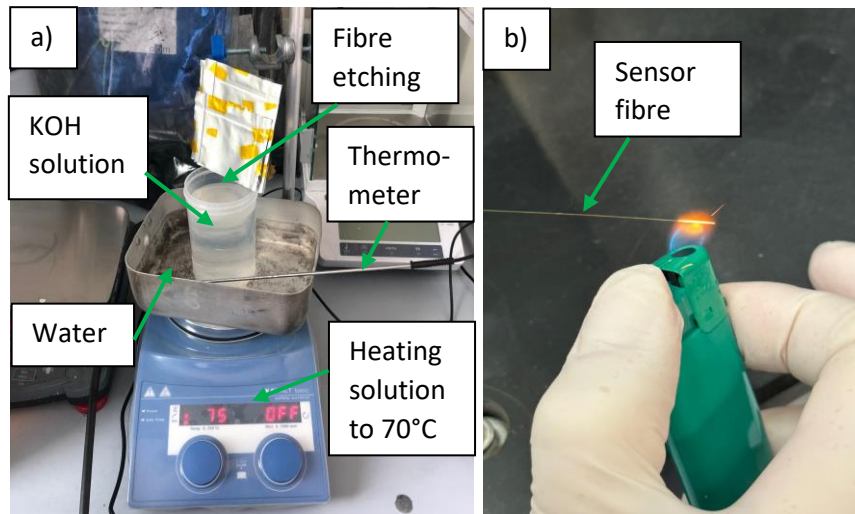


Figure 3-10- Methods tested to remove polyamide from ends of sensor fibre to allow fusion splicing to pigtails, a) KOH etching method, b) burning method using simple lighter

Once these techniques had been established the process of assembling the sensors inside full cells could begin. The optical fibre sensor was introduced through the electrode stack along the vertical axis centred in parallel between the two cell tabs, adjacent to the anode three electrodes in from the edge of the stack. This location was chosen as the centre of an electrode a few layers in is likely to be more representative of the overall cell state than an edge case. Additionally, as the sensing region is 50mm in length means it should take an average of the behaviour over that length. The plasmonic sensor has a shallow sensing range, approximately 1000nm [4,170], so the position of the sensor should mean it only detects the electrode immediately adjacent to it. The sensors positioned in the cell stacks can be seen in Figure 3-11.



Figure 3-11- Plasmonic based fibre optic sensor fibres introduced through the centre of cell stacks, adjacent to an electrode

The stacks with fibres are then placed inside the pouch material and the fibres are held in place for the sealing process using kapton tape, additional glue is placed around fibre at the point it will cross the pouch seal to act as sealant and also held in place with Kapton tape. Once the fibre is placed in position the first pouch cell seals along the top and bottom of the cell, through which the fibre optic passes, are made using a sealing machine (MSK-140 sealing machine, MTI). A rubber layer on one of the sealing bars was considered beneficial to give some flexibility around the fibre and not damage it. One long edge was a fold of the pouch material and the remaining long edge is left unsealed to allow the electrolyte to be added later. (Note: Sealed corners again to ensure no leakage at corners, a potential point of weakness in the battery seal). Figure 3-12 shows the stack in the pouch material before sealing, with the stack, fibres and glue held in place with Kapton tape, and the cell after the top and bottom edges have been sealed in the sealing machine.

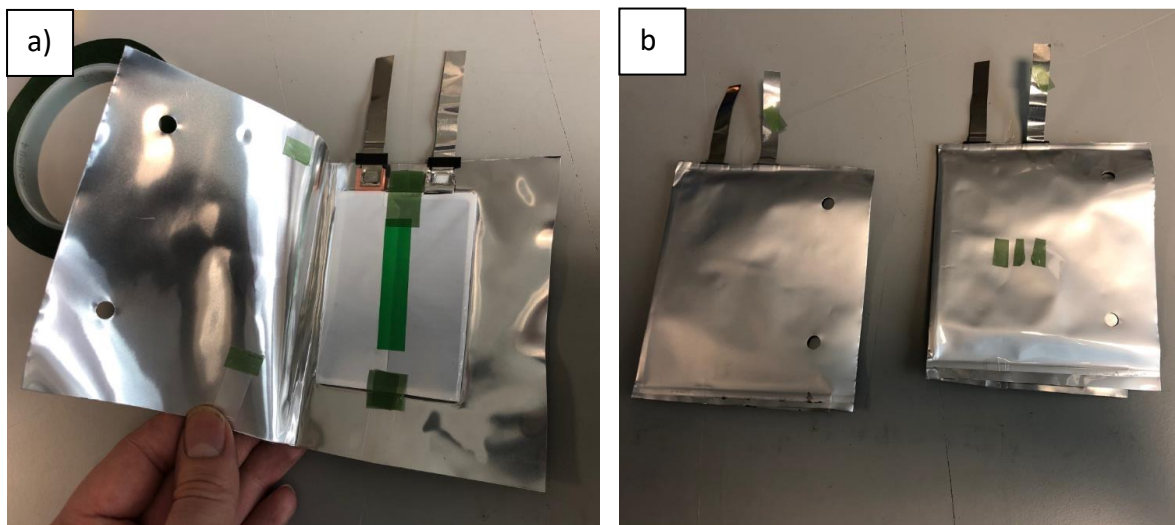


*Figure 3-12- a) Fibre and stack in pouch material before sealing and b) after top and bottom edges sealed*

Subsequently the cell was filled with electrolyte inside an argon atmosphere glovebox and the final seal made under vacuum. The process for drying the cells, adding the electrolyte and making the final seal is the same as described in Section 3.3.1. A pouch cell with fibre sensor can be seen in the sealing machine in Figure 3-13.



Figure 3-13- A cell with fibre sensor incorporated before final seal under vacuum takes place

Completed cells with integrated fibre sensors can be seen in Figure 3-14, along with dimensions.

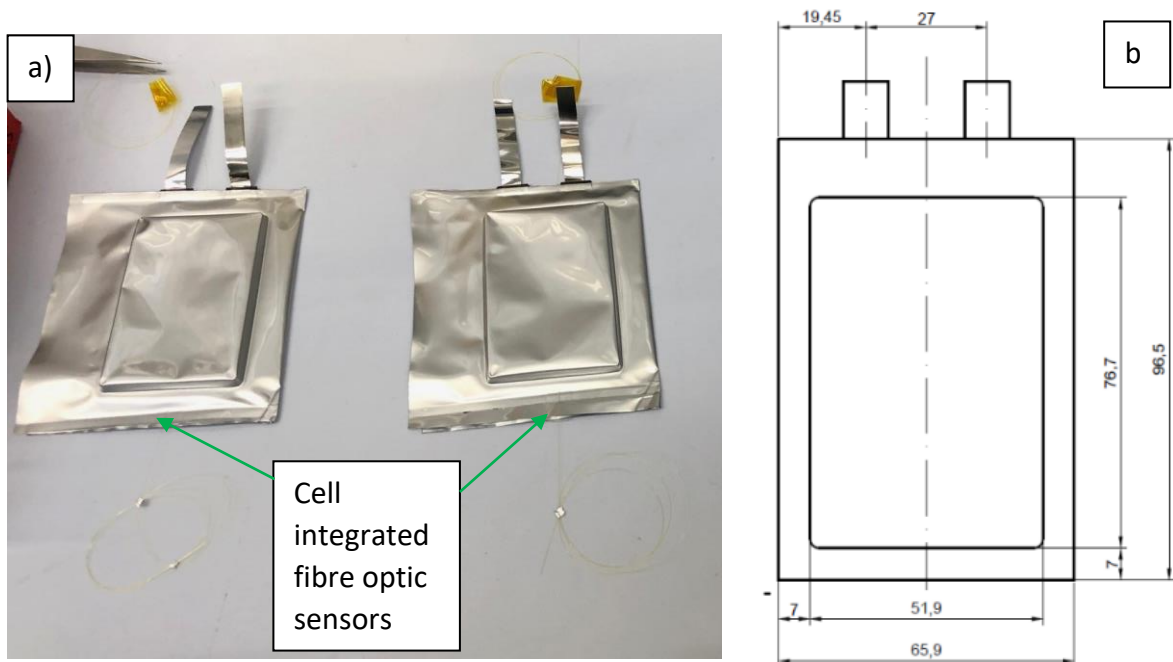
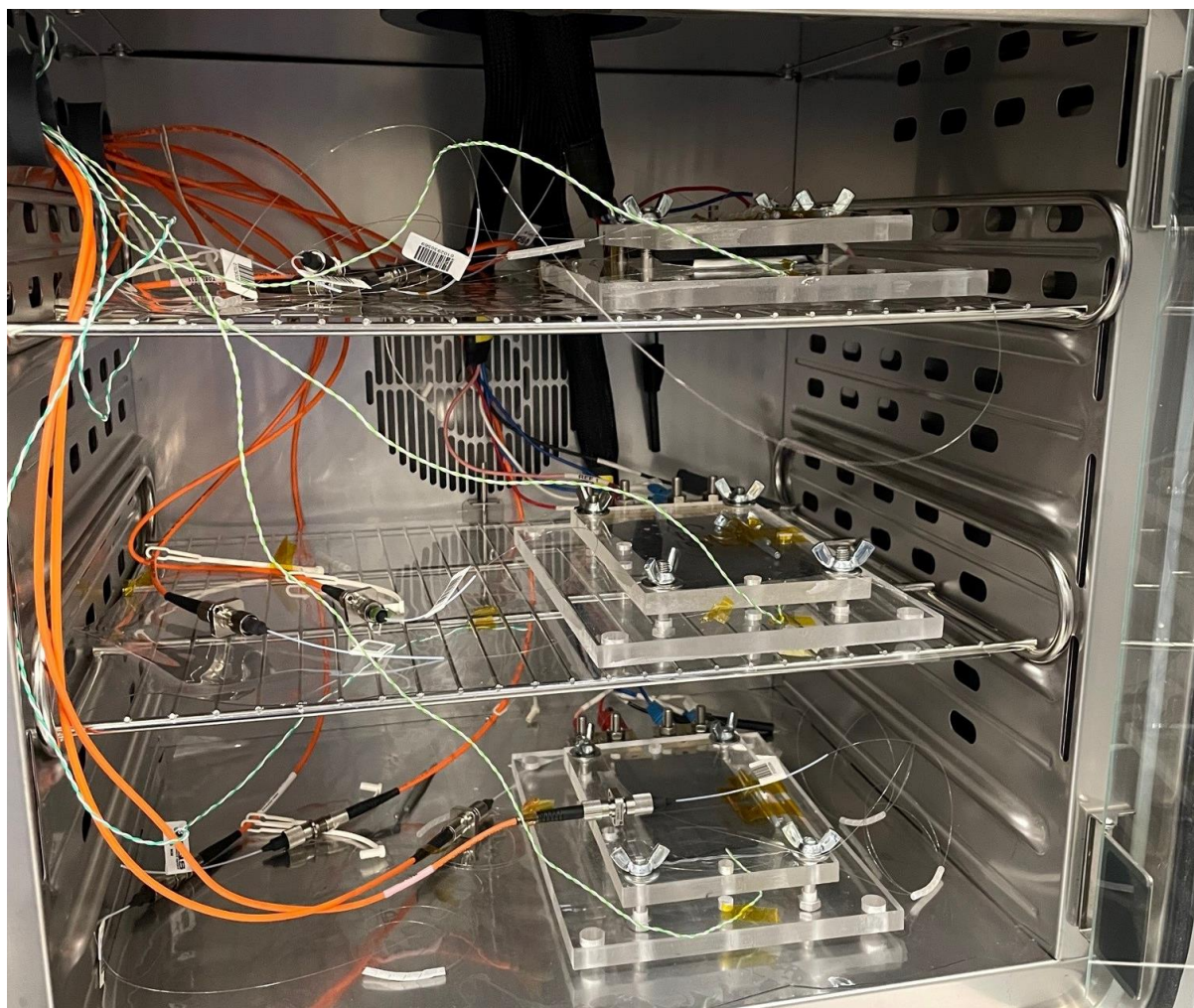


Figure 3-14- a) Assembled cells with integrated fibre optic sensor and b) cell dimensions (mm)

The plasmonic based optical fibre sensors must then be spliced to pigtail fibres with FC/PC connectors to allow them to be connected to the optical unit's broadband light transmitter and receiver. As noted previously, to assist with this process a request was made to Inpslorion to increase the length of the

SPR sensor fibres to 1 metre, this ensured there was sufficient length of material to allow if necessary multiple attempts to make a successful fusion splice to the pigtails at both ends of the SPR fibre- the fusion splicing process is described previously in Section 3.1. The cells can then be placed in jigs and connected to the potentiostat and optical unit, thermocouples are also connected for temperature monitoring. The thermocouples (PicoLog, Cambridgeshire, United Kingdom) are placed adjacent to the external surface of the pouch cells; a PicoLog TC-08 measurement device is used with 'K-type' thermocouple sensors and PicoLog software edition 6.2.5. The connected cells are shown in Figure 3-15 while the system setup is discussed in more detail in 3.4.1.



*Figure 3-15- Cell with fibre sensors in jigs, connected to optical patch cables, potentiostat and thermocouples*

Additionally some cells were made with two fibre optic sensors inside, one on an anode and one on a cathode. The process for these cells is essentially the same as above, but with two fibre optics inserted into the stack at the initial stage.

### 3.3.3. Manufacture of cells with reference electrode

A lithium reference electrode was placed in one of the cells with fibres and one of the cells without fibres, to create 3-electrode system allowing independent readings from the anode and cathode. Lithium metal reference electrodes have been shown to have good reading stability over initial cycling

(at least 20 cycles) [171]. The lithium reference electrode should be placed in the cell after formation cycling. To do this the cell must be placed inside the glovebox and an incision made to allow the insertion of the reference electrode, which is then sealed with a 2-component resin. Care must be taken when placing the formed cell back in the glovebox, thus the entry chamber was cleared with five purge half-cycles (half vacuum emptying) to avoid delamination due to internal pressure of the gases created during the formation cycling.

The reference electrode is made by wrapping lithium strip around a metal wire added for contact with the potentiostat channel measurement (via a crocodile clip). Polymer separator material is stuck on the bottom of the reference electrode as an extra precaution to prevent contact, such as in the event of tearing the battery separator during the use of the scalpel to open the pouch cell or in the process of inserting the electrode.

An incision is made on side of cell to place the electrode in, the reference electrode is then slid underneath the separator at the bottom of the stack. The lithium strip on the reference electrode is pushed most of the way into the cell, however care is taken that the wire connected to the lithium strip does not go into the cell. The resin used to seal the cell mixes two agents to create a polymerisation and solidification reaction, sealing the hole and covering the exposed lithium. A typical glue will not work in the glove box as it requires oxygen to react and set, additionally the mixed resin has the advantages that it does not give off gases and only requires about 10 minutes to set. The cell can then be removed from the glovebox and set up in the jig again- Figure 3-16 shows the reference electrode being inserted in the cell, the resin applied and the final cell setup.

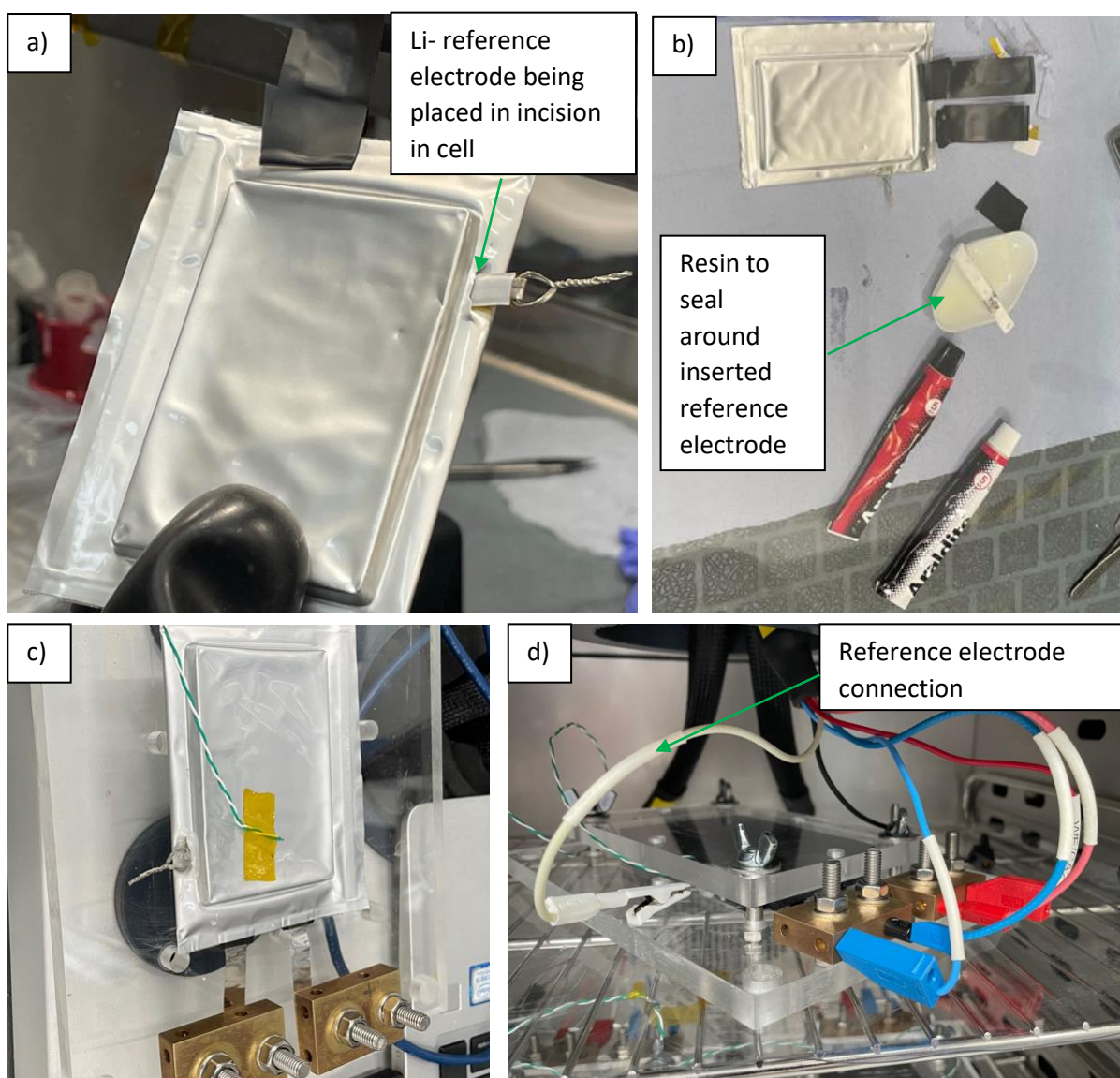


Figure 3-16- a) A lithium reference electrode being placed in formed cell inside a glovebox, b) preparing to mix the resin, c) the inserted and sealed electrode in a cell, d) a 3 electrode cell connected to a potentiostat

## 3.4. Cell and optical sensors characterisation and cycling

### 3.4.1. Test setup and formation cycling

Once the cell has been placed in the jig the tabs of the cell are then connected to multi-channel potentiostats in a 4-wire configuration. In the case of the cell with a reference electrode a 5-wire configuration is used, with the fifth wire connecting to and recording the reference electrode readings. All cells were formed using two cycles of constant current charge at C/20 to 4.2V, with constant voltage to a current of C/100 with subsequent discharge to 2.5V at C/20, as detailed in Table 3-1. The cells are placed inside chambers (Binder, Tuttlingen, Germany) during cycling to control the atmospheric temperature- formation cycling and the majority of testing is carried out at an chamber set temperature of 25°C, although it is noted where this is not the case.

Table 3-1- Cell formation cycling procedure

Formation cycle	Formation Cycle Steps	Current/ Voltage input	Until limit
1	Constant Current (CC) Charge	70mA (Capacity (C)/20)	4.2V
	Constant Voltage (CV) Charge	4.2V, variable current	First of C/100 or 4 hours.
	Constant Current Discharge	70mA (C/20)	2.5V
2	Repetition of cycle 1		

The fibre-instrumented cells are simultaneously connected to the optical unit and potentiostat test equipment (BioLogic, VMP3). The simultaneous collection of optical and electrochemical data allows for the evaluation and correlation between the battery state and the optical signal response. The initial optical unit provided by Insplorion only allowed for one fibre optic sensor to be connected at a time, at a later stage a multiplexor unit was provided (M8 eight channel analyzer, Insplorion) to allow up to eight fibre sensors to be connected simultaneously. Figure 3-17 shows a schematic of the system setup, while Figure 3-18 shows a photograph of three cells in a chamber connected to the optical unit, potentiostat and thermocouples.

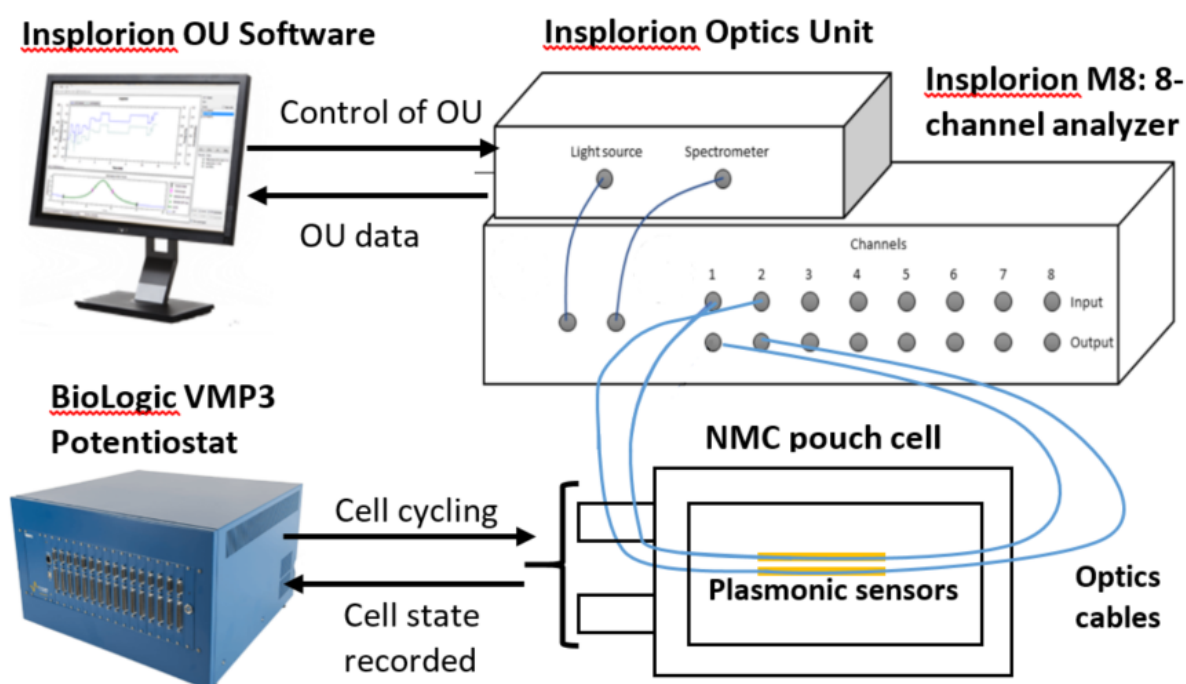


Figure 3-17- Schematic of test setup, cell with two fibre sensor connected to OU and potentiostat

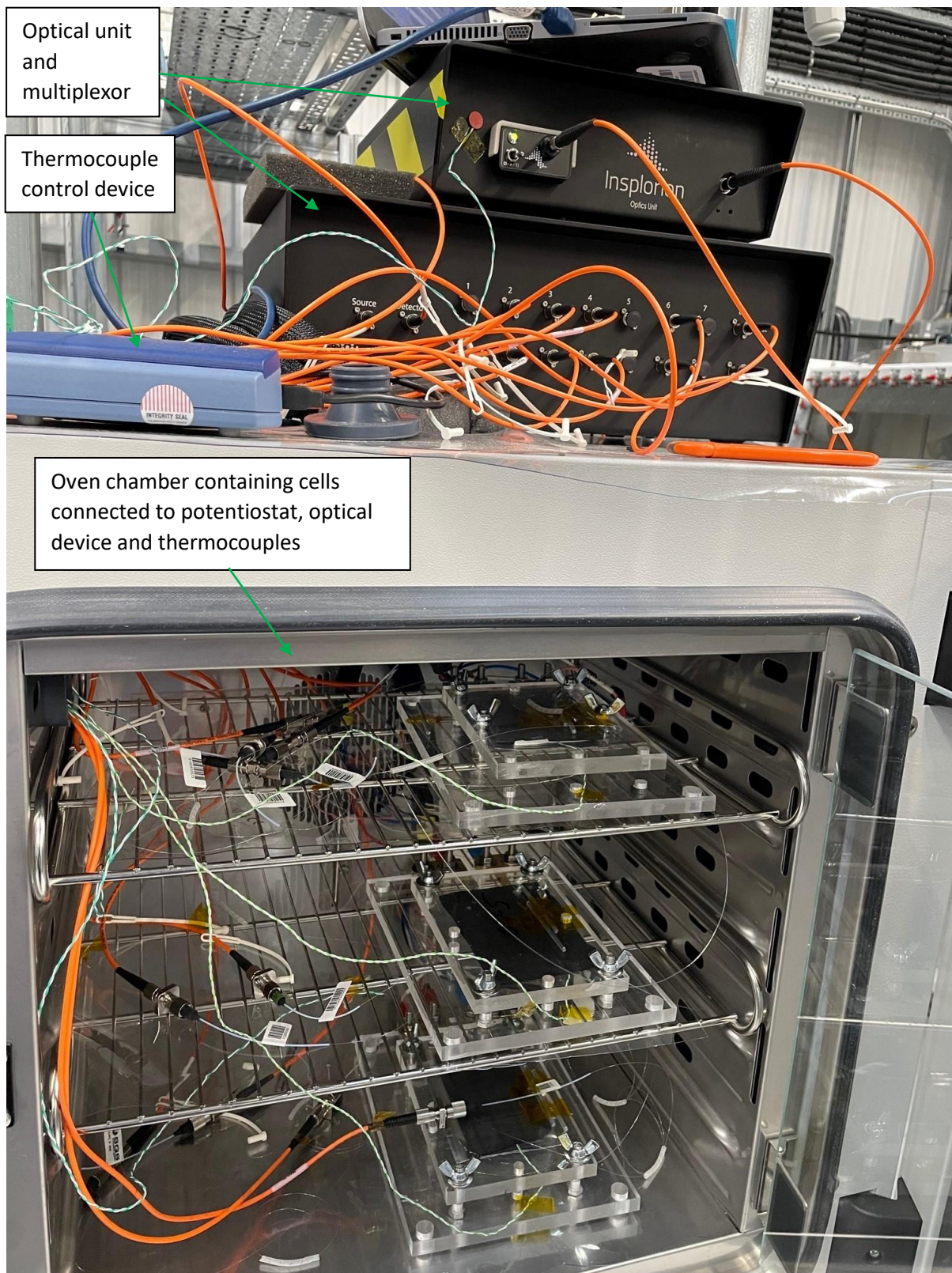


Figure 3-18- Cells in chamber connected to potentiostat channels and OU multiplexor, thermocouples can also be seen

We can also consider here the relationship between c-rate, current and current density for these cells accounting for the geometric electrode surface area. The cells have 21 electrode layers of 11 anodes and 10 cathodes, giving an active surface area of 2 surfaces over 10 electrodes. The area of the electrode is approximately 50mm by 75mm equating to a total geometric surface area of 750cm<sup>2</sup>. Given this surface area, a table of charge density of the cell at different C-rates is shown in Table 3-2.

Table 3-2- Table showing c-rate, current and current density values for the cells used in this study

<b>C-rate</b>	<b>Current (mA)</b>	<b>Current per unit area (mA.cm<sup>-2</sup>)</b>
<b>C/20</b>	70	0.093
<b>C/10</b>	140	0.187
<b>C/5</b>	280	0.373
<b>C/3</b>	466.7	0.622
<b>C/2</b>	700	0.933
<b>C</b>	1400	1.867
<b>1.5C</b>	2100	2.8
<b>2C</b>	2800	3.733
<b>3C</b>	4200	5.6

### 3.4.2. Cell characterisation

To characterise the cells in terms of working capacity, C-rate limitations and temperature profiles during charging, an increasing charge rate ‘waterfall test’ cell characterisation was carried out on reference cells without fibre optic sensors. Electrochemical Impedance Spectroscopy (EIS) testing is also carried out on the cell in the fully discharged and fully charged states after the first 10 cycles, this test was applied at the same point in the cell life to cells with fibres and cells without fibres, to allow observation of the impact of the presence of the fibres on the cell response to EIS testing. Figure 3-19 shows the prepared cells inside the Binder chamber set to maintain a temperature of 25° C, the cells are connected to the potentiostat while thermocouples (Picolog TC-08 unit with K-Type thermocouples, ±1.5K accuracy) monitor the cell temperatures. Additionally two extra thermocouples were also placed inside the chamber to confirm the ambient temperature at all times.

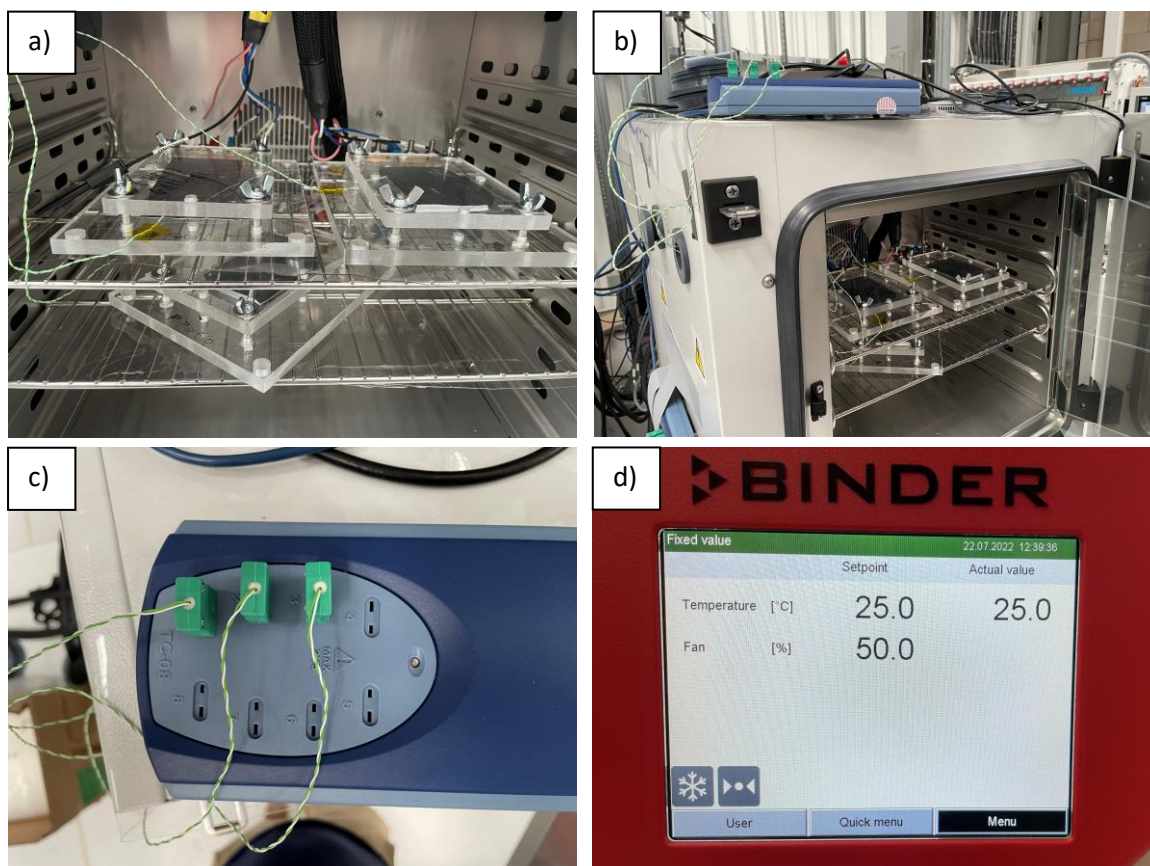


Figure 3-19- a) and b) Three reference cells (no fibre sensors) in an chamber with thermocouples attached to each cell, c) thermocouple control device, d) oven temperature settings

Following the 2 formation cycles (as set out in Table 3-1) an initial ten galvanostatic cycles were run to settle the cell, followed by EIS testing in the discharged and charged states, as detailed in Table 3-3.

Table 3-3- First ten galvanostatic cell cycles followed by EIS testing in discharged and charged states

Test type	Steps	Current/ Voltage input	Limit
<b>10 cycles charge and discharge</b>	Constant Current (CC) Charge	280mA (C/5)	First of 4.2V or 10 hours
	Constant Voltage (CV) Charge	4.2V	First of 70mA (C/20) or 2 hours.
	Rest		1 hour
	Constant Current Discharge	280mA (C/5)	First of 2.5V or 10 hours
	Rest		1 hour
	Repeat above (10 cycles total)		
<b>EIS test in discharged state</b>	EIS testing, full details in section 3.4.3.	70mA amplitude	Frequency range of 100kHz to 10 mHz
<b>EIS test in charged state</b>	Constant Current (CC) Charge	280mA (C/5)	First of 4.2V or 10 hours
	Constant Voltage (CV) Charge	4.2V	First of 70mA (C/20) or 2 hours.

Rest	1 hour
EIS testing, full details in section 3.4.3.	70mA amplitude Frequency range of 100kHz to 10 mHz

Subsequently the cell was discharged again, and then a waterfall test was carried out at C-rates from C/5 to 3C, as shown in Table 3-4. Here the cells are charged at increasing C-rates, while being discharged at a consistent D/5 discharge rate. This procedure tests the capacity of cells to accept charge at different charge rates, as well as checking if the cell has lost overall capacity after charging at high c-rates. The test is therefore an effective way of determining cell capacity, cell charge rate limits and indicating the detrimental impact of high charge rates on cell state of health.

Table 3-4- Cell characterisation 'waterfall test' settings

			Limit
<b>10 cycles charge and discharge</b>	Constant Current (CC) Charge	280mA (C/5)	First of 4.2V or global time limit (CC+CV) of 5 hours
	Constant Voltage (CV) Charge	4.2V	First of 0.1mA or global time limit (CC+CV) of 5 hours
	Rest		1 hour
	Constant Current Discharge	280mA (C/5)	First of 2.5V or 10 hours
	Rest		1 hour
Repeat above (10 cycles total)			
<b>5 cycles charge and discharge</b>	Constant Current (CC) Charge	466.7mA (C/3)	First of 4.2V or global time limit (CC+CV) of 3 hours
	Constant Voltage (CV) Charge	4.2V	First of 0.1mA or global time limit (CC+CV) of 3 hours
	Rest		1 hour
	Constant Current Discharge	280mA (C/5)	First of 2.5V or 10 hours
	Rest		1 hour
Repeat above (5 cycles total)			
<b>5 cycles charge and discharge</b>	Constant Current (CC) Charge	700mA (C/2)	First of 4.2V or global time limit (CC+CV) of 2 hours
	Constant Voltage (CV) Charge	4.2V	First of 0.1mA or global time limit (CC+CV) of 2 hours
	Rest		1 hour
	Constant Current Discharge	280mA (C/5)	First of 2.5V or 10 hours
	Rest		1 hour
Repeat above (5 cycles total)			
<b>5 cycles charge and discharge</b>	Constant Current (CC) Charge	1400mA (C)	First of 4.2V or global time limit (CC+CV) of 1 hour
	Constant Voltage (CV) Charge	4.2V	First of 0.1mA or global time limit (CC+CV) of 1 hour
	Rest		1 hour
	Constant Current Discharge	280mA (C/5)	First of 2.5V or 10 hours
Rest		1 hour	

	Repeat above (5 cycles total)		
<b>5 cycles charge and discharge</b>	Constant Current (CC) Charge	2100mA (1.5C)	First of 4.2V or global time limit (CC+CV) of 40 minutes
	Constant Voltage (CV) Charge	4.2V	First of 0.1mA or global time limit (CC+CV) of 40 minutes
	Rest		1 hour
	Constant Current Discharge	280mA (C/5)	First of 2.5V or 10 hours
	Rest		1 hour
	Repeat above (5 cycles total)		
<b>5 cycles charge and discharge</b>	Constant Current (CC) Charge	2800mA (2C)	First of 4.2V or global time limit (CC+CV) of 30 minutes
	Constant Voltage (CV) Charge	4.2V	First of 0.1mA or global time limit (CC+CV) of 30 minutes
	Rest		1 hour
	Constant Current Discharge	280mA (C/5)	First of 2.5V or 10 hours
	Rest		1 hour
	Repeat above (5 cycles total)		
<b>5 cycles charge and discharge</b>	Constant Current (CC) Charge	4200mA (3C)	First of 4.2V or global time limit (CC+CV) of 20 minutes
	Constant Voltage (CV) Charge	4.2V	First of 0.1mA or global time limit (CC+CV) of 20 minutes
	Rest		1 hour
	Constant Current Discharge	280mA (C/5)	First of 2.5V or 10 hours
	Rest		1 hour
	Repeat above (5 cycles total)		
<b>5 cycles charge and discharge</b>	Constant Current (CC) Charge	280mA (C/5)	First of 4.2V or global time limit (CC+CV) of 5 hours
	Constant Voltage (CV) Charge	4.2V	First of 0.1mA or global time limit (CC+CV) of 5 hours
	Rest		1 hour
	Constant Current Discharge	280mA (C/5)	First of 2.5V or 10 hours
	Rest		1 hour
	Repeat above (5 cycles total)		
<b>5 cycles charge and discharge</b>	Constant Current (CC) Charge	466.7mA (C/3)	First of 4.2V or global time limit (CC+CV) of 3 hours
	Constant Voltage (CV) Charge	4.2V	First of 0.1mA or global time limit (CC+CV) of 3 hours
	Rest		1 hour
	Constant Current Discharge	280mA (C/5)	First of 2.5V or 10 hours
	Rest		1 hour
	Repeat above (5 cycles total)		

### 3.4.3. Cell cycling and testing

During this study a number of cells were cycled and tested utilising a variety of techniques, including galvanostatic cycling, galvanostatic intermittent titration technique (GITT), cyclic voltammetry (CV) and electrochemical impedance spectroscopy (EIS). In addition to the three cells that underwent characterisation testing as described in Section 3.4.2, a further 27 cells were tested throughout the study. Table 3-5 gives a synopsis of the cells assembled and the testing carried out on them. Unless stated otherwise, all galvanostatic cycling carried out was followed by a CV step with limits of C/20 (70mA) or 2 hours and then a one hour rest period after the charge step, and a one hour rest period after the discharge step, with upper and lower cut-off voltages of 4.2V and 2.5V respectively. All cells also underwent formation according to the procedure set out in Section 3.4.1, and unless stated otherwise all tests took place at an ambient chamber temperature of 25°C. The CV, EIS and GITT procedures referenced in this table are described in more detail later in this section. Additionally a 'test group' number has been assigned to each set of tests, to allow easier reference of the results to the cells tested later.

Table 3-5- Overview of cells assembled and testing carried out

Test Group	Cells assembled	Testing undertaken	Intended learning
1	3 'reference' cells	EIS and waterfall testing as described in Section 3.4.2.	Performance characterisation
2	3 'reference' cells	Cycling over 100's of cycles with EIS.	Further characterisation of this batch of cells, such that EIS and longer term performance data could be compared with the cells that had fibre sensors inside.
3	3 cells with a single optical fibre adjacent to the anode	The fibres were not connected to the OU due to issues with the splicing, so the cells were used for longer term cycling testing.	Impact of fibre on cell performance over a long period of time and cycling.
4	4 cells with a single optical fibre adjacent to the anode (3 <sup>rd</sup> electrode down in stack). One of which also had a lithium reference electrode.	Galvanostatic cycling at C/5 (280mA) for 50 cycles.	Establishing the optical signal response to cell SOC change over a number of cells. Reference electrode added to one cell to provide individual electrode data.
5	1 cell with a single optical fibre adjacent to the anode (3 <sup>rd</sup> electrode down in stack).	Galvanostatic cycling at C/5 (280mA) for 20 cycles.	Additional cell cycling data and a GITT test to observe the response of the optical signal to voltage 'pulses'.
		GITT test	
5	1 cell with a single optical fibre adjacent to the anode (3 <sup>rd</sup> electrode down in stack).	Galvanostatic cycling at C/5 (280mA) for 30 cycles.	Additional cell cycling data and a GITT test to observe the response of the optical signal to voltage 'pulses'.
		Galvanostatic cycling at C/5 (280mA) for 50 cycles.	
6	1 cell with a single optical fibre adjacent to the cathode (2 <sup>nd</sup> electrode down in stack).	Galvanostatic cycling at C/5 (280mA) for 50 cycles.	Initial investigation of the optical response of the sensor adjacent to

			a cathode as opposed to an anode.
<b>7</b>	3 cells with two optical fibres in each cell, one sensor adjacent to the anode and one adjacent to the cathode (3 <sup>rd</sup> and 4 <sup>th</sup> electrodes in stack).	Galvanostatic cycling at C/5 (280mA) for 10 cycles.	Collected optical data simultaneously from sensors on the anode and cathode sides of the cell. Further GITT testing. Testing at different C rates to observe optical signal response. CV testing to observe OU response to linearly increasing voltage. Longer term cycling to observe impact of fibres on cell performance over longer period, and the impact on the sensors.
		Galvanostatic cycling at C/5 (280mA) for 23 cycles.	
		GITT test	
		Galvanostatic cycling at C/3 (466.6mA) for 5 cycles.	
		Galvanostatic cycling at C/2 (700mA) for 2 cycles.	
		Galvanostatic cycling at C/3 (466.6mA) for 5 cycles.	
		Galvanostatic cycling at C/2 (700mA) for 2 cycles.	
		Cyclic voltammetry test 0.1mVs <sup>-1</sup>	
		Cyclic voltammetry test 0.05mVs <sup>-1</sup>	
		Galvanostatic cycling at C/5 (280mA) for 100 cycles.	
<b>8</b>	3 cells with two optical fibres in each cell, one sensor adjacent to the anode and one adjacent to the cathode (3 <sup>rd</sup> and 4 <sup>th</sup> electrodes in stack). A further 'reference' cell without any sensors present.	Galvanostatic cycling at C/5 (280mA) for 10 cycles.	Attempt to force lithium plating at 25°C and observe if OU signal shows a response to lithium plating.
		Lithium plating attempt at room temperature, described in more detail in Section 3.5.2.	
<b>9</b>	3 'reference' cells without added sensors. Once cell also had a reference electrode.	Galvanostatic cycling at C/5 (280mA) for 10 cycles.	Testing lithium plating methodology at low temperatures, with a reference electrode on one cell to provide further data. The urban test profile is also tested prior to using it on cells with fibre sensors.
		Galvanostatic cycling at C/5 (280mA) for 5 cycles.	
		Forced lithium plating at 0°C, described in more detail in Section 3.5.2.	
		Tested urban profile test cycle, described in more detail later in this section.	
		Forced lithium plating	
<b>10</b>	2 cells with two optical fibres in each cell, one sensor adjacent to the anode and one adjacent to the cathode (3 <sup>rd</sup> and 4 <sup>th</sup> electrodes in stack). Additionally these cells were compressed in copper plates rather than an acrylic jig, this setup is described further in Section 3.5.2.	Galvanostatic cycling at C/5 (280mA) for 10 cycles.	Galvanostatic cycling at different temperatures to observe the impact of temperature on optical signal. Carrying out lithium plating testing on cells at low temperatures to observe the impact of lithium plating on optical signal. Test
		EIS in fully charged and fully discharged states.	
		Galvanostatic cycling at C/5 (280mA) for 15 cycles, 5 cycles each at 25°C, 12.5°C and 0°C. Described in more detail in Section 3.4.4.	
		Forced lithium plating testing at 0°C, described in more detail in Section 3.5.2.	

			carried out with copper jig, described in Section 3.5.2.
<b>11</b>	3 cells with two optical fibres in each cell, one sensor adjacent to the anode and one adjacent to the cathode (3 <sup>rd</sup> and 4 <sup>th</sup> electrodes in stack).	Galvanostatic cycling at C/5 (280mA) for 10 cycles.	Extensive test program observing optical signal response to temperature, pressure, urban profile cycling and forced lithium plating. Tests carried out with usual acrylic jigs.
		EIS in fully charged and fully discharged states.	
		Galvanostatic cycling at C/5 (280mA) for 15 cycles, 5 cycles each at 35°C, 25°C and 15°C. Described in more detail in Section 3.4.4.	
		Pressure testing by adding placing weight on cell jig, described in more detail in Section 3.4.4.	
		Urban profile test cycle, described in more detail later in this section.	
		Forced lithium plating testing at 0°C, described in more detail in Section 3.5.2.	

The GITT, CV, EIS and Urban Profile (UP) procedures noted in Table 3-5 are expanded in detail in the following paragraphs. GITT testing was carried out on cell test groups 5 and 7. The intention of this test is to apply pulses of voltage to the cell, as detailed in Table 3-6, and then to see how the optical signal reacts to the change in cell state. In applying pulses of voltage we allow certain mechanisms to take place, such as increased concentration of lithium-ions in the electrode boundary layer during charge, before diffusion of those Li-ions into the electrode bulk material during rest. The response of the optical signal to these mechanisms can give potentially give us insight into what the sensor is measuring, how sensitive it is and other such insights.

Table 3-6- GITT test profile

Test type	Steps	Current/ Voltage input	Limit	
<b>GITT</b>	Constant Current (CC) Charge	280mA (C/5)	15 minutes	
	Rest	-	45 minute	
	Repeat steps (40 pulses)			4.2V
	Constant Current (CC) Discharge	280mA (C/5)	15 minutes	
	Rest	-	45 minutes	
	Repeat steps (40 pulses)			2.5V

Cyclic voltammetry testing was carried out on the cells in test group 7. Cyclic voltammetry requires increasing the voltage of the cell incrementally, this was done according to the test profiles set out in Table 3-7. Cyclic voltammetry is particularly utilised to identify reduction and oxidation peaks in an electrochemical redox reaction, as described in more detail in Section 2.1.5. This experiment allows evaluation of the optical signal response to steadily increasing voltage and redox peaks, again allowing

us to learn more about the responsiveness and mechanisms of the sensing operation. Two scan rates were used, with the slower scan rate applied to provide greater definition of the redox peaks.

Table 3-7- Cyclic voltammetry test profiles.

Test type	Cycle Steps	Scan rate	Until limit
<b>Cyclic Voltammetry</b>	Linear Voltage increase Charge	0.1mVs <sup>-1</sup>	4.2V
	Linear Voltage decrease Discharge	0.1mVs <sup>-1</sup>	2.5V
<b>Cyclic Voltammetry</b>	Linear Voltage increase Charge	0.05mVs <sup>-1</sup>	4.2V
	Linear Voltage decrease Discharge	0.05mVs <sup>-1</sup>	2.5V

EIS testing was carried out with measurements at 42 frequencies across the range of 10mHz to 100KHz, the current amplitude applied was 70mA (C/20) and 3 measurements were taken at each frequency. The settings for the test as input into the BioLogic EC-Lab potentiostat control software and full list of frequency values can found in Appendix F. The EIS testing was carried out on 'reference' cells from test group 1 and cells with fibre optics sensors from test group 11, in both cases after the first 10 cycles of cycling at C/5 and in fully discharged and charges states, so the EIS profiles and real resistance values could be compared for cells with and without fibres at the same point in the cell life. Similarly this was also done for the cells with fibre sensors in the copper jigs in test group 10, allowing a further comparison- additionally some EIS testing was carried out on these cells after the forced lithium plating, to see what impact the lithium plating had on the EIS signal. EIS is often carried out at multiple SOC's with rest periods [106][105], in this case EIS is just carried out in the charged and discharged states as a point of reference to observe the impact of the presence of the optical fibres. The EIS steps are shown in Table 3-8.

Table 3-8- EIS procedure, EIS carried out in cell discharged and charged states.

Step	Current/ Voltage	Until limit
<b>EIS (settings details in Appendix F)</b>	70mA	Measurements at 42 frequencies across the range of 10mHz to 100KHz
<b>Constant current charge</b>	280mA	8 hours or 4.2V
<b>Constant voltage charge</b>	4.2V	2hours or 70mA
<b>EIS (settings details in Appendix F)</b>	70mA	Measurements at 42 frequencies across the range of 10mHz to 100KHz
<b>Rest</b>		1 hour
<b>Constant current discharge</b>	280mA	8 hours or 2.5V

In terms of its design, the EIS experiment makes an AC oscillation in the cell charge state without changing the mean SOC across a range of oscillation frequencies. At low frequencies reactants have time to diffuse further, so diffusion impedance (or Warburg impedance) comes into play. At lower frequencies the capacitive resistance is also higher. Conversely at very high frequencies the capacitive resistance becomes negligible and there is limited diffusion, so the charge transfer resistance becomes dominant, as noted in Section 2.2.1. Adsorption is another step in the electrochemical process that occurs at a different rate. As such the application of EIS across a range of frequencies in conjunction with a suitable equivalent circuit model allows the identification of the behavior of steps in the electrochemical process, for different electrochemical systems and in different conditions [172].

Additionally cycling was carried out with an urban profile (UP) test, this was initially tested on 'reference' cells from test group 9, before being utilised on cells with optical fibres from test group 11. This test was employed to see how the optical signal responded to a more varied change in cell SOC. The urban profile utilised has a charge and discharge cycle that is based on the FTP (Federal Test Procedure) drivecycle, with the current magnitudes scaled according to the capacity of the battery cell- this cycle provided a good real world example of a varied cycle. The cell was first charged in a none linear way, before discharging the cell according to the UP (which discharged approximately 0.94A) and then a C/5 CC discharge to 2.5V, as described in Table 3-9. This was repeated 3 times, and the detailed urban profile based cycle can be found in Appendix G.

Table 3-9- Cell cycling with urban profile cycle on discharge

<b>Step</b>	<b>Current/ Voltage</b>	<b>Until limit</b>
<b>Constant current charge</b>	280mA	3 hours or 4.2V
<b>Rest</b>		5 minutes
<b>Constant current discharge</b>	280mA	1 hour or 2.5V
<b>Rest</b>		5 minutes
<b>Constant current charge</b>	280mA	3 hours or 4.2V
<b>CV</b>	4.2V	2hours or 70mA
<b>Rest</b>		5 minutes
<b>Urban Profile Cycle</b>	Discharge according to urban profile cycle, see Appendix G for full cycle details.	5 hours or 2.5V
<b>Rest</b>		5 minutes
<b>Constant current discharge</b>	280mA	4 hours or 2.5V
<b>Repeated above steps 2 more times</b>		

### 3.4.4. Impact of temperature and pressure on optical signal

Experiments were designed to specifically isolate and test the impact of temperature and pressure on the optical signal, particularly on cells in test groups 10 and 11 in Table 3-5. The cells were placed in a small Binder chamber so that it was possible to control the ambient temperature of the cells. Thermocouples were placed at the surface of each cell to monitor cell temperature and in the chamber space to provide an additional ambient reference temperature. The cells in test groups 10 and 11 set up in the chamber with thermocouples can be seen in Figure 3-20.

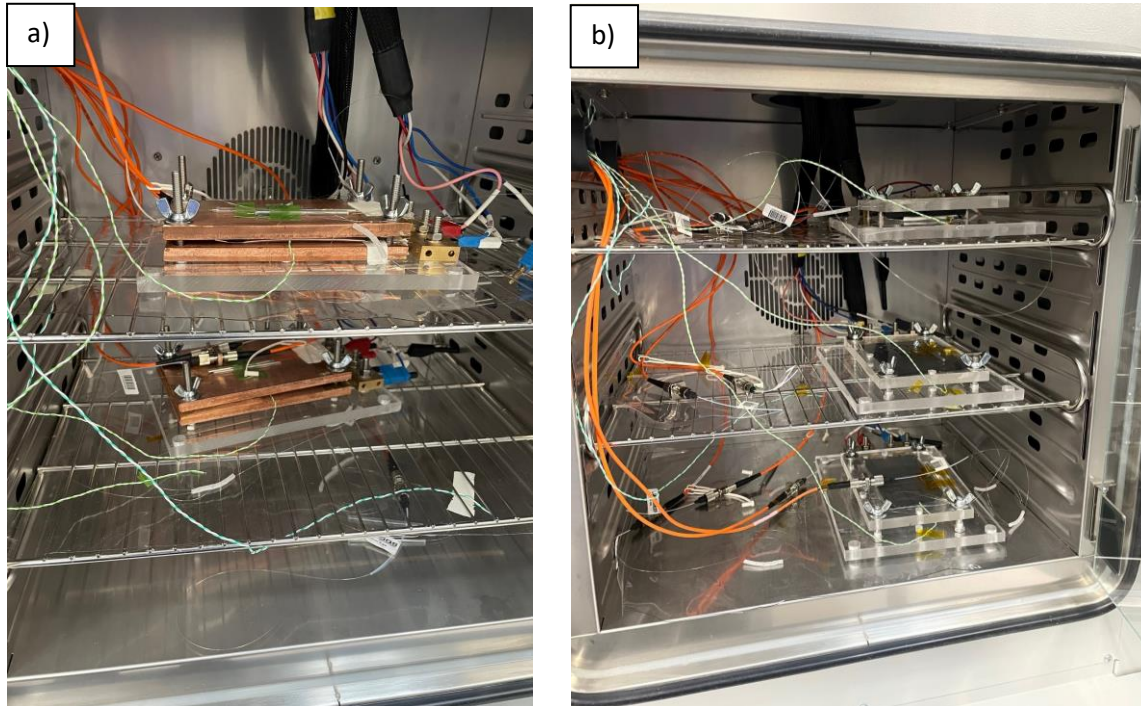


Figure 3-20- a) Cells in copper jigs and b) cells in acrylic jigs, with thermocouples (green and white cables)

The cells in test group 10 (cells in copper jigs) were cycled according to the conditions detailed in Table 3-10. The optical signal behaviour was also recorded in the periods where the chamber ambient temperature was being cooled down or heated up. The cells in test group 11 (acrylic jigs) were cycled according to the same approach, except that the cycling temperatures were 35°C, 25°C and 15°C.

Table 3-10- Cell cycling at different temperatures to observe impact of temperature on signal

Test type	Steps	Current/ Voltage input	Limit
5 cycles charge and discharge at 25°C	Constant Current (CC) Charge	280mA (C/5)	First of 4.2V or global time limit (CC+CV) of 5 hours
	Constant Voltage (CV) Charge	4.2V	First of 0.1mA or global time limit (CC+CV) of 5 hours
	Rest		1 hour
	Constant Current Discharge	280mA (C/5)	First of 2.5V or 10 hours
	Rest		1 hour
	Repeat above (5 cycles total)		
5 cycles charge	Constant Current (CC) Charge	280mA (C/5)	First of 4.2V or global time limit (CC+CV) of 5 hours

<b>and discharge at 12.5°C</b>	Constant Voltage (CV) Charge	4.2V	First of 0.1mA or global time limit (CC+CV) of 5 hours 1 hour
	Rest		
	Constant Current Discharge	280mA (C/5)	First of 2.5V or 10 hours 1 hour
	Rest		
Repeat above (5 cycles total)			
<b>5 cycles charge and discharge at 0°C</b>	Constant Current (CC) Charge	280mA (C/5)	First of 4.2V or global time limit (CC+CV) of 5 hours
	Constant Voltage (CV) Charge	4.2V	First of 0.1mA or global time limit (CC+CV) of 5 hours 1 hour
	Rest		
	Constant Current Discharge	280mA (C/5)	First of 2.5V or 10 hours 1 hour
	Rest		
Repeat above (5 cycles total)			

Additionally the cells in test group 11 also had weights incrementally applied to observe the impact of pressure on the optical signal, this can be seen in Figure 3-21. The cumulative weight added is shown in Table 3-11, while the equivalent pressures are also given based on the force being spread across a cell stack area of 39.8cm<sup>2</sup> (0.0519m x 0.0767m).

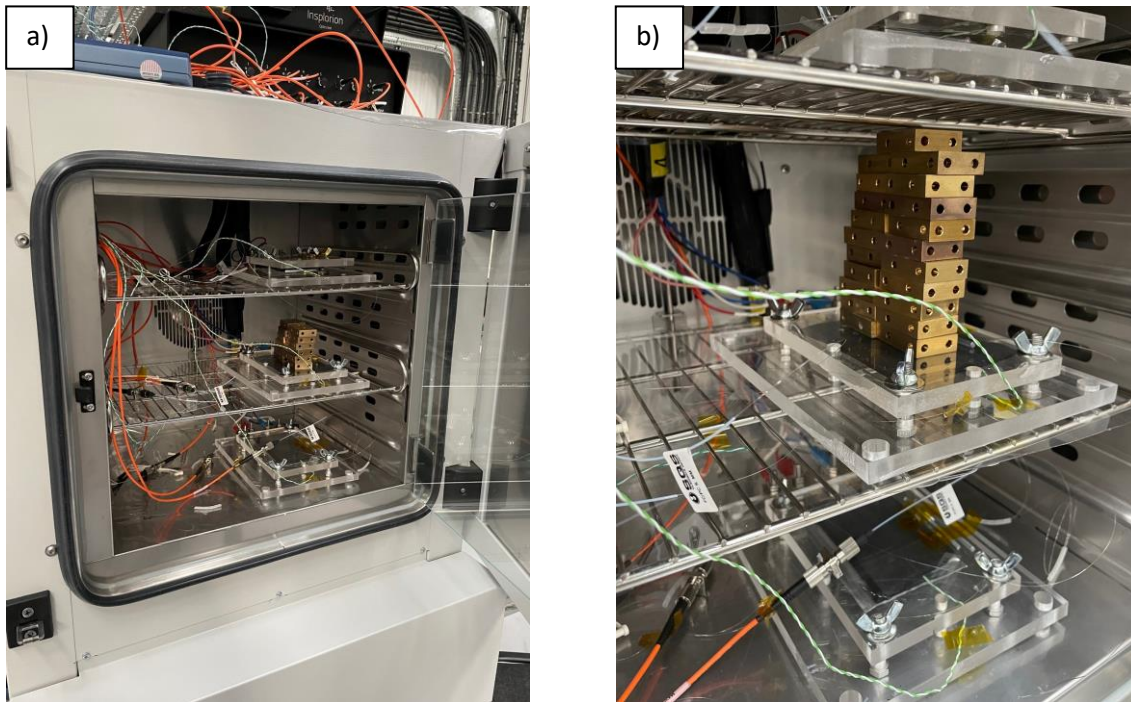


Figure 3-21- Brass block weights incrementally added on top of jigs, to observe pressure impact on optical signal, a) 12 blocks totalling 744g on cell, b) 21 blocks totalling 1302g on cell

Table 3-11- Table of weight added to and removed from cell

Incremental weight change	Cumulative weight (g)	Equivalent pressure (Pa)
0g added	0	0
186g added	186	458
186g added	372	917

<b>186g added</b>	558	1375
<b>186g added</b>	744	1833
<b>186g added</b>	930	2292
<b>186g added</b>	1116	2750
<b>186g added</b>	1302	3209
<b>186g removed</b>	1116	2750
<b>186g removed</b>	930	2292
<b>186g removed</b>	744	1833
<b>186g removed</b>	558	1375
<b>186g removed</b>	372	917
<b>186g removed</b>	186	458
<b>186g removed</b>	0	0

## 3.5. Forced Lithium Plating testing

### 3.5.1. Open cell

A dry (no electrolyte) commercial cell with graphite electrode was cut open to obtain graphite material for an open cell lithium plating test. A strip of anode material was cut, and the graphite on the upper half was wiped from the copper substrate with an alcohol wipe to provide a contact area to connect the potentiostat channel with a crocodile clip. As a geometric proportion the anode material taken is approximately 1.5% that of the total cell anode material. The total cell has a capacity of 1Ah therefore the strip of material placed in the open cell has an approximate capacity of 15mAh. The graphite electrode is placed in a 3-neck flask, with the optical fibre sensor adjacent to it and a piece of separator material holding the optical fibre sensor close to the graphite electrode. Then inside the glovebox a lithium metal strip is added through another neck of the flask as the working electrode; an excess of lithium metal is added to ensure that lithium plating can be achieved through overcharge. Finally approximately 40 ml of 1M LiPF<sub>6</sub> in EC/EMC (3/7 v/v) electrolyte is added to the cell to cover the electrodes on the flask, and bungs are placed on the flask necks to stop the electrolyte evaporating.

The open cell is charged at a C-rate of 3mA (C/5), with a high impedance expected due to the distance of the two electrodes from each other in the electrolyte solution, as well as some additional resistance due to the using crocodile clips to connect the potentiostat channel to the electrodes. The 4 wire channel setup, with separate wires for current delivery and measurement, ensures the potentiostat measurements are taken at the point just prior to the crocodile clip connections. The open cell setup can be seen in Figure 3-22. The open cell is charged at 3mA for 8 hours to ensure lithium plating through overcharge, and then discharged at 3mA for 8 hours or until a limit of 1.5V (Table 3-12), while the optical signal is simultaneously recorded.

Table 3-12- Open cell cycling parameters

Steps	Current Input	Limits
Constant current charge	-3mA (C/5)	8 hours
Constant current discharge	3mA (C/5)	First of 8 hours or 1.5V

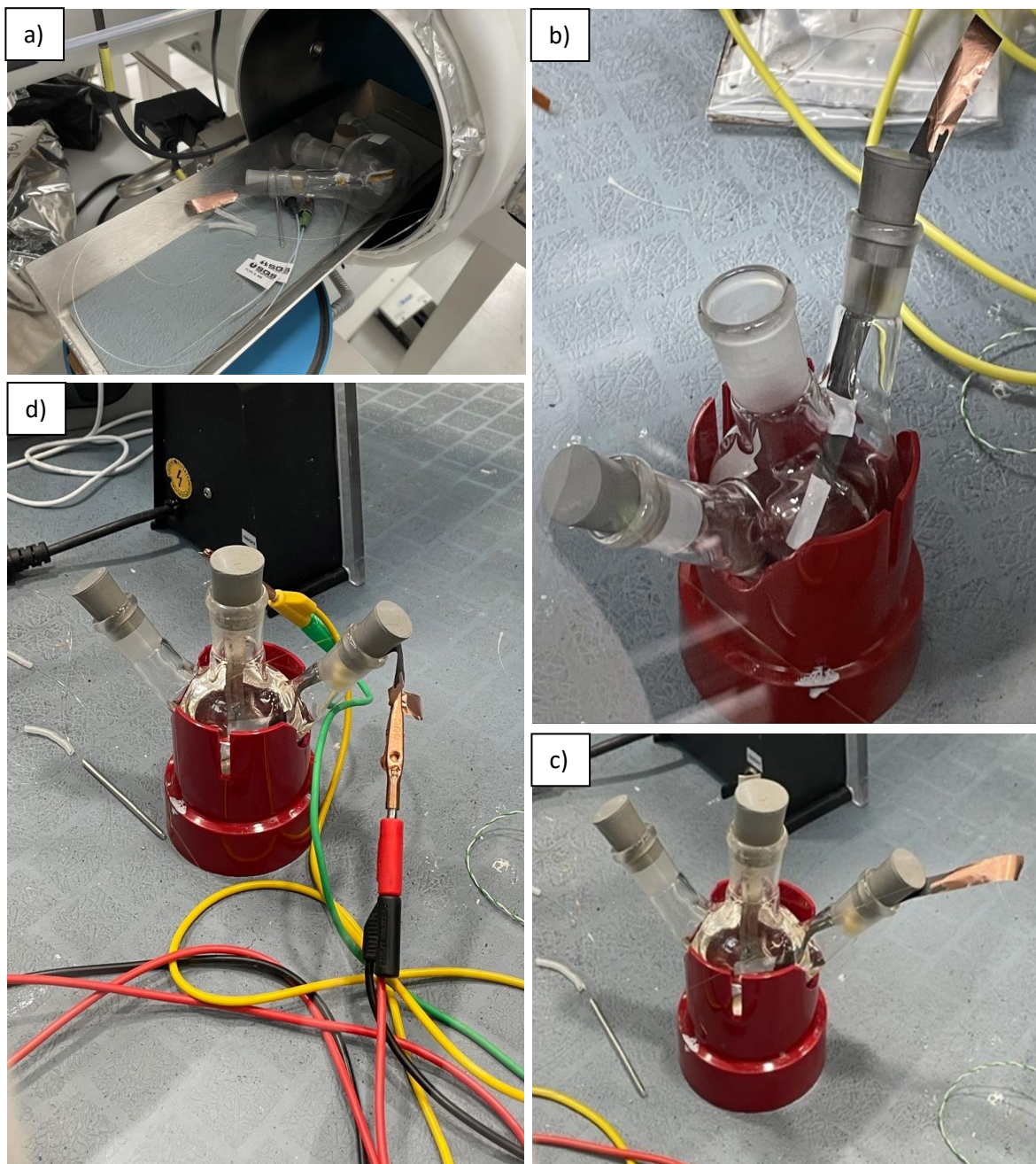


Figure 3-22- a) Open cell being placed into glovebox entry chamber, b) Open cell inside glovebox, c) Open cell with lithium electrode and electrolyte added, d) Open cell connected to potentiostat with 4-wire setup

### 3.5.2. Lithium plating in pouch cells

Initially the attempt was made to force lithium plate cells at room temperature, this group of four cells contained three with fibre optics sensors and one without (test group 8). The approach adopted was to charge the cell at a high c-rate, followed by a CV step, rest, and discharge at a slow discharge rate (D/20) The experiment aim was to prove the occurrence of lithium plating by identifying a lithium stripping peak on the rest and slow discharge part of the cycle [85], while simultaneously observing the optical signal and if there was evidence in the optical signal of a response to the lithium plating (if confirmed via electrochemical techniques and teardown). Initially the cell was charged at a slower C/5 rate (280mA) as a reference before carrying out faster 1.5C (2100mA) charging, the full cycling regime is specified in Table 3-13.

Table 3-13- Forced lithium plating testing carried out at 25°C

Test type	Steps	Current/ Voltage input	Limit
<b>5 cycles charge and discharge</b>	Constant Current (CC) Charge	280mA (C/5)	First of 4.2V or 10 hours
	Constant Voltage (CV) Charge	4.2V	First of 70mA (C/20) or 2 hours.
	Rest		1 hour
	Constant Current Discharge	280mA (C/20)	First of 2.5V or 30 hours
	Rest		1 hour
	Repeat above (5 cycles total)		
<b>2 cycles charge and discharge</b>	Constant Current (CC) Charge	2100mA (1.5C)	First of 4.2V or 1 hours
	Constant Voltage (CV) Charge	4.2V	First of 70mA or 4 hours
	Rest		1 hour
	Constant Current Discharge	70mA (C/20)	First of 2.5V or 30 hours
	Rest		1 hour
	Repeat above (2 cycles total)		

Subsequently the forced lithium plating method was tested on the ‘reference’ cells without fibres in test group 9, this testing was carried out at low temperatures due to the availability of a small Binder chamber that could be utilised, the intent was to see if the forced lithium plating experiment could be carried out more effectively at low temperatures. One of the these cells also had a lithium reference electrode inserted, the three electrode system allowing observation of the voltage across both anodes; theoretically the anode can reach 0V versus lithium when lithium plated and this has been utilised experimentally as a metallic lithium detection method [173]. The primary methodology utilised to detect lithium plating is that of observing a plateau on the discharge cycle time-voltage profile [85], which can identified more clearly as a peak through IC analysis. Additionally cell teardown is also carried out to confirm if lithium plating occurred, as described further in Sections 3.6.2 and 3.6.3.

The cells were cooled to 0°C to encourage lithium plating by slowing the Li-ion diffusion kinetics, and then cycled according to the cycles shown in Table 3-14. Note that the last three sets of 20 cycles was only carried out on two cells, one of the cells (without a reference electrode) was torn down before

that set of cycles to look for physical evidence of lithium plating from the prior cycling. The initial set of 3 cycles was done at a very slow charge rate (C/40) to give a reference for the cell time-voltage profile at that temperature, at a charge rate that should not cause lithium plating. The subsequent higher C/2 charge rate was then designed to induce lithium plating, and the time-voltage profile could be compared to that of the initial slow charge rate. Note that in this case the cycle went directly into slow discharge after the constant current charge, without CV or rest steps, in order to try to more effectively identifying any lithium stripping plateau on the discharge step.

Table 3-14- Forced lithium plating cycling of reference cells

Test type	Steps	Current/ Voltage input	Limit
<b>3 cycles charge and discharge at 0°C</b>	Constant Current (CC) Charge	35mA (C/40)	First of 4.2V or 60 hours
	Constant Current Discharge Rest	70mA (C/20)	First of 2.5V or 30 hours 1 hour
	Repeat above (5 cycles total)		
<b>5 cycles charge and discharge at 0°C</b>	Constant Current (CC) Charge	700mA (C/2)	First of 4.2V or 2 hours
	Constant Current Discharge Rest	70mA (C/20)	First of 2.5V or 30 hours 1 hour
	Repeat above (5 cycles total)		
<b>5 cycles charge and discharge at 0°C</b>	Constant Current (CC) Charge	700mA (C/2)	First of 4.2V or 2 hours
	Constant Current Discharge Rest	70mA (C/20)	First of 2.5V or 30 hours 1 hour
	Repeat above (5 cycles total)		
<b>20 cycles charge and discharge at 0°C</b>	Constant Current (CC) Charge	700mA (C/2)	First of 4.2V or 2 hours
	Constant Current Discharge Rest	70mA (C/20)	First of 2.5V or 30 hours 1 hour
	Repeat above (20 cycles total)		
<b>20 cycles charge and discharge at 0°C</b>	Constant Current (CC) Charge	700mA (C/2)	First of 4.2V or 2 hours
	Constant Current Discharge Rest	70mA (C/20)	First of 2.5V or 30 hours 1 hour
	Repeat above (20 cycles total)		
<b>20 cycles charge and discharge at 0°C</b>	Constant Current (CC) Charge	700mA (C/2)	First of 4.2V or 2 hours
	Constant Current Discharge Rest	70mA (C/20)	First of 2.5V or 30 hours 1 hour
	Repeat above (20 cycles total)		

A forced lithium plating experiment was additionally carried out on two cells with sensors (test group 10) placed in a chamber cooled to 0°C, and cycled at a high C rate. The optical signal is again analysed to look for evidence of a response to lithium plating, while the cell will then be discharged at a slower rate and IC analysis carried out to look for a higher voltage  $dQ/dV$  peak as evidence of the presence of lithium plating [85].

During the high charge the cell will heat up, raising the temperature from the 0°C ambient. In order to mitigate this copper plates were purchased and prepared to act as a 'heat sink' during the lithium plating process, absorbing some of the heat and keeping the cell at a lower temperature. The copper plates were drilled with four holes to fit on the battery jig, polished, and then sprayed with polyurethane coating at the ends where the battery tabs will be to prevent a short circuit. The prepared cells with fibre sensors are then clamped inside the battery jig between two copper plates, before being placed inside a binder chamber and connected to the OU, potentiostat and with thermocouples (shown in Figure 3-23).

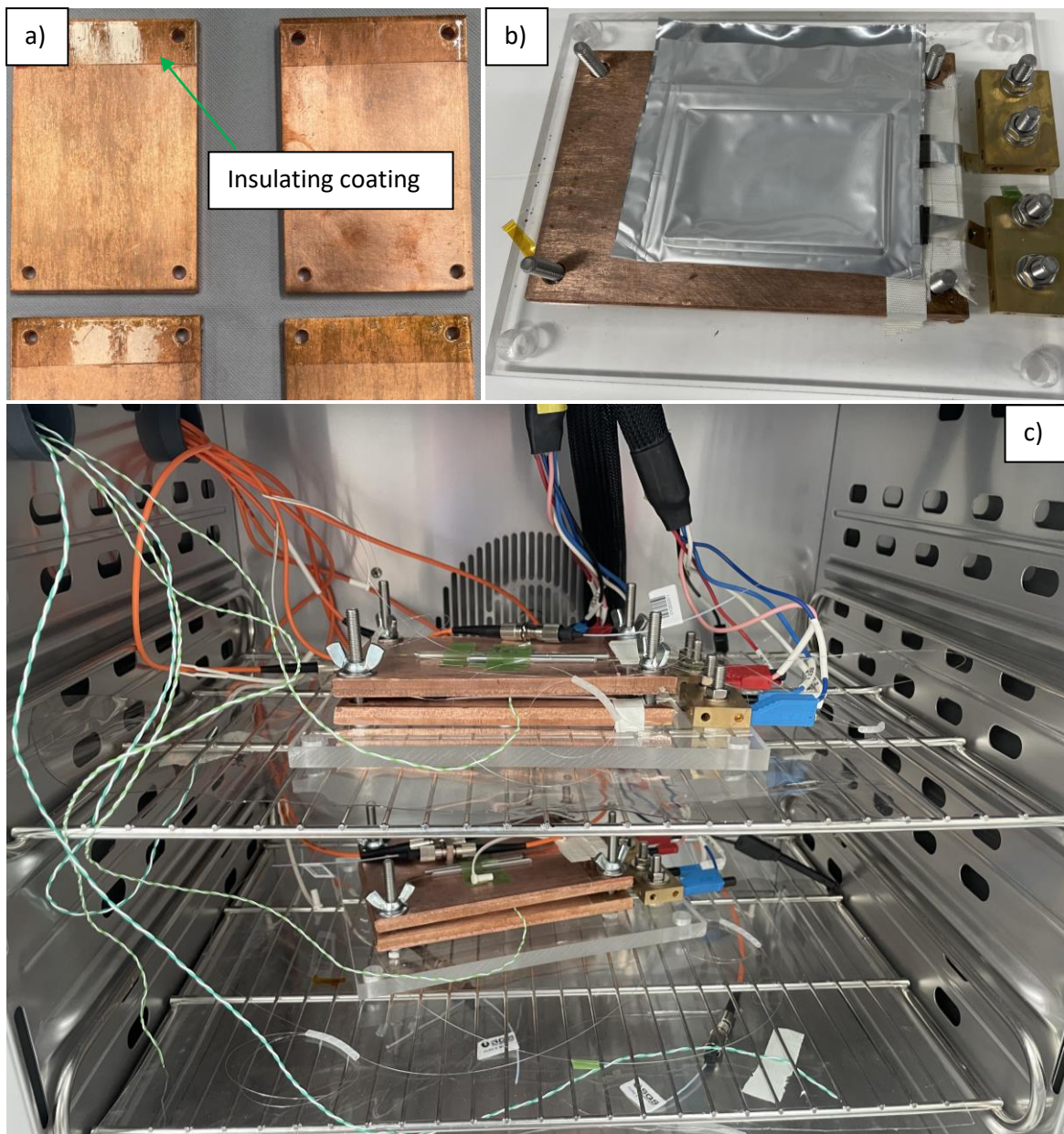


Figure 3-23- a) Prepared copper plates, b) cell being placed in jig, c) two cells in jigs with copper plates acting as heat sinks (inside binder chamber, with thermocouples, optical sensors and potentiostat cables)

The cells were then cycled according to the cycling regime set out in Table 3-15. Initially the cells were cycled at a slower C/10 charge rate as a reference cycle, before being cycled at 3C to try to force lithium plating. EIS testing was also then carried out to see if the lithium plating could be detected in the EIS response. Subsequent lower charge rates of C and C/2 were then tried as 3C caused the cell voltage limit to be reached with only a small amount of charge being transferred, and finally the cells were cycled at C/2 for a high number of cycles to try to cycle them to destruction.

Table 3-15- Cells in copper plates forced lithium plating cycling.

Test type	Steps	Current/ Voltage input	Limit
<b>3 cycles charge and discharge at 0°C</b>	Constant Current (CC) Charge	140mA (C/10)	First of 4.2V or 12 hours
	Constant Current Discharge Rest	70mA (C/20)	First of 2.5V or 30 hours 1 hour
	Repeat above (3 cycles total)		
<b>3 cycles charge and discharge at 0°C</b>	Constant Current (CC) Charge	4200mA (3C)	First of 4.2V or hours
	Constant Current Discharge Rest	70mA (C/20)	First of 2.5V or 30 hours 1 hour
	Repeat above (3 cycles total)		
<b>2 cycles charge and discharge at 0°C</b>	Constant Current (CC) Charge	4200mA (3C)	First of 4.2V or hours
	Constant Current Discharge Rest	70mA (C/20)	First of 2.5V or 30 hours 1 hour
	Repeat above (2 cycles total) followed by EIS (next line below)		
<b>EIS</b>	Steps as set out in Table 3-8 in Section 3.4.3		
<b>5 cycles charge and discharge at 0°C</b>	Constant Current (CC) Charge	700mA (C/2)	First of 4.2V or 2 hours
	Constant Current Discharge Rest	70mA (C/20)	First of 2.5V or 30 hours 1 hour
	Repeat above (5 cycles total) followed by EIS (next line below)		
<b>EIS</b>	Steps as set out in Table 3-8 in Section 3.4.3		
<b>6 cycles charge and discharge at 0°C</b>	Constant Current (CC) Charge	1400mA (C)	First of 4.2V or 1 hours
	Constant Voltage (CV) Charge	4.2V	First of 140mA or 10 hours
	Constant Current Discharge Rest	70mA (C/20)	First of 2.5V or 30 hours 1 hour
	Repeat above (6 cycles total) followed by EIS (next line below)		
<b>EIS</b>	Steps as set out in Table 3-8 in Section 3.4.3		
<b>20 cycles charge and discharge at 0°C</b>	Constant Current (CC) Charge	700mA (C/2)	First of 4.2V or 2 hours
	Constant Current Discharge Rest	70mA (C/20)	First of 2.5V or 30 hours 1 hour
	Repeat above (20 cycles total)		

<b>30 cycles charge and discharge at 0°C</b>	Constant Current (CC) Charge	700mA (C/2)	First of 4.2V or 2 hours
	Constant Current Discharge Rest	280mA (C/5)	First of 2.5V or 8 hours 1 hour
	Repeat above (30 cycles total)		
<b>30 cycles charge and discharge at 0°C</b>	Constant Current (CC) Charge	700mA (C/2)	First of 4.2V or 2 hours
	Constant Current Discharge Rest	280mA (C/5)	First of 2.5V or 8 hours 1 hour
	Repeat above (30 cycles total)		
<b>120 cycles charge and discharge at 0°C</b>	Constant Current (CC) Charge	700mA (C/2)	First of 4.2V or 2 hours
	Constant Current Discharge Rest	700mA (C/2)	First of 2.5V or 2 hours 1 hour
	Repeat above (120 cycles total)		
<b>120 cycles charge and discharge at 0°C</b>	Constant Current (CC) Charge	700mA (C/2)	First of 4.2V or 2 hours
	Constant Current Discharge Rest	700mA (C/2)	First of 2.5V or 2 hours 1 hour
	Repeat above (120 cycles total)		

The forced lithium plating testing was also carried out on cells with fibre sensors (test group 11) in acrylic jigs at 0°C. This acrylic jigs do not have the same capacity to regulate the cell temperature as the copper jigs, but do not introduce the added variable of additional pressure on the cell. Forced lithium plating attempts were carried out on these cells according to the cycling regime set out in Table 3-16. The C/2 rate was selected having established from the testing on the previous cells, in particular the testing on reference cells detailed in Section 3.4.2, that it is an effective C-rate to cause lithium plating on this batch of cells at 0°C.

Table 3-16- Cycling for forced lithium plating on cells with fibre sensors in acrylic jigs, at 0°C

<b>Test type</b>	<b>Steps</b>	<b>Current/ Voltage input</b>	<b>Limit</b>
<b>10 cycles charge and discharge at 0°C</b>	Constant Current (CC) Charge	700mA (C/2)	First of 4.2V or 2 hours
	Constant Current Discharge Rest	280mA (C/20)	First of 2.5V or 30 hours 1 hour
	Repeat above (10 cycles total)		
<b>10 cycles charge and</b>	Constant Current (CC) Charge	700mA (C/2)	First of 4.2V or 2 hours
	Constant Current Discharge Rest	280mA (C/20)	First of 2.5V or 30 hours 1 hour

discharge at 0°C	Repeat above (10 cycles total)	
---------------------	--------------------------------	--

## 3.6. Materials analysis

### 3.6.1. X-ray tomographic imaging of cell

High energy lab-based X-ray imaging of one of the 1.4 Ah pouch cells was performed on a Nikon XTH 225 instrument (Nikon Metrology, UK) using a W target and a 1 mm Cu filter, this testing was carried out in the facilities of the University College of London. The scan of the cell with internal fibre sensor was carried out using a voltage of 160 kV and a total power of 12.8 W. For CT dataset, 3185 projections were obtained with an exposure time of 1 second to minimize the artefacts. The fibre was maintained within the field of view (FOV) to obtain a spatial resolution with voxel size of ca.15  $\mu\text{m}$ . Reconstruction of obtained projections was conducted using Nikon CT Pro 3D software (Version XT 4.4.4, Nikon Metrology, Tring, UK) with three-dimensional visualisation of the dataset being performed using Avizo 2019. 4 (FEI, France). The resulting x-ray images show the position of the fibre within the cell as well as the electrode stacks from different angles.

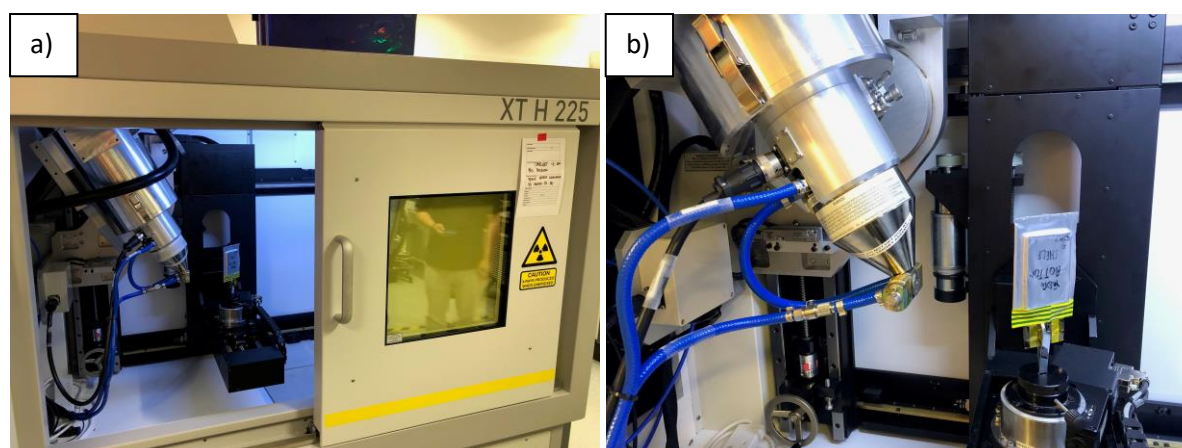


Figure 3-24- X-ray instrumentation (Nikon XTH 225, Nikon Metrology, UK) with sample cell, a) complete unit including shielding, b) zoomed in image of scanner and cell sample in holder

### 3.6.2. Cell teardown

Cell teardown was carried out inside the argon atmosphere glovebox. Plastic scissors (which can't generate a spark and are not conductive to avoid a short circuit) are used to cut the sides off the cell. The three edges off the pouch at the sides and bottom around the stack are cut off first, before cutting the top edge with the tabs off. A plastic scalpel can also be used to aid with the initial cell incisions. Rubber coated tweezers are then used to take off the top and bottoms layer of pouch materials and start separating the cell electrodes, some of the remaining tab material may need to be further cut from the electrodes to allow them to fully separate. The tape holding the separator together is

removed with the tweezers to allow the separator and electrodes to be unrolled. The separator can then be unrolled and the electrodes can be removed individually from the stack. When removing the electrodes the anodes and cathodes must be separated from each other and out of contact, to avoid any residual discharge- the unwanted anodes and cathodes are separated for disposal according to local health and safety regulations, while any electrodes to be taken for material analysis are set aside. The electrode material for analysis can then be processed accordingly, including preparing samples for SEM and EDX and carrying out lithium plating testing with deionised water. Figure 3-25 shows some images from the pouch cell teardown process.

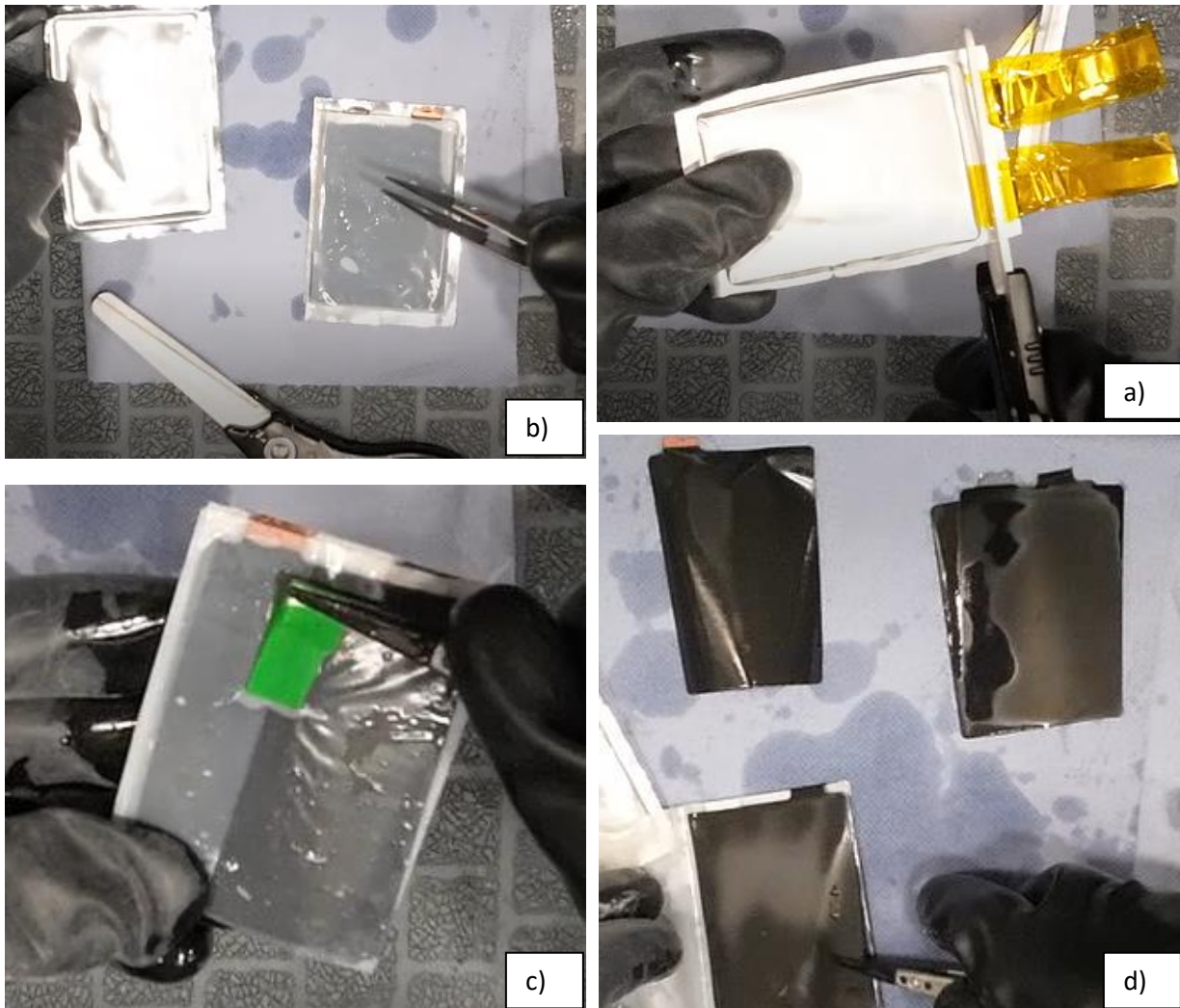


Figure 3-25- a) after cutting the other 3 edges of the cell off the top edge of the cell with the tabs is cut with plastic scissors, b) the cell is peeled apart, c) the separator is unwrapped and d) the electrodes are separated.

### 3.6.3. Lithium presence testing

Physical lithium presence testing was carried out on some anode samples, from cell test group 9, as a further check to confirm if the forced lithium plating attempts had been successful. After cell teardown the samples were taken directly to a fume cupboard. De-ionised water was dripped onto the surface of the anode to observe the reaction, a strong 'fizzing' reaction is indicative of lithium deposition on the surface of the anode. This reaction is expected due to the easily displaced electron of the reactive lithium ions reacting with water to form hydrogen gas (H<sub>2</sub>) and hydroxide ions (OH<sup>-</sup>), the creation of the hydrogen gas causes bubbles to form in the water.

### 3.6.4. SEM and EDX

Samples of the electrode and sensor fibres following teardowns were taken for microscopic analysis; the morphology of the electrode samples and sensors after cell cycling are studied using scanning electron microscopy (SEM, ZEISS Sigma 500) at an electron high tension (EHT) voltage in the range of 5 kV to 10 kV for electrode imaging and 1 kV for fibre sensors, using a secondary electron detector. High magnification images of the samples are taken, ranging from 100x to 300x magnification.

Material analysis of the sample materials composition is further carried out on the electrode and sensors using Energy Dispersive X-Ray Analysis (EDX, Oxford Instruments). EDX determines the chemical elements present in the sample and their distribution and quantity, via detection of the x-rays released from the atoms when hit by a beam of accelerated electrons; however the method does not detect low atomic number elements such as lithium [174].

The SEM and EDX analysis was utilised to analyse the impact of the presence of the fibre sensors on the electrode material, to check for the presence of lithium plating in the experiments in which forced lithium plating was attempted and to see what impact the cell cycling has on degradation of the fibre sensor.

In total the following SEM and EDX analysis was carried out:

- Cell from test group 4, SEM and EDX on an anode layer
- Cell from test group 4, SEM on fibre optic sensor
- Cell from test group 8, anode and cathode electrode SEM and EDX after 150+ cycles
- Cell from test group 8, anode and cathode side fibre sensors SEM and EDX
- Cell from test group 9, forced lithium plated cell, SEM and EDX of anode
- Cell from test group 10, SEM and EDX of new design fibre sensors after many cycles, from anode and cathode side of cells
- Cell from test group 11, SEM and EDX of new design fibres after many cycles, from anode and cathode side of cells

## 4. Results and Discussion

### 4.1. Sensor and Cell Characterisation

Characterisation of the sensor performance was undertaken by testing the response of the sensors to electrolyte with different concentrations of Li-ion salts, as described in Section 3.2. In addition, as described in Section 3.4, various cell characterisation tests were carried out to understand the baseline performance of the batch of cells used in this study; cell characterisation data was gathered as a baseline, to be able to measure the impact of the inclusion of the fibre optic sensors on the cell performance and to assist in designing tests such as forced lithium plating. The results of the sensor and cell characterisation testing are described in this section.

#### 4.1.1. Fibres response to Li-ion battery electrolyte

Sensor reading characterisation was initially established through observing the sensor signal response to the electrolyte used in the cells, 15ml of 1M Lithium hexafluorophosphate ( $\text{LiPF}_6$ ) in Ethylene

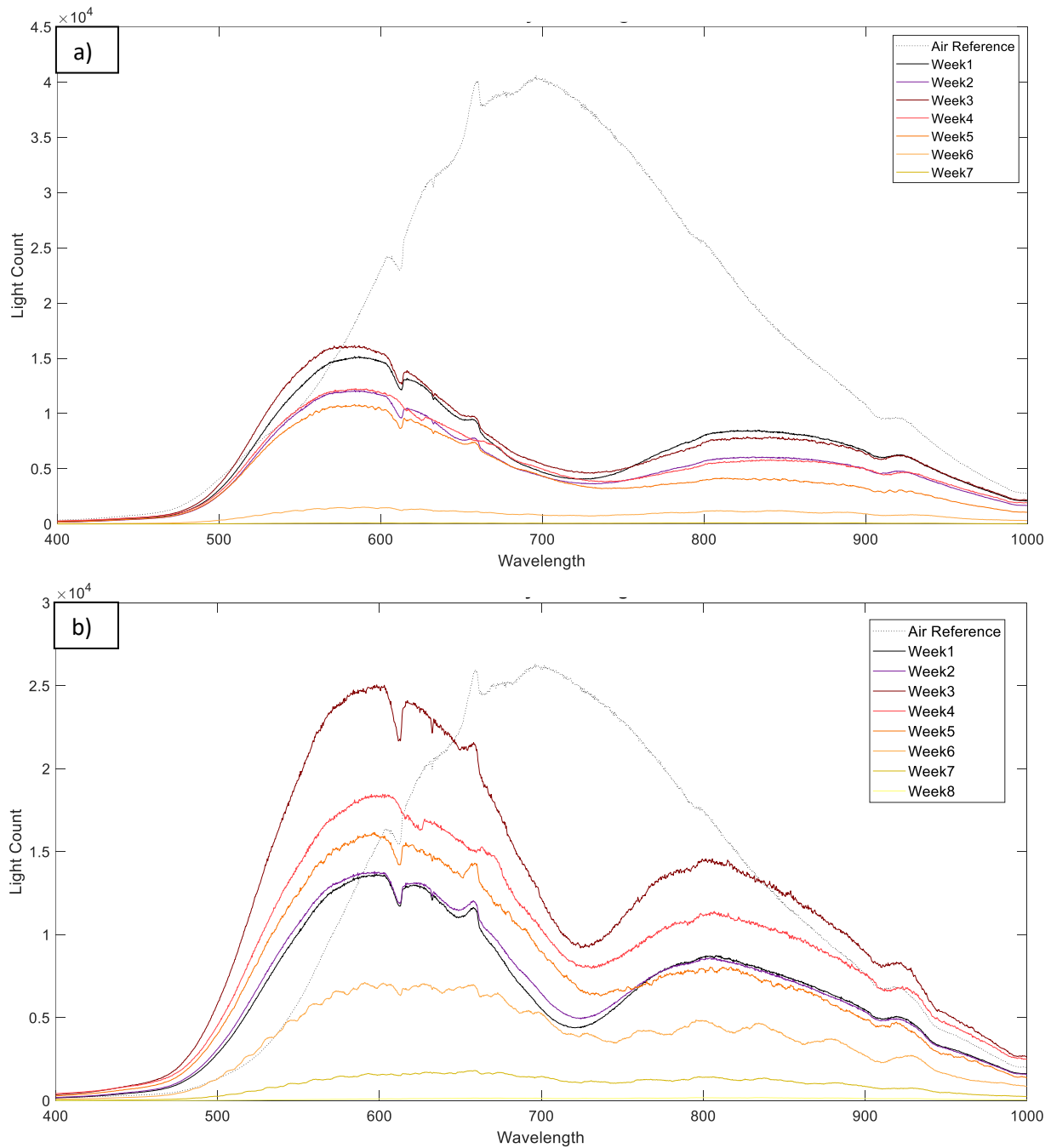


Figure 4-1- Sensor reading in electrolyte over time in enclosed space outside glovebox, a) sensor one, and b) sensor two

Carbonate/ Ethyl Methyl Carbonate (EC/EMC - 3/7 v/v) +2% weight Vinylene Carbonate (VC) placed inside a glass three neck flask; the optical signal response of two plasmonic sensors to air as a reference and then the electrolyte is illustrated in Figure 4-1. The most significant increase in light extinction is observed in the 725nm region, indicating the strongest plasmonic response to the lithium salt electrolyte solution is in that region (the detection range of the sensor is approximately 1000nm with exponentially decreasing sensitivity across that range); it is expected that this is due to the overall refractive index of the solution, rather than any particular element or compound adjacent to the surface of the sensor. We can also see that the sensor signal deteriorates over time, although the

solution is inside a 3 neck flask with bungs, this is not a perfect seal and it is likely that moisture (H<sub>2</sub>O) ingress is reacting with the electrolyte, forming corrosive substances such as hydrofluoric acid which degrade the sensor.

A further experiment in which electrolyte was incrementally added to a pure solvent was carried out inside a glovebox as described in Section 3.2.2, and the resulting optical signal reading can be seen in Figure 4-2. The sensor reading in the pure solvent indicated a limited plasmonic response in the region of 680nm. However, as the electrolyte with lithium salt was added to the mixture the profile of the OU response began to change, creating a significantly stronger plasmonic response in the 725nm region in line with prior test observations. Making the reasonable assumption of homogenous solution distribution, this implies the refractive index of the pure solvent elicits a plasmonic response in the 680nm region, while increasing the lithium salt concentration alters the refractive index such that the wavelength of the plasmonic response increases. As such, in testing utilising the sensors inside active cells, the light count of the wavelengths in the region around 725nm are considered of particular interest. This conclusion is supported by a similar study conducted into utilisation of plasmonic sensors in prototype cells [169].

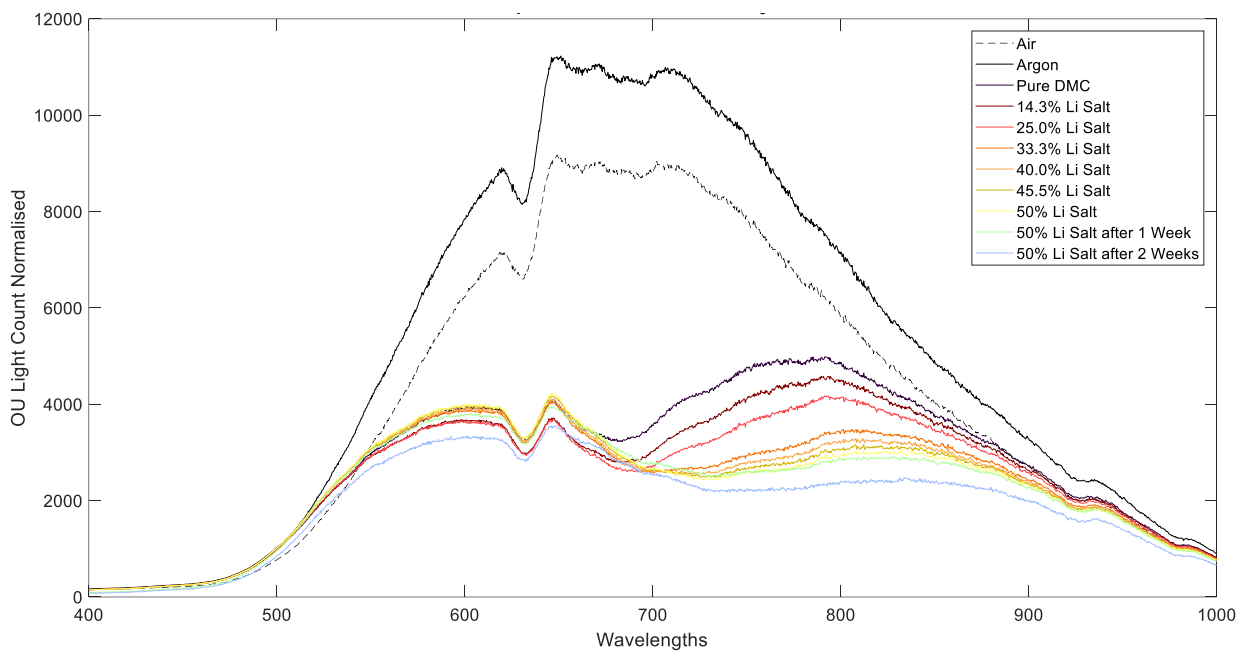


Figure 4-2- Plasmonic sensor optical reading change as lithium salt (LiPF<sub>6</sub>) is added to solvent, experiment carried out inside an argon atmosphere glovebox.

The proportionality of the light extinction with Lithium salt concentration increase at different wavelengths can be explored further. Considering three discrete wavelengths, including the 725nm wavelength for which the Li salt extinction peak is developing, and the 680nm wavelength for which there is an extinction peak with pure DMC, the extinction at these wavelengths with increasing salt concentration can be seen in Figure 4-3. At the 725nm wavelength the light extinction increases with Li Salt concentration, however while it appears linear up to 25% concentration, it can be seen that the gradient of change subsequently decreases with further concentration increases.

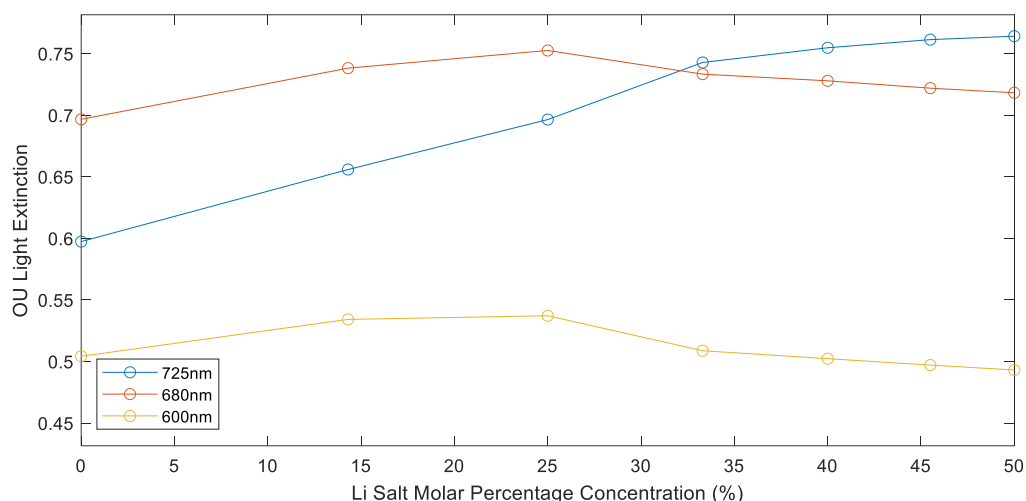


Figure 4-3- The light extinction at different wavelengths plotted against increasing Lithium salt concentration

#### 4.1.2. Baseline cell characterisation

In order to provide a baseline of cell performance, a number of unmodified cells (ie. without sensors added) from the batch were put through cell characterisation testing. The cells used in this study have 21 electrode layers of 11 anodes and 10 cathodes, therefore the active surface area is 2 surfaces over 10 electrodes. The area of the electrode is approximately 48.5mm by 68.5mm, multiplied by 20 surfaces this equates to a geometric surface area of 664.5cm<sup>2</sup>. Given this geometric surface area, a table of charge density of the cell at different C-rates is shown in

Table 4-1 for reference.

Table 4-1- Equivalent c-rates, currents and charge densities for cells

C- rate	Current (mA)	Current per unit area (mA.cm <sup>-2</sup> )
<b>C/20</b>	70	0.11
<b>C/10</b>	140	0.21
<b>C/5</b>	280	0.42
<b>C/3</b>	466.7	0.70
<b>C/2</b>	700	1.05
<b>C</b>	1400	2.111
<b>1.5C</b>	2100	3.16
<b>2C</b>	2800	4.21
<b>3C</b>	4200	6.32

The profiles of the formation cycles of the cell can be seen in Figure 4-4. The charge rate is C/20 as described in the Methodology section, this slow charge rate encourages the formation of the SEI layer and allows us to utilise the full capacity range of the battery cell within its safe operating voltage window. We can see that the cells accept approximately 1450mAh of charge with consistent behaviour between the cells on the first charge. Due to the irreversible process of the initial formation of the SEI layer not all of this capacity can be discharged, additionally the cell is not fully discharged, being discharged to a cut-off limit of 2.5V - below this range (2.5V in this case) the redox potential of copper can be hit which causes dissolution of the copper from the current collector on the anode side, repeated deep discharge also leads to gas generation (primarily carbon dioxide) and swelling of the cells [78,175]. As such the experimental capacity of the cells are shown to be approximately 1250mAh.

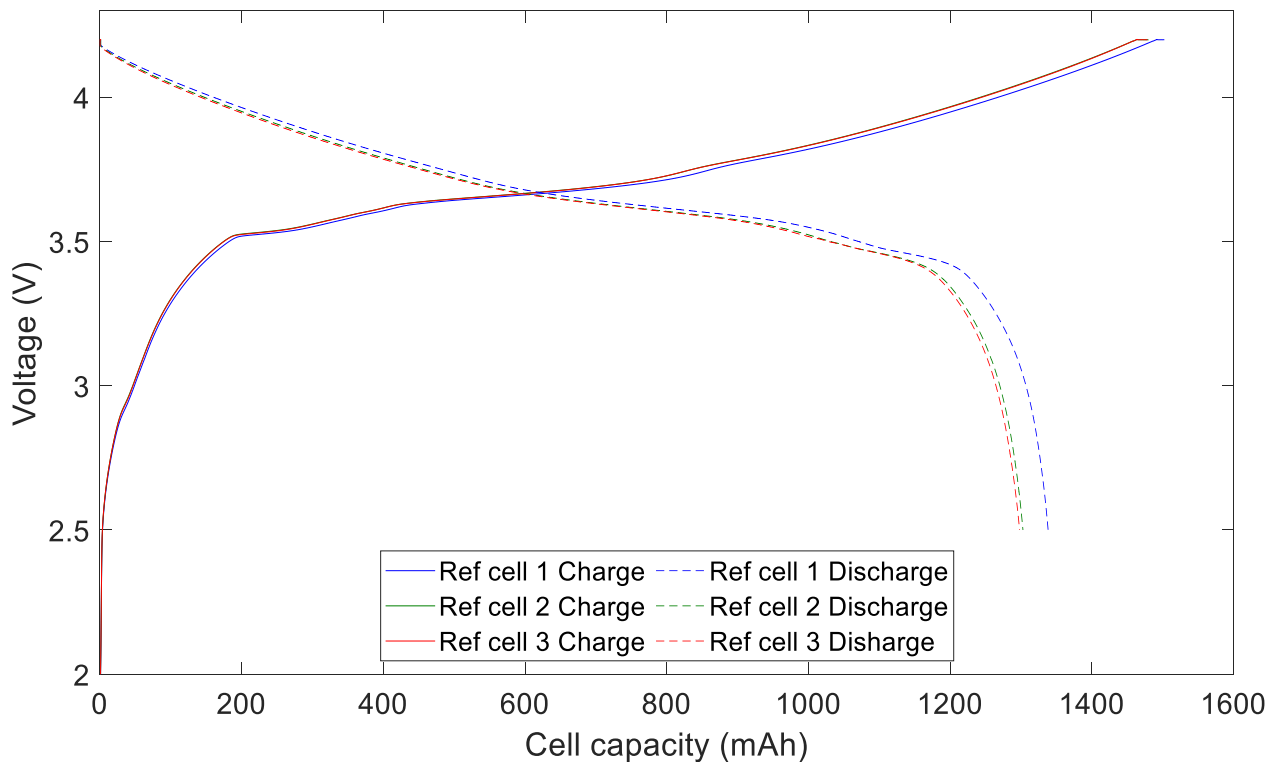


Figure 4-4- Formation cycle of three reference cells, capacity-voltage profile

Subsequent rate testing provides cell performance characterisation data as shown in Figure 4-5. This indicates the charge the cells will accept at different charge rates, charge rate limitations and the impact of high charge current on the cells; the cells are inside a chamber set to a temperature of 25°C as per the methodology described in Section 3.4.2. At the C/5 and C/3 charge rates the cell capacity reached in each case is the same, and there is no deterioration with cycling, indicating the cells are comfortable at C/5 and C/3 in these conditions (25°C). At C/2 we see both an approximately 5% drop in capacity on the first cycle and further slight dropping of capacity with repeated cycling. A rapid decrease in the discharge capacity can be observed after C/2 cycling, dropping by one third from the C/3 to the 3C charge rates. On the 3C cycle cell 2 did not cycle correctly, and cell 1 only completed 3 of the 5 cycles, indicating that the cell was struggling to accept that rate of charge. Nonetheless, while the cells are energy cells and not designed to accept the higher rates of charge, the subsequent C/5 and C/3 cycles only show a small capacity fade, indicating minimal irreversible damage and capacity loss due to the higher cycling rates used. This cell characterisation gives a good indication of the charge rate limitations of the cell; based on these results we can be confident cycling at C/5 will have minimal

detrimental effect on the cell, while cycling at C/2 or above should be used to encourage forced lithium plating.

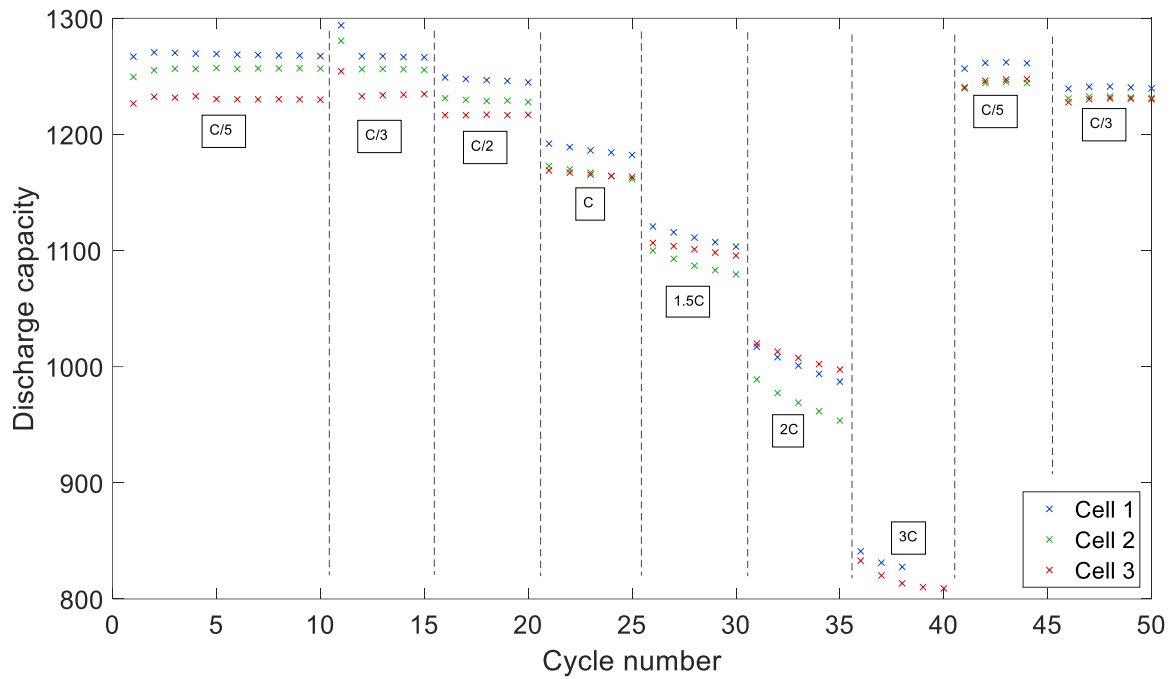


Figure 4-5- Waterfall test cell characterisation on reference cells, from C/5 to 3C charge rates

Considering the temperature behaviour of the cells during cycling, we can see the temperature response at C/5 charge and discharge in Figure 4-6. The temperature does not deviate greatly from the 25°C ambient chamber temperature, we see the cell temperature is typically at least 0.4°C greater than ambient, peaking at 0.6°C greater during charge and 1.2°C greater during discharge. While the internal cell temperature can be expected to be slightly greater than the surface temperature, we can see that at this cycling rate the temperature increase in the cell is minimal; we can also note the temperature change profile for comparison with the optical signal and consideration of temperature effects on the optical signal.

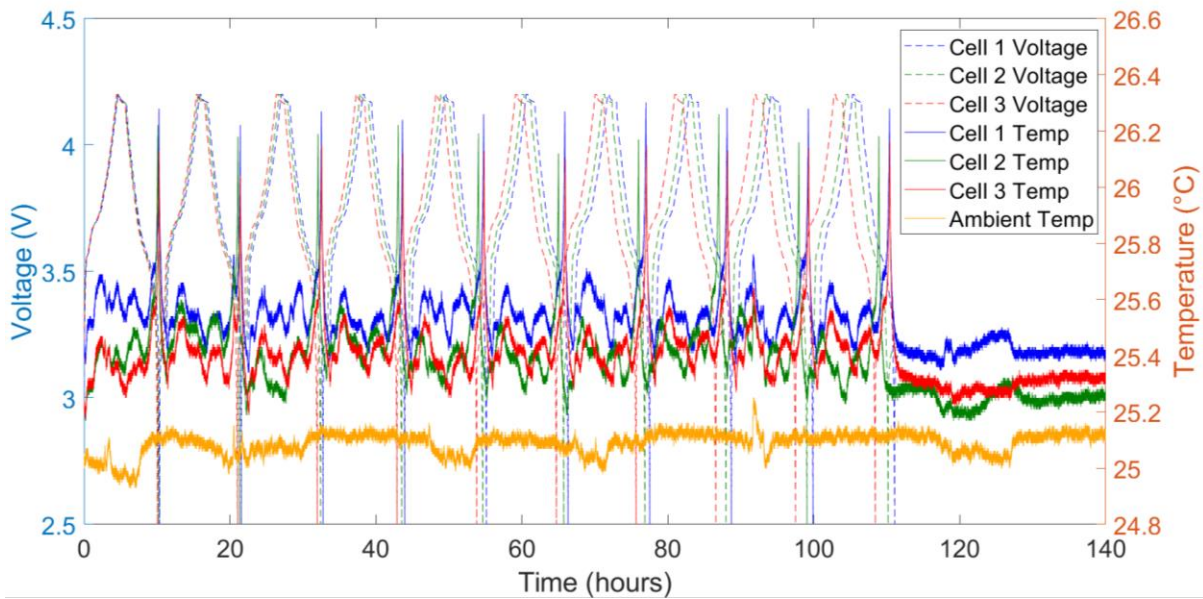


Figure 4-6- Pouch cell surface temperatures recorded during C/5 (280mAh) cycling in 25°C ambient

Temperature response to a range of higher C-rates (C/3 to 3C) during the waterfall test can be seen in Figure 4-7 in which three cells are cycled according to the same cycling regime; of particular interest is the peak temperature change at different cycle rates which indicates the thermal stress a cell will be under at a given charge rate. The increase from the base temperature is approximately 1/3°C at the C/3 charge rate, up to an increase of approximately 5°C at the 3C charge rate. All cycles are discharged at a rate of C/5, reflected in an approximately 0.5°C temperature increase at the point of maximum discharge across all cycles. The rest temperature should return to 25°C (set chamber temperature), the difference in the measured and set temperature can be explained by the  $\pm 1.5\text{K}$  accuracy of the thermocouples. The data also shows the temperature change across the three cells is consistent, while there is some minor variation across them which could be explained by thermocouple accuracy, cell to cell variation or slightly different positioning or contact of the thermocouples on the cells.

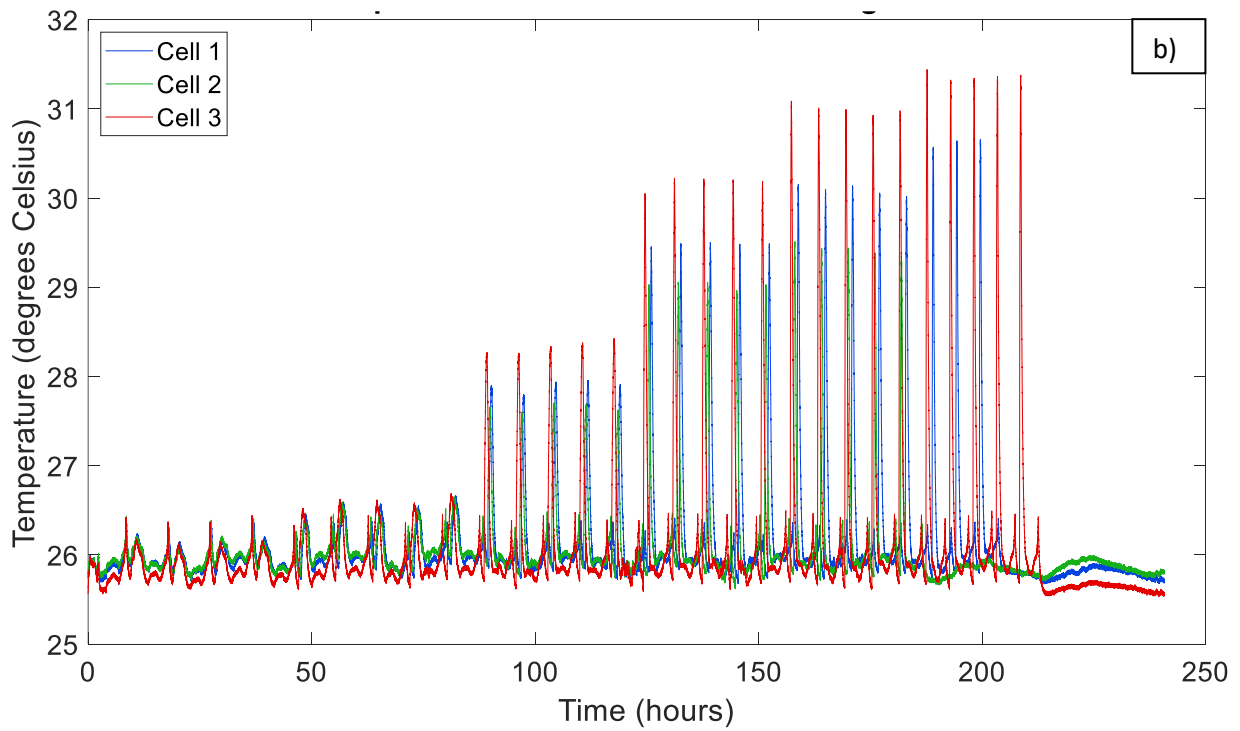
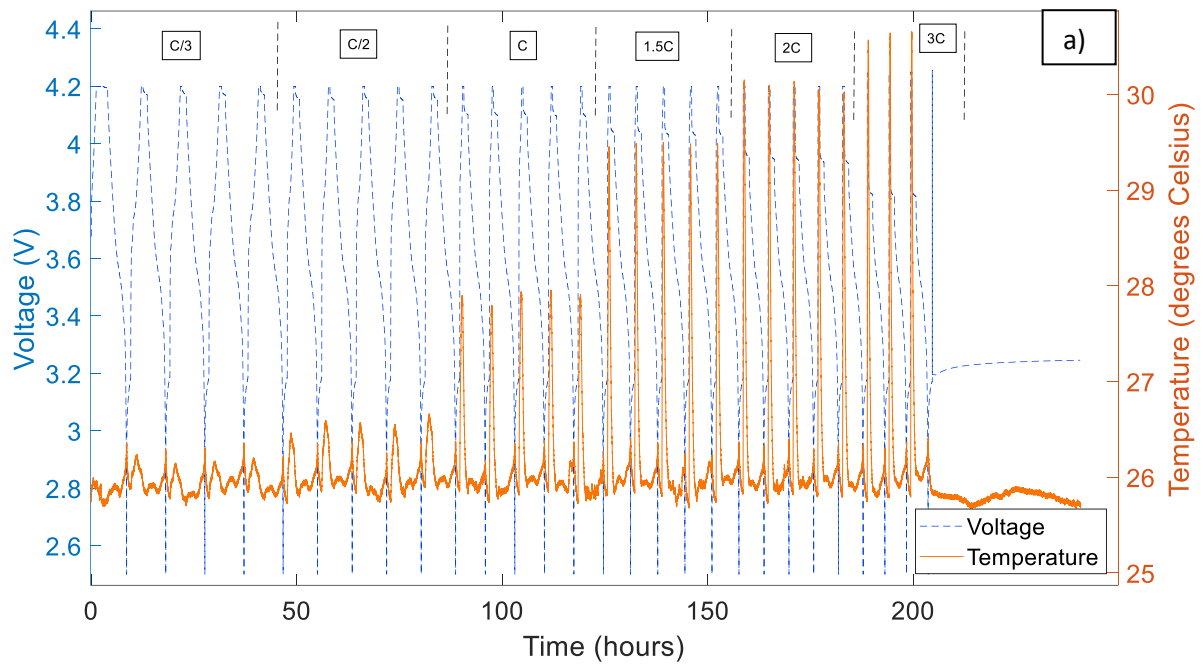


Figure 4-7- a) temperature of one cell at different charge rates and D/5 (top), b) temperature of multiple cells

EIS testing has also been carried out, as can be seen in Figure 4-8, to characterise the cells' response to the procedure in the fully charged and fully discharged states. This data can be compared to the cells with fibre sensors and after lithium plating to help evaluate the impact of those events on the cell kinetics, and indicates a series resistance value (where the imaginary resistance component is zero) for the cells of approximately 0.019 ohms. The arc diameter is much larger for the discharged cells, it is a known effect that the charge transfer resistance increases dramatically when the cell is in the fully discharged state.

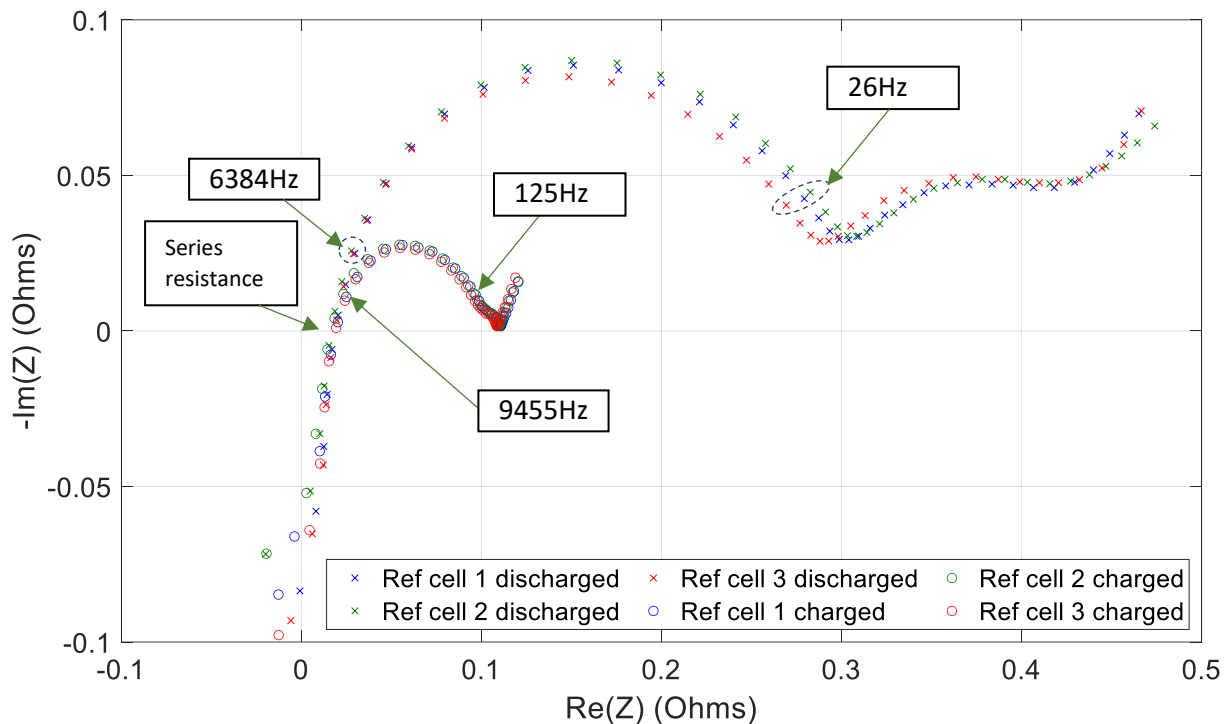


Figure 4-8- EIS testing of the reference cells in the charged and discharged states after 10 cycles

#### 4.1.3. Evaluation of impact of sensor presence on cell

While the 'observer effect' dictates that act of observation disturbs the physical system in question, it is paramount we aim to minimise the effect on the system so it remains as close to original as possible. Insertion of a foreign body – a fibre – into the cell further creates a risk that the cell could leak at the point where the fibre is sealed into the cell pouch material. As shown in Figure 3-9 this part of the process was tested by sealing fibre sensors in empty pouch material and filling the pouch material with water- after leaving these items for one week no water leaks were found through the seal, which provided some confidence that the sealing method was effective and the presence of the fibre was not leading to leakage from the cell.

Subsequently, as set out in Sections 3.4.2 and 3.4.3, various characterisation tests were carried out for cells with and without fibres, allowing a comparison of the impact of the fibre sensors on cell performance. Formation cycles of three cells without fibre sensors compared to three cells with a

single optical fibre sensor in each (from test group 4) are shown in Figure 4-9. The data shows that the presence of fibre optic sensor has a negligible impact on the cell charge, capacity and voltage during cell formation.

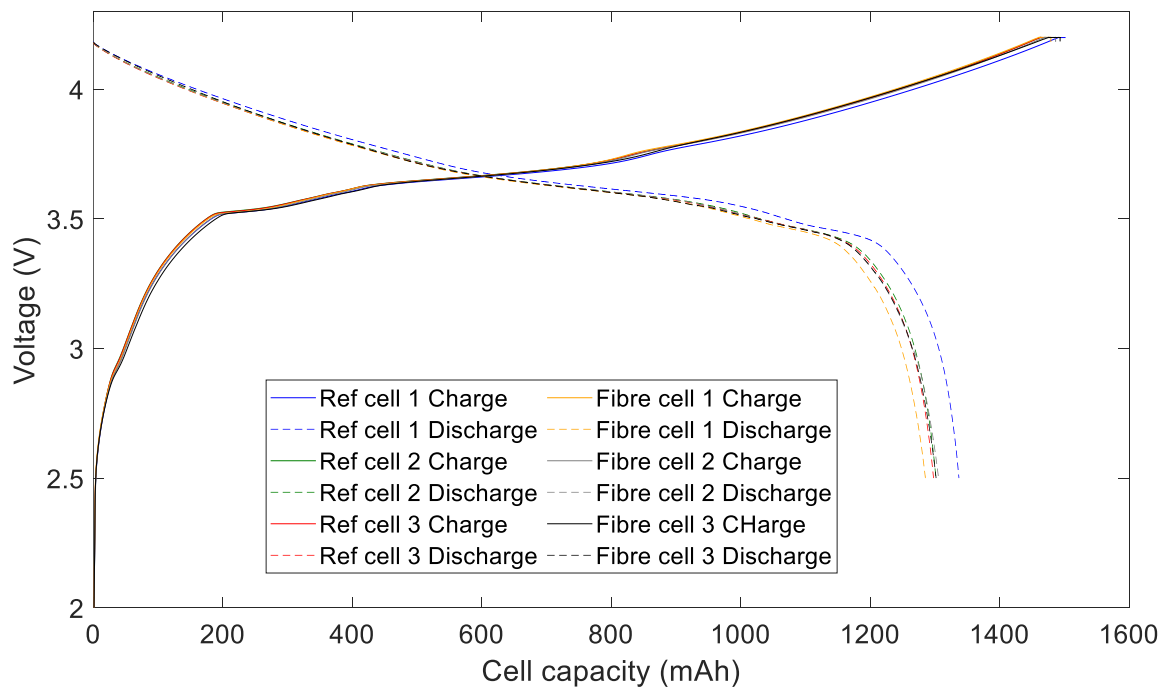


Figure 4-9- Formation cycles capacity-voltage profiles of three cells with one fibre sensor in each and three cells without fibres, for comparison

Longer term impact is evaluated in Figure 4-10, showing the coulombic efficiencies of three fibre instrumented cells over 50 cycles compared to a benchmark cell without the sensor. The data indicates that the presence of the sensor has little to no impact on the coulombic efficiency; this is significant, as an ideal diagnostic method should not interfere with the measured process, while high coulombic efficiency and long stable cycle life are required for commercially relevant applications. Deviation observed around the 16<sup>th</sup> and 28<sup>th</sup> cycles is due to test stop and restarts to allow adjustment of the optical equipment integration time.

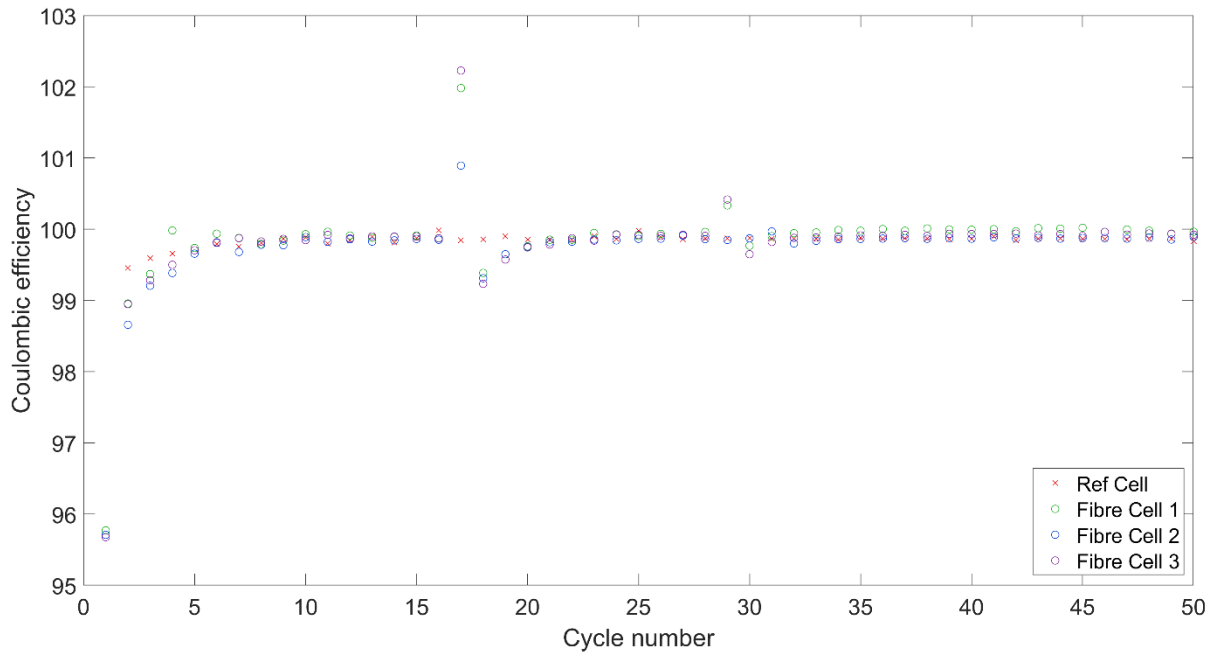


Figure 4-10- Coulombic efficiencies of cells with one fibre optic sensor compared a reference cell

Subsequent cell teardown of a cell that has been cycled for 50 cycles shows a discoloration on the surface of the anode that follows the line of the fibre, visible in Figure 4-11. This can be caused by pooling of electrolyte around the fibre or uneven drying during cell disassembly. The gold coating on the sensing area of the fibre also appears to have been delaminated or corroded in patches; this could be due to deposition or corrosion and requires further study. This degradation is hypothesised to be the cause of the increasing light extinction trend shown which is discussed further in Section 4.2.2. SEM scans of an electrode sample from the centre of the anode, with part of the discoloration on, are also shown in Figure 4-11. The SEM images suggest that the line of lighter patches aligned to the fibre position on the electrode can be identified as lithium salt deposits. These can be explained as appearing in a greater concentration in this area due to ‘pooling’ of electrolyte around the fibre sensor during disassembly. While this creates a potential failure point for the cell, it has not been observed to have a significant effect during this and subsequent testing.

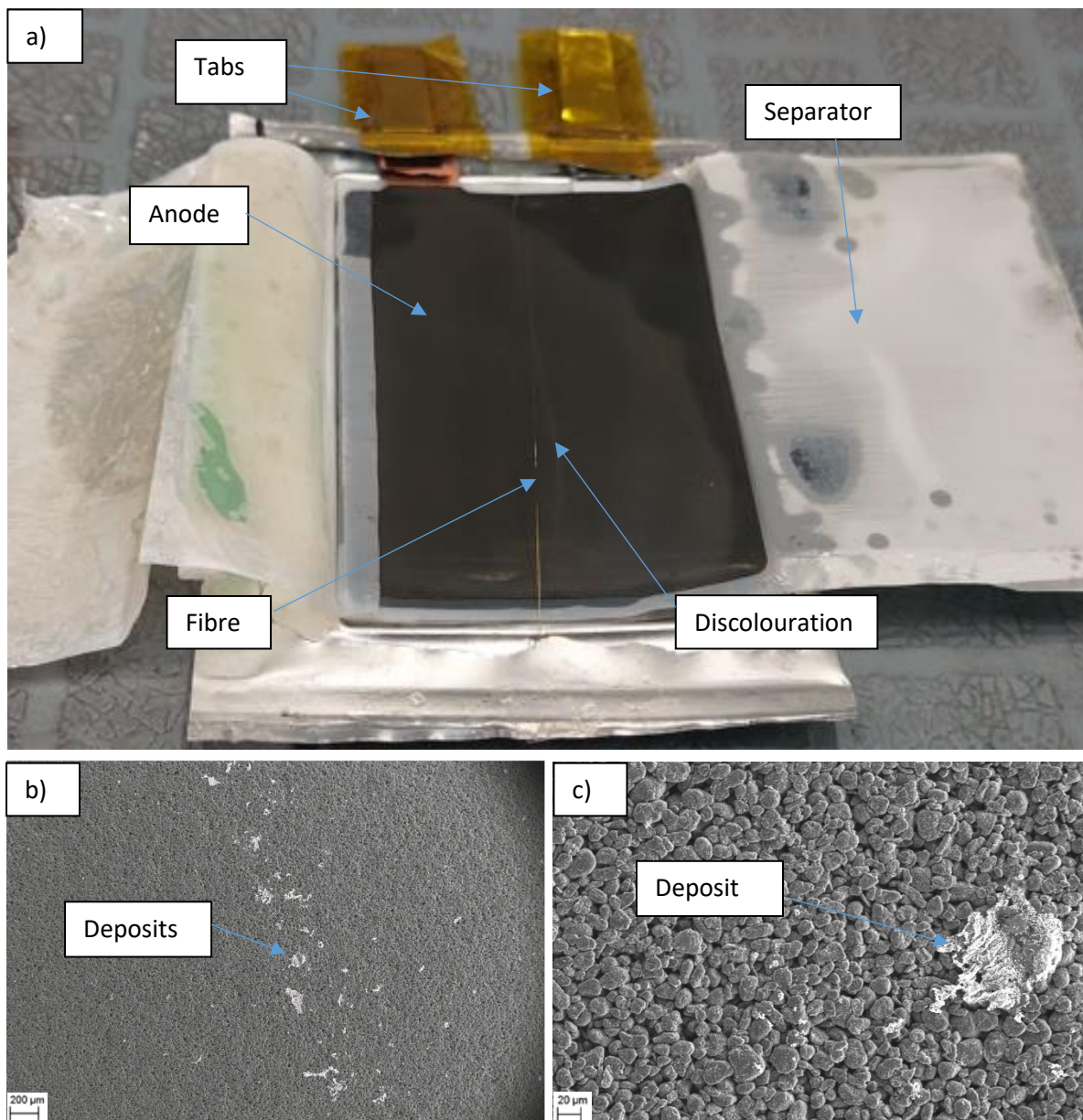


Figure 4-11- a) Autopsied cell with sensor fibre, opened after 50 cycles, b) SEM image of discoloured region on electrode at x73 magnification c) SEM image at x566 magnification (enlarged section of figure b)

Additionally the data gathered with cells with two fibre optic sensors inside, one adjacent to an anode and one adjacent to a cathode, can also be compared to the reference cell data. Figure 4-12 compares the charge-voltage profiles during the formation cycles of reference cells and cells with two fibre optic sensors in. The results show that the presence of two fibre optic sensors has no discernible impact on the charging profile of the cells or their capacity, with the variation that is there within a normal level of variation that can be seen from cell to cell.

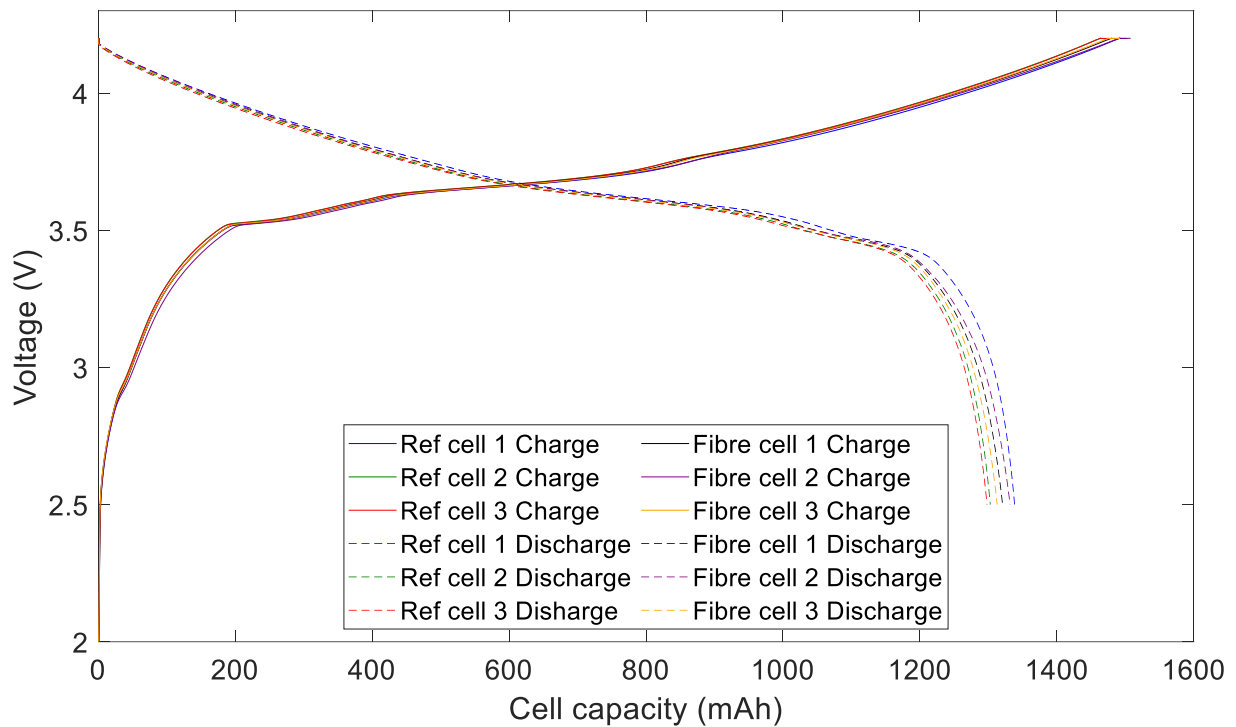


Figure 4-12- Formation cycle capacity-voltage profile comparison for reference cells and cells with two fibre optic sensors

Considering the longer term impact of the presence of the fibre optic sensors on the cells, coulombic efficiencies of the cells with two fibre optic sensors versus reference cells over 150 cycles is shown in Figure 4-13. The cycling regime of the cells with two fibre sensors can be seen, most cycles are carried out galvanostatically at C/5, however some of the cycles are also carried out at C/3 and C/2, as well as some CV and GITT testing- the reason for conducting a variety of testing on the same samples was to allow the maximum data analysis from the available materials. The reference cells are galvanostatically cycled consistently at C/5, which can be considered a less demanding cycling regime overall. The coulombic efficiency data further indicates that the presence of the fibre optic sensors has no degrading effects on the cell capacity over the longer cycling period, with both reference and fibre cells retaining coulombic efficiencies of greater than 99.8% after 150 cycles and all cells being

within an approximately 0.1% range. The anomalous coulombic efficiency data points that are a consequence of the testing being stopped and restarted.

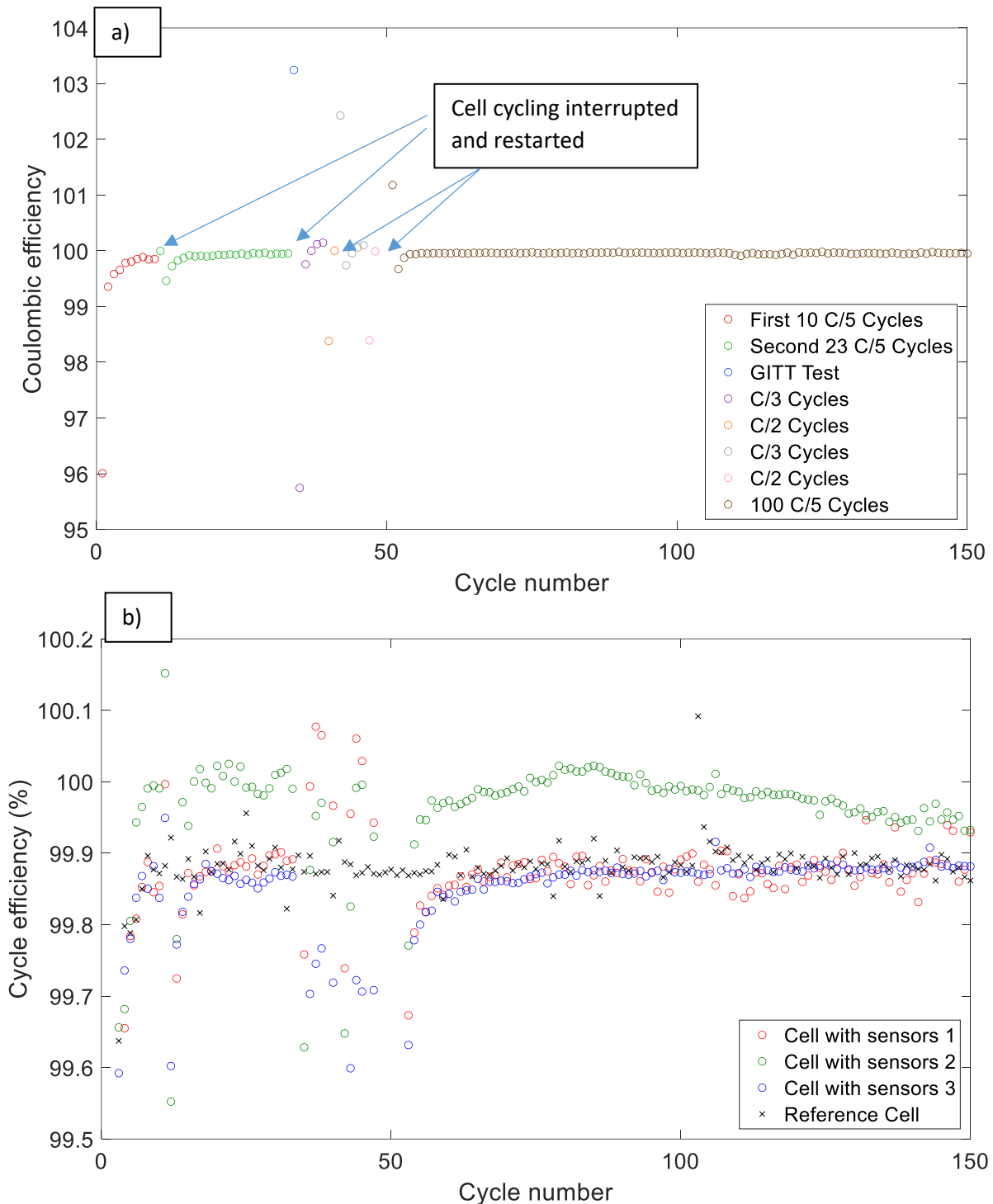


Figure 4-13- a) Cycling carried out on 3 cells with two sensors in, with coulombic efficiencies for each cycle (the cycles with efficiencies that deviate significantly from the mean are due to the testing being stopped and started) b) Comparison of coulombic efficiencies of the cells with two sensors to a reference cell cycled at C/5 for 150 cycles, shown at higher resolution.

This data can further be plotted in terms of the discharge capacity on each cycle as shown in Figure 4-14, here we can see the discharge capacity variation after 125 cycles is approximately 5% not including the cell with sensor two which is an outlier; this can be considered a consistent range for

prototype cell manufacturing and accounting for additional potential assembly issues due to assembling the cells with the sensors. The data demonstrates that over 150 cycles the presence of two fibre optic sensors does not noticeably impact the coulombic efficiencies of the cells, this is further important evidence that the presence of the sensors has negligible impact on the processes being measured, at least in the initial period of cycling.

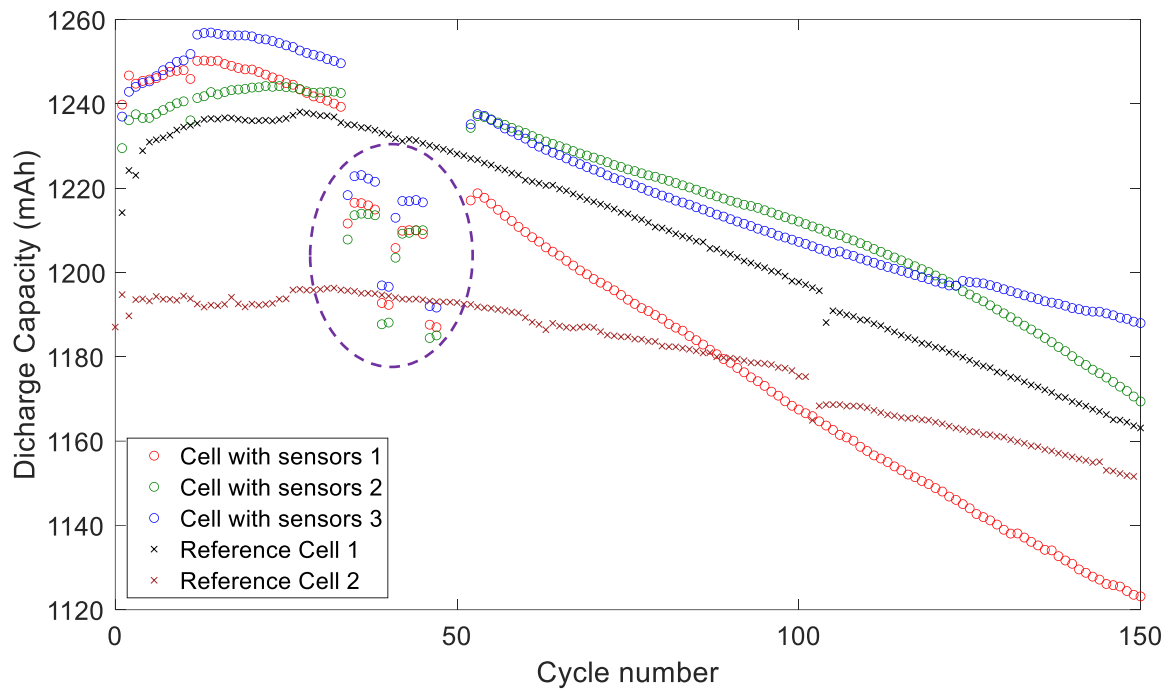


Figure 4-14- Cycling carried out on 3 cells with two sensors in with discharge capacities for each cycle, compared to two reference cells without fibres. The discharge capacities in the purple dashed circle deviate from the trend due to stopping and restarting the cycling, to carry out other testing including higher C rate (C/2 and C/3) cycling, CV and GITT- all other cycles for the cells carried out galvanostatically at C/5.

As a further measure of the impact of sensors on the cells, EIS data after the first 10 cycles of reference cells and cells with two fibre sensors is shown in Figure 4-15. In this instance EIS testing has just been carried out in the fully discharged and fully charged states, to allow a comparison of the real resistance

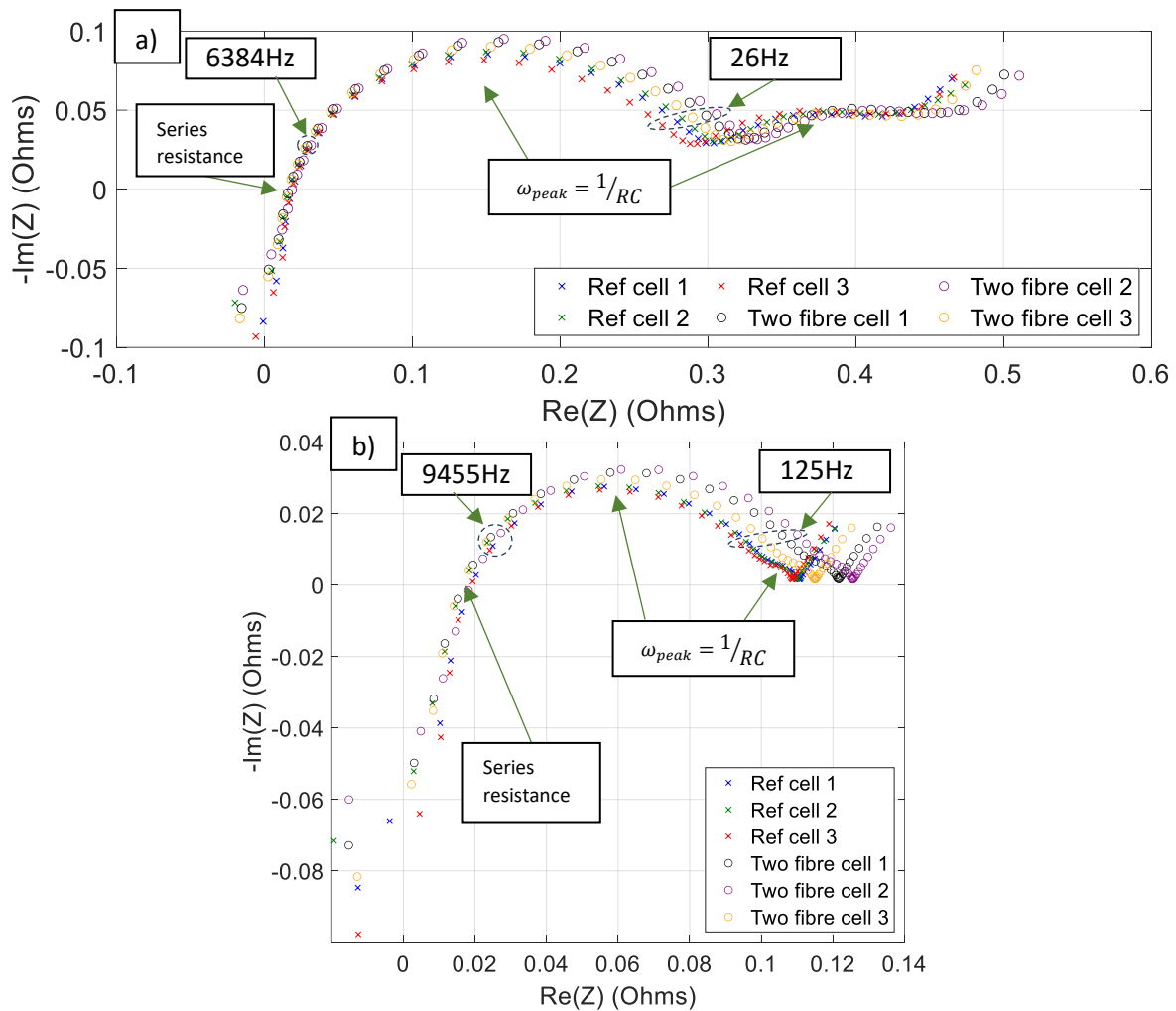


Figure 4-15- EIS response comparison for reference and fibre cells in a) fully discharged state and b) fully charged state

values and cell kinetics with and without fibre optic sensors. The EIS testing indicates a real resistance value of approximately  $0.019\Omega$  for both the cells with and without fibre sensors; the real resistance value may be lower after accounting for the inductance element, although any adjustment should be equally applicable to all cells due similar testing conditions in all cases. The RC semi-circle component is different, with a higher frequency value at the peak of the semi-circle and longer semi-circles in the case of the sensed cells, indicating lower responsivity and higher resistance respectively. However, the magnitude of the differences can be attributed to expected cell to cell or experimental setup variations.

An equivalent circuit model (ECM) was used to fit the EIS data, utilising two resistor and constant phase element parallel pairs and a mixed kinetic and charge-transfer control model. In Figure 4-19 the ECM and EIS plots with fitting according to this model are shown for reference cell and fibre cell one. In Table 4-2 the circuit element values are given according to this fitting; while there is some variation in the values, as is expected using iterative EIS curve fitting, the values can be seen to be of a consistent order of magnitude.

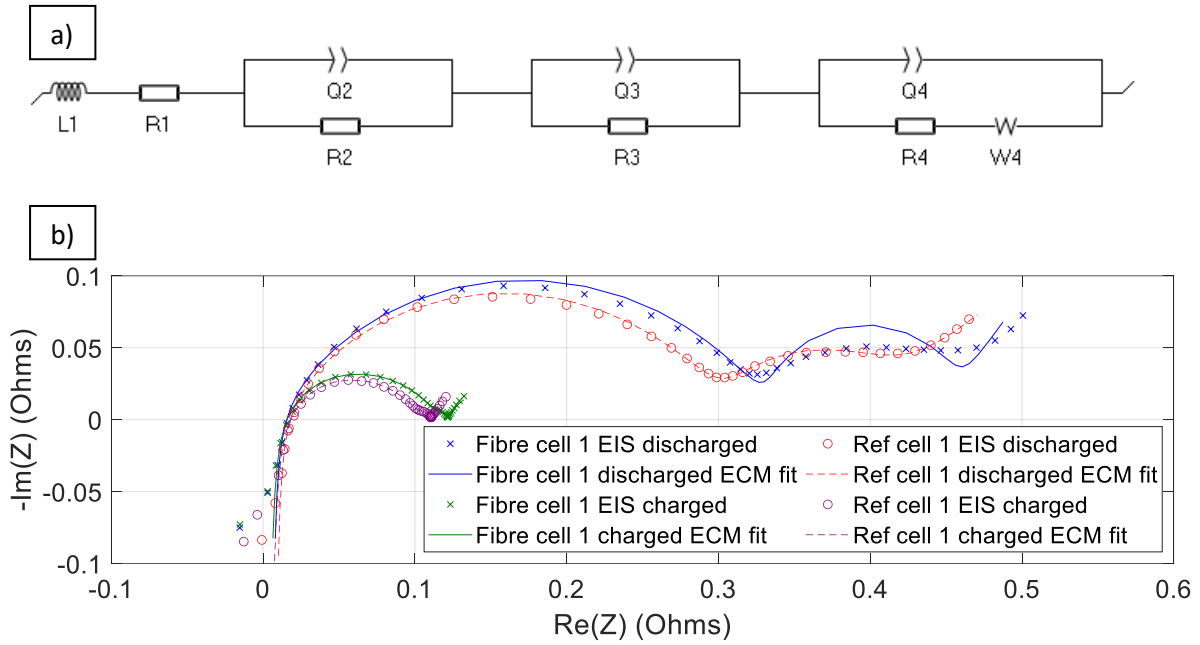


Figure 4-16- Equivalent Circuit Model EIS data fitting, a) ECM consisting of inductor (L), resistors (R), constant phase elements (Q) and Warburg diffusion coefficient (W), b) Fitted ECM plot overlaid onto EIS data for reference cell 1 and fibre cell 1, both in median positions of respective groupings in Figure 4-15.

Table 4-2- Iteratively calculated ECM element values (BioLogic EC-Labs software), according to the ECM model and fitting shown in Figure 4-16.

ECM element	ECM element values				Units
	Ref Cell 1 Charged	Ref Cell 1 Discharged	Fibre Cell 1 Charged	Fibre Cell 1 Discharged	
<b>L1 (Induction)</b>	$0.159 \times 10^{-6}$	$0.166 \times 10^{-6}$	$0.140 \times 10^{-6}$	$0.141 \times 10^{-6}$	H
<b>R1 (Resistor)</b>	$1.595 \times 10^{-3}$	$3.76 \times 10^{-3}$	$2.598 \times 10^{-3}$	$4.548 \times 10^{-3}$	Ohms
<b>Q2 (CPE- constant phase element)</b>	$8.858 \times 10^{-9}$	2.43	2.79	3.518	$F.s^{(a_2 - 1)}$
<b><math>a_2</math> (time constant for Q2 CPE)</b>	0.999	0.999	0.999	0.999	
<b>R2</b>	$5.27 \times 10^{-3}$	$6.912 \times 10^{-3}$	$6.751 \times 10^{-3}$	0.117	Ohms
<b>Q3</b>	0.018	0.016	0.016	0.017	$F.s^{(a_3 - 1)}$
<b><math>a_3</math></b>	0.674	0.674	0.674	0.674	
<b>R3</b>	0.300	0.101	0.113	0.332	Ohms
<b>Q4</b>	3.456	506.3	481.2	106.5	$F.s^{(a_4 - 1)}$
<b><math>a_4</math></b>	0.822	0.822	0.822	0.822	
<b>R4</b>	0.107	0.209	0.045	0.120	Ohms
<b>W4 (Warburg element)</b>	0.016	$5.186 \times 10^{-3}$	$1.007 \times 10^{-3}$	0.030	$Ohm.s^{-1/2}$

Subsequent to this cycling the cells were autopsied and the electrodes and fibres observed with SEM and EDX analysis to assess the impact of the presence of the fibres on the cells. Figure 4-17 shows that there is a visible deposit on the anode electrode where the fibre optic sensor had been, however as noted previously in the section this could again be 'pooling' of dried electrolyte in the area of the fibre resulting in  $\text{LiPF}_6$  salt deposits. The EDX data in Figure 4-18 further supports the proposal that this is  $\text{LiPF}_6$  salt, as consistent levels of fluorine and phosphorus are detected in the area. In Figure 4-19 images of the cathode adjacent to the fibre optic sensor can be seen, in this case there is no visible evidence of the prior presence of the fibre optic sensor.

EDX analysis of the cathode sample shown in Figure 4-20 also reveals expected results, with nickel, manganese and cobalt identified which are present in the cathode, fluorine and phosphorus detected from the lithium salt left by the dried electrolyte, carbon present due to the binder and oxygen detected from oxidation on exposure to atmospheric oxygen. In this case EDX mapping has been used rather than spectrum, to determine if there are any spatially related features that could indicate disturbance caused by the presence of the fibre sensor, however no disturbance is apparent. The presence of lithium is inferred as the presence of fluorine and phosphorus indicates  $\text{LiPF}_6$  salt resulting from dried out electrolyte, although EDX is not actually able to detect lithium due to the low atomic number of the element. Both the anode and cathode material analysis indicates a negligible physical impact on the cell materials due to the presence of the fibre optic sensors, further important evidence of the non-invasive impact of the sensor technology.

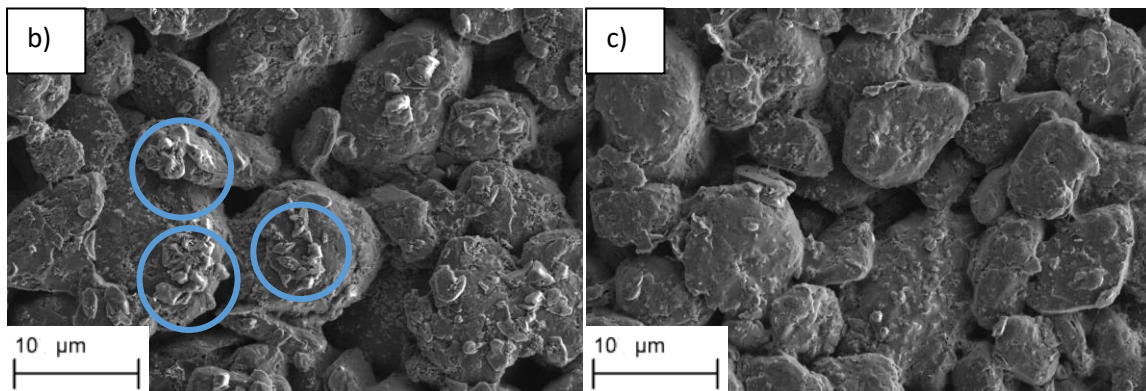
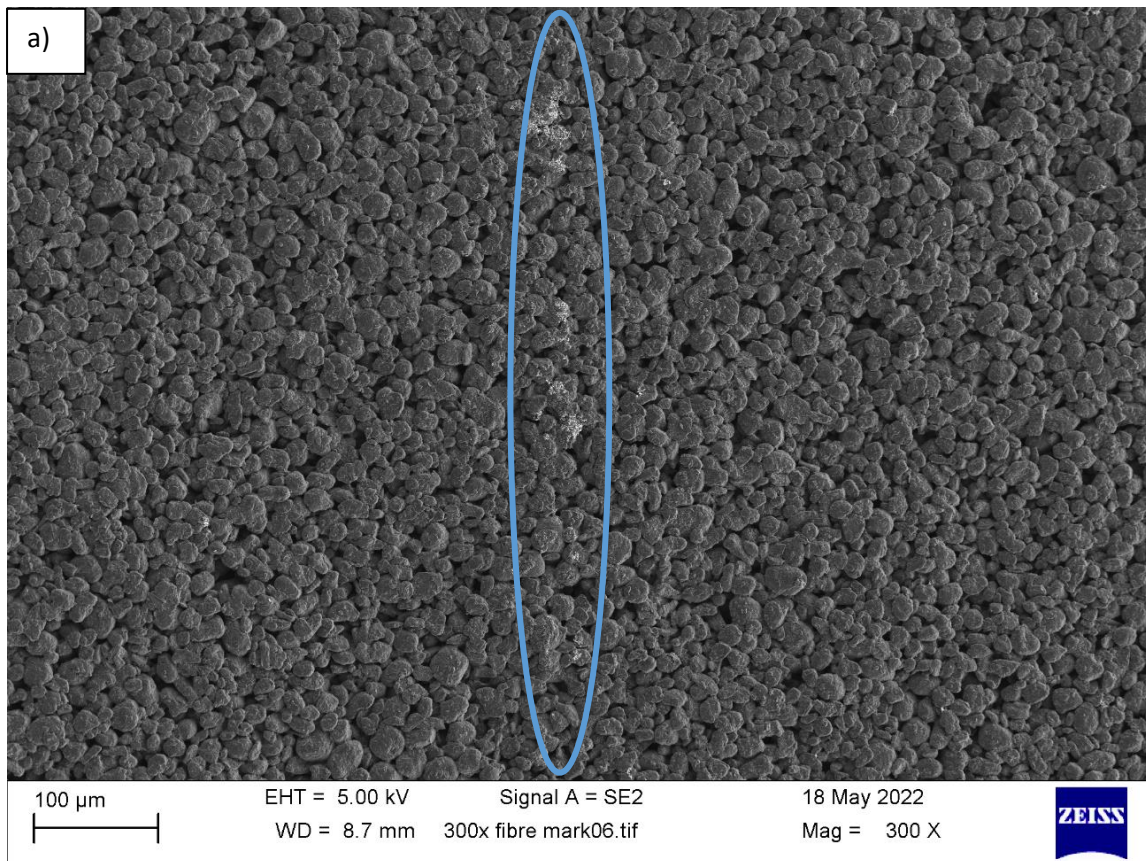


Figure 4-17- SEM images of anode from cell cycled for over 150 cycles with fibre optic sensors inside. Lithium salt deposits can be seen in blue circles. a) shows section of electrode at 300 magnification, line of lithium salt deposit can be seen where the fibre was previously. b) 3000x magnification of area of electrode that had visible deposits, where fibre had been. c) 3000x magnification of area of electrode without visible deposits, where fibre had not been present.

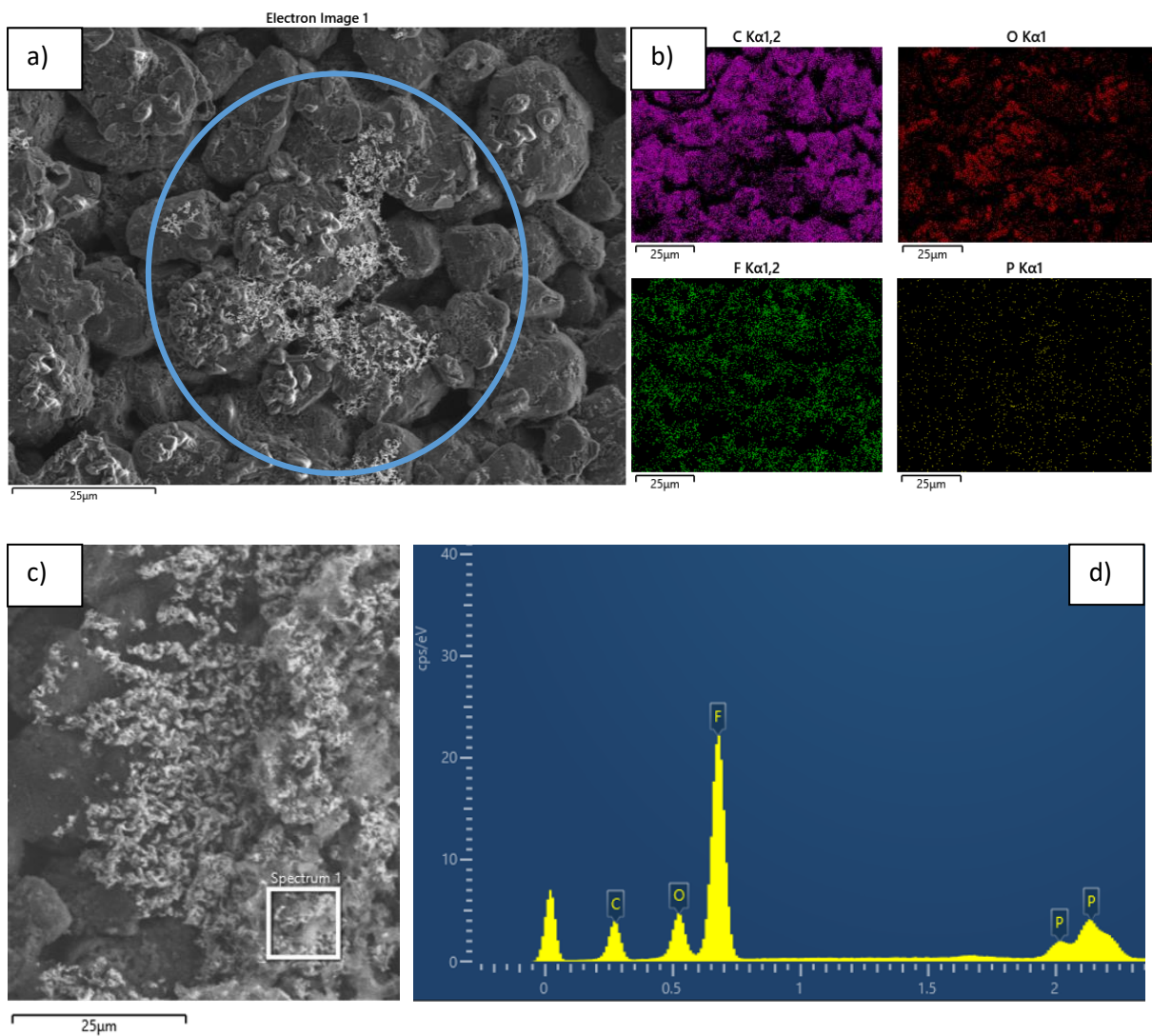


Figure 4-18- EDX analysis of section graphite anode from cycled cell with fibre sensors, including deposit in region of fibres. a) SEM image of region- profile could be indicative of poorly mixed carbon black b) Carbon, oxygen, fluorine and potassium detected by EDX c) Second SEM image of region d) Carbon, oxygen, fluorine and potassium distribution as detected by EDX spectrum analysis of region in blue box in image c).

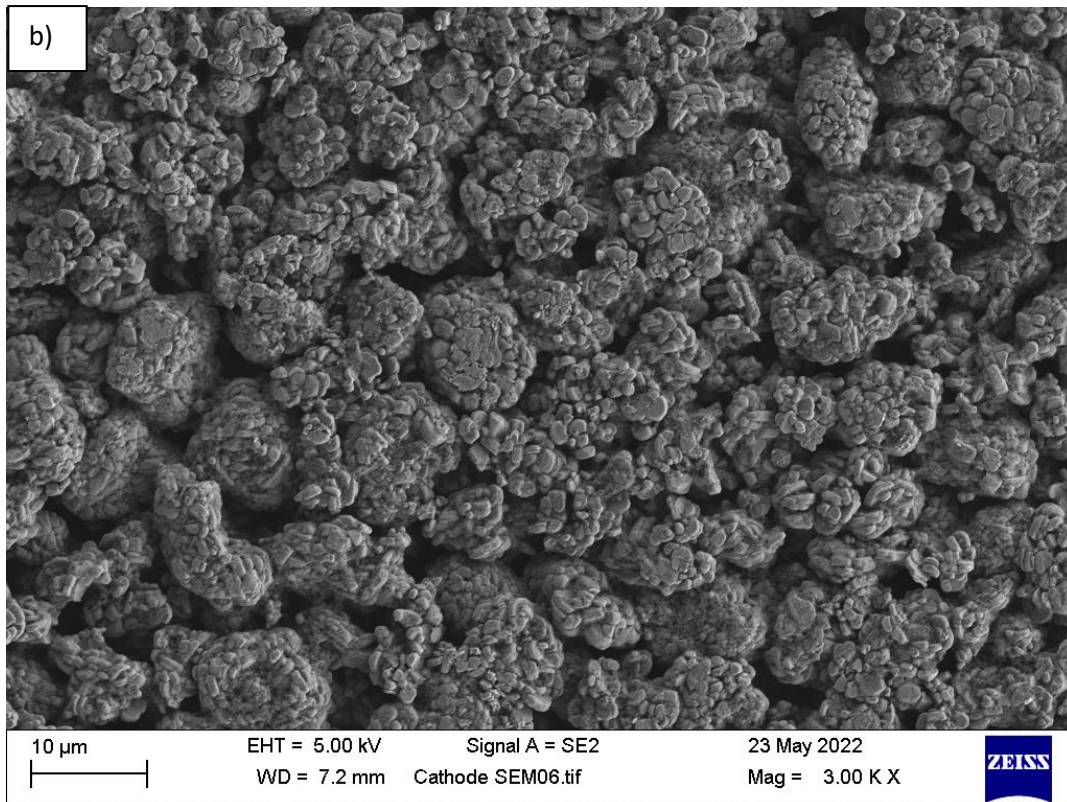
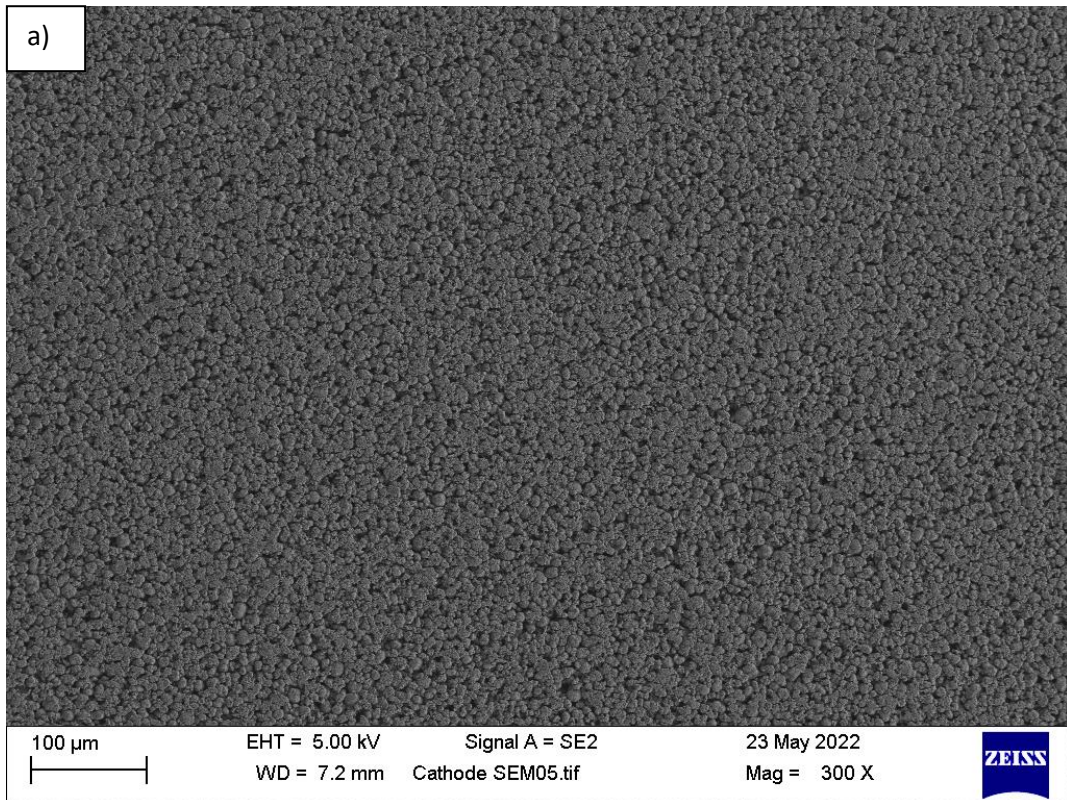


Figure 4-19- SEM images of cathode adjacent to sensor, at 300× (a) and 3000× (b) magnification.

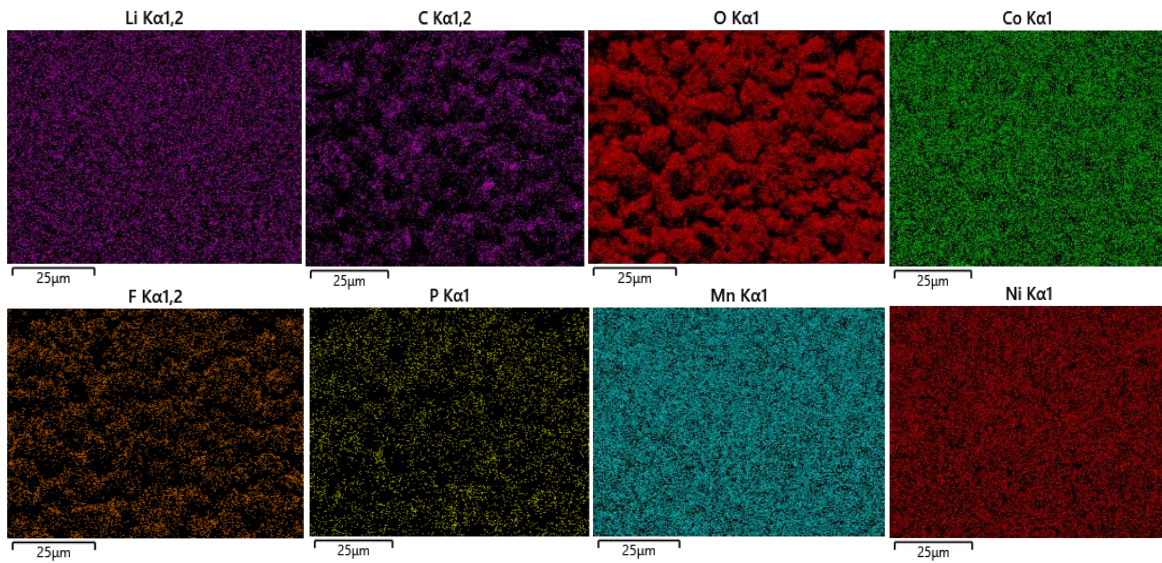


Figure 4-20- EDX mapping of cathode area in Figure 4-16 b)

#### 4.1.4. X-ray tomographic images of sensor in cell

X-ray tomographic imaging shows the position of the fibre sensor within the cell and the layout of the electrode stack. There is some evidence of small gas bubbles between the stacks which can be attributed to gas formed during cycling, now free to move around the cell with the removal of the compression plates. We can see that the sensor remains intact and in position within the cell, with no

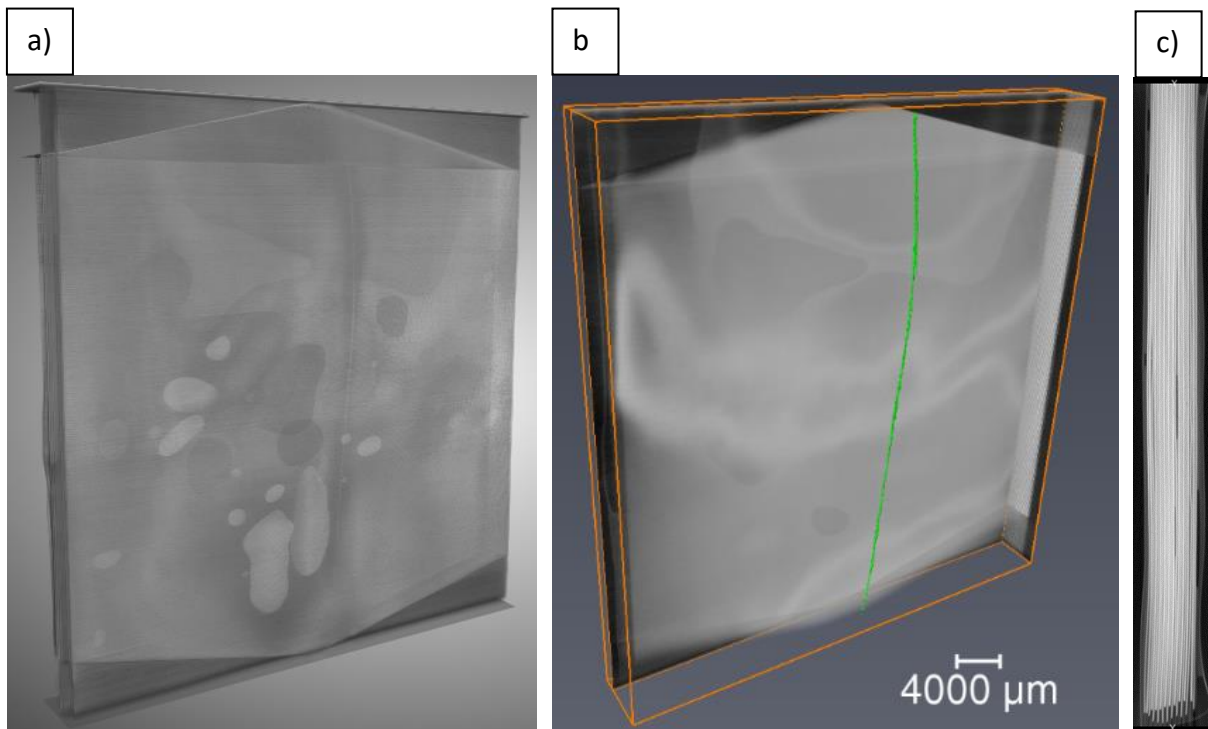


Figure 4-21- a), b) X-ray of fibre in cell and c) cell stack X-ray side profile (5mm width)

obvious deformation or damage to the cell in the region of the fibre sensor. The x-ray tomographic images in Figure 4-21 show the position of the fibre within the cell as well as the electrode stacks from the side view. This technique allows us to see that the sensor is unbroken and aligned as expected in the cell.

## 4.2. Optical signal correlation with cell cycling

Following on from establishing the sensor in cell assembly method, and the separate characterisation of reference cells and optical sensor performance in electrolyte, experiments were conducted with the optical sensors inside Li-ion pouch cells with the aim of testing the experimental setup and gathering initial optical data that could be compared to changing cell state and analysed for correlation. This section documents the optical response to changing cell state, looking initially at the formation cycles and galvanostatic cycling, with fibre optic sensors placed adjacent to both anode and the cathode electrodes. Data relating to the longevity of the sensors over time is also included, as well as data relating to the impact of temperature and pressure on the optical signal.

### 4.2.1. Formation and initial cycling optical data

As described in Section 3.4.1 formation cycling was carried out consistently across all cells, at a c-rate of C/20 (280mA). The data in Figure 4-22 shows the optical fibre signal during the cell formation cycle (from test group 8), with the optical signal from the sensor adjacent to the anode in figure a) and the optical signal from the sensor adjacent to the cathode in figure b). According to the findings in Section 4.1.1 the signal in the 725nm wavelength region is of particular interest, as such Figure 4-23 shows the data from Figure 4-23 at the 725nm wavelength only rather than across the whole optical spectrum. The technique of plotting the optical data at the 725nm wavelength only is subsequently applied throughout this study for easier visual correlation of the optical data with electrochemical data, allowing a 2D graphical form.

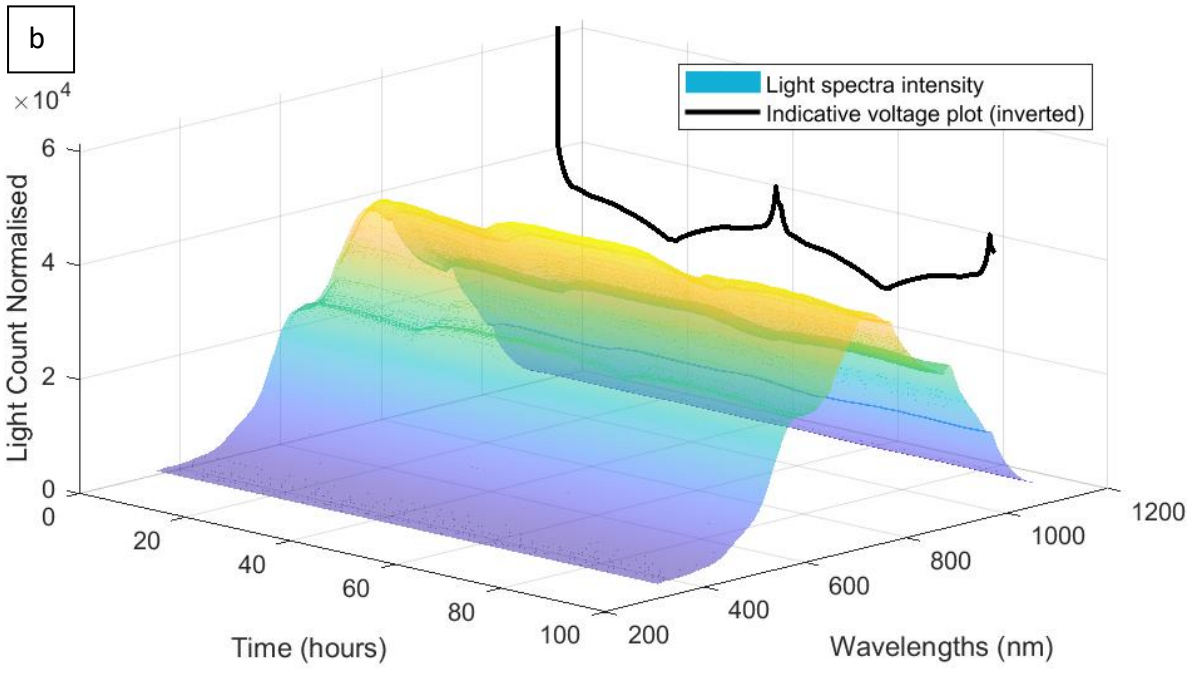
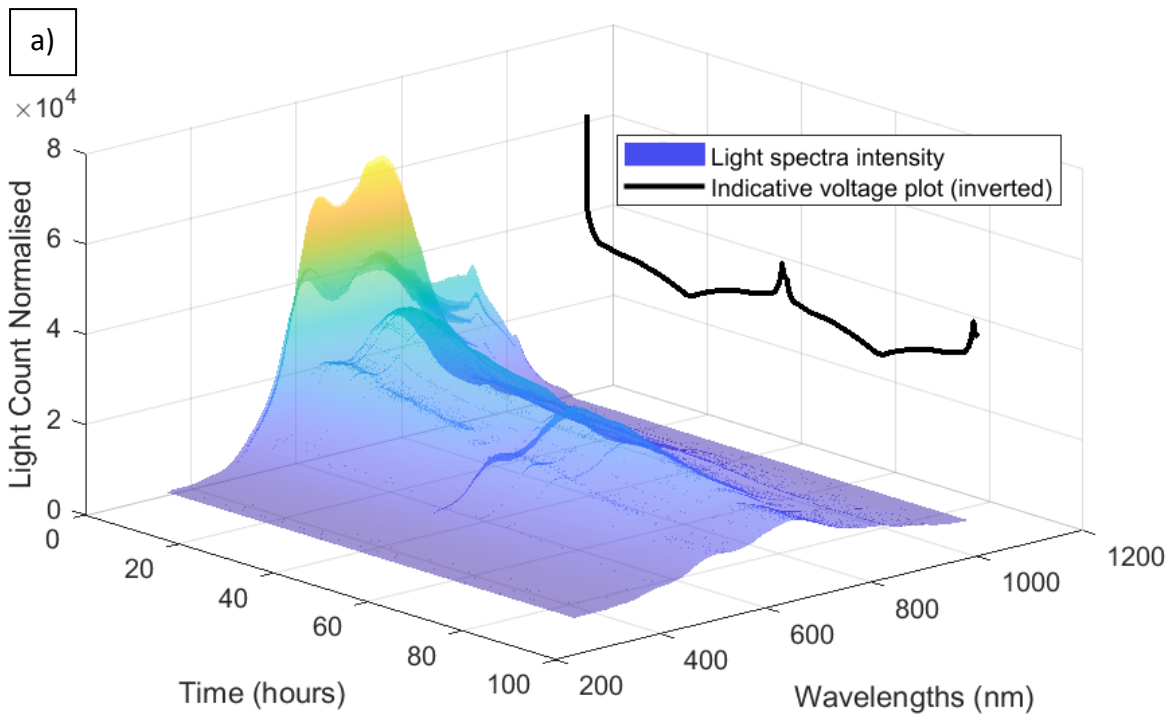


Figure 4-22- Formation cycle optical spectra data from fibres adjacent to a) anode and b) cathode

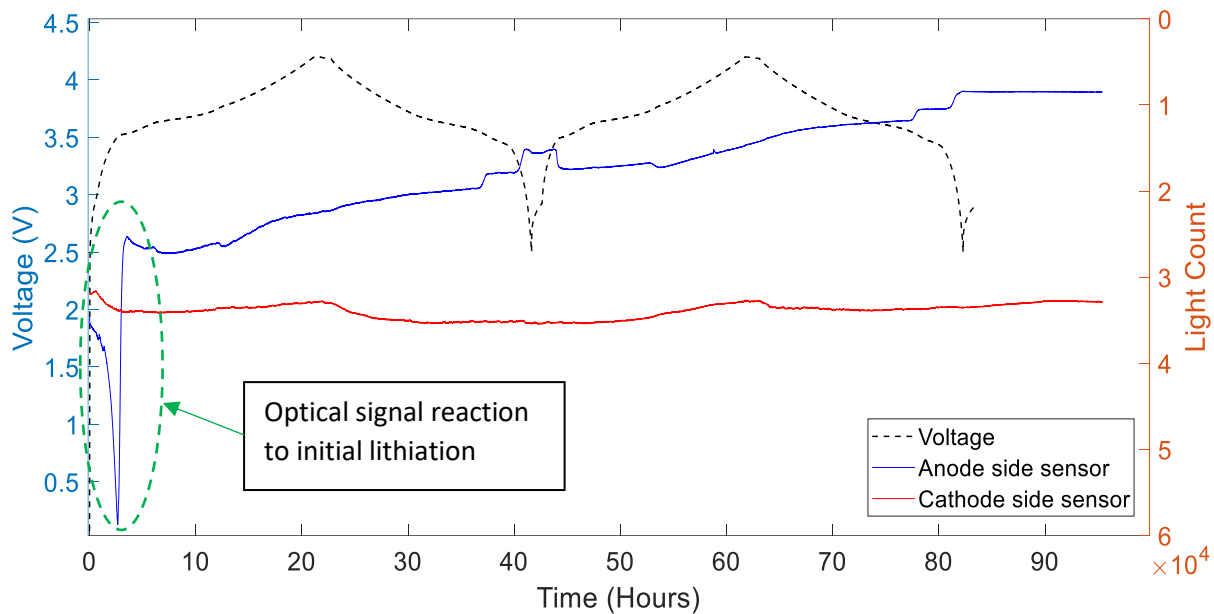


Figure 4-23- Formation cycle data with 725nm wavelength optical data from fibres adjacent to anode and cathode

There is a notable optical response upon the cell being charged to approximately 3.5V for the first time, this can be observed on both the anode and cathode side fibres but with a much greater response on the anode side. This is hypothesised as an optical response to initial lithiation of the cell and the beginning of SEI layer formation, the optical signal shows considerably greater light extinction on the anode side fibre than on the cathode side fibre over the two formation cycles. The optical signal demonstrates responsiveness to the cell charge and discharge but with limited correlation at this stage; as can be seen in Figure 4-24 the optical signal shows better correlation with cell state during cycling after the cell settles following formation and the first approximately five cycles.

Figure 4-24 demonstrates the correlation of the optical sensor signal with cell state, showing optical data from both the anode and cathode side fibres, in the first ten galvanostatic (C/5) cycles after cell formation. As noted the optical signal is more erratic in the in the initial few cycles, particularly on the anode side fibre, before settling into a more repeatable and steady correlation- the initial unsteadiness can be attributed to the initial lithiation of the cell and SEI layer formation. The profile of the anode signal is notably different in form and range from that of the cathode signal, with the anode signal more closely following the voltage profile and showing greater responsiveness. The sensor could measure Li-ion concentration change at the electrolyte- electrode boundaries, therefore the signal profile difference can be attributed to greater charge transfer and Li-ion intercalation resistance in the anode than the cathode, with Li-ion movement in the anode boundary layer being the rate determining step.

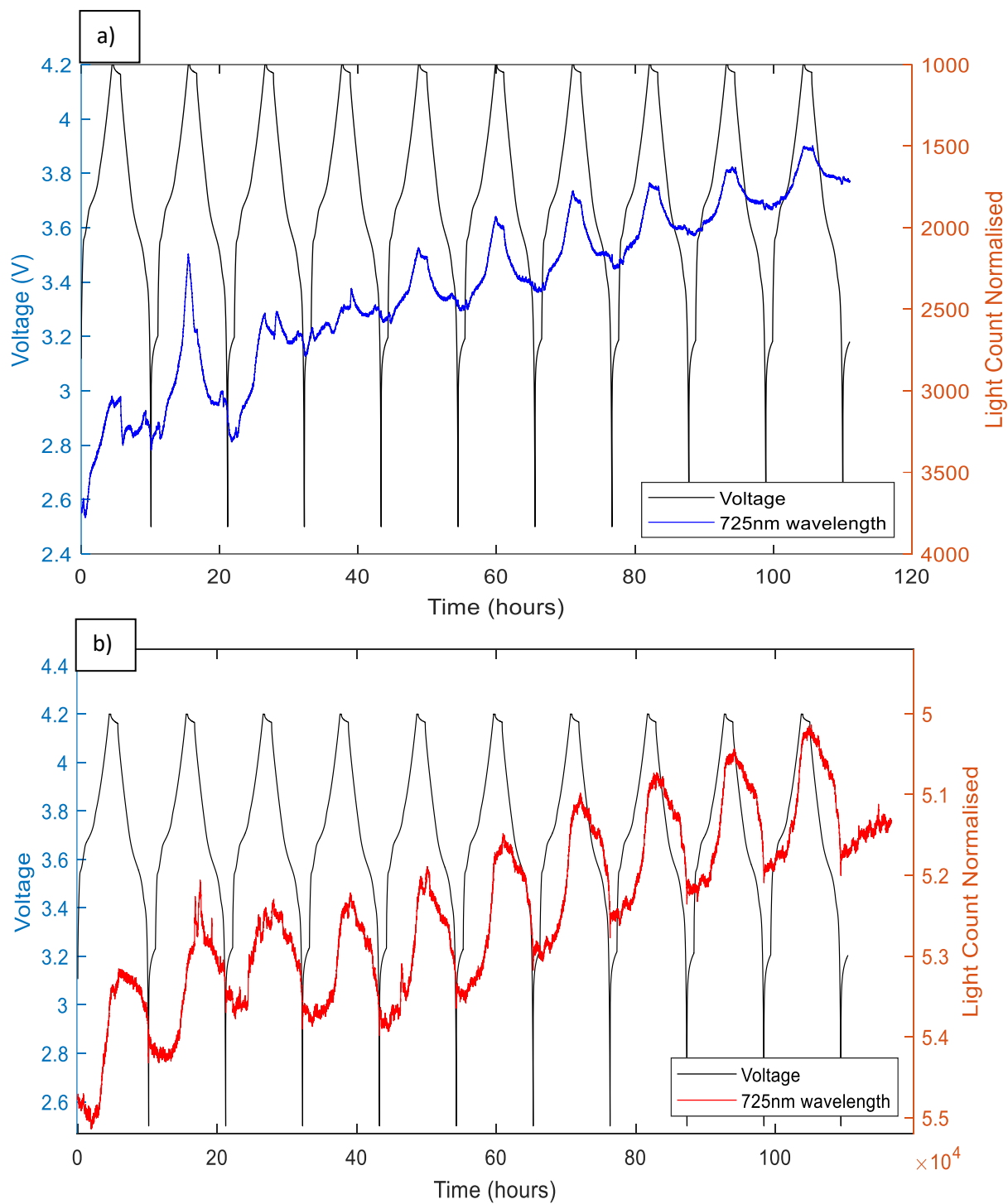


Figure 4-24- First 10 galvanostatic cycles (C/5) after formation cycles with 725nm optical signals from a sensor on a) the anode side and b) the cathode side of the cell

Focusing on the 6<sup>th</sup> and 7<sup>th</sup> cycles in which the optical signal shows a good correlation with cell state, the full spectra data is shown in Figure 4-25, which represents the comprehensive broadband optical

signal response over two cycles. The black line shows the indicative cell voltage (inverted), while the coloured spectrum contains the optical light intensity data between 400 and 1000nm wavelengths at 1nm increments. The correlation is most discernible in the 700nm wavelength region, while a small degree of correlation can be observed across the entire 400nm to 1000nm spectrum.

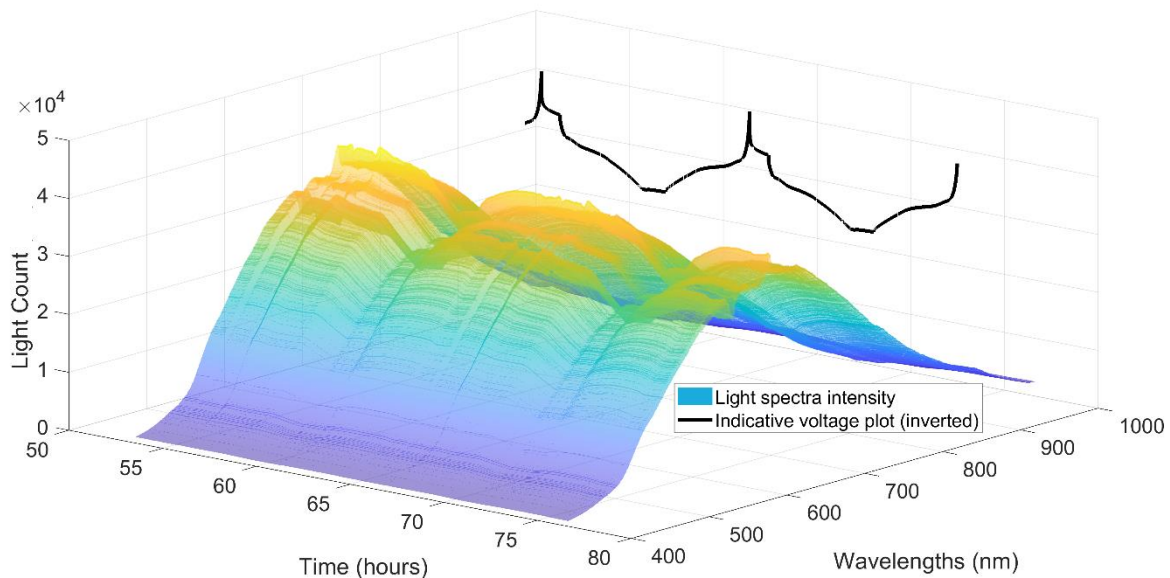


Figure 4-25- Optical spectra of fibre adjacent to anode during 6<sup>th</sup> and 7<sup>th</sup> galvanostatic cycles (C/5) of cell after formation, with indicative inverted voltage plot in background.

Focusing specifically on the 725nm wavelength noted earlier, the correlation between the optical signal and the measured cell voltage is displayed more clearly in Figure 4-26. This correlation is strongest for the parts of the cycle above a full cell voltage of approximately 3.6V, where the profile very clearly matches, while the profile correlates more loosely at the lower voltage regions of the cycle, irrespective of the Ohmic potential drop. Notably 3.5 to 3.6V is the voltage at which lithiation starts to occur in NMC versus graphite Li-ion batteries, which supports the hypothesis of the optical response related to anode lithiation. Figure 4-26 also displays the cathode and anode voltages respectively, obtained using the implanted reference electrode, allowing observation of the optical signal relative to the separate electrode voltage profiles. Whether the light signal correlation is stronger with the anode, cathode or full cell voltage is not immediately obvious visually, although it is noted that light intensity change is positively correlated with the anode voltage change but inversely correlated with the cathode and full cell voltage change.

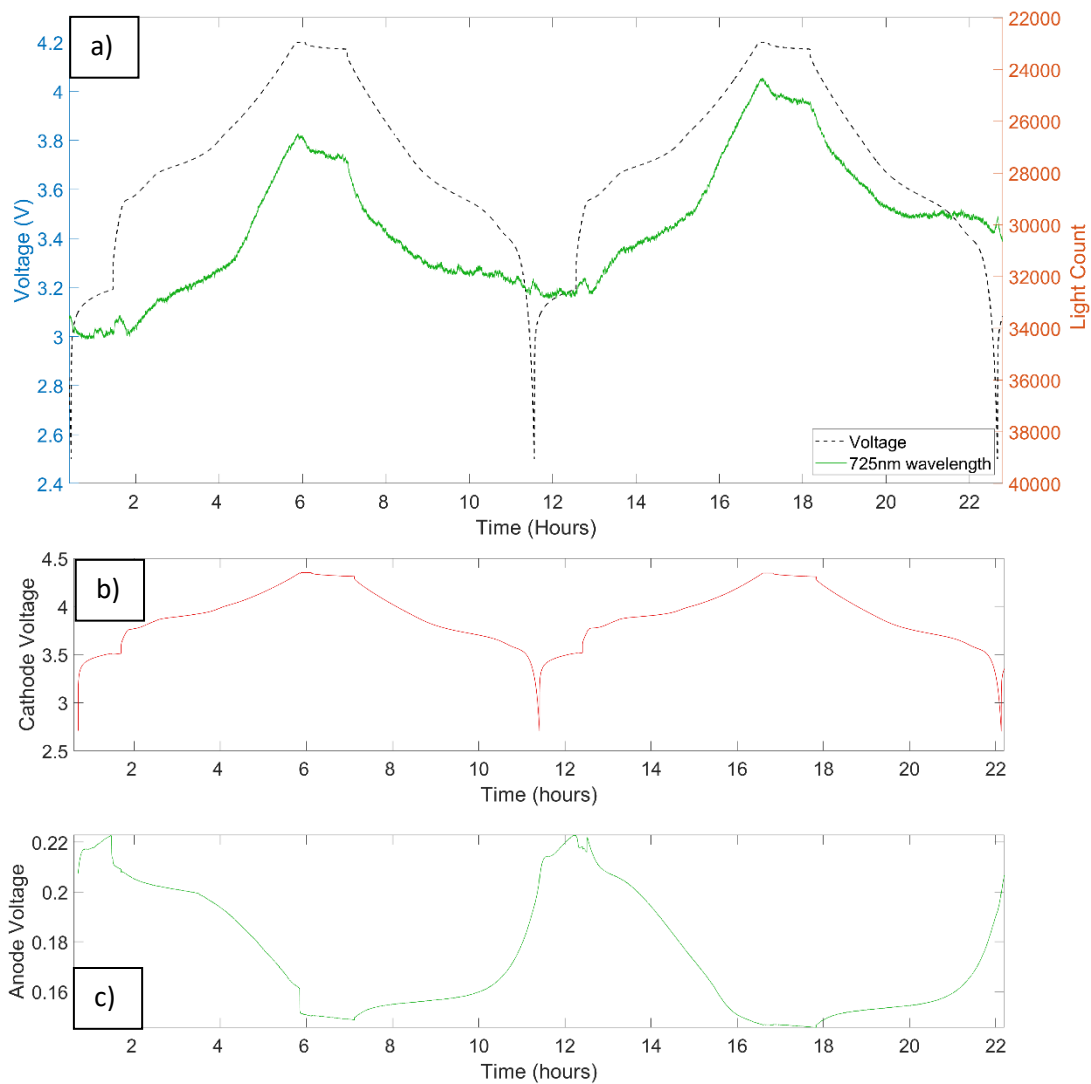


Figure 4-26- a) 725nm wavelength optical signal and voltage profile during 6<sup>th</sup> and 7<sup>th</sup> galvanostatic cycles (C/5) after formation, with corresponding electrode voltages at that stage of cycling for the b) cathode and c) anode

The mechanism by which the optical signal correlates to the cell voltage is hypothesized to be the sensor responding to the changing lithium concentrations at the surface of the anode, supported by the correlation of the impact on the optical sensor signal and the state of lithiation with increasing cell voltage / dropping anode voltage. The fact that there is a correlated response across the entire spectrum suggests that the optical sensor signal is also impacted by other measurands. Other variables that could impact the sensors include temperature, strain and pressure; another study has demonstrated that the sensor fibre signal is also sensitive to cell temperature and pressure [176]. The complete signal response can therefore be a combination of effects. Understanding the effects and mechanisms causing the correlation of battery state and optical signal and deconvolution of measurands will be the subject of further work to enable wider application.

The hypothesis that Li-ion concentration is being measured by the sensor via refractive index change has been put forward and is supported by findings in other studies. Plasmonic sensing has been used to measure the Li-ion concentration in electrolyte in an aqueous battery [162], it has also been demonstrated that attenuated total reflection can measure changes in Li-ion concentration in a liquid electrolyte in a lithium metal anode half cell [76]. Optical scattering microscopy carried out on a Li-ion NMC cell also allowed detection of the degree of lithiation during operando cycling; it was observed

that the local dielectric properties of the NMC particles, which could be observed through the measurement technique, were sensitive to and strongly dependant on the degree of lithiation of the particles [177]. Due to the close relationship between dielectric properties and refractive index this adds weight to the theory that the plasmonic based fibre optic sensors should be sensitive to Li-ion concentration change via the refractive index change. The 3D plot of the optical signal of the cathode side sensor 6<sup>th</sup> and 7<sup>th</sup> cycles is similarly shown in Figure 4-27, and focusing on the 725nm wavelength again allows the close correlation with cell state to be seen. As noted the profile and responsiveness of the signal differs on the cathode side of the cell when compared to the anode.

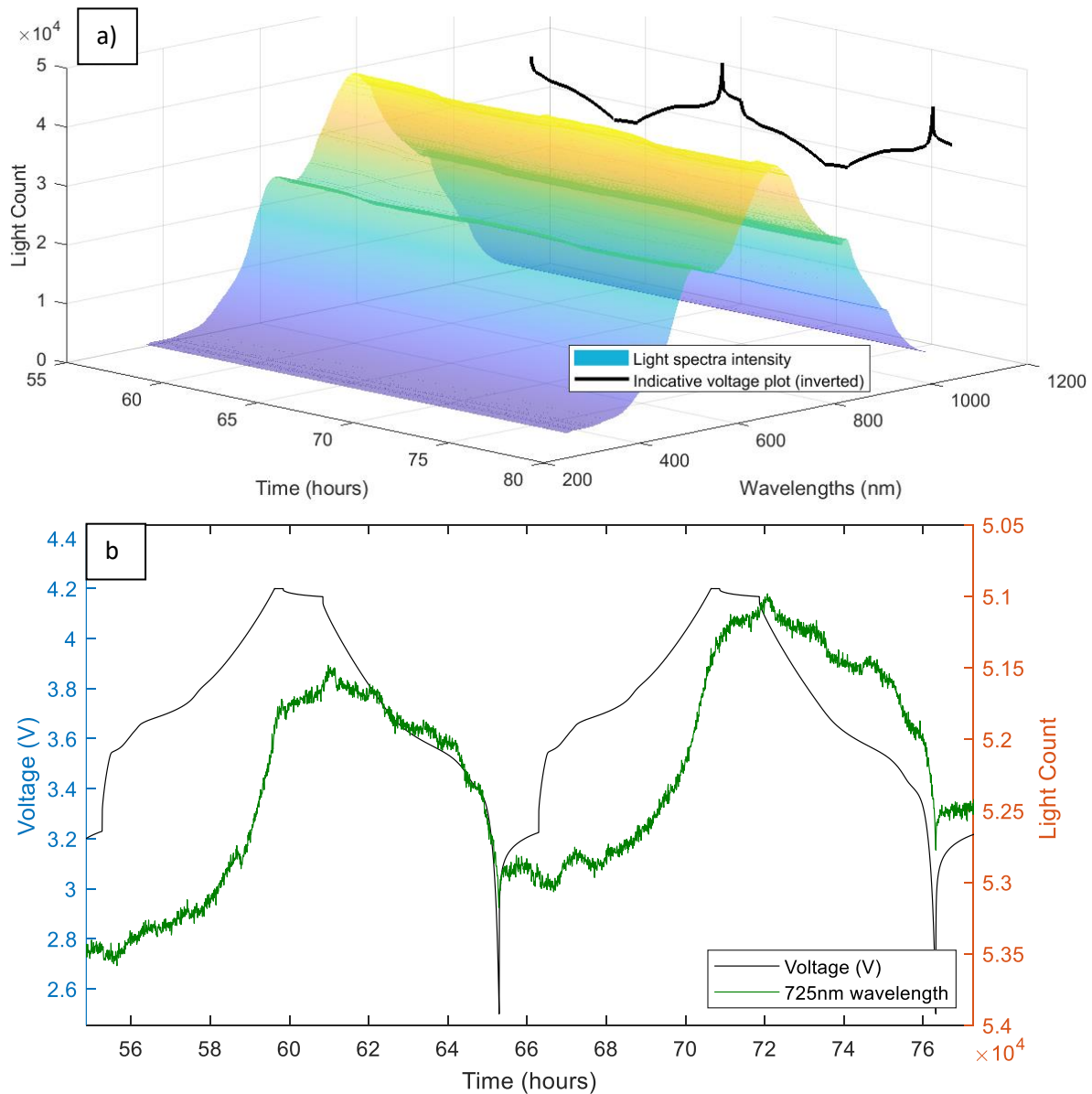


Figure 4-27- a) Optical signal light spectra for the 6<sup>th</sup> and 7<sup>th</sup> galvanostatic cycles (C/5) after formation, with the indicative inverted voltage profile in the background, and b) the same signals showing specifically the 725nm wavelength

#### 4.2.2. Fibre optic sensor performance over repeated cycling

As has been noted previously the cell seems unaffected by the presence of the fibre sensor, however Figure 4-28 illustrates that the fibre sensor signal deteriorates significantly as the cycling progresses, with light count dropping significantly over a number of cycles. The cell was subsequently cycled for a full 50 cycles, by the end of the which the light intensity declined asymptotically to 0. There is a slight discontinuity in the data caused by the fact that 50 cycles were carried out in three runs, first 16 cycles, then 12 more cycles, then a further 22 cycles. The light count has been normalised for the separate runs by dividing the light intensity by integration time in each case.

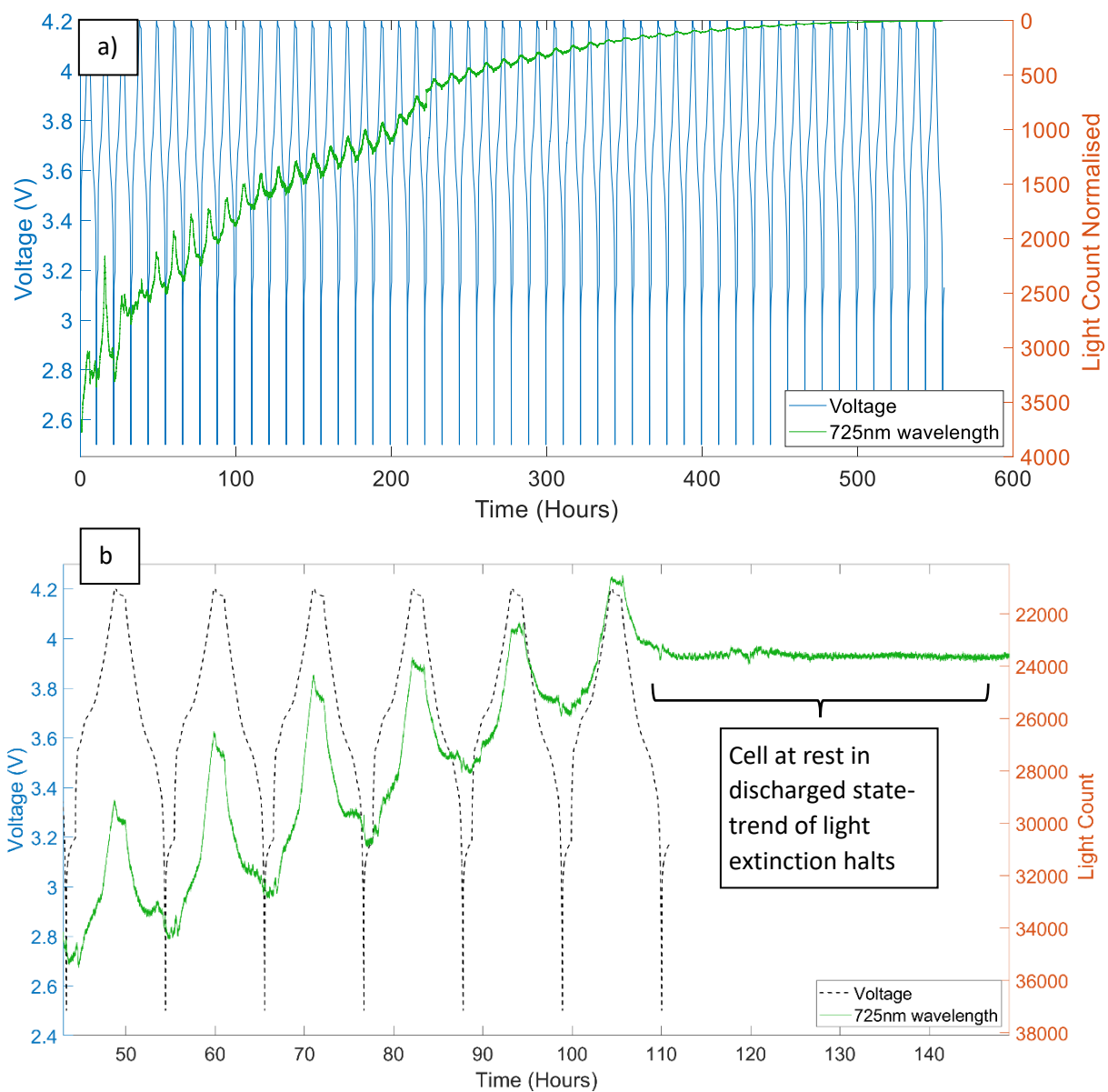


Figure 4-28- a) Light extinction of the fibre optic signal of the sensor adjacent to the anode over 50 cycles of galvanostatic cycling (C/5) and b) A section of that cycling showing the behaviour of the signal when the cell was at rest.

The trend of increasing light extinction as the cell cycling progresses can be due to factors such as chemical corrosion of the sensor, internal battery changes such as SEI layer growth on the anode and/or around the fibre, or even potentially penetration and alloying of the lithium ions with the gold. Notably it can be seen in Figure 4-30 that the light extinction is apparent while the cell is cycling but appears to stop when the cell is at rest after being discharged. This observation supports the hypothesis of electrode processes during cycling causing the signal loss; possible mechanisms include electrolyte decomposition and SEI growth around the sensor or lithium ion and gold alloying during cycling.

Figure 4-29 shows the anode sensor and cathode sensor optical signal strength at 725nm during cycling. Both signals demonstrate a qualitative correlation with cell voltage state during charge and discharge. Notable differences include the anode side optical signal more closely following the profile of the voltage, while also exhibiting greater light extinction over time. Greater anode side extinction could be explained by SEI layer growth or electrical contact between the sensor and anode causing lithiation of the gold at low voltages. The fact the sensor signal extinction is not as significant on the sensor on the cathode side indicates that the extinction is not just a consequence of sensor deterioration due to the corrosive environment in the cell.

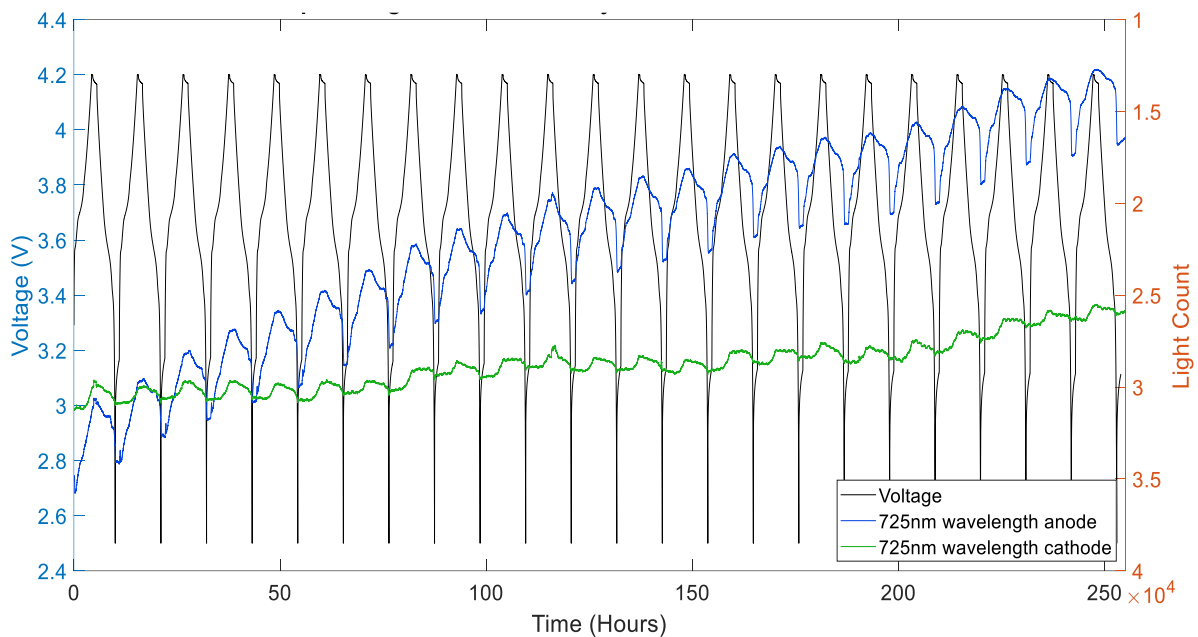


Figure 4-29-Optical signal strength at 725nm for optical fibres adjacent to an anode and cathode electrode during galvanostatic cycling (C/5)

Optical imaging was carried out to gain further insight into the sensor degradation, Figure 4-30 shows microscope images of the unused fibres, while Figure 4-31 shows SEM imaging of the same. This could then be compared to sensors removed from the cells initially cycled for 50 cycles. Visual and physical inspection of the fibre optic sensors on performing a cell teardown indicated that the sensors had become much more brittle in the sensing area, with delamination of the sensor coating occurring. SEM analysis of the sensor confirmed corrosion of the sensing region and delamination of the coating, exposing the silica fibre underneath, this can be seen in Figure 4-32. The delamination and corrosion is likely caused or at least exacerbated by the corrosive environment of the battery cell, including the presence of hydrofluoric acid which can be generated as an unwanted and corrosive product of parasitic reactions in the cell. This information was fed back to Insplorion AB who felt that a step in

the coating process during manufacture could be contributing to this, the company subsequently updated their manufacturing process and sent new versions of the sensors for testing.

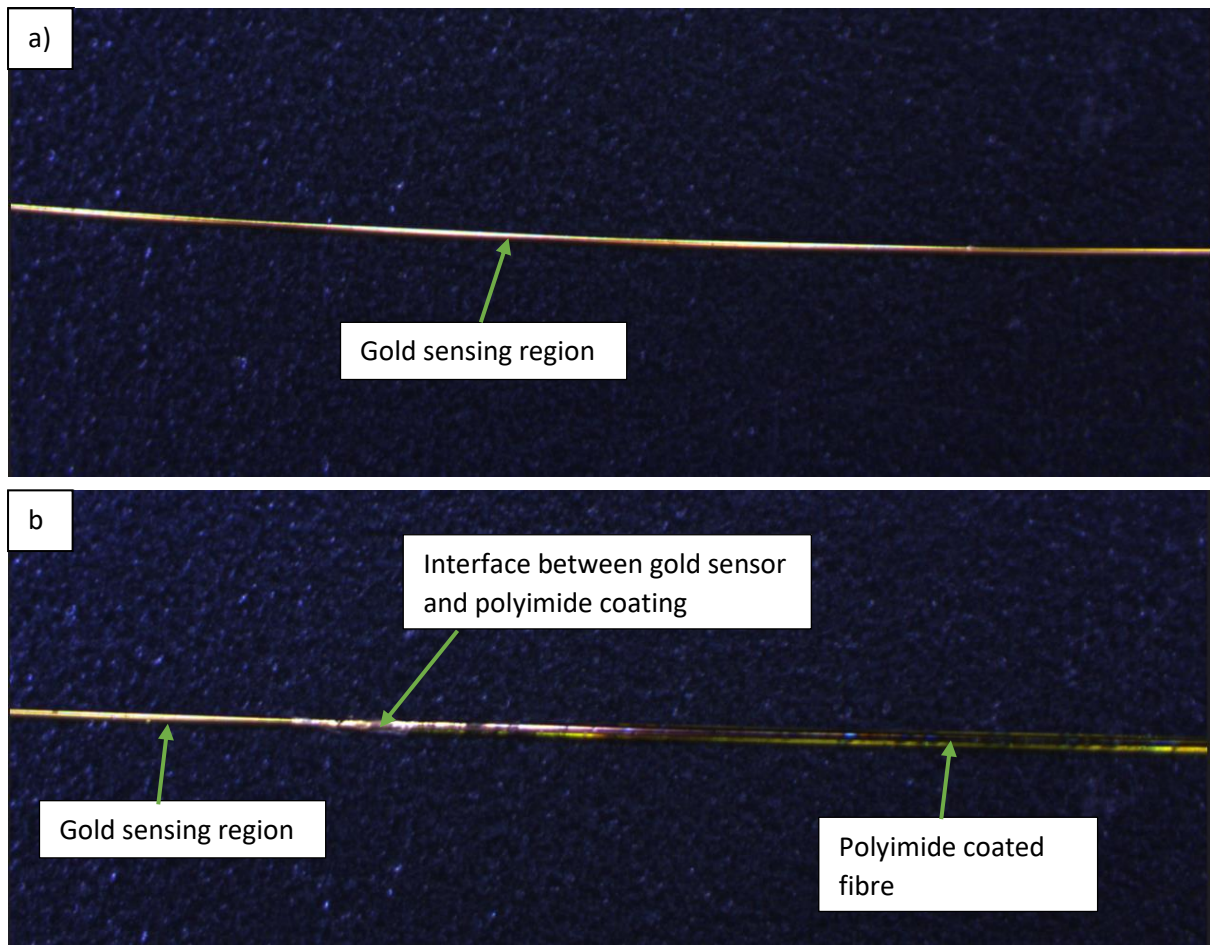


Figure 4-30- Microscope photographs of the a) middle and b) edge of the sensing region of an unused plasmonic based fibre optic sensor, at approximately 10x magnification.



Figure 4-31- SEM images of the sensing region of an unused plasmonic based fibre optic sensor, at magnifications of a) 66x, b) 170x and c) 381x.

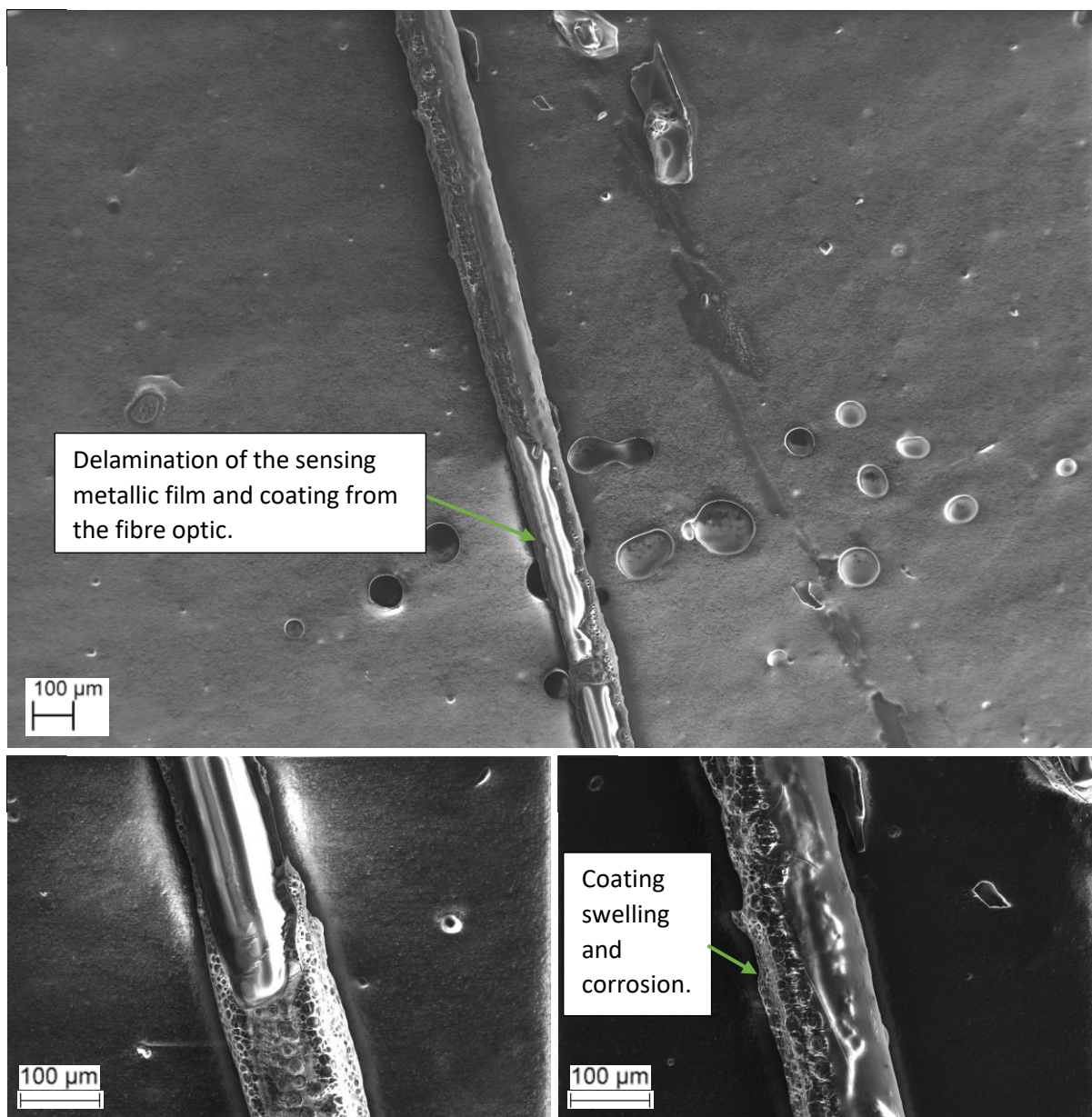


Figure 4-32- SEM images of sensing region of a sensor from the initial batch of sensors, after being adjacent to the anode of a cell galvanostatically cycled for 50 cycles, at a) 100x magnification and b) and c) at 400x magnification.

The new fibre optic sensor design was utilised in test groups 10 and 11, and the data indicates that the new method did improve the longevity of the sensors. The optical signal continued to be transmitted even after 300 charge and discharge cycles on the cells, before subsequently deteriorating. The condition of the anode and cathode side fibre optic sensors of a cell from test group 11, which had undergone 50 charge and discharge cycles including forced lithium plating attempts and still had a good optical signal, can be seen in the images in Figure 4-33. The sensors on both the cathode and anode side of the cell can be seen to still be in good condition, with possibly some signs of corrosion or deposits on the surface of the anode side fibre. A notable feature however is that while the cathode side fibre remained gold, the anode side fibre sensor had turned black- this could indicate that the low voltages on the anode side of the cell and insufficient insulation of the metal film led to the lithiation of the gold metal film.

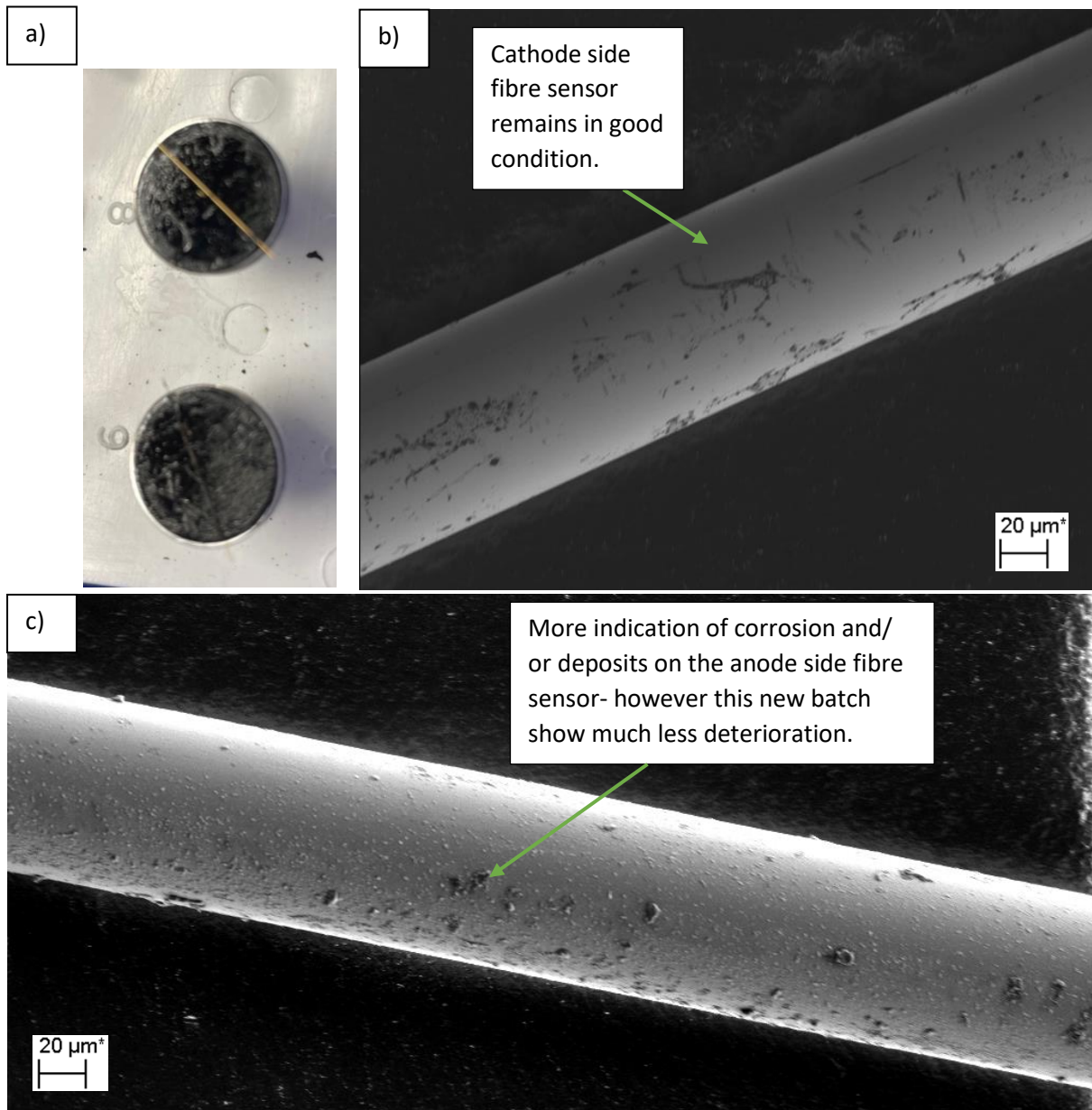


Figure 4-33- a) Photograph of used cathode side (top) and anode side (bottom) fibre sensors prepared for SEM analysis, b) SEM analysis of cathode side fibre sensing region at 582x magnification, c) SEM analysis of anode side fibre sensing region at 582x magnification

#### 4.2.3. Effect of temperature, pressure and impact on optical signal

As noted in Section 3.4.4 testing was carried out on the cells in test groups 10 and 11 to specifically identify the impact of temperature and pressure on the optical signal. The change in the optical signal was observed when the cells were heated and cooled in a steady discharged state, as well as being cycled at different temperatures. The results show that as the chamber is heated the optical light

count increases and conversely when the chamber is cooled the light count decreases. In the case of the reference fibre the optical response to the changing temperature is immediate but then proceeds at a steady rate, probably reflective of the fact that the air would take time to heat the fibre to the same temperature due to the low thermal conductivity. In the case of the fibre in the cell the optical signal is slower to respond to the temperature change but then responds more dramatically, with the light count increasing by 6% as opposed to 4% over the period, this can be explained by the cell taking time to heat up first, but then more rapidly heating the fibre up due to the greater thermal conductivity. Cycling of the cells at C/5 at different temperature provides similar findings in terms of higher light count at higher temperatures. Notably the profile of the optical signal is less well correlated to the cell state when cycling at the higher 35°C temperature, but the reason for this is not clear.

This data also shows us that while temperature has clear effect on the optical signal it is not dominant when the cell is being cycled, for example Section 4.1.2 shows that during C/5 cycling the temperature variation is just 1.5°C, which only equates to an approximately 0.5 to 1% change in the optical signal according to the below figures- however at higher C-rates the temperature effect would be more significant. With the cell at rest we can also see that the impact of the temperature change on the optical signal is similar for the fibre on both the anode and cathode side of the cells, this is expected as there is no electrochemical variation in this test. Another point which is also clear in these graphs is that the fibre optic signal response to temperature change takes a longer period of time to reach steady state than the thermocouple does, this can be attributed to the thermocouple being designed to be responsive to temperature, while the silica fibre optics have low thermal conductivity and take longer to heat.

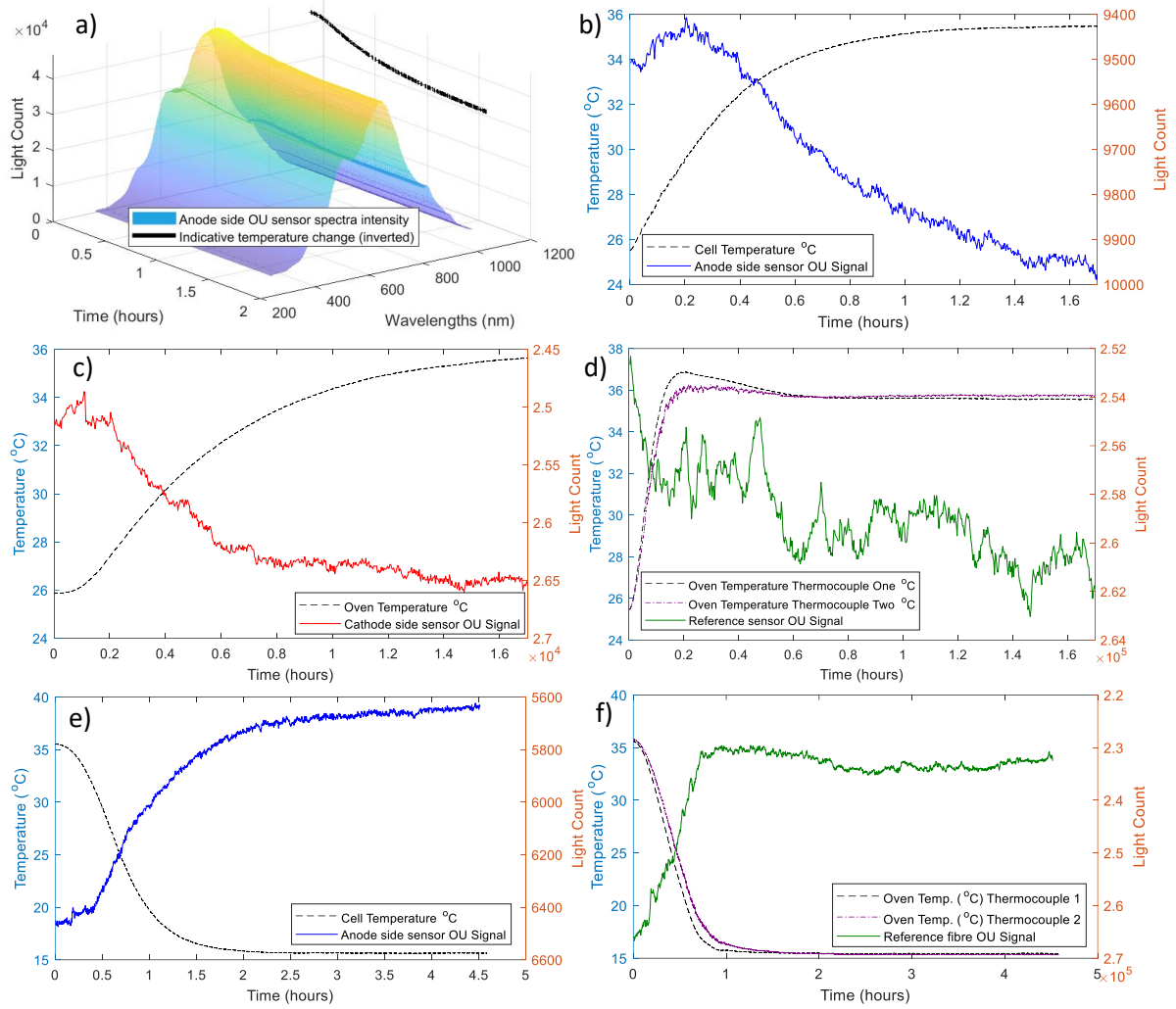


Figure 4-34- Response of optical fibre signals to temperature change while cell is at rest, a) anode side fibre optical spectrum with indicative inverted temperature change (from 25°C to 35°C), b) anode side fibre signal at 725nm wavelength during 25°C to 35°C temperature change, c) cathode side fibre signal at 725nm wavelength during 25°C to 35°C temperature change, d) optical signal of reference fibre in oven during 25°C to 35°C temperature change, e) anode side fibre signal at 725nm wavelength during 35°C to 15°C temperature change, f) cathode side fibre signal at 725nm wavelength during 35°C to 15°C temperature change

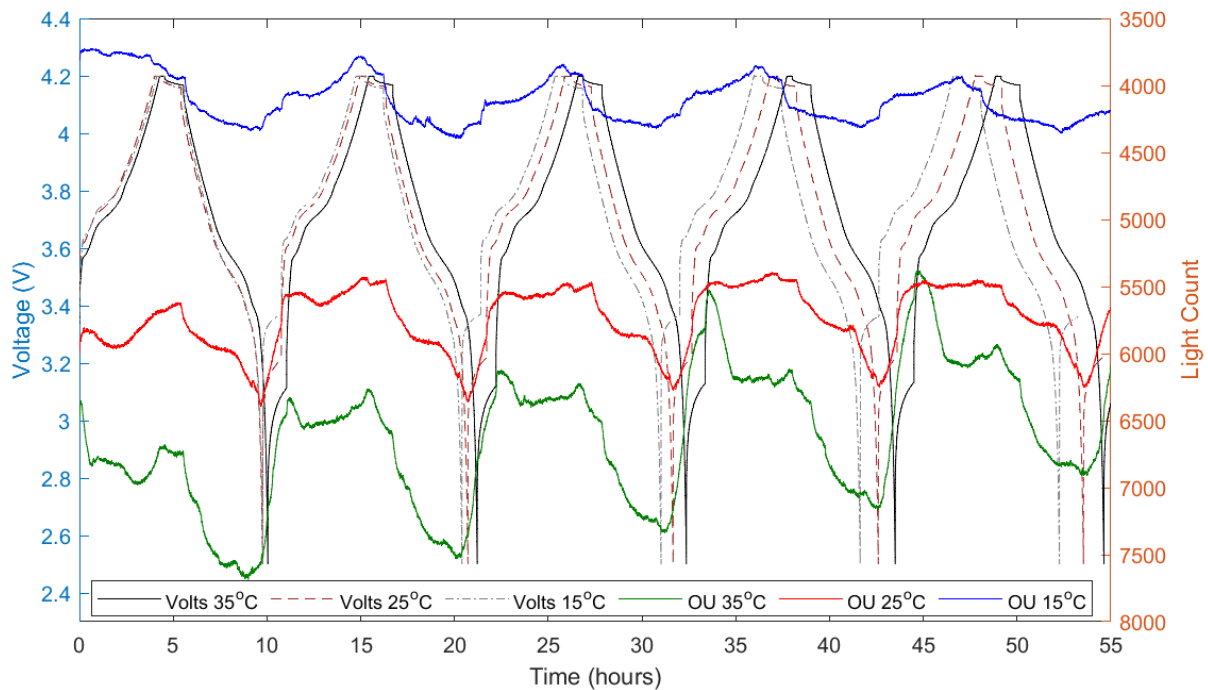


Figure 4-35- Cell cycled at C/5 at 3 different temperatures, with corresponding optical response

Also it is noted here that the fibre signal is highly sensitive to movement or impact that causes the fibre to flex or bend, as shown in Figure 4-36. The blip in the optical signal was caused when the oven door was opened and closed, causing a physical disturbance to the fibre optics, and smaller disturbances caused by environmental effects such as the convection of air in the chamber caused via the chamber fan could contribute to noise in the optical signal.

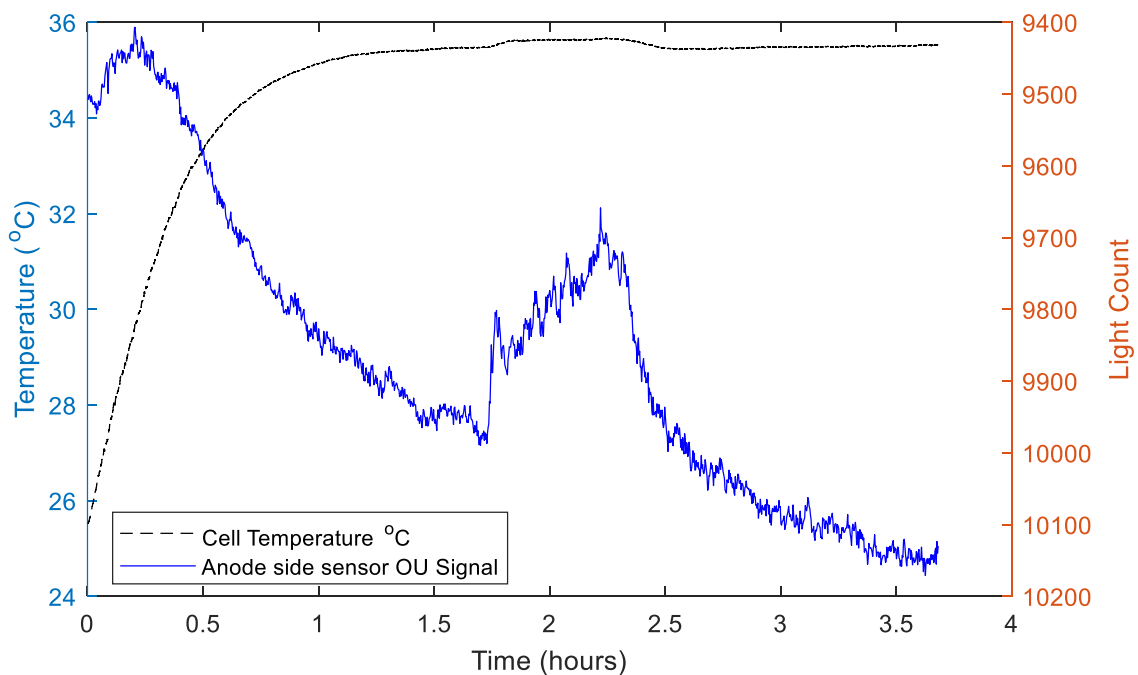


Figure 4-36- fibre optic 725nm wavelength signal change due to physical disturbance

As described in Section 3.4.4 weights were incrementally added to a cell at rest, that had previously been through formation and initial cycling, to observe the impact of the pressure on the optical signal. As can be seen in Figure 4-37 this has negligible impact on the optical signal outside of the typical noise seen for the signal, there are some larger spikes in the signal but due to their random and anomalous nature these are attributed to impact and bending of the fibres when adding and removing the weights. Additionally however it is noted that only up to approximately 3kPa of pressure was applied to the cell, while pressures of around 20kPa and higher have been reported in Li-ion based cells (while these had silicon-graphite anodes which should reach a higher pressure) [178]. Furthermore measurements of pressure in a Li-ion NMC vs graphite-silicon cylindrical cell [179] showed similar profiles in the pressure change during charge and discharge and the GITT tests as can be seen for the optical signal during those tests, in Sections 4.2.1 and 4.3.1 respectively. A significant

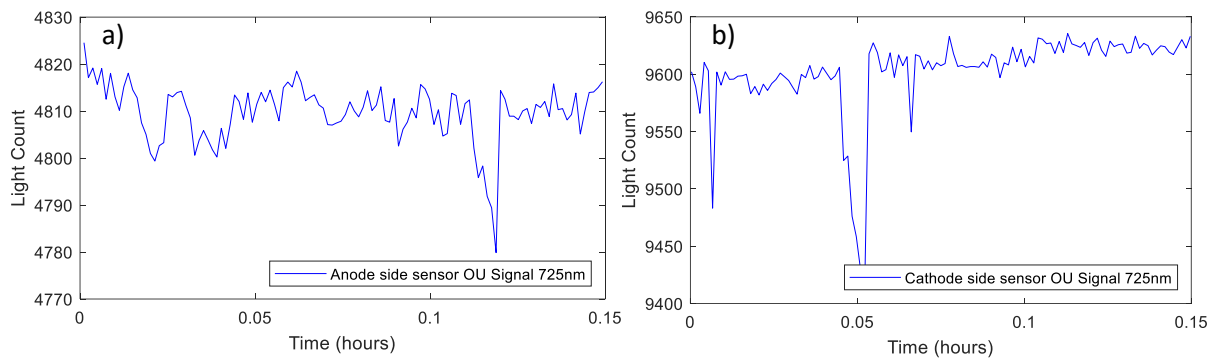


Figure 4-37- 725nm wavelength optical signal from a) anode side and b) cathode side of a cell during pressure testing

difference is in the IC analysis however, where the pressure changes seemed to be sensitive to anode phase transitions, while the optical signal in Section 4.3.2. indicates much greater sensitivity to the cathode phase transitions than the anode phase transitions. This could indicate that both signal are influenced by linked mechanisms, for example if the optical signal is sensitive to Li-ion concentration, this could also have a correlation to pressure as movement of Li-ions into the anode would cause expansion and a pressure increase. As such, while this test indicates the impact of pressure on the optical signal is minimal, further work should be done utilising a purpose built setup to test the impact of higher pressure conditions on the optical signal and to understand the relationship of pressure and the optical signal measurement, this recommendation is discussed in more detail in the further work Section 6.

### 4.3. Optical response to different cell phenomena and insight into underlying mechanisms

As described in Section 3.4.3 a number of specific testing techniques were employed to gain insight into the optical response to different cell phenomena and to gain insight into the working mechanisms behind the optical response. In the following section the results of these tests are displayed and discussed, including GITT testing, IC analysis, CV cycling and urban profile cycling.

### 4.3.1. GITT test

GITT cycling was used to observe the reaction of the signal to the voltage pulses, to further evaluate the correlation and relationship between cell state and optical signal and gain insight into the mechanisms behind this relationship. Figure 4-38 shows the optical signal response to the GITT testing at a range of different wavelengths. A Savitzky–Golay filter has been used to slightly smooth the signal and reduce noise. A correlation between voltage and optical signal can be observed, however this is ‘masked’ somewhat by the trend of increase in extinction over time for the sensors on the anode, particularly when the cell is at higher states of charge.

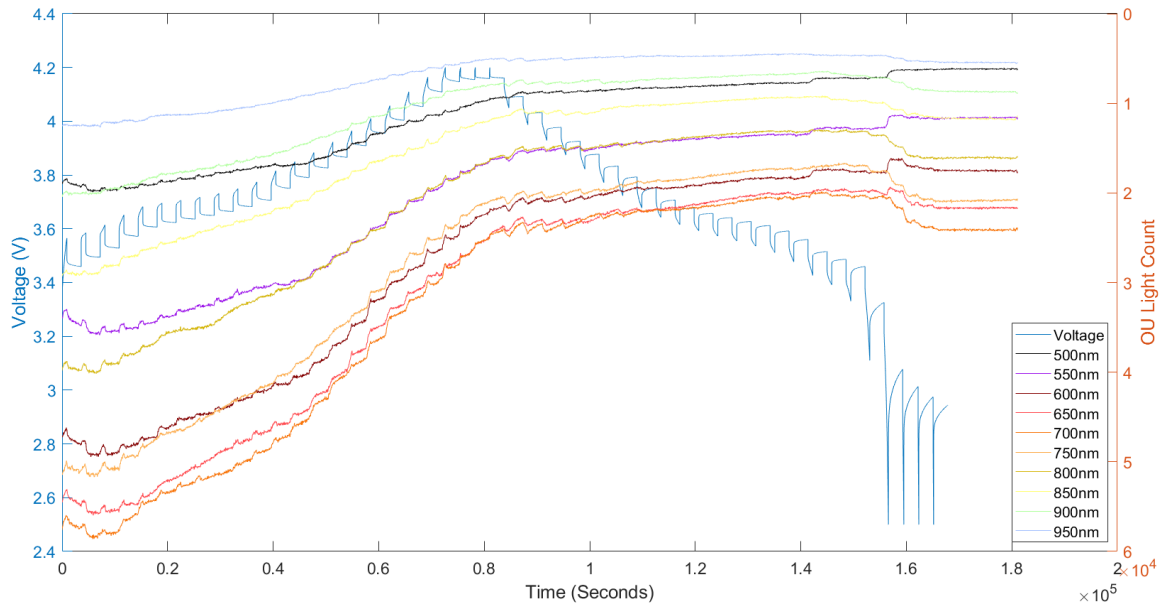


Figure 4-38- GITT testing time-voltage profile and optical response at different wavelengths

Focusing in specifically on some of the earlier GITT pulses and the 725nm wavelength which is considered to be the most responsive, Figure 4-39 shows the wavelength optical response over two pulses. Again the OU signal has been filtered with a Savitzky–Golay filter to reduce noise without distorting signal tendency.

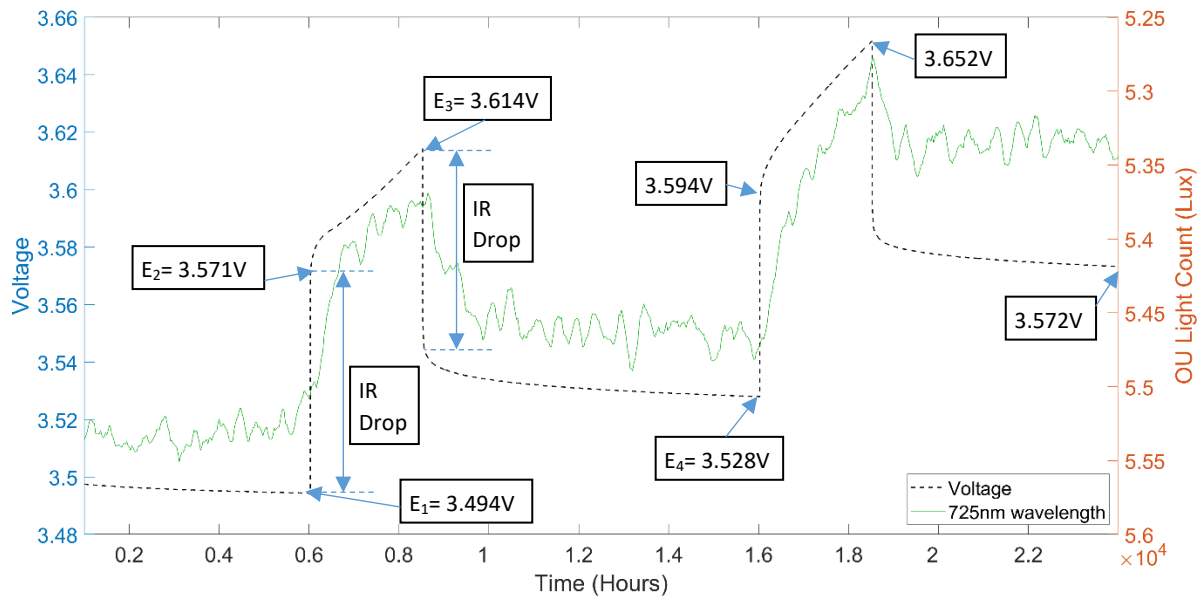


Figure 4-39- Cell voltage and OU response over two GITT cycles. The IR drop regions on the first GITT pulse are indicatively identified, along with the voltage values that can be used in diffusion coefficient calculations. The difference between the pulsed voltage and relaxed voltage is described as the overpotential and includes elements such as the electrical resistance IR drop, and kinetic steps such as adsorption, mass transfer and charge transfer [180].

The light extinction increases as voltage and charge increase, but does so with a steady and lagging response compared to the voltage increase. This indicates the signal does not directly correlate to the applied and measured cell voltage, and is more likely to correlate to a secondary effect of the applied voltage. Subsequently when the cell is at rest such that the charge is not increasing and the voltage relaxes as the lithium diffuses more equally into the anode, we see a relaxation in the optical signal with light extinction decreasing. This in turn demonstrates that the OU signal is not directly correlated to charge voltage and is potentially responding to secondary electro-chemical effects within the cell.

A potential mechanism that could explain this response is that the sensor is measuring or responding to lithium concentration at the surface of the anode. As the cell is charged the lithium concentration at the anode surface is increasing, while when the cell is relaxing at rest the lithium is diffusing around the anode and the concentration decreases at the surface. This supports the previous conclusion about lithium concentration at the anode surface being the primary measurand.

We can further estimate the lithium diffusion coefficient with the data provided in the GITT charging pulses. The diffusion coefficient can be found according to the relationship in Equation 9 if the current pulse time and voltage change are sufficiently small [180]:

$$D_{Li^+} = \frac{4}{\pi\tau} \left( \frac{m_B V_M}{M_B S} \right)^2 \left( \frac{\Delta E_S}{\Delta E_t} \right)^2 \quad \text{for } \left( t \ll \frac{L^2}{D} \right)$$

Where:

- $\tau$  = pulse duration (s)
- $m_B$  = host material mass (g)
- $V_M$  = molar volume ( $\text{cm}^3 \text{mol}^{-1}$ )
- $M_B$  = host material molecular weight ( $\text{gmol}^{-1}$ )
- $S$  = area of the electrode electrolyte interface ( $\text{cm}^2$ )

- $\Delta E_S = E_4 - E_1 =$  OCV steady state voltage change before and after pulse (values shown in Figure 4-39)
- $\Delta E_t = E_3 - E_2 =$  transient voltage change after initial IR increase when pulse is applied (values shown in Figure 4-39)
- $t =$  test time (s)
- $L =$  diffusion length (cm)
- $D =$  diffusion coefficient ( $\text{cm}^2\text{s}^{-1}$ )

*Equation 9- Diffusion coefficient calculation, simplified form when current pulse time and voltage change is sufficiently small.*

Equation 10 can be used to calculate electrode specific surface area if we make the approximation that the electrode particles are perfect spheres:

$$a = \frac{3\varepsilon}{r_s}$$

Where:

- $a =$  specific surface area ( $\text{m}^2/\text{m}^3 = \text{m}^{-1}$ )
- $\varepsilon =$  electrode porosity
- $r_s =$  mean particle radius (m)

*Equation 10- Electrode surface area assuming particles are perfect spheres.*

This component of Equation 10 ' $\frac{m_B V_M}{M_B S}$ ', is equivalent the volume of the host material divided by the surface area, which if we assume perfectly spherical particles can then be replaced with ' $\frac{r_s}{3}$ ' as per Equation 10. This leads to Equation 11, which allows the lithium-ion diffusion coefficient to be calculated from the GITT pulse data and the mean particle size radius value.

$$D_{Li^+} = \frac{4}{\pi\tau} \left(\frac{r_s}{3}\right)^2 \left(\frac{E_4 - E_1}{E_3 - E_2}\right)^2 \quad \text{for} \left(t \ll \frac{L^2}{D}\right)$$

*Equation 11- Diffusion coefficient calculation in terms of GITT pulse data and mean particle radius.*

The mean particle radius can be approximated at 4 micrometres, as per the SEM imaging in Figure 4-17. The value of  $\tau$  can be taken from Figure 4-39 as the length of time of the GITT pulse, which is 900 seconds. Taking the values for  $E_1$ ,  $E_2$ ,  $E_3$  and  $E_4$  from the data points on Figure 4-39, the diffusion coefficient values for the two pulses shown in Figure 4-39 are calculated as  $1.57 \times 10^{-15} \text{ m}^2\text{s}^{-1}$  and  $1.45 \times 10^{-15} \text{ m}^2\text{s}^{-1}$  respectively.

### 4.3.2. IC analysis and phase transitions

Incremental capacity analysis has been carried out on the prepared cells to identify phase transitions during charge and discharge, and to determine if the optical response is similarly able to detect the phase changes. Further to this IC analysis has been carried out on the three electrode cells prepared with lithium reference electrodes, to identify the phase changes on the anode and cathode electrodes separately. Full cell and individual electrode voltage profiles for a full charge and discharge cycle are shown in Figure 4-40. The associated IC plots are also shown, for which the total cell charge has been differentiated with respect to the respective voltages.

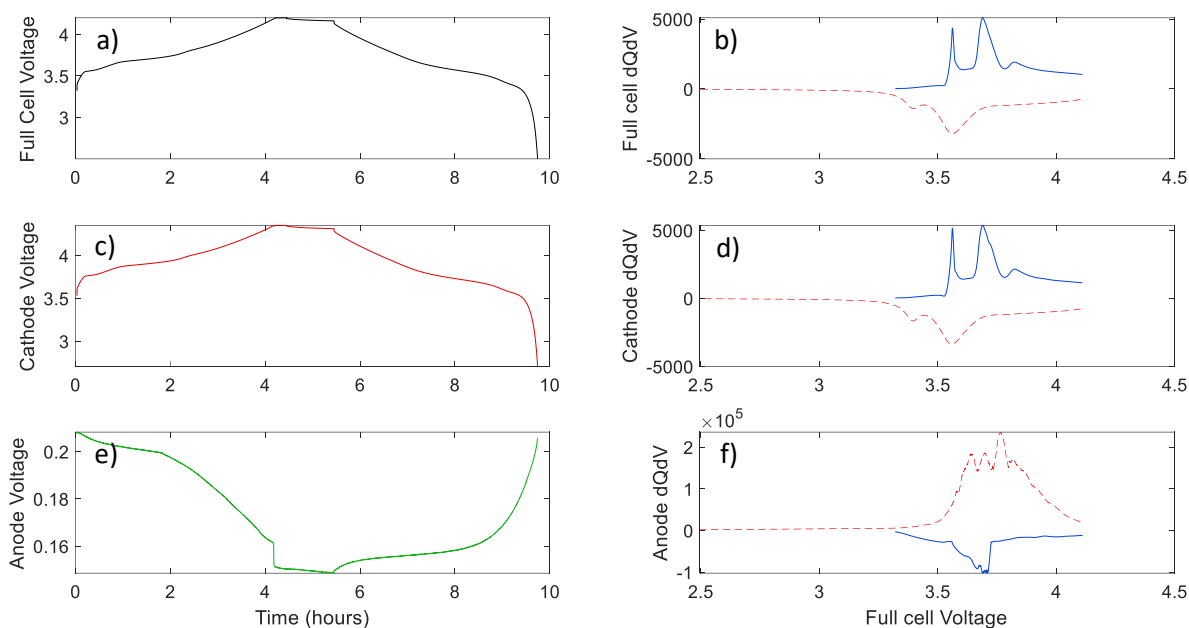


Figure 4-40- Time- Voltage (T-V) and IC plots (solid blue line is charge, dotted red line is discharge) on NMC111 cell with graphite anode and Lithium reference electrode cycles at 280mA (C/5); a) Full T-V plot, b) Full cell IC plot, c) Cathode Time-Voltage plot, d) Cathode IC Plot, e) Anode T-V Plot, f) Anode IC Plot

The full cell IC plot has two clear peaks on the charge and the discharge cycles, indicating two reversible phase transitions. This profile is closely matched by that of the cathode IC plot, indicating that the phase changes are being measured at the cathode and that the cathode is the dominant influencing electrode on overall cell voltage change during cycling. A third smaller peak can be seen on the charge cycle but not the discharge cycle, this suggests an irreversible process and has been attributed in other studies to SEI layer formation [181][182]. The cyclic voltammetry plots which are discussed further in Section 4.3.3 similarly indicates the presence of two peaks. Notably the peaks express a shift as compared to the IC plots. The greater polarisation can be explained by current reaching up to 480mA in the CV scan, higher than the cycles under constant current of 280mA (C/5) used for IC analysis.

Full cell IC plots obtained here match existing literature on cells with NMC111 cathodes and graphite electrodes, with the same distinctive double peak on the charge and discharge cycles [181][51]. The first peak is identified as the lithium intercalation into the graphite anode ( $C_6 \rightarrow LiC_x$ ) and the second peaks as the phase transition from a hexagonal to a monoclinic ( $H1 \rightarrow M$ ) lattice of the NMC [181][182][51]. The author notes however that use of the reference electrode identifies that both of these peaks are predominant on the cathode IC plot shown in Figure 4-40, this suggests either a cathode phase transition is taking place at both of these peaks or that it is a secondary effect being measured at the cathode.

Exploring this idea further, on NMC111 half cells with a lithium working and reference electrode there is only one clear peak instead of two [52,183,184], this supports the identification of the first peak as a graphite anode phase change. Nonetheless, while the double peak is not clear in those studies, the cyclic voltammetry plot in Figure 3b of Noh *et al.* [52] and diffusion coefficient during cycling plot in Figure 5 of Fröhlich *et al.* [183] do indicate a possibility of two peaks, with a smaller

initial first shoulder peak within a larger second peak. Further to this, first principle calculations of the expected charge compensation reactions are  $\text{Ni}^{2+}/\text{Ni}^{3+}$  and  $\text{Ni}^{3+}$  and  $\text{Ni}^{4+}$  as the lithium concentration on the cathode decreases during charging [49][48]. Experimentally Yoon *et al.* investigated NMC111 at different charge states utilising X-ray absorption spectroscopy (XAS), concluding that Ni ions at the surface are oxidized to  $\text{Ni}^{3+}$  during charge and Ni ions in the bulk are further oxidized to  $\text{Ni}^{4+}$  during charge [47]. The observation of the cathode IC in this paper coupled with the above discussed literature suggest that the two measured peaks could represent a two stage process of phase transition in the NMC through the  $\text{Ni}^{2+} \rightarrow \text{Ni}^{3+}$  and  $\text{Ni}^{3+} \rightarrow \text{Ni}^{4+}$  oxidation steps. Factors that could influence this process include rate of charge, material of counter electrode and particle size of the working electrode.

The anode IC plot demonstrates multiple small peaks within a larger peak, this suggests measurement of lithium intercalation stages in the graphite anode. There are seemingly four features, that is consistent with the literature in which there are the broader major  $\text{LiC}_{12}$  and  $\text{LiC}_6$  intercalation compounds during cell charge, and within those the dilute stage 1' and 4L to 2L group of phases, superseded by stages 3, 2 and 1, in an inhomogeneous process with overlapping stages. Studies have shown the graphite phase change process is not symmetrically reversible [54–59], which is also reflected in the asymmetric IC curves for the anode from charge to discharge in Figure 4-40 f).

Considering now the measured optical data, both the anode and cathode side sensors seem to respond in line with the two large full cell IC peaks, as shown in Figure 4-41 and Figure 4-42, an interesting finding for this diagnostic method. The optical signal recorded is the 725nm wavelength, previously identified as the most attuned to the analyte change of interest [185]. The reference cell data shown in Figure 4-40 d) indicates these are phase changes occurring across the cathode, an assumption that has some support in literature noted earlier but is not established. This suggests that optical sensors in this study are responding to the diffusion coefficient changes caused by the phase changes in the cathode.

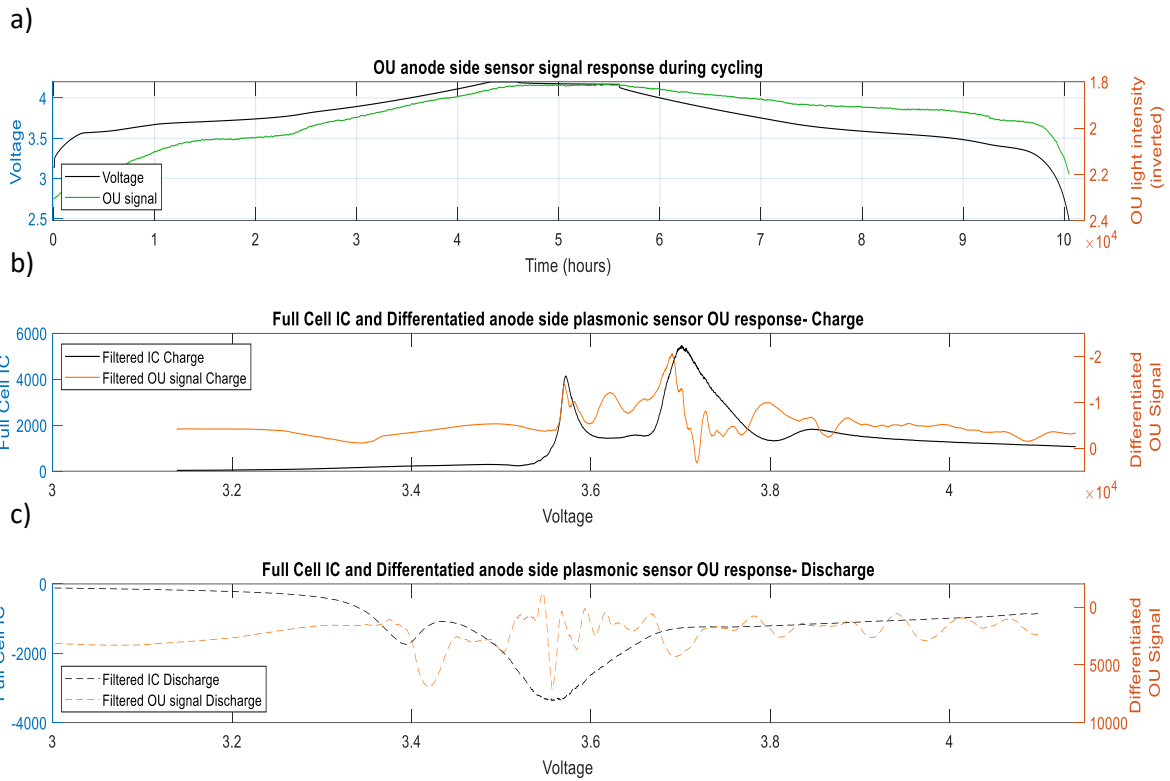


Figure 4-41- a) Cell voltage and anode side sensor optical response (lux) over time, b) Full cell IC plot and differentiated optical signal plot during charge, c) Full cell IC plot and differentiated optical signal plot during discharge

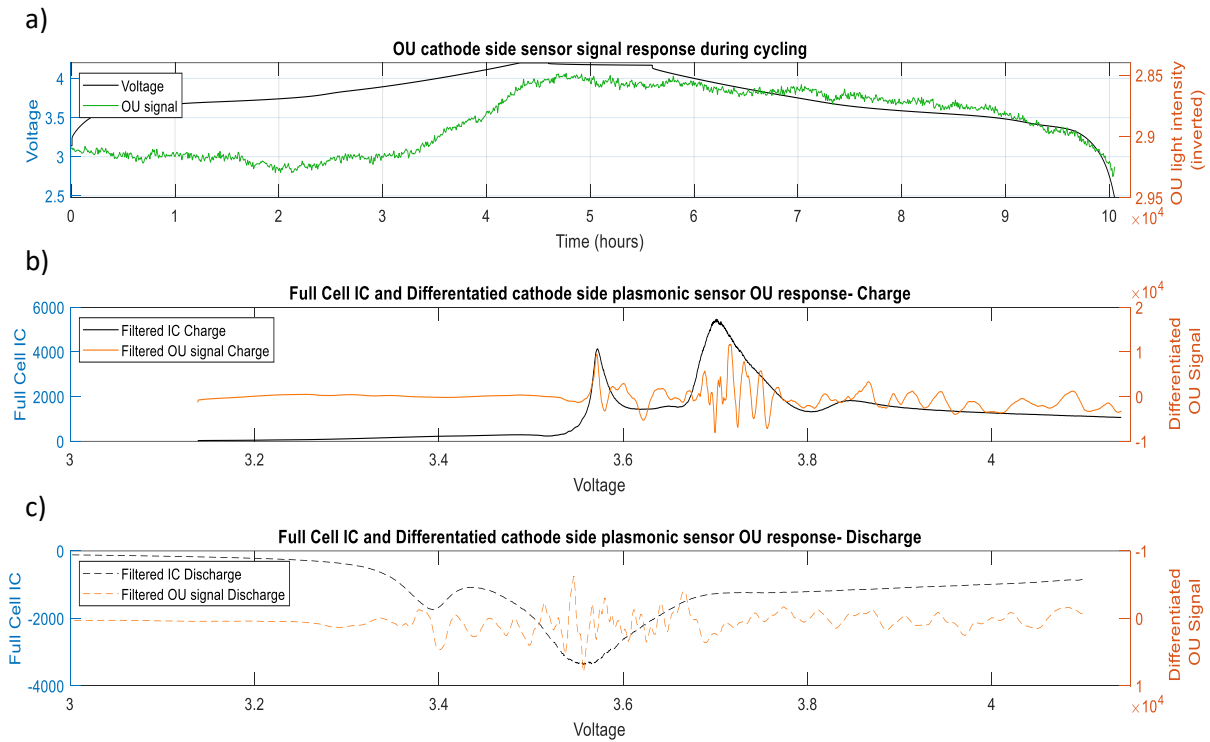


Figure 4-42- a) Cell Discharge and cathode side sensor optical response (lux) over time, b) Full cell IC plot and differentiated optical signal plot during charge, c) Full cell IC plot and differentiated optical signal plot during discharge

This IC analysis characteristics support the previously stated hypothesis that Li-ion concentration is being measured by the sensors in a number of ways. The fact the sensors adjacent to both anode and cathode respond most strongly to the full cell IC peaks suggest more sensitivity to a full cell characteristic such as diffusion coefficient rather than individual electrode behaviour such as electrode volume expansion. For example, anode expansion during charging has been measured at 6.1% by Stage 2 ( $\text{LiC}_{12}$ ) and 13.2% by stage 1 ( $\text{LiC}_6$ ) [59,60], while NMC111 cathode volume change during cycling is typically  $\sim 1\%$  [186]. As such, while the change in diffusion coefficient associated with a cathode phase transition could change the rate of expansion of the anode, the expansion caused by anode phase transitions should be more significant and therefore should be more strongly detected by the optical sensor were it a dominant measurand.

The relationship between cell charge and electrode expansion is well documented, explained by intercalation of lithium ions and corresponding changes in the electrode lattice structures [138]. Numerous fibre optic based sensor studies, utilising techniques such as FBG's [94,137,140,187] and Rayleigh Scattering [188] have demonstrated the relationship between cell cycling and strain. This likely plays a role in the plasmonic based sensor fibre readings as well, however due to the fibre not being mechanically adhered to the electrode, it is unlikely the sensor is responding to direct strain. It may be responding indirectly to electrode expansion, bending the sensor slightly or pressing the sensor more closely into the surface of the electrode. However it is noted that SEM images of the electrodes after cell cycling do not show obvious visual signs of electrode deformation due to pressure from the optical fibre [185]. Temperature effects should also be minimal, due to the slow rate of cycling and controlled chamber temperature.

In Figure 4-43 the optical data for the cycling is shown with lesser filtering, this makes the peaks associated with the full cell IC and cathode IC peaks less obvious, but demonstrates the volatility and other features of the signal. The volatility could be related to noise factors or micro-scale behaviour within the cell, but it's also possible the other smaller peaks could relate to the anode phase changes and a corresponding impact on Li-ion transport behaviour. Figure 4-43 also superimposes the optical signal on the anode IC information obtained from a reference electrode on an equivalent cycle, it is possible there is a correlation between the peaks but it is difficult to determine conclusively due to the noisy nature of the optical signal. The start of the cycle is also shown including the initial clear optical response to the start of the cycle after rest.

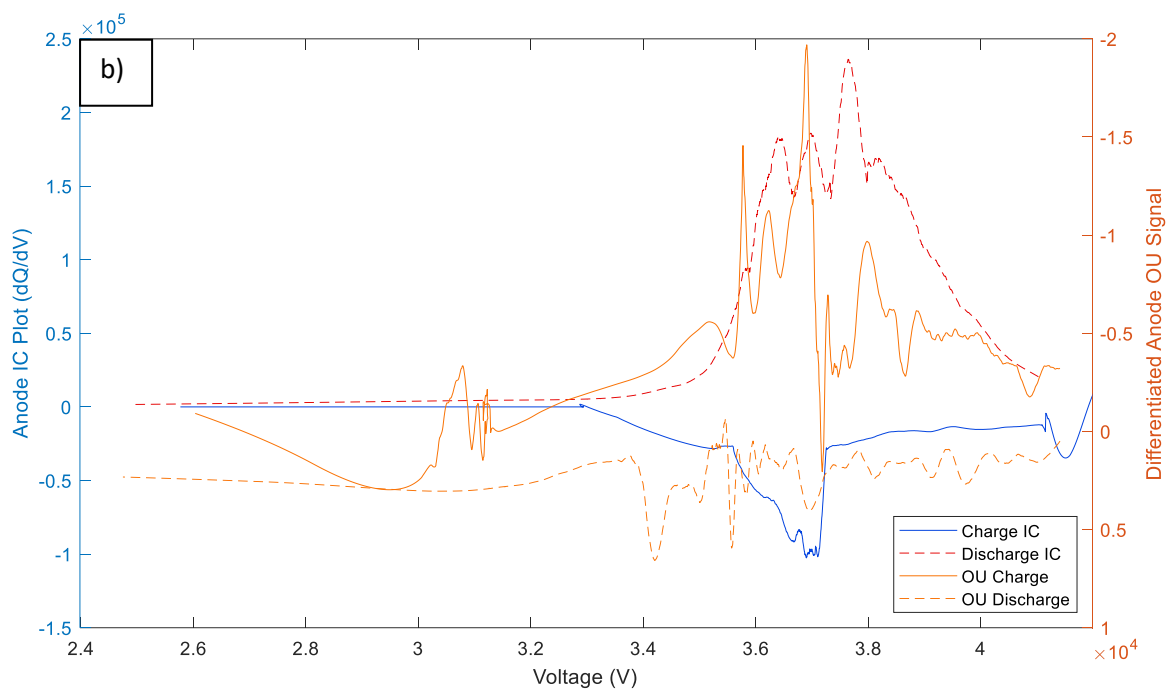
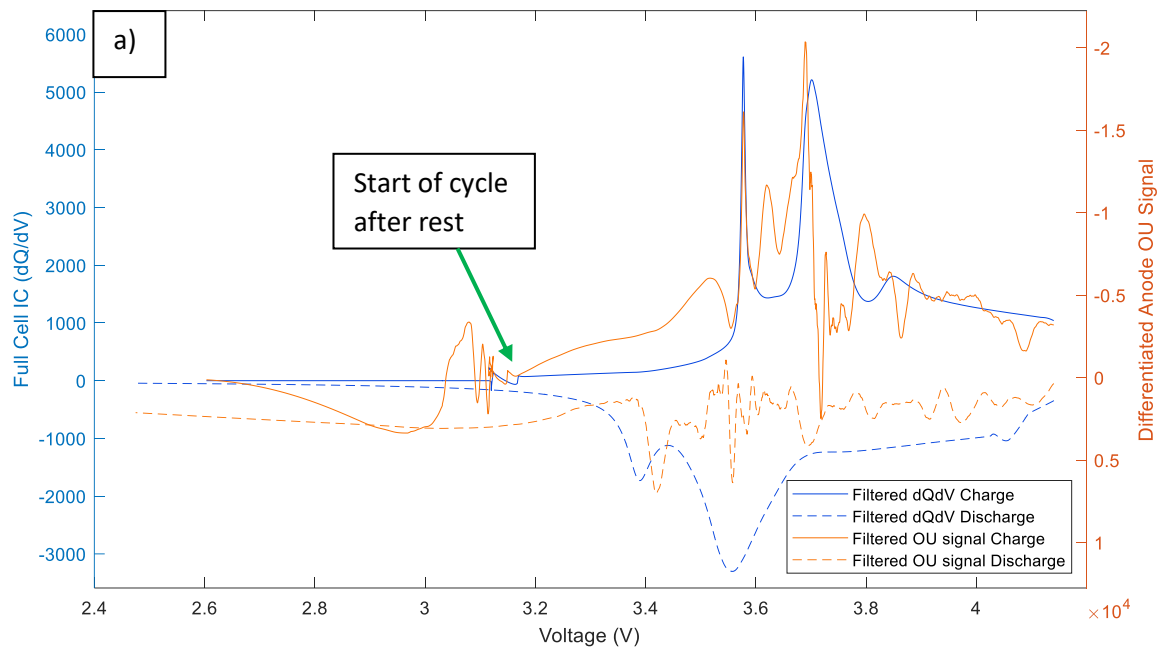


Figure 4-43- a) Anode side differentiated optical signal, with lesser filtering, and full cell IC plot, b) Anode side differentiated optical signal, with lesser filtering, and anode voltage data IC plot

### 4.3.3. Cyclic Voltammetry analysis

Cyclic voltammetry cycling was carried out on a number of cells, as set out in Section 3.4.3. This testing type allows observation of peaks in redox reactions that occur when the current is at its maximum, additionally the reaction rate up until redox peak is controlled by electrode kinetics (the speed at which

the redox reaction takes place at the surface), while diffusion mass transport is the limiting step after that [69]. Cell cycling was carried out at two different scan rates, 0.1mV/s initially and then a slower scan rate of 0.05mV/s, as shown in Figure 4-44. The faster scan rate indicates two redox peaks, which typically aligns with phase transitions, however the first peak is not well defined and so the slower scan rate of 0.05mV/s was used to increase the peak definition; slowing the scan rate decreases the concentration gradient between the electrode surface and electrolyte bulk resulting in a lower peak redox reaction rate and current. The presence of two peaks aligns with the IC analysis findings of two phase transitions set out in Section 4.3.2.

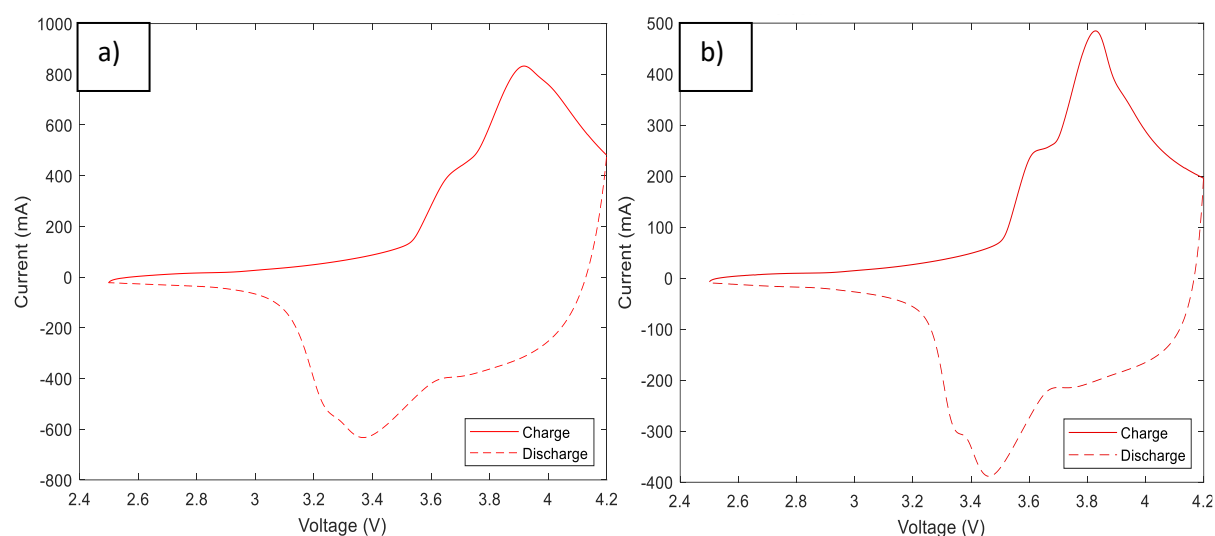


Figure 4-44- Cyclic voltammetry plots at scan rates of a) 0.1mV/s and b) 0.05mV/s

Comparing the optical signal with the CV plot can give further insight into the sensor capabilities and detection mechanisms, as can be seen in Figure 4-45. The anode side fibre CV plot displays a sensitivity to the redox peaks on the charge cycle, as corresponding peaks can be seen in the optical signal. On the discharge cycle the redox peaks cannot be clearly identified, but there is a notable change in gradient after a certain point in the cycle. The identification of the redox peaks in the optical signal on the charge cycle could be due to the peaks corresponding to phase changes which correspond a lithium transport rate change, influencing the lithium concentration at the anode surface while the cell is in the diffusion mass transport limited stage. In the case of the discharge cycle the redox peaks are not clearly detected, which could be due to the lithium-ion being able to intercalate back into the NMC cathode more easily and not cause the same Li-ion concentration changes caused by the rate limiting step of intercalation into the anode. A change in gradient of the optical signal can be observed after the redox peaks on the charge and discharge cycles, this can indicate a change in the rate of Li-ion concentration change when the reaction changes between being charge transfer limited and diffusion mass transport limited.

The optical signal of the cathode side sensor displays much less sensitivity to the CV cycling with a smaller range of light intensity change, thereby also attenuating the signal noise; the sensitivity to the redox peaks is also reduced while there is a clear signal gradient change following the second redox peak on the charge cycle and a possible but lesser response on the discharge cycle. The lesser response on the cathode side can be explained by a lesser refractive index change in the NMC material and lesser build up of Li-ions at the cathode surface due to Li-ions de/intercalating more easily in the metal oxide than the graphite anode. Similarly the greater response to the redox peak on the charge cycle,

as the reaction moves from being charge transport limited to mass diffusion transport limited, can be explained by the charge transport step be more limiting at the anode than the cathode (ie. the cell discharges more easily than it charges). There are also two anomalous spikes on the 1<sup>st</sup> discharge cycle cathode signal that could be attributed to a physical disturbance or micro-event in the cell.

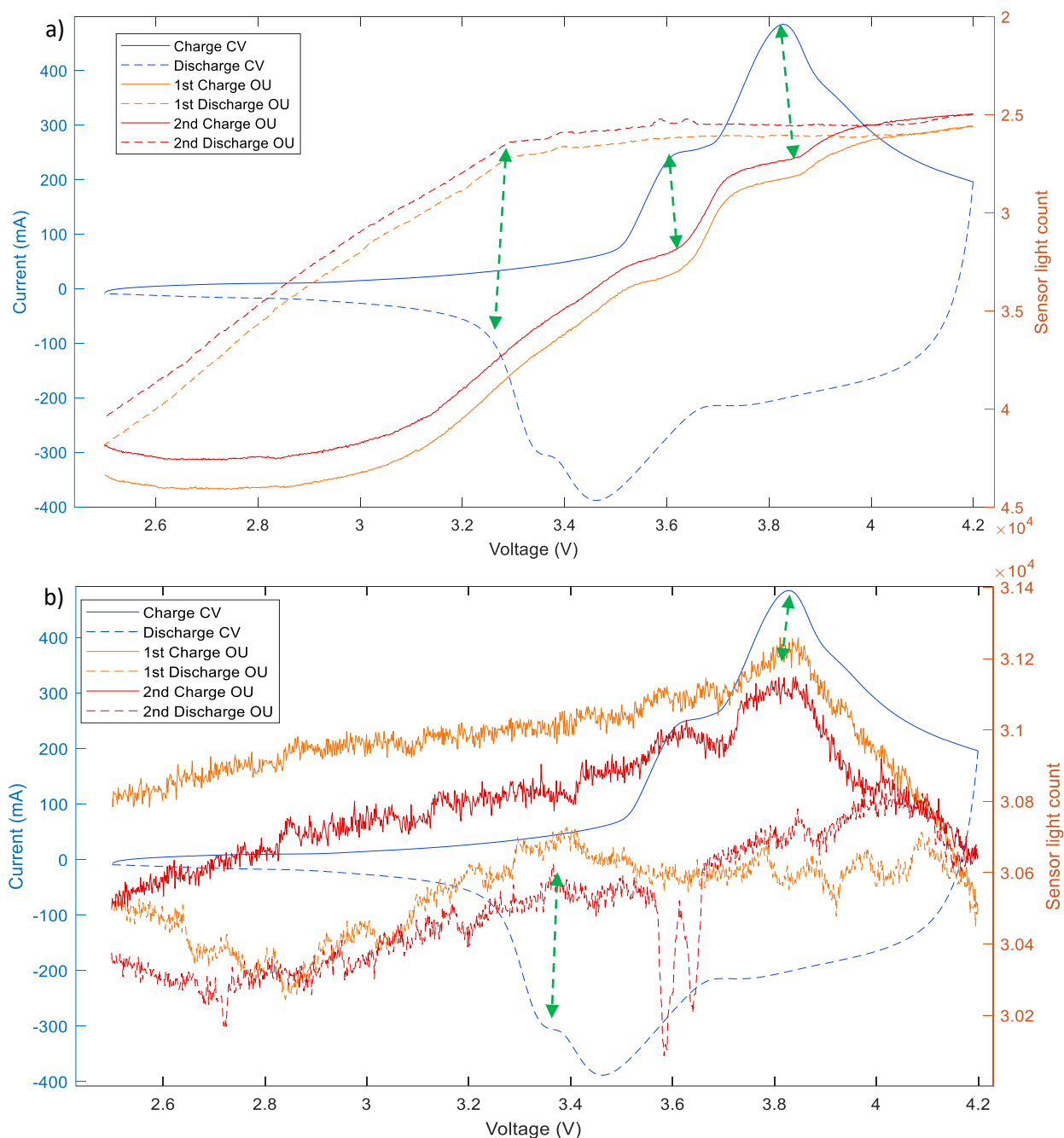


Figure 4-45- Voltage-current cyclic voltammetry plots for a cell with two fibre optic sensors, one adjacent to an anode and one adjacent to a cathode, at a scan rate of  $0.05\text{mVs}^{-1}$ . On both graphs only one voltage-current cycle is shown representatively, while a) includes the optical response of optical sensor adjacent to the anode over two CV cycles and b) includes the optical response of optical sensor adjacent to the cathode over two CV cycles. Here we can see how the optical signal follows the cycle profile including the redox peak. The green dashed arrows show apparently corresponding inflections between the CV cycling profile and optical signal, including redox peaks. The green dashed circle shows an apparently anomalous response, possibly due to a disturbance of the system.

#### 4.3.4. Urban Profile cycling

Varied charge profiles and urban cycling discharge profiles were utilised to gain further understanding of how the optical signal responds to the cells state in more varying scenarios simulating real world conditions. Figure 4-46 shows the 3 cycles of staggered charge followed by urban profile cycle discharge, with a zoomed in section of the urban profile cycle discharge part of the second cycle. The profile of the staggered charge cell voltage and optical signal seems to correlate well after an initial adjustment at the start of the cycling. However, the optical signal of the urban profile part of the cycle doesn't seem to effectively relate to the minute cell discharge rate changes, as the variations are too small to be picked up outside the normal volatility/ noise range of the optical signal

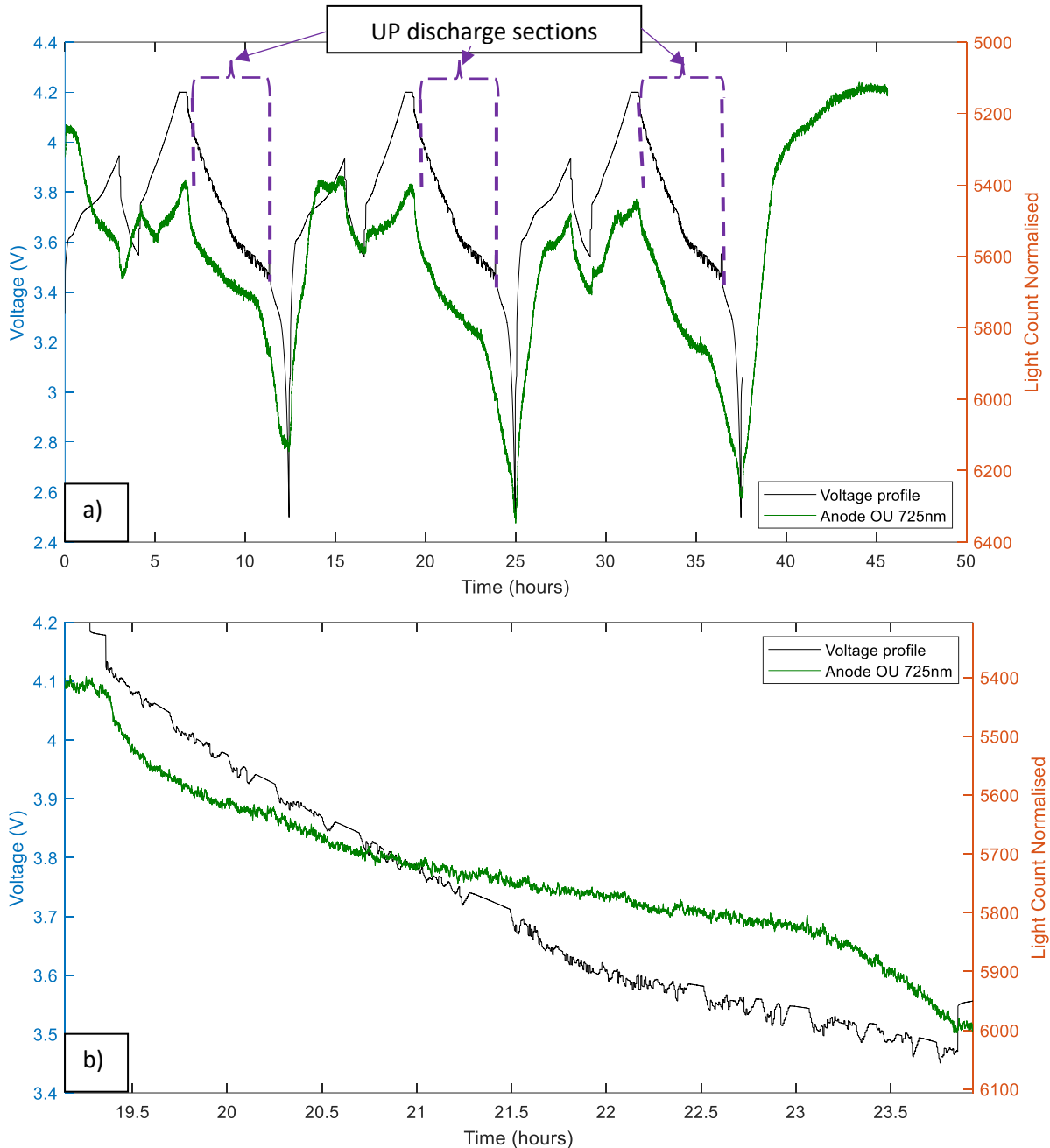


Figure 4-46- a) Three cycles of partial charge and discharge with discharge according to UP cycling, anode side sensor optical signal and cell voltage, b) Zoomed in focus on urban profile discharge section of 2<sup>nd</sup> cycle.

Figure 4-47 focuses on just the urban profile region of the second cycle discharge, looking instead at the optical signal alongside the cell SOC. As noted it is clear again that the step changes in the urban profile cycle are too small to be able to see a reaction in the optical signal outside of the range of the noise/ volatility of the signal. However it is also worth noting that the rate of SOC changes during UP cycling discharge are marginal and difficult to distinguish from the overall trend, as such a high resolution would be required to detect the adjustments, and the optical signal does still capture the overall trend.

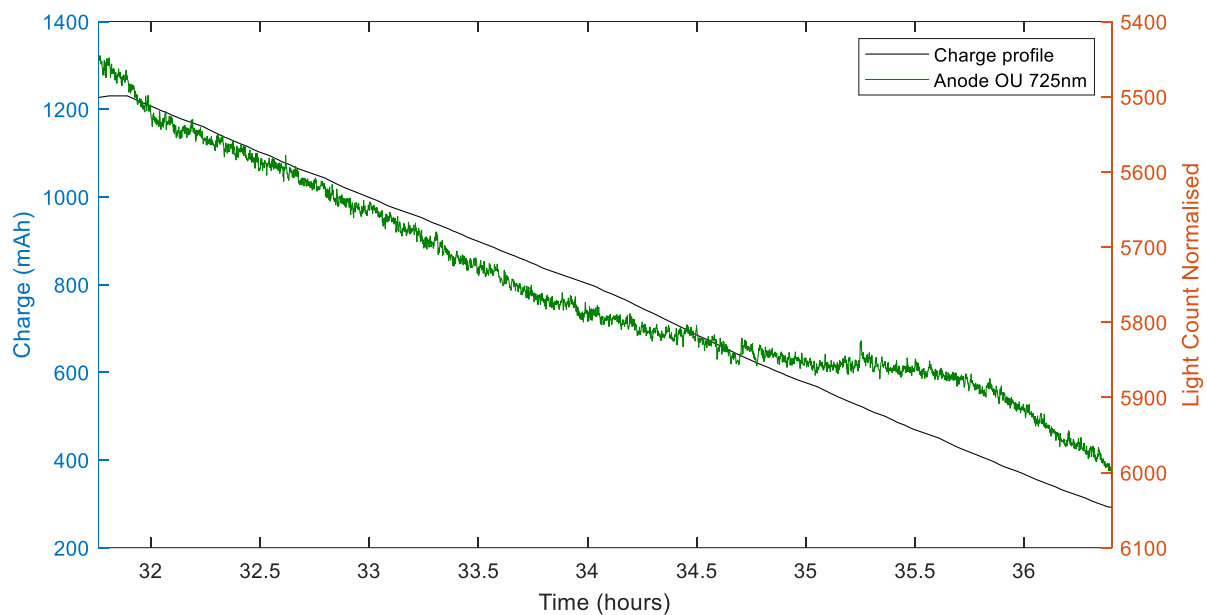


Figure 4-47- Figure of optical signal and cell SOC during urban profile cycling discharge

This testing shows use that the optical sensor indicates correlation to varied charging cycles, and as such has potential as an SOC measurement tool based on the extraction of internal cell data. The limitations of this setup are shown by the inability to distinguish the much smaller change in discharge rates in observed in the urban profile discharge simulation cycle. Nonetheless correlation to overall trend can be observed in both cases, and both improved physical setup and signal processing could increase the resolution of the optical signal. For example, the fibres are currently loose inside the chamber, and as such could be oscillated by the fan in the chamber circulating the air leading to perturbations in the optical signal- more rigidly fixed fibre could address this. Other elements of micro oscillations in the signal could potentially be filtered out by suitable signal processing, but care must be taken to filter out micro oscillations without distorting macro trends .

#### 4.3.5. Optical signal behaviour at different charge rates

Through the high c-rate testing carried out on cell test group 10, with 3C charge followed by D/20 discharge for 3 cycles on cells that are at 0°C, it is possible to gain further insight into the mechanisms influencing the optical signal reading. Figure 4-48 shows that when the cell is charged at 3C the 4.2V limit is hit within seconds and negligible charge is passed into the cell, the lack of optical signal response to this event confirms that the optical signal is not directly responding to voltage. Due to the seconds long period of charge followed by a slower discharge step, the cell SOC is registered as falling

by around 35mAh over the 3 cycles, and there is a general correlation with this in the optical signal, in which a 10mAh drop in cell capacity approximately corresponds to 1% change in optical signal light extinction. While Section 4.2 shows an interesting correlation in the profile of the optical signal and cell voltage, this data is a further indication that there is a cell SOC component to the signal measurement and it is not for example a direct measurement of the voltage. This is consistent with the hypothesis that Li-ion concentration is being measured by the optical sensor.

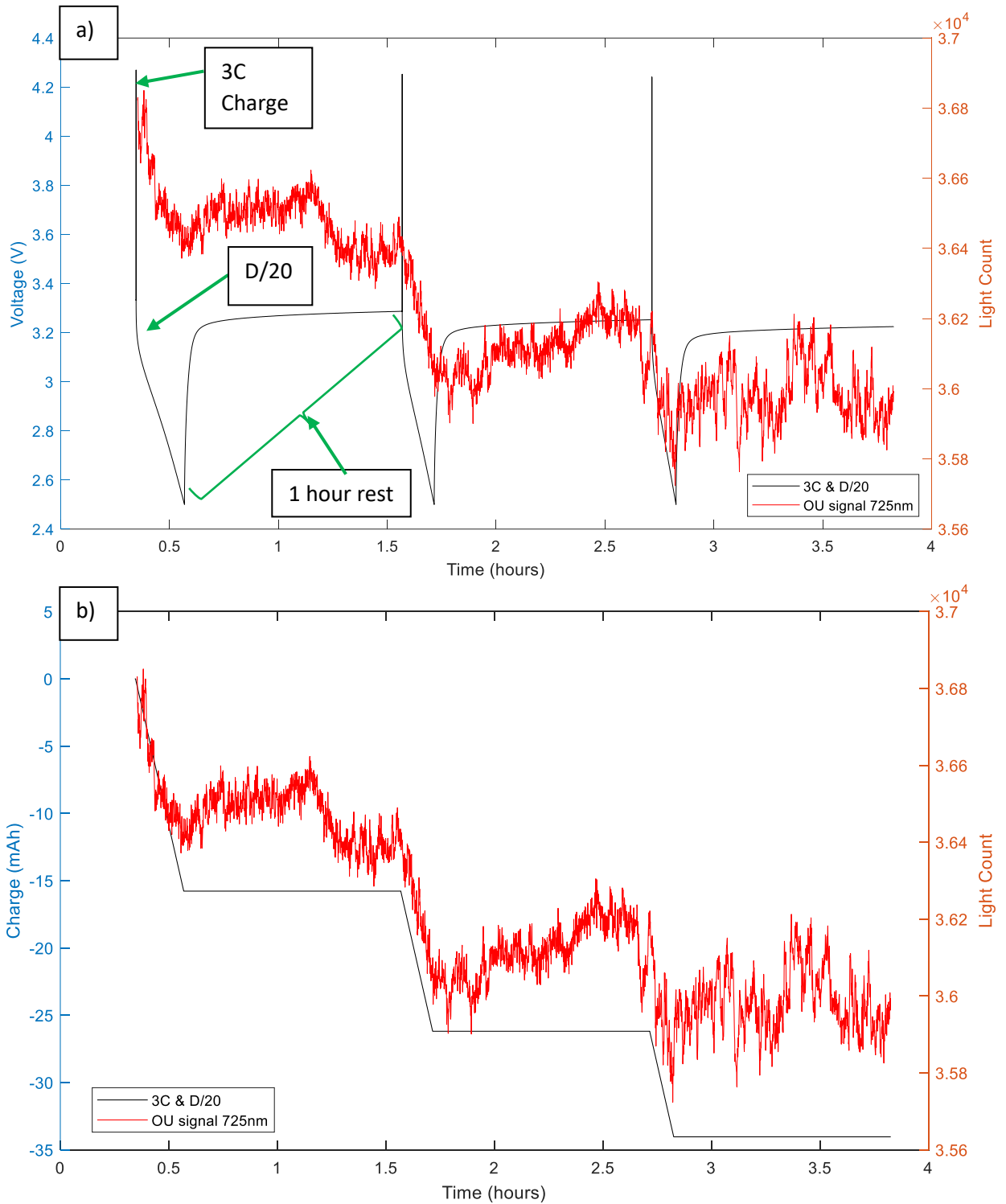


Figure 4-48- a) Cells at 0°C, charged at 3C and discharged at D/20 for 3 cycles, with corresponding anode side sensor optical signal and cell voltage, b) Same cycling data showing SOC profile instead of voltage.

## 4.4. Lithium plating detection with optical sensor

### 4.4.1. Open cell forced lithium plating

The lithium metal vs graphite open cell developed was charged at C/5 for a number of hours to force lithium plating on the graphite. The optical response of the sensor which was adjacent to the graphite anode can be seen in Figure 4-49, the data set indicates correlation to the open cell charge and lithium plating. There is a notable optical response on initial lithiation of the graphite electrode, then a second response which could be associated with the onset of lithium plating, followed by a gradient change in the optical signal over time as the voltage tends towards 0V (an indication of lithium plating).

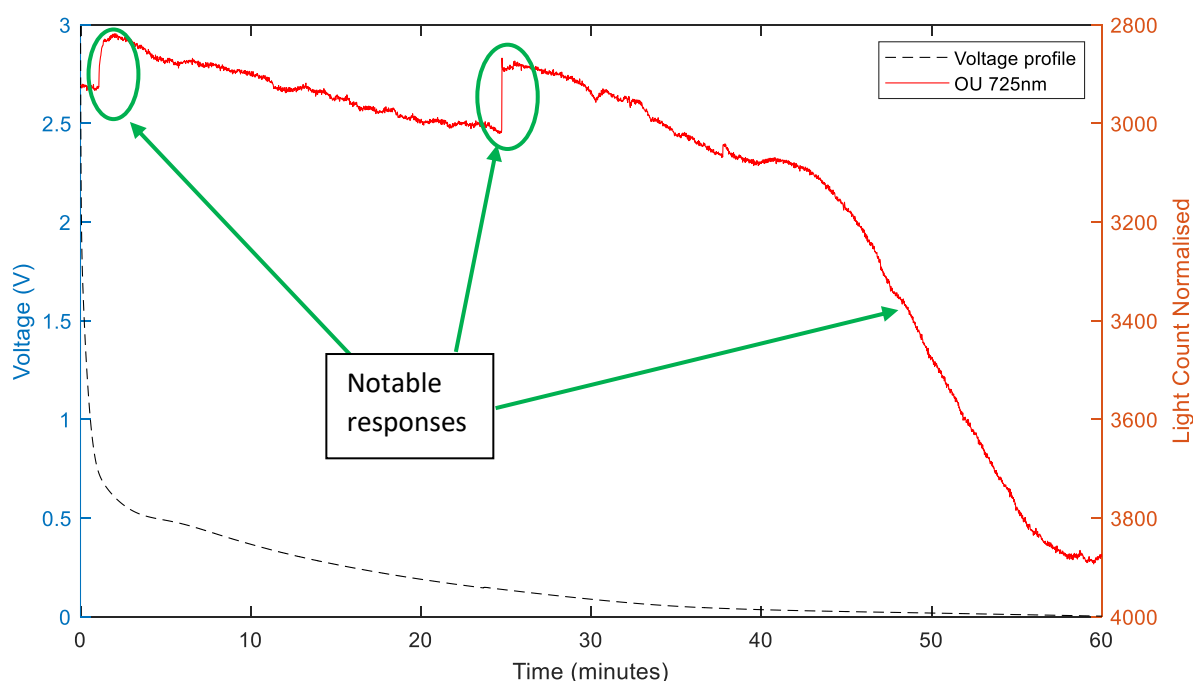


Figure 4-49- Open cell charged at C/5, showing voltage profile of cell and optical signal at the 725nm wavelength

After cycling the open cell was disassembled due to the clear deterioration of the electrodes, the pictures in Figure 4-50 show the degradation to the electrolyte, graphite electrode and optical sensor after disassembly. The lithium electrode has lithium dendrites, pitting and a black deposits at some parts of the surface and the part of the graphite electrode immersed in the electrolyte and closest to the lithium strip delaminated from the copper strip upon removal. Sediment of lithium dendrites and carbon particles that have broken off from the electrodes can be seen floating in the electrolyte. The optical sensor has also deteriorated considerably, a small region of gold can still be seen on the fibre, possibly this region of the sensor was above the level of the electrolyte, the rest of the sensor has

either blackened (indicating lithiated gold) or delaminated completely revealing the silica fibre underneath.

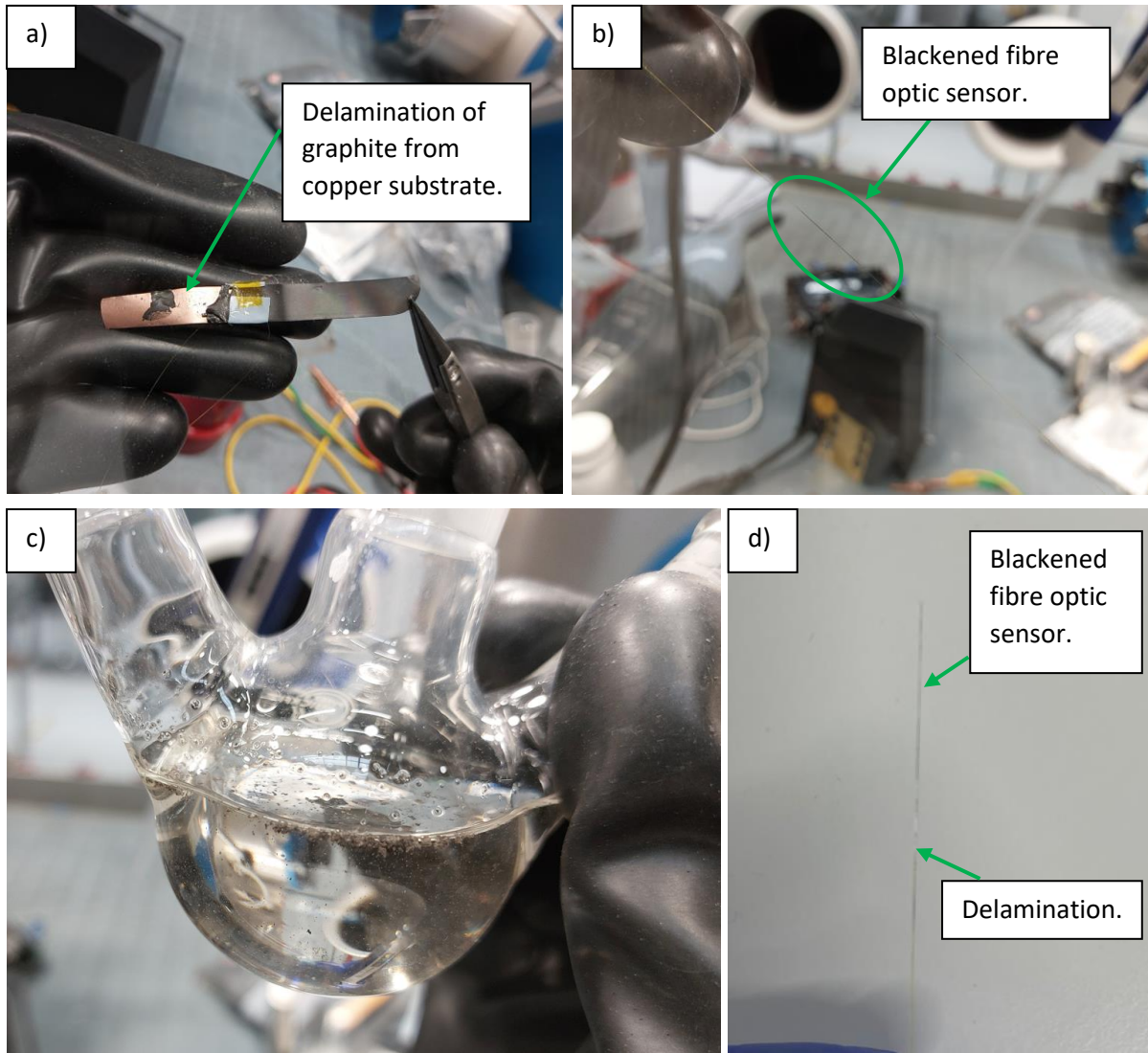


Figure 4-50- Pictures of open cell materials after forced lithium plating and dendrite formation, a) The graphite in the electrolyte delaminated from copper substrate, b) Fibre optic sensor blackened, c) Material deposits in electrolyte, d) Additional picture showing damage to fibre optic sensor

#### 4.4.2. Identifying forced lithium plating in pouch cells

In Section 3.5 the methodology to observe the impact of lithium-plating on the optical signal of a sensor inside a full pouch cell was set out. To determine whether lithium plating has taken place, the primary electrochemical approach used is to rapidly charge the cell and then slowly discharge it,

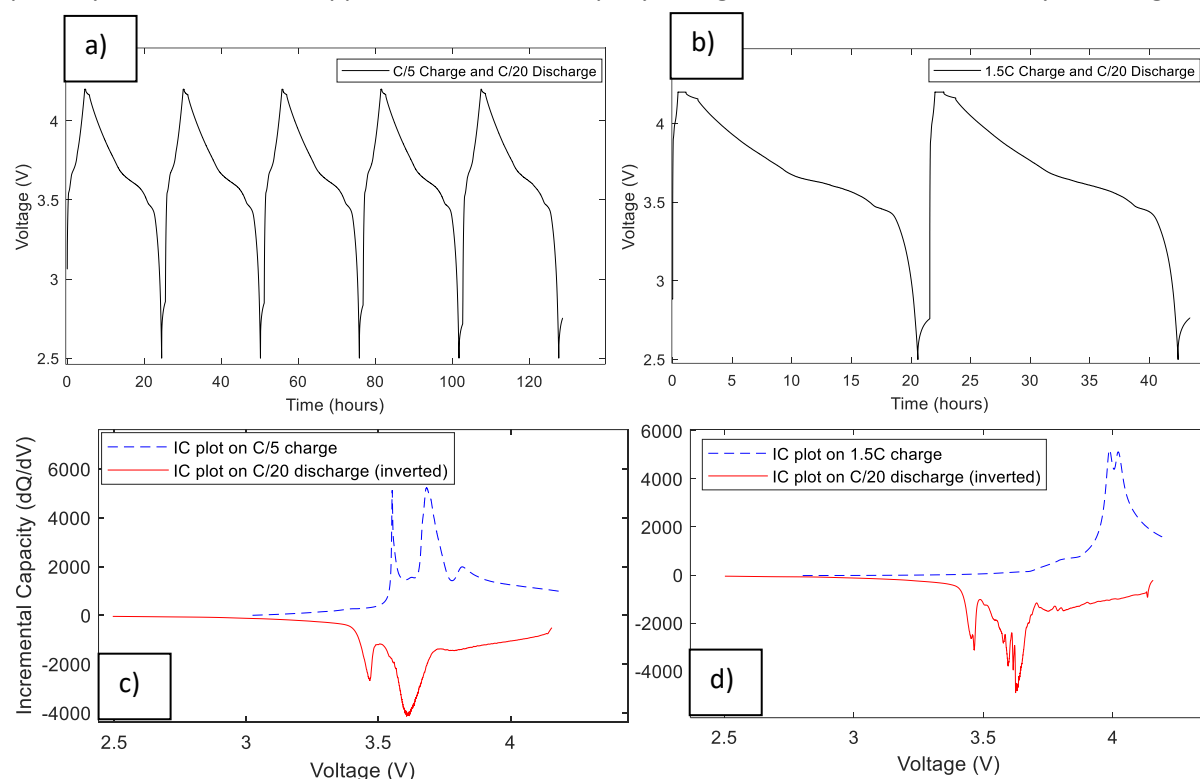


Figure 4-51- Cells cycled at 25°C ambient, a) Cell cycled at C/5 charge and C/20 discharge for 5 cycles, b) Cell cycled at 1.5C charge and C/20 discharge for 5 cycles, c) IC analysis of first cycle from Figure a, d) IC analysis of first cycle from Figure b

lithium plating during a cycle can then often be detected via an extra lithium stripping step on the discharge cycle [85]. Lithium stripping is visible as an extra high-voltage plateau on the SOC-Voltage or Time-Voltage plot, which can be made more apparent as a peak via IC (dQ/dV) or DV (dQ/dV) analysis [85]. Initially this testing was carried out at room temperature, the cells in test group 8 being charge at c-rates of 1.5C at room temperature before resting for 1 hour and then being discharged at C/20. The IC plot of 1.5C charge rate is shown in Figure 4-51, compared to the same C/20 discharge after a C/5 charge, where it can be seen that while the discharge curve is more irregular after 1.5C (with the same signal filtering) there is not an obvious additional peak that could be associated with lithium stripping. In the case of this testing a CV and 1 hour rest step was included before the discharge, the rest step was also inspected for evidence of a lithium stripping dT/dV peak- however there was no evidence of a peak, and it was determined to remove the CV and rest steps from future lithium plating attempts, i.e. to go directly from CC charge to CC discharge.

To create more favourable conditions for lithium plating the testing was then carried out at 0°C, causing the Li-ion movement and intercalation in the anode to be restricted, on reference cells in test group 9 (one of which has a lithium metal reference electrode). The cells in these conditions are cycled at C/40 charge (which should be a small enough c-rate not to cause lithium plating) before being directly discharging at C/20, then cycled at C/2 before being directly discharging at C/20. The comparison of the IC peaks in these two case can be seen in Figure 4-52, in which there is a distinct additional high voltage IC peak on the discharge curve that is present in the C/2 cycle case but not the

C/40 cycle case. This indicates that lithium-plating does occur at this temperature and in these conditions at C/2 and that it can be detected via this method.

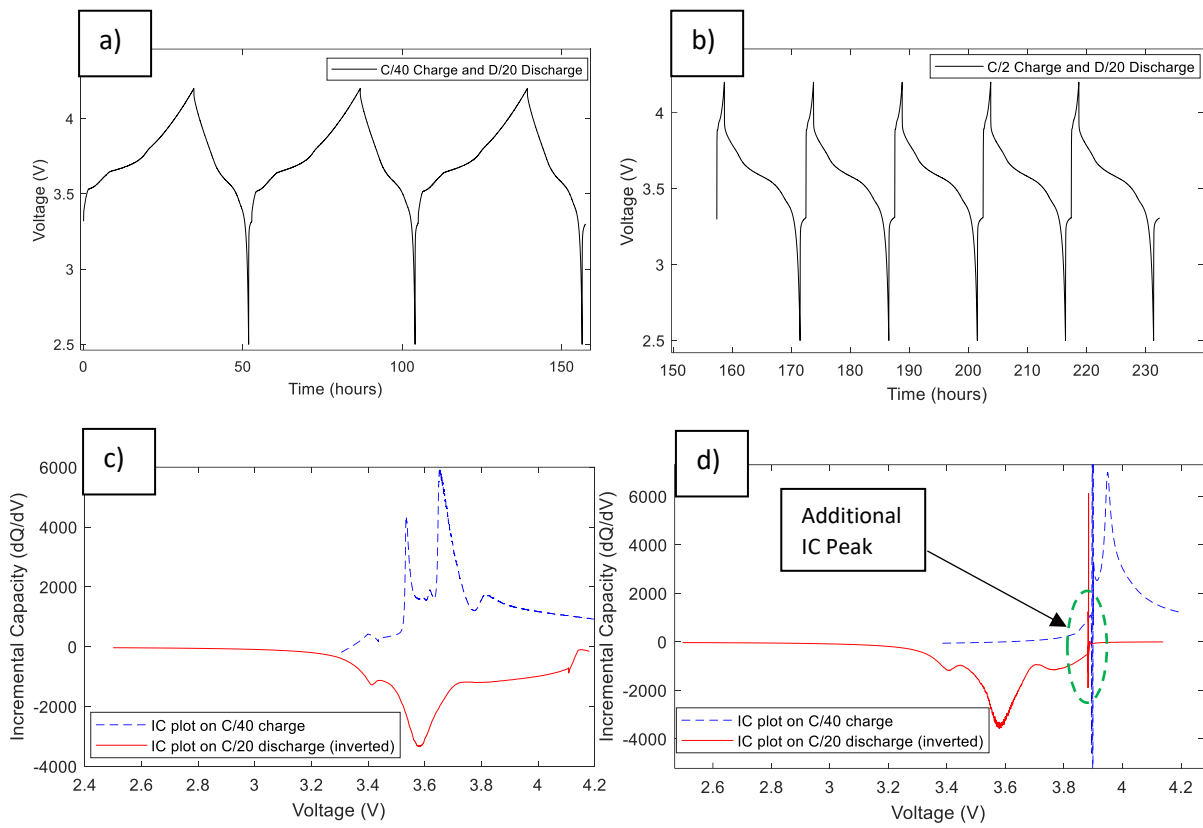


Figure 4-52- Cells cycled at 0°C ambient, a) Cell cycled at C/40 charge and C/20 discharge for 3 cycles, b) Cell cycled at C/2 charge and C/20 discharge for 5 cycles, c) IC analysis of first cycle from Figure a, d) IC analysis of second cycle from Figure b

Interestingly, lithium plating is not conclusively detected by the reference electrode in the cell; the anode voltage did drop to around 0 volts but then subsequently recovered to a more typical voltage range after a rest and further C/2 charge and C/20 discharge cycling, as can be seen in Figure 4-53. This could be because the lithium-plating is not necessarily homogeneous, so while lithium-plating may have occurred on some of the anode surface, subsequent stripping effects and incomplete coverage may not be sufficient to drive the overall anode voltage to 0V.

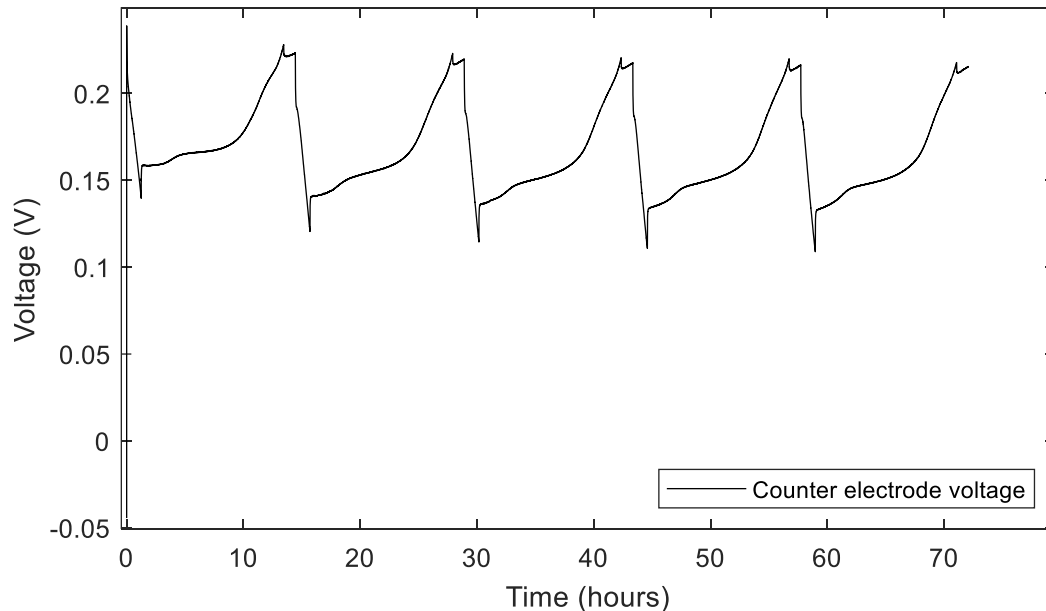


Figure 4-53- Graphite counter electrode voltage, on further C/2 charge and C/20 discharge cycling.

Further confirmation that lithium-plating had occurred was nonetheless provided upon cell teardown, physical inspection revealed there was visible lithium plating on some areas of the anode. On application of de-ionised water this was a strong reaction as can be seen in the images in Figure 4-54, this is strong evidence of lithium deposition on the surface and hence lithium plating. Many pouch cells are reported to start plating in a narrow area near the cell's margin [86], however that does not appear to have happened in this case, possibly due to greater anode overhang, or the lithium plating locations may have been driven by scratches or other imperfections on the anode surface.

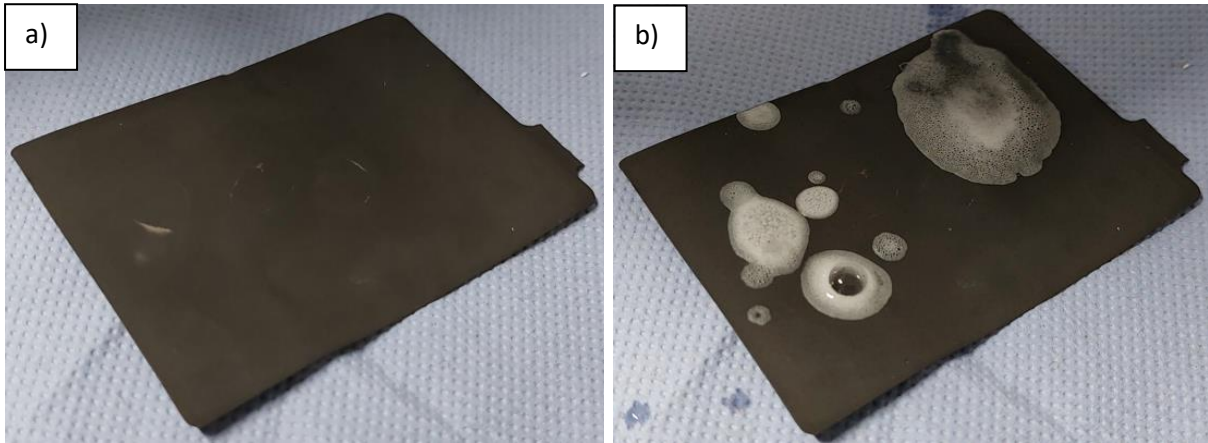


Figure 4-54- a) anode from torndown cell with visible lithium plating (left), b) reaction to water indicating lithium presence

Due to the increase in temperature caused by high c-rate charging, particularly from 0°C conditions, testing was also conducted with the inclusion of heat sinks. The cells are again in a 0°C environment, in this case with copper plates compressing the cell and providing a thermal heat sink effect during the temperature rise induced by fast charging. The cell is charged at a C-rate of C/2 (700mA, 0.933 mA.cm<sup>-2</sup>) until a cut-off of 4.2V and discharged at C/20 (-70mA, -0.093mA.cm<sup>-2</sup>). The time-voltage profile of the cells over this cycling can be seen in Figure 4-55, as well as IC analysis of one of the cycles. The IC analysis similarly reveals an additional high voltage peak on the discharge cycle that can be associated with lithium stripping, indicating lithium plating on the charge cycle. The data suggests that lithium plating has occurred in these conditions and that we can identify which cycles lithium plating occurred on, data which we can then use to evaluate the corresponding optical signal with.

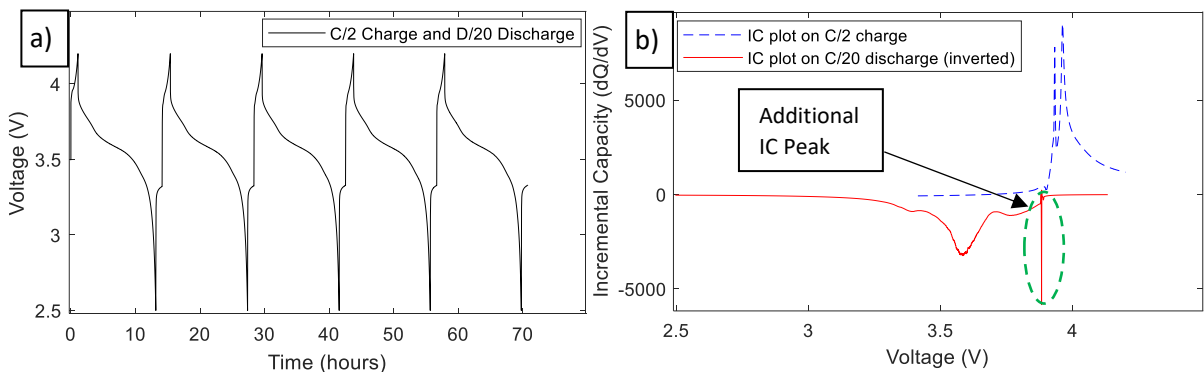


Figure 4-55- Copper plate cells with C/2 charge and C/20 discharge, a) Time versus voltage plot of 5 cycles and b) IC plot of the first cycle

In the case of the cells with the copper plate heat sinks it is interesting to investigate the impact of the plates on the cell temperature, and the impact of the additional weight on the cell performance. Figure 4-56 indicates that the copper plates have a moderating effect on the temperature at the surface of the cell, with a range of approximately 1.3 to 1.8°C on the cell with the copper plates compared to 0.5

to 2.5°C on the cell in the acrylic jigs, in the same cycling conditions; however it should be noted that the thermocouples have a tolerance of  $\pm 1.5\text{K}$  and the internal temperature of the cell may not be as moderated due to heat transfer limitations within the cell, so the results are not conclusive. The capacity-voltage plots for the cells during formation cycling indicates the additional weight of the copper jig does not affect the cell when compared to cells in an acrylic jig, with similar profiles in both cases. However interestingly it seems that the EIS response has a notable difference in the case of the cells compressed with the additional weight of the copper jig plates, the EIS response of the cells under the heavier compression of the copper plates indicates a lower charge transfer resistance across the electrodes and more responsive cells (lower RC value due to semi-circle peaks being at a higher frequency); this could be test to test variation (slightly differently prepared cells and testing environment), or a consequence of the increased pressure on the cell leading to a change in the cell kinetics, possibly due to improved contact.

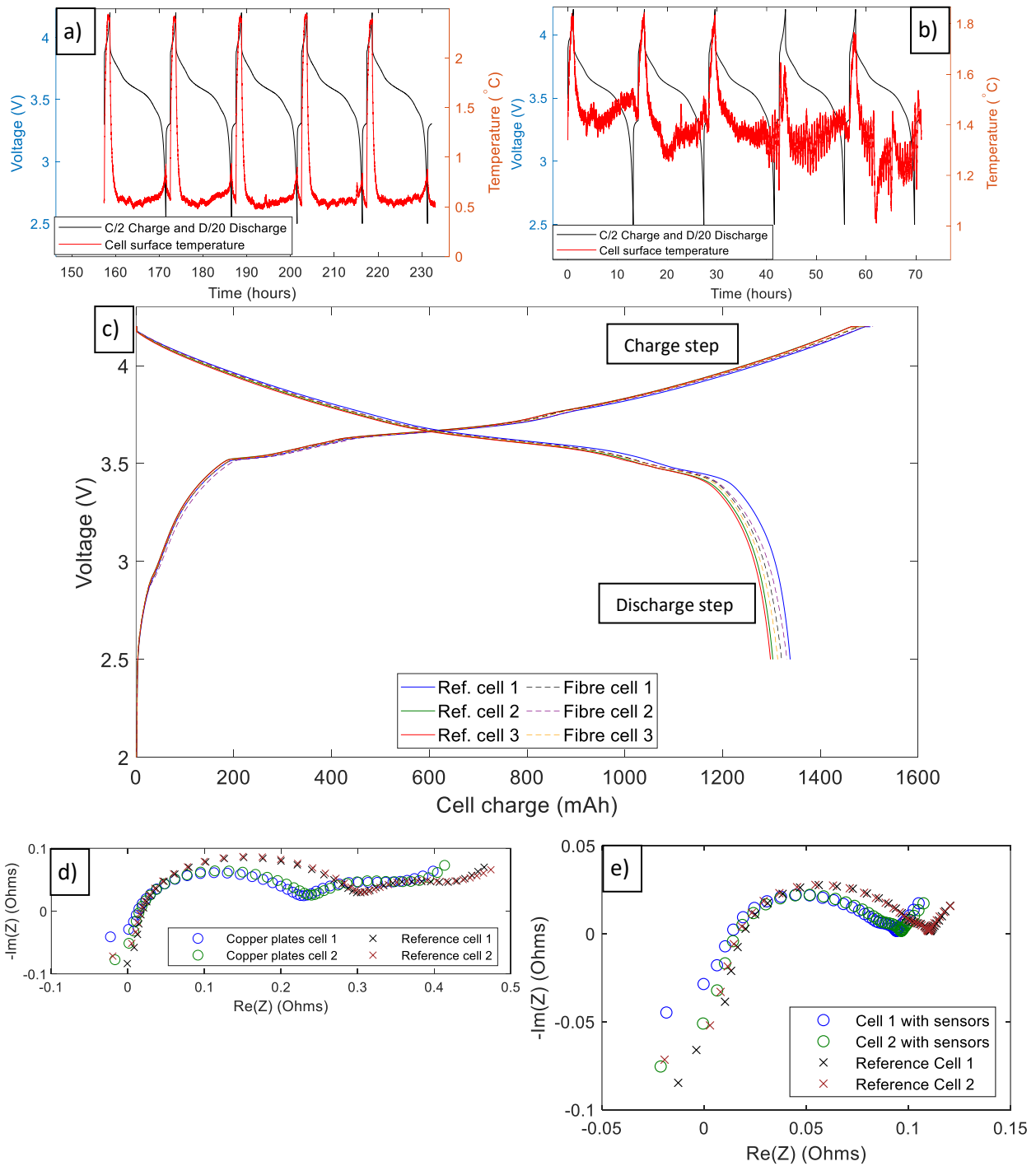


Figure 4-56- a) Cell surface temperature of cells in acrylic jigs, b) Cell surface temperature of cells in copper jigs, c) Comparison of formation cycles of cells in acrylic and copper jigs, d) Comparison of EIS of cells in acrylic jigs and copper jigs at same early stage of life in discharged state, e) Comparison of EIS of cells in acrylic jigs and copper jigs at same early stage of life in charged state

### 4.4.3. Forced lithium plating cycles optical data analysis

After establishing the optimum cycling regime for forced lithium plating for these cells, and verifying the occurrence of lithium plating through electrochemical methods and physical inspection, the optical signal can be compared and inspected to determine if there is any responsiveness to the lithium plating. Figure 4-57 shows the optical response of an anode side sensor to ten C/2 charge and C/20 discharge cycles at 0°C, conditions which have been shown in Section 4.4.2 to cause lithium plating within these cells. The optical response shows an increase in extinction on the first charge cycle, followed by similar but smaller increases on subsequent charge cycles. There is also an initial drop before the increase at the start of the cycle which has different potential explanations; this could be a response to the initial temperature change, or the lithium concentration at the anode surface could briefly decrease as the lithium in the anode is pulled towards the current collector at high charge rates, before further lithium arrives via diffusion mass transport and charge transfer. There is an ongoing increase in light extinction throughout the cycling and the light extinction does not decrease on the discharge cycles as is normally seen, this could be due to the accumulation of lithium at the surface via lithium plating, but it is also possible that the sensor is damaged or degraded during lithium plating.

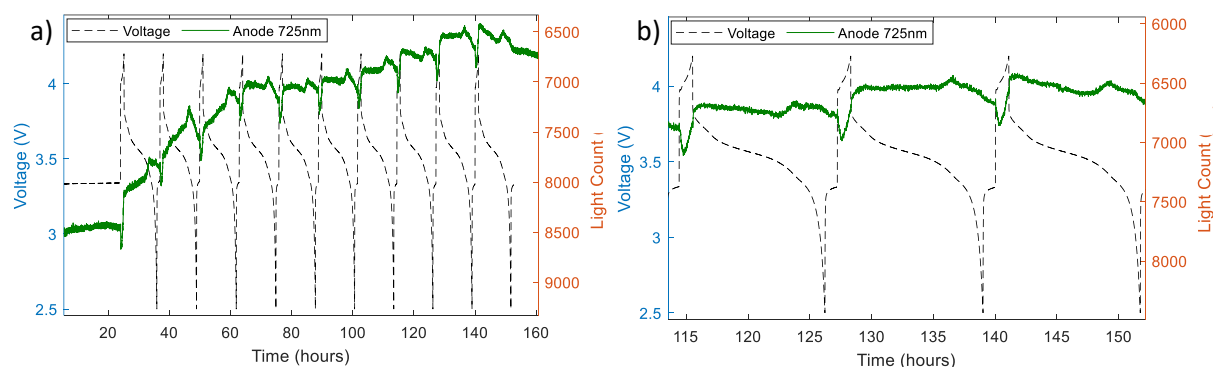


Figure 4-57- Cell at 0°C cycled at C/2 charge and then C/20 discharge, a) showing 10 cycles and b) zoomed in on 3 cycles, with the voltage profile and optical signal response from anode side fibres at 725nm

At this stage, while the sensor signal exhibits different a different response during these cycling conditions, it cannot be conclusively stated from this data that the response is directly due to lithium plating. The effects of temperature are likely to be more pronounced due to fast charging at low temperatures, and there it is also possible the sensors is suffering degradation. Nonetheless the results show a response that could be associated with lithium plating, and further work can be carried out to test this in different conditions and ideally with an internal temperature sensor to more accurately deconvolute temperature impacts on the signal. A challenge with the approach taken in this study to force lithium plating in a balanced cell, is that it requires high charge rates and low temperatures which introduce additional variables into the measurement. A more effective way to test the responsiveness of the sensor to lithium plating and deconvolute it from other variables could be to build an unbalanced cell with cathode capacity in excess of anode capacity, and then overcharge the anode until lithium plating is forced, this can be the subject of future work.

## 5. Conclusions

This study has demonstrated the potential of plasmonic based fibre optic sensors as a technique capable of extracting data from directly inside Li-ion cells in real time, providing an optical response that correlates with changes in cell state and electrochemical events. Insplorion AB's plasmonic based fibre optic sensing platform has been shown to have promise as a lithium-ion battery diagnostic tool, a novel use for this sensing technology, through the successful integration of the sensors into production type Li-ion pouch cells. In addition to the learning around this specific sensing technique, this work adds to the body of work around the methodology for the agnostic installation of fibre optic based diagnostic sensors inside Li-ion cells.

We have demonstrated that the sensor responds to changes in Li-ion concentration in electrolyte solution. Subsequently, through the installation of sensors in Li-ion pouch cells, we have then demonstrated a correlation between the optical signal and cell state during simple galvanostatic cycling, with differing signal profiles obtained by placing the sensor adjacent to the anode and cathode electrodes. Further to this, the responsiveness of the optical signal to partial charge and discharge cycles was shown. The hypothesis has been proposed that the sensors' optical signal is responding to Li-ion concentration in the electrode boundary layer, explaining the way in which the optical signal profile approximately follows cell SOC but with features associated with the voltage profile that can be explained by Li-ion diffusion kinetics.

Analysis of further cell testing techniques has further supported the working hypothesis of a sensitivity to Li-ion concentration. GITT testing shows a peak and then relaxation of the optical signal in correlation with the voltage pulses, while the redox peak identified during cyclic voltammetry is also identifiable in the optical signal. The potential of the sensors to detect cell events is also shown, with the IC analysis and the differential of the optical signal showing that the phase transition IC peaks are detected. The phase transition analysis was further expanded with the use of a lithium reference electrode, this allowed conclusions into which IC peaks can be associated with which electrode and indicated that the cathode phase transitions had the greatest impact on cell kinetics as simultaneously detected by the optical sensors.

The area of Li-ion plating has also been studied by observing the optical response to forced lithium plating in both an open cell and pouch cells. In both cases promising optical responses are observed that could be associated with the onset of lithium plating; while the data is not conclusive and other possibilities must be ruled out, this invites further testing of this methodology in different conditions and ideally with internal temperature sensors to deconvolute the temperature impacts of high charge rate at low temperature. The recommendation is made to build an unbalanced cell with excess cathode capacity and test the sensor responsiveness to lithium plating through overcharging, thereby not introducing the high charge rate and low temperature variables required in the forced lithium plating of a balanced cell as per this study.

Further observations have been made around the sensors longevity and the differing condition of the sensors on the anode and cathode sides of the cell after cycling. Initially the sensor on the anode side of the cell was lasting for approximately 50 cycles before the signal stopped transmitting and showed signs of sensor delamination and corrosion under SEM analysis. Following feedback to the sensor manufacturer (Insplorion AB) and a manufacturing change the longevity of the sensor increased to in excess of 300 cycles. Nonetheless even after the sensor modification the sensors on the cathode side of the cell showed less loss of light transmission after repeated cycling. Material analysis from a

torndown cell showed that after 48 cycles of testing including forced lithium plating, the sensor on the cathode side of the cell showed minimal physical deterioration, while the sensor on the anode side of the cell showed signs of deposition or corrosion on the surface and the colour had turned from gold to black. The blackened colour possibly indicates permeability or failure of the coating during cycling, allowing the gold sensing film to be lithiated. While the sensors have shown robustness within the corrosive environment inside the cell and the continued ability to extract data from inside the cell of many cycles, and even with the improvement in sensor robustness seen within the project, further work can be considered to further insulate the sensors from damaging electrochemical effects within the cell.

Similar analysis of the cells and electrode materials has shown the sensors have negligible impact on the performance of the cells over repeated cycling. Electrochemical analysis of the cells with and without sensors present, including comparing formation cycling profiles, coulombic efficiencies over 150 cycles and EIS comparisons at the same point in life showed negligible difference between the cells. Further to this SEM and EDX material analysis of the electrodes after teardown showed no indications of the presence of the sensors on the cathodes, and only some indication of electrolyte lithium-salt deposits on the anode where the sensor had been, likely due to pooling of electrolyte in the area

More widely the combination of promising data and the fibres not negatively impacting cell performance gives weight to utilising a variety of optical fibre based in-situ diagnostic techniques. This also supports the concept of a fibre optic based battery management system rather than an electrically based one, which can have the advantages of utilisation of cheap fibre optics, no electrical interference and ability to obtain data from directly inside cells; while the cost of optical interrogator equipment can be significant, this can be reduced by tailoring it to the specific required functions and has the advantage that though multiplexing one interrogator can potentially support a multitude of sensors.

Taken as a whole this study has demonstrated the novel use of a plasmonic sensing diagnostic technique inside Li-ion pouch cells for the first time, testing the three hypotheses set out in Section 2.5. The data obtained from directly inside the cell suggests a direct insight into the cell kinetics and has been shown to correlate with cell cycling and electrochemical events as externally detected by highly accurate potentiostat equipment; additionally the cell performance has been shown to be agnostic to the presence of two sensors. The promising findings in this study invite more research into this diagnostic technique, adding to a limited number of cell research and diagnostic tools able to obtain data from directly inside the cell, and an even more limited number able to do so using unmodified commercial type cells.

## 6. Further Work

Further work to develop this sensing technique should include assembling multi-sensored cells, to quantitatively deconvolute the temperature and pressure effects on the cell from the electrochemical effects detected by the plasmonic based sensors. Effective data deconvolution could then support further correlation analysis with a refined data set and a more quantitative approach to utilisation of the optical signal to ascertain cell state. The sensors could also be placed inside a cell simultaneously with bare fibre optic sensors to investigate the effect of possible Li-ion doping of the silica fibres, and with ATR based fibre optic sensors to directly compare an ATR based response. The sensors have shown robustness to the cell environment but additional research could be undertaken to further insulate them from damaging effects within the cell, a sensor with longer term stability would have better potential to monitor cell SOH by measuring material composition change (electrolyte degradation) without distortion, unless the deterioration of the sensor itself could be correlated to internal cell condition.

Furthermore the hypothesis of sensor sensitivity to Li-ion concentration could be tested via modelling. Battery cells tested with the fibre optic sensors could be modelled using existing modelling techniques to observe the predicted Li-ion concentration change in the anode boundary region in the same cycling conditions. This data could be compared to the optical signal to see if it correlates and corroborates the hypothesis.

The sensors are small by design (approximately 50mm in length and 0.1mm in diameter) and therefore measure only a micro area of the cell surface, while battery materials and behaviour is known to be heterogeneous at multiple scales. Sensors could be placed at multiple points along the cell surface, using quasi-distributed sensing techniques to have multiple sensing points on a single fibre, and then multiple fibres to form a grid of sensors. This could give better average readings and an indication of the distribution of cell kinetics behaviour across the surface, although it has to be considered that the more sensors are added the more potential interference there would be in the cell behaviour.

Further testing of the sensors responsiveness to forced lithium plating in different conditions should be carried out, establishing if a consistent response is produced which can be associated with the onset of lithium plating. The sensors can be further evaluated in cycling conditions that simulate real world performance, understanding the resolution limits of the optical sensors and if that can be improved through approaches such as signal noise reduction. Other different electrolyte types or cells chemistries can also be explored, such as LFP and Na-ion. The data around the none interference of the sensors on cell performance also provides support to the concept of an optical fibre based BMS, rather than an electrically based one; a multi-sensored cell base on optical fibre diagnostics such as TFBG's could be developed as a proof of concept. The wider concept of fibre optics also opens up the possibility of other 'lab-on-fibre' techniques, potentially techniques such as Raman Spectroscopy and colourimetry can be introduced into an unmodified cell through fibre optics.

## 7. References

- [1] P. A. Sohi, M. Kahrizi, Principles and Applications of Nanoplasmonics in Biological and Chemical Sensing: A Review, in: Recent Adv. Nanophotonics-Fundamentals Appl. [Working Title], IntechOpen, 2020. <https://doi.org/10.5772/intechopen.93001>.
- [2] J. Homola, J. Čtyroký, M. Skalský, J. Hradilová, P. Kolářová, A surface plasmon resonance based integrated optical sensor, *Sensors Actuators, B Chem.* 39 (1997) 286–290. [https://doi.org/10.1016/S0925-4005\(97\)80220-1](https://doi.org/10.1016/S0925-4005(97)80220-1).
- [3] E.M. Larsson, S. Syrenova, C. Langhammer, H. Giessen, Nanoplasmonic sensing for nanomaterials science, *Nanophotonics.* 1 (2012) 249–266. <https://doi.org/10.1515/nanoph-2012-0029>.
- [4] C. Caucheteur, T. Guo, J. Albert, Review of plasmonic fiber optic biochemical sensors: improving the limit of detection, *Anal. Bioanal. Chem.* 407 (2015) 3883–3897. <https://doi.org/10.1007/s00216-014-8411-6>.
- [5] Q.Q. Meng, X. Zhao, C.Y. Lin, S.J. Chen, Y.C. Ding, Z.Y. Chen, Figure of merit enhancement of a surface plasmon resonance sensor using a low-refractive-index porous silica film, *Sensors (Switzerland).* 17 (2017). <https://doi.org/10.3390/s17081846>.
- [6] Y. Jiang, J. Jiang, C. Zhang, W. Zhang, Y. Gao, N. Li, State of health estimation of second-life LiFePO<sub>4</sub> batteries for energy storage applications, *J. Clean. Prod.* 205 (2018) 754–762. <https://doi.org/10.1016/j.jclepro.2018.09.149>.
- [7] M.S. Whittingham, Electrical energy storage and intercalation chemistry, *Science (80-. ).* 192 (1976) 1126–1127. <https://doi.org/10.1126/science.192.4244.1126>.
- [8] G. Zubi, R. Dufo-López, M. Carvalho, G. Pasaoglu, The lithium-ion battery: State of the art and future perspectives, *Renew. Sustain. Energy Rev.* 89 (2018). <https://doi.org/10.1016/j.rser.2018.03.002>.
- [9] M. V. Reddy, A. Mauger, C.M. Julien, A. Paoletta, K. Zaghib, Brief history of early lithium-battery development, *Materials (Basel).* 13 (2020). <https://doi.org/10.3390/MA13081884>.
- [10] X. Shen, H. Liu, X.B. Cheng, C. Yan, J.Q. Huang, Beyond lithium ion batteries: Higher energy density battery systems based on lithium metal anodes, *Energy Storage Mater.* 12 (2018) 161–175. <https://doi.org/10.1016/j.ensm.2017.12.002>.
- [11] Lithium-Ion Battery - Clean Energy Institute, Univ. Washingt. (2020). <https://www.cei.washington.edu/education/science-of-solar/battery-technology/> (accessed August 14, 2020).
- [12] H.N. Masaki Yoshio, *Lithium-Ion Batteries*, 2009. <https://doi.org/10.1007/978-0-387-34445-4>.
- [13] I. Tsiropoulos, D. Tarvydas, N. Lebedeva, Li-ion batteries for mobility and stationary storage applications, 2018. <https://doi.org/10.2760/87175>.
- [14] eVTOL Aircraft Market Size & Trends | Global Analysis, (n.d.). <https://www.fortunebusinessinsights.com/evtol-aircraft-market-106298> (accessed January 28, 2023).
- [15] C.P. Aiken, E.R. Logan, H. Hebecker, J.M. Oxner, J. Harlow, M. Metzger, J.R. Dahn, Li[Ni 0.5 Mn 0.3 Co 0.2 ]O<sub>2</sub> As a Superior Alternative to LiFePO<sub>4</sub> for Long-Lived Low Voltage Li-ion Cells ,

- ECS Meet. Abstr. MA2021-02 (2021) 1893–1893. <https://doi.org/10.1149/ma2021-0251893mtgabs>.
- [16] EVO Report 2022 | BloombergNEF | Bloomberg Finance LP, (n.d.). <https://about.bnef.com/electric-vehicle-outlook/>.
- [17] A. Tomaszewska, Z. Chu, X. Feng, S. O’Kane, X. Liu, J. Chen, C. Ji, E. Endler, R. Li, L. Liu, Y. Li, S. Zheng, S. Vetterlein, M. Gao, J. Du, M. Parkes, M. Ouyang, M. Marinescu, G. Offer, B. Wu, Lithium-ion battery fast charging: A review, *ETransportation*. 1 (2019) 100011. <https://doi.org/10.1016/j.etrans.2019.100011>.
- [18] J. Lao, P. Sun, F. Liu, X. Zhang, C. Zhao, W. Mai, T. Guo, G. Xiao, J. Albert, *In situ* plasmonic optical fiber detection of the state of charge of supercapacitors for renewable energy storage, *Light Sci. Appl.* 7 (2018). <https://doi.org/10.1038/s41377-018-0040-y>.
- [19] Tesla Begins Construction Of World’s Largest Battery Storage Facility, *Forbes*. (2020). <https://www.forbes.com/sites/arielcohen/2020/08/13/tesla-begins-construction-of-worlds-largest-energy-storage-facility/#32bb32624fde> (accessed August 14, 2020).
- [20] P. Harrop, X. He, D. Gatti, Distributed Generation: Off-Grid Zero-Emission kW-MW 2020-2040: IDTechEx, 2020. <https://www.idtechex.com/en/research-report/distributed-generation-off-grid-zero-emission-kw-mw-2020-2040/730> (accessed August 17, 2020).
- [21] E. Martinez-Laserna, E. Sarasketa-Zabala, D.I. Stroe, M. Swierczynski, A. Warnecke, J.M. Timmermans, S. Goutam, P. Rodriguez, Evaluation of lithium-ion battery second life performance and degradation, in: *ECCE 2016 - IEEE Energy Convers. Congr. Expo. Proc.*, 2016. <https://doi.org/10.1109/ECCE.2016.7855090>.
- [22] X. Luo, J. Wang, M. Dooner, J. Clarke, Overview of current development in electrical energy storage technologies and the application potential in power system operation, *Appl. Energy*. 137 (2015) 511–536. <https://doi.org/10.1016/j.apenergy.2014.09.081>.
- [23] R.A. Huggins, *Energy storage: Fundamentals, materials and applications*, second edition, Springer International Publishing, 2015. <https://doi.org/10.1007/978-3-319-21239-5>.
- [24] Lithium-ion battery demand 2030: Resilient, sustainable, and circular | McKinsey, (n.d.). <https://www.mckinsey.com/industries/automotive-and-assembly/our-insights/battery-2030-resilient-sustainable-and-circular> (accessed February 9, 2023).
- [25] A. Kasliwal, N.J. Furbush, J.H. Gawron, J.R. McBride, T.J. Wallington, R.D. De Kleine, H.C. Kim, G.A. Keoleian, Role of flying cars in sustainable mobility, *Nat. Commun.* 10 (2019) 1555. <https://doi.org/10.1038/s41467-019-09426-0>.
- [26] W. Chen, J. Liang, Z. Yang, G. Li, A review of lithium-ion battery for electric vehicle applications and beyond, in: *Energy Procedia*, Elsevier Ltd, 2019: pp. 4363–4368. <https://doi.org/10.1016/j.egypro.2019.01.783>.
- [27] Y. Liang, C. Zhao, H. Yuan, Y. Chen, W. Zhang, J. Huang, D. Yu, Y. Liu, M. Titirici, Y. Chueh, H. Yu, Q. Zhang, A review of rechargeable batteries for portable electronic devices, *InfoMat*. 1 (2019) 6–32. <https://doi.org/10.1002/inf2.12000>.
- [28] J. Xie, Y.C. Lu, A retrospective on lithium-ion batteries, *Nat. Commun.* 2020 111. 11 (2020) 1–4. <https://doi.org/10.1038/s41467-020-16259-9>.
- [29] N. Nitta, F. Wu, J.T. Lee, G. Yushin, Li-ion battery materials: present and future, *Mater. Today*. 18 (2015) 252–264. <https://doi.org/10.1016/J.MATTOD.2014.10.040>.
- [30] M. Abdollahifar, H. Cavers, S. Scheffler, A. Diener, M. Lippke, A. Kwade, Insights into Influencing

- Electrode Calendering on the Battery Performance, *Adv. Energy Mater.* (2023). <https://doi.org/https://doi.org/10.1002/aenm.202300973>.
- [31] I. Buchmann, [batteryuniversity.com](https://batteryuniversity.com/learn/article/types_of_battery_cells), (2020). [https://batteryuniversity.com/learn/article/types\\_of\\_battery\\_cells](https://batteryuniversity.com/learn/article/types_of_battery_cells) (accessed September 7, 2020).
- [32] R. Raccichini, M. Amores, G. Hinds, Critical review of the use of reference electrodes in Li-ion batteries: A diagnostic perspective, *Batteries*. 5 (2019) 1–24. <https://doi.org/10.3390/batteries5010012>.
- [33] L.K. Willenberg, P. Dechent, G. Fuchs, D.U. Sauer, E. Figgemeier, High-precision monitoring of volume change of commercial lithium-ion batteries by using strain gauges, *Sustain*. 12 (2020). <https://doi.org/10.3390/su12020557>.
- [34] A. Casimir, H. Zhang, O. Ogoke, J.C. Amine, J. Lu, G. Wu, Silicon-based anodes for lithium-ion batteries: Effectiveness of materials synthesis and electrode preparation, *Nano Energy*. 27 (2016) 359–376. <https://doi.org/10.1016/j.nanoen.2016.07.023>.
- [35] M. Broussely, P. Biensan, F. Bonhomme, P. Blanchard, S. Herreyre, K. Nechev, R.J. Staniewicz, Main aging mechanisms in Li ion batteries, in: *J. Power Sources*, 2005: pp. 90–96. <https://doi.org/10.1016/j.jpowsour.2005.03.172>.
- [36] S.J. An, J. Li, C. Daniel, D. Mohanty, S. Nagpure, D.L. Wood, The state of understanding of the lithium-ion-battery graphite solid electrolyte interphase (SEI) and its relationship to formation cycling, *Carbon N. Y.* 105 (2016) 52–76. <https://doi.org/10.1016/J.CARBON.2016.04.008>.
- [37] S.K. Heiskanen, J. Kim, B.L. Lucht, Generation and Evolution of the Solid Electrolyte Interphase of Lithium-Ion Batteries, *Joule*. 3 (2019) 2322–2333. <https://doi.org/10.1016/J.JOULE.2019.08.018>.
- [38] J. Ming, Z. Cao, Y. Wu, W. Wahyudi, W. Wang, X. Guo, L. Cavallo, J.Y. Hwang, A. Shamim, L.J. Li, Y.K. Sun, H.N. Alshareef, New Insight on the Role of Electrolyte Additives in Rechargeable Lithium Ion Batteries, *ACS Energy Lett.* 4 (2019) 2613–2622. <https://doi.org/10.1021/acsenergylett.9b01441>.
- [39] Z. Zhang, J. Yang, W. Huang, H. Wang, W. Zhou, Y. Li, Y. Li, J. Xu, W. Huang, W. Chiu, Y. Cui, Cathode-Electrolyte Interphase in Lithium Batteries Revealed by Cryogenic Electron Microscopy, *Matter*. 4 (2021) 302–312. <https://doi.org/10.1016/J.MATT.2020.10.021>.
- [40] J. Gao, S.Q. Shi, H. Li, Brief overview of electrochemical potential in lithium ion batteries, *Chinese Phys. B*. 25 (2015). <https://doi.org/10.1088/1674-1056/25/1/018210>.
- [41] R. Weber, M. Genovese, A.J. Louli, S. Hames, C. Martin, I.G. Hill, J.R. Dahn, Long cycle life and dendrite-free lithium morphology in anode-free lithium pouch cells enabled by a dual-salt liquid electrolyte, *Nat. Energy*. 4 (2019) 683–689. <https://doi.org/10.1038/s41560-019-0428-9>.
- [42] B. Sundén, Battery technologies, *Hydrog. Batter. Fuel Cells*. (2019) 57–79. <https://doi.org/10.1016/B978-0-12-816950-6.00004-X>.
- [43] P. Jehnichen, K. Wedlich, C. Korte, Degradation of high-voltage cathodes for advanced lithium-ion batteries—differential capacity study on differently balanced cells, *Sci. Technol. Adv. Mater.* 20 (2019) 1–9. <https://doi.org/10.1080/14686996.2018.1550625>.
- [44] A. Manthiram, A reflection on lithium-ion battery cathode chemistry, *Nat. Commun.* 11 (2020) 1–9. <https://doi.org/10.1038/s41467-020-15355-0>.

- [45] A. Fly, R. Chen, Rate dependency of incremental capacity analysis (dQ/dV) as a diagnostic tool for lithium-ion batteries, *J. Energy Storage*. 29 (2020) 101329. <https://doi.org/10.1016/J.EST.2020.101329>.
- [46] K. Fröhlich, I. Abrahams, M. Jahn, Determining phase transitions of layered oxides via electrochemical and crystallographic analysis, *Sci. Technol. Adv. Mater.* 21 (2020) 653–660. [https://doi.org/10.1080/14686996.2020.1814116/SUPPL\\_FILE/TSTA\\_A\\_1814116\\_SM7890.PDF](https://doi.org/10.1080/14686996.2020.1814116/SUPPL_FILE/TSTA_A_1814116_SM7890.PDF).
- [47] W.S. Yoon, M. Balasubramanian, K.Y. Chung, X.Q. Yang, J. McBreen, C.P. Grey, D.A. Fischer, Investigation of the charge compensation mechanism on the electrochemically Li-ion deintercalated  $\text{Li}_{1-x}\text{Co}_{1/3}\text{Ni}_{1/3}\text{Mn}_{1/3}\text{O}_2$  electrode system by combination of soft and hard X-ray absorption spectroscopy, *J. Am. Chem. Soc.* 127 (2005) 17479–17487. <https://doi.org/10.1021/ja0530568>.
- [48] Y. Koyama, I. Tanaka, H. Adachi, Y. Makimura, T. Ohzuku, Crystal and electronic structures of superstructural  $\text{Li}_{1-x}[\text{Co}_{1/3}\text{Ni}_{1/3}\text{Mn}_{1/3}]\text{O}_2$  ( $0 \leq x \leq 1$ ), in: *J. Power Sources*, 2003: pp. 644–648. [https://doi.org/10.1016/S0378-7753\(03\)00194-0](https://doi.org/10.1016/S0378-7753(03)00194-0).
- [49] B.J. Hwang, Y.W. Tsai, D. Carlier, G. Ceder, A combined computational/experimental study on  $\text{LiNi}_{1/3}\text{Co}_{1/3}\text{Mn}_{1/3}\text{O}_2$ , *Chem. Mater.* 15 (2003) 3676–3682. <https://doi.org/10.1021/cm030299v>.
- [50] H. Sun, K. Zhao, Electronic Structure and Comparative Properties of  $\text{LiNi}_x\text{Mn}_y\text{Co}_z\text{O}_2$  Cathode Materials, *J. Phys. Chem. C*. 121 (2017) 6002–6010. <https://doi.org/10.1021/acs.jpcc.7b00810>.
- [51] R. Jung, M. Metzger, F. Maglia, C. Stinner, H.A. Gasteiger, Oxygen Release and Its Effect on the Cycling Stability of  $\text{LiNi}_x\text{Mn}_y\text{Co}_z\text{O}_2$  (NMC) Cathode Materials for Li-ion Batteries, *J. Electrochem. Soc.* 164 (2017) A1361–A1377. <https://doi.org/10.1149/2.0021707jes>.
- [52] H.J. Noh, S. Youn, C.S. Yoon, Y.K. Sun, Comparison of the structural and electrochemical properties of layered  $\text{Li}[\text{Ni}_x\text{Co}_y\text{Mn}_z]\text{O}_2$  ( $x = 1/3, 0.5, 0.6, 0.7, 0.8$  and  $0.85$ ) cathode material for lithium-ion batteries, *J. Power Sources*. 233 (2013) 121–130. <https://doi.org/10.1016/j.jpowsour.2013.01.063>.
- [53] D. Anseán, M. González, C. Blanco, J.C. Viera, Y. Fernández, V.M. García, Lithium-ion battery degradation indicators via incremental capacity analysis, *Conf. Proc. - 2017 17th IEEE Int. Conf. Environ. Electr. Eng. 2017 1st IEEE Ind. Commer. Power Syst. Eur. IEEEIC / I CPS Eur. 2017*. (2017). <https://doi.org/10.1109/EEEIC.2017.7977776>.
- [54] Y. Guo, R.B. Smith, Z. Yu, D.K. Efetov, J. Wang, P. Kim, M.Z. Bazant, L.E. Brus, Li Intercalation into Graphite: Direct Optical Imaging and Cahn-Hilliard Reaction Dynamics, *J. Phys. Chem. Lett.* 7 (2016) 2151–2156. <https://doi.org/10.1021/acs.jpcllett.6b00625>.
- [55] W. Li, J. Zhu, Experimental Study on Lithium Ion Diffusion of Graphite Anode Based On In-Situ Optics, *IOSR J. Eng.* 09 (2019) 62–65.
- [56] P. Maire, A. Evans, H. Kaiser, W. Scheifele, P. Novák, Colorimetric Determination of Lithium Content in Electrodes of Lithium-Ion Batteries, *J. Electrochem. Soc.* 155 (2008) A862. <https://doi.org/10.1149/1.2979696>.
- [57] J.J. Lodico, C.H. Lai, M. Woodall, H.L. Chan, E. Garcia, W.A. Hubbard, B. Dunn, B.C. Regan, Irreversibility at macromolecular scales in the flake graphite of the lithium-ion battery anode, *J. Power Sources*. 436 (2019) 226841. <https://doi.org/10.1016/j.jpowsour.2019.226841>.
- [58] S. Taminato, M. Yonemura, S. Shiotani, T. Kamiyama, S. Torii, M. Nagao, Y. Ishikawa, K. Mori,

- T. Fukunaga, Y. Onodera, T. Naka, M. Morishima, Y. Ukyo, D.S. Adipranoto, H. Arai, Y. Uchimoto, Z. Ogumi, K. Suzuki, M. Hirayama, R. Kanno, Real-time observations of lithium battery reactions - Operando neutron diffraction analysis during practical operation, *Sci. Rep.* 6 (2016) 1–12. <https://doi.org/10.1038/srep28843>.
- [59] S. Schweidler, L. De Biasi, A. Schiele, P. Hartmann, T. Brezesinski, J. Janek, Volume Changes of Graphite Anodes Revisited: A Combined Operando X-ray Diffraction and *in situ* Pressure Analysis Study, *J. Phys. Chem. C.* 122 (2018) 8829–8835. <https://doi.org/10.1021/acs.jpcc.8b01873>.
- [60] J.R. Dahn, Phase diagram of  $\text{Li}_x\text{C}_6$ , *Phys. Rev. B.* 44 (1991) 9170–9177. <https://doi.org/10.1103/PhysRevB.44.9170>.
- [61] C. Gardner, E. Langhammer, A.J. Roberts, T. Amietszajew, Plasmonic based fibre optic detection and electrochemical identification of phase transitions in NMC111/graphite lithium-ion pouch cells, *J. Energy Storage.* 63 (2023) 107105. <https://doi.org/10.1016/J.EST.2023.107105>.
- [62] J.L. Lorie Lopez, P.J. Grandinetti, A.C. Co, Enhancing the real-time detection of phase changes in lithium–graphite intercalated compounds through derivative operando (dOp) NMR cyclic voltammetry, *J. Mater. Chem. A.* 6 (2017) 231–243. <https://doi.org/10.1039/C7TA07521A>.
- [63] A. Bard, L. Faulkner, *Electrochemical Methods: Fundamentals and Applications*, Second Ed, John Wiley and Sons, 2010.
- [64] H. Lee, M. Yanilmaz, O. Toprakci, K. Fu, X. Zhang, A review of recent developments in membrane separators for rechargeable lithium-ion batteries, *Energy Environ. Sci.* 7 (2014) 3857–3886. <https://doi.org/10.1039/c4ee01432d>.
- [65] P.M. Biesheuvel, J.E. Dykstra, The difference between Faradaic and Nonfaradaic processes in Electrochemistry, (2018). <http://arxiv.org/abs/1809.02930> (accessed September 22, 2020).
- [66] U.R. Koleti, A. Rajan, C. Tan, S. Moharana, T.Q. Dinh, J. Marco, A Study on the Influence of Lithium Plating on Battery Degradation, *Energies.* 13 (2020) 3458. <https://doi.org/10.3390/en13133458>.
- [67] A. Barai, K. Uddin, M. Dubarry, L. Somerville, A. McGordon, P. Jennings, I. Bloom, A comparison of methodologies for the non-invasive characterisation of commercial Li-ion cells, *Prog. Energy Combust. Sci.* 72 (2019) 1–31. <https://doi.org/10.1016/j.pecs.2019.01.001>.
- [68] V.J. Ovejas, A. Cuadras, Effects of cycling on lithium-ion battery hysteresis and overvoltage, *Sci. Rep.* 9 (2019) 1–9. <https://doi.org/10.1038/s41598-019-51474-5>.
- [69] A.C. Fisher, *Electrode Dynamics*, Oxford University Press, 1996.
- [70] T.R. Jow, S.A. Delp, J.L. Allen, J.-P. Jones, M.C. Smart, Factors Limiting  $\text{Li}^+$  Charge Transfer Kinetics in Li-ion Batteries, *J. Electrochem. Soc.* 165 (2018) A361–A367. <https://doi.org/10.1149/2.1221802jes>.
- [71] R.R. Thakkar, R.R. Thakkar, Electrical Equivalent Circuit Models of Lithium-ion Battery, *Manag. Appl. Energy Storage Devices.* (2021). <https://doi.org/10.5772/INTECHOPEN.99851>.
- [72] F. Scholz, *Voltammetric techniques of analysis: the essentials*, ChemTexts. 1 (2015) 1–24. <https://doi.org/10.1007/S40828-015-0016-Y/TABLES/1>.
- [73] B. Nan, L. Chen, N.D. Rodrigo, O. Borodin, N. Piao, J. Xia, T. Pollard, S. Hou, J. Zhang, X. Ji, J. Xu, X. Zhang, L. Ma, X. He, S. Liu, H. Wan, E. Hu, W. Zhang, K. Xu, X.Q. Yang, B. Lucht, C. Wang, Enhancing  $\text{Li}^+$  Transport in NMC811 | Graphite Lithium-Ion Batteries at Low Temperatures by Using Low-Polarity-Solvent Electrolytes, *Angew. Chemie Int. Ed.* 61 (2022) e202205967.

- <https://doi.org/10.1002/ANIE.202205967>.
- [74] J.H. Park, H. Yoon, Y. Cho, C.Y. Yoo, Investigation of lithium ion diffusion of graphite anode by the galvanostatic intermittent titration technique, *Materials (Basel)*. 14 (2021). <https://doi.org/10.3390/MA14164683/S1>.
- [75] J.S. Horner, G. Whang, D.S. Ashby, I. V. Kolesnichenko, T.N. Lambert, B.S. Dunn, A.A. Talin, S.A. Roberts, Electrochemical Modeling of GITT Measurements for Improved Solid-State Diffusion Coefficient Evaluation, *ACS Appl. Energy Mater.* 4 (2021) 11460–11469. [https://doi.org/10.1021/ACSAEM.1C02218/ASSET/IMAGES/LARGE/AE1C02218\\_0007.JPEG](https://doi.org/10.1021/ACSAEM.1C02218/ASSET/IMAGES/LARGE/AE1C02218_0007.JPEG).
- [76] L. Meyer, D. Curran, R. Brow, S. Santhanagopalan, J. Porter, Operando Measurements of Electrolyte Li-ion Concentration during fast charging with FTIR/ATR, *J. Electrochem. Soc.* 168 (2021) 090502. <https://doi.org/10.1149/1945-7111/ac1d7a>.
- [77] K. Hongyou, T. Hattori, Y. Nagai, T. Tanaka, H. Nii, K. Shoda, Dynamic *in situ* fourier transform infrared measurements of chemical bonds of electrolyte solvents during the initial charging process in a Li ion battery, *J. Power Sources.* 243 (2013) 72–77. <https://doi.org/10.1016/J.JPOWSOUR.2013.05.192>.
- [78] C.R. Birkel, M.R. Roberts, E. McTurk, P.G. Bruce, D.A. Howey, Degradation diagnostics for lithium ion cells, *J. Power Sources.* 341 (2017) 373–386. <https://doi.org/10.1016/j.jpowsour.2016.12.011>.
- [79] J.T. Warner, Lithium-ion battery operation, in: *Lithium-Ion Batter. Chem.*, Elsevier, 2019: pp. 43–77. <https://doi.org/10.1016/b978-0-12-814778-8.00003-x>.
- [80] F. Orsini, A. Du Pasquier, B. Beaudouin, J.M. Tarascon, M. Trentin, N. Langenhuizen, E. De Beer, P. Notten, *In situ* SEM study of the interfaces in plastic lithium cells, *J. Power Sources.* 81–82 (1999) 918–921. [https://doi.org/10.1016/S0378-7753\(98\)00241-9](https://doi.org/10.1016/S0378-7753(98)00241-9).
- [81] M. Petzl, M.A. Danzer, Nondestructive detection, characterization, and quantification of lithium plating in commercial lithium-ion batteries, *J. Power Sources.* 254 (2014) 80–87. <https://doi.org/10.1016/j.jpowsour.2013.12.060>.
- [82] S.S. Zhang, K. Xu, T.R. Jow, Study of the charging process of a LiCoO<sub>2</sub>-based Li-ion battery, *J. Power Sources.* 160 (2006) 1349–1354. <https://doi.org/10.1016/J.JPOWSOUR.2006.02.087>.
- [83] J. Vetter, P. Novák, M.R. Wagner, C. Veit, K.C. Möller, J.O. Besenhard, M. Winter, M. Wohlfahrt-Mehrens, C. Vogler, A. Hammouche, Ageing mechanisms in lithium-ion batteries, *J. Power Sources.* 147 (2005) 269–281. <https://doi.org/10.1016/j.jpowsour.2005.01.006>.
- [84] M. Tang, P. Albertus, J. Newman, Two-Dimensional Modeling of Lithium Deposition during Cell Charging, *J. Electrochem. Soc.* 156 (2009) A390. <https://doi.org/10.1149/1.3095513/XML>.
- [85] I.D. Campbell, M. Marzook, M. Marinescu, G.J. Offer, How Observable Is Lithium Plating? Differential Voltage Analysis to Identify and Quantify Lithium Plating Following Fast Charging of Cold Lithium-Ion Batteries, *J. Electrochem. Soc.* 166 (2019) A725–A739. <https://doi.org/10.1149/2.0821904jes>.
- [86] U. Janakiraman, T.R. Garrick, M.E. Fortier, Review—Lithium Plating Detection Methods in Li-ion Batteries, *J. Electrochem. Soc.* 167 (2020) 160552. <https://doi.org/10.1149/1945-7111/abd3b8>.
- [87] L.J. Aaldering, C.H. Song, Tracing the technological development trajectory in post-lithium-ion battery technologies: A patent-based approach, *J. Clean. Prod.* 241 (2019). <https://doi.org/10.1016/j.jclepro.2019.118343>.

- [88] W.K. Tan, G. Kawamura, H. Muto, A. Matsuda, Current progress in the development of Fe-air batteries and their prospects for next-generation batteries, in: *Sustain. Mater. Next Gener. Energy Devices Challenges Oppor.*, Elsevier, 2020: pp. 59–83. <https://doi.org/10.1016/B978-0-12-820628-7.00003-4>.
- [89] H. Zhang, C. Sun, Cost-effective iron-based aqueous redox flow batteries for large-scale energy storage application: A review, *J. Power Sources.* 493 (2021). <https://doi.org/10.1016/j.jpowsour.2020.229445>.
- [90] J. Kasemchainan, P.G. Bruce, All-solid-state batteries and their remaining challenges, *Johnson Matthey Technol. Rev.* 62 (2018) 177–180. <https://doi.org/10.1595/205651318X696747>.
- [91] S. Gifford, Lithium-Sulfur Batteries: Transformative Technology, Global Commercial Activity and Building a British Industrial Hub – The Faraday Institution, (n.d.). <https://faraday.ac.uk/lis-transformative-tech/> (accessed October 6, 2020).
- [92] S. Gifford, Lithium-Sulfur Batteries: Advantages – The Faraday Institution, (n.d.). <https://faraday.ac.uk/lis-advantages/> (accessed October 6, 2020).
- [93] N. Kheirabadi, A. Shafiekhani, Graphene/Li-ion battery, *J. Appl. Phys.* 112 (2012). <https://doi.org/10.1063/1.4771923>.
- [94] A.J. Louli, L.D. Ellis, J.R. Dahn, Operando Pressure Measurements Reveal Solid Electrolyte Interphase Growth to Rank Li-ion Cell Performance, *Joule.* 3 (2019) 745–761. <https://doi.org/10.1016/j.joule.2018.12.009>.
- [95] J.Y. Hwang, S.T. Myung, Y.K. Sun, Sodium-ion batteries: Present and future, *Chem. Soc. Rev.* 46 (2017) 3529–3614. <https://doi.org/10.1039/c6cs00776g>.
- [96] T. Shang, Y. Wen, D. Xiao, L. Gu, Y.-S. Hu, H. Li, Atomic-Scale Monitoring of Electrode Materials in Lithium-Ion Batteries using *In situ* Transmission Electron Microscopy, *Adv. Energy Mater.* 7 (2017) 1700709. <https://doi.org/10.1002/aenm.201700709>.
- [97] T. Amietszajew, E. McTurk, J. Fleming, R. Bhagat, Understanding the limits of rapid charging using instrumented commercial 18650 high-energy Li-ion cells, *Electrochim. Acta.* 263 (2018) 346–352. <https://doi.org/10.1016/j.electacta.2018.01.076>.
- [98] N. Kirkaldy, M.A. Samieian, G.J. Offer, M. Marinescu, Y. Patel, Lithium-Ion Battery Degradation: Measuring Rapid Loss of Active Silicon in Silicon–Graphite Composite Electrodes, *ACS Appl. Energy Mater.* 17 (2022) 41. [https://doi.org/10.1021/ACSAEM.2C02047/ASSET/IMAGES/LARGE/AE2C02047\\_0006.JPEG](https://doi.org/10.1021/ACSAEM.2C02047/ASSET/IMAGES/LARGE/AE2C02047_0006.JPEG).
- [99] J. Tian, R. Xiong, W. Shen, A review on state of health estimation for lithium ion batteries in photovoltaic systems, *ETransportation.* 2 (2019) 100028. <https://doi.org/10.1016/j.etrans.2019.100028>.
- [100] C. Li, Z. Yu Wang, Z. Jiang He, Y. Jiao Li, J. Mao, K. Hua Dai, C. Yan, J. Chao Zheng, An advance review of solid-state battery: Challenges, progress and prospects, *Sustain. Mater. Technol.* 29 (2021) e00297. <https://doi.org/10.1016/J.SUSMAT.2021.E00297>.
- [101] A.J. Louli, A. Eldesoky, R. Weber, M. Genovese, M. Coon, J. DeGooyer, Z. Deng, R.T. White, J. Lee, T. Rodgers, R. Petibon, S. Hy, S.J.H. Cheng, J.R. Dahn, Diagnosing and correcting anode-free cell failure via electrolyte and morphological analysis, *Nat. Energy.* (2020). <https://doi.org/10.1038/s41560-020-0668-8>.
- [102] B. Mosallanejad, S.S. Malek, M. Ershadi, A.A. Daryakenari, Q. Cao, F. Boorboor Ajdari, S. Ramakrishna, Cycling degradation and safety issues in sodium-ion batteries: Promises of

- electrolyte additives, *J. Electroanal. Chem.* 895 (2021) 115505. <https://doi.org/10.1016/j.jelechem.2021.115505>.
- [103] K.S. Ng, C.-S. Moo, Y.-P. Chen, Y.-C. Hsieh, Enhanced coulomb counting method for estimating state-of-charge and state-of-health of lithium-ion batteries, *Appl. Energy*. 86 (2009) 1506–1511. <https://ideas.repec.org/a/eee/appene/v86y2009i9p1506-1511.html> (accessed August 16, 2020).
- [104] D. Qu, W. Ji, H. Qu, Probing process kinetics in batteries with electrochemical impedance spectroscopy, *Commun. Mater.* 2022 31. 3 (2022) 1–9. <https://doi.org/10.1038/s43246-022-00284-w>.
- [105] L.A. Middlemiss, A.J.R. Rennie, R. Sayers, A.R. West, Characterisation of batteries by electrochemical impedance spectroscopy, in: *Energy Reports*, Elsevier Ltd, 2020: pp. 232–241. <https://doi.org/10.1016/j.egy.2020.03.029>.
- [106] I.A.J. Gordon, S. Grugeon, H. Takenouti, B. Tribollet, M. Armand, C. Davoisne, A. Débart, S. Laruelle, Electrochemical Impedance Spectroscopy response study of a commercial graphite-based negative electrode for Li-ion batteries as function of the cell state of charge and ageing, *Electrochim. Acta*. 223 (2017) 63–73. <https://doi.org/10.1016/j.electacta.2016.12.013>.
- [107] D. Ren, H. Hsu, R. Li, X. Feng, D. Guo, X. Han, L. Lu, X. He, S. Gao, J. Hou, Y. Li, Y. Wang, M. Ouyang, A comparative investigation of aging effects on thermal runaway behavior of lithium-ion batteries, *ETransportation*. 2 (2019) 100034. <https://doi.org/10.1016/j.etrans.2019.100034>.
- [108] Z. Wang, G. Feng, D. Zhen, F. Gu, A. Ball, A review on online state of charge and state of health estimation for lithium-ion batteries in electric vehicles, *Energy Reports*. 7 (2021) 5141–5161. <https://doi.org/10.1016/J.EGYR.2021.08.113>.
- [109] L. Yao, S. Xu, A. Tang, F. Zhou, J. Hou, Y. Xiao, Z. Fu, A Review of Lithium-Ion Battery State of Health Estimation and Prediction Methods, *World Electr. Veh. J.* 2021, Vol. 12, Page 113. 12 (2021) 113. <https://doi.org/10.3390/WEVJ12030113>.
- [110] F. Heinrich, P. Klapper, M. Pruckner, A comprehensive study on battery electric modeling approaches based on machine learning, *Energy Informatics*. 4 (2021) 1–17. <https://doi.org/10.1186/S42162-021-00171-7/FIGURES/9>.
- [111] B. Wu, W.D. Widanage, S. Yang, X. Liu, Battery digital twins: Perspectives on the fusion of models, data and artificial intelligence for smart battery management systems, *Energy AI*. 1 (2020) 100016. <https://doi.org/10.1016/J.EGYAI.2020.100016>.
- [112] P.P.R.M.L. Harks, F.M. Mulder, P.H.L. Notten, *In situ* methods for Li-ion battery research: A review of recent developments, *J. Power Sources*. 288 (2015) 92–105. <https://doi.org/10.1016/j.jpowsour.2015.04.084>.
- [113] J.R. Goldstein, J., Newbury, D.E., Joy, D.C., Lyman, C.E., Echlin, P., Lifshin, E., Sawyer, L., Michael, Scanning Electron Microscopy and X-ray Microanalysis - | Joseph Goldstein | Springer, Springer US, 2003. <https://doi.org/10.1007/978-1-4615-0215-9>.
- [114] P.P.R.M.L. Harks, F.M. Mulder, P.H.L. Notten, *In situ* methods for Li-ion battery research: A review of recent developments, *J. Power Sources*. (2015). <https://doi.org/10.1016/j.jpowsour.2015.04.084>.
- [115] A.J. Merryweather, C. Schnedermann, Q. Jacquet, C.P. Grey, A. Rao, Operando optical tracking of single-particle ion dynamics in batteries, *Nat.* 2021 5947864. 594 (2021) 522–528. <https://doi.org/10.1038/s41586-021-03584-2>.

- [116] A.L. Lipson, R.S. Ginder, M.C. Hersam, Nanoscale *In situ* Characterization of Li-ion Battery Electrochemistry Via Scanning Ion Conductance Microscopy, *Adv. Mater.* 23 (2011) 5613–5617. <https://doi.org/10.1002/ADMA.201103094>.
- [117] H.L. Wu, L.A. Huff, J.L. Esbenschade, A.A. Gewirth, *In situ* EQCM Study Examining Irreversible Changes the Sulfur-Carbon Cathode in Lithium-Sulfur Batteries, *ACS Appl. Mater. Interfaces.* 7 (2015) 20820–20828. [https://doi.org/10.1021/ACSAMI.5B05955/SUPPL\\_FILE/AM5B05955\\_SI\\_001.PDF](https://doi.org/10.1021/ACSAMI.5B05955/SUPPL_FILE/AM5B05955_SI_001.PDF).
- [118] J. Fleming, T. Amietszajew, J. Charmet, A.J. Roberts, D. Greenwood, R. Bhagat, The design and impact of in-situ and operando thermal sensing for smart energy storage, *J. Energy Storage.* 22 (2019) 36–43. <https://doi.org/10.1016/J.EST.2019.01.026>.
- [119] E. McTurk, C.R. Birkl, M.R. Roberts, D.A. Howey, P.G. Bruce, Minimally invasive insertion of reference electrodes into commercial lithium-ion pouch cells, *ECS Electrochem. Lett.* 4 (2015) A145–A147. <https://doi.org/10.1149/2.0081512eel>.
- [120] F. La Mantia, C.D. Wessells, H.D. Deshazer, Y. Cui, Reliable reference electrodes for lithium-ion batteries, *Electrochem. Commun.* 31 (2013) 141–144. <https://doi.org/10.1016/j.elecom.2013.03.015>.
- [121] J.B. Robinson, R.E. Owen, M.D.R. Kok, M. Maier, J. Majasan, M. Braglia, R. Stocker, T. Amietszajew, A.J. Roberts, R. Bhagat, D. Billsson, J.Z. Olson, J. Park, G. Hinds, A.A. Tidblad, D.J.L. Brett, P.R. Shearing, Identifying Defects in Li-ion Cells Using Ultrasound Acoustic Measurements, *J. Electrochem. Soc.* 167 (2020) 120530. <https://doi.org/10.1149/1945-7111/ABB174>.
- [122] N. Zhou, X. Cui, C. Han, Z. Yang, Analysis of Acoustic Characteristics under Battery External Short Circuit Based on Acoustic Emission, *Energies* 2022, Vol. 15, Page 1775. 15 (2022) 1775. <https://doi.org/10.3390/EN15051775>.
- [123] S. Schweidler, M. Bianchini, P. Hartmann, T. Brezesinski, J. Janek, The Sound of Batteries: An Operando Acoustic Emission Study of the LiNiO<sub>2</sub> Cathode in Li-Ion Cells, *Batter. Supercaps.* 3 (2020) 1021–1027. <https://doi.org/10.1002/BATT.202000099>.
- [124] J.O. Majasan, J.B. Robinson, R.E. Owen, M. Maier, A.N.P. Radhakrishnan, M. Pham, T.G. Tranter, Y. Zhang, P.R. Shearing, D.J.L. Brett, Recent advances in acoustic diagnostics for electrochemical power systems, *J. Phys. Energy.* 3 (2021) 032011. <https://doi.org/10.1088/2515-7655/ABFB4A>.
- [125] J. Fleming, T. Amietszajew, E. McTurk, D. Greenwood, R. Bhagat, Development and evaluation of in-situ instrumentation for cylindrical Li-ion cells using fibre optic sensors, *HardwareX.* 3 (2018) 100–109. <https://doi.org/10.1016/j.ohx.2018.04.001>.
- [126] X. Dong, H. Zhang, B. Liu, Y. Miao, Tilted fiber bragg gratings: Principle and sensing applications, *Photonic Sensors.* 1 (2011) 6–30. <https://doi.org/10.1007/s13320-010-0016-x>.
- [127] J. Hedman, D. Nilebo, E. Larsson Langhammer, F. Björefors, Fibre Optic Sensor for Characterisation of Lithium-Ion Batteries, *ChemSusChem.* (2020) cssc.202001709. <https://doi.org/10.1002/cssc.202001709>.
- [128] A. Raghavan, P. Kiesel, L.W. Sommer, J. Schwartz, A. Lochbaum, A. Hegyi, A. Schuh, K. Arakaki, B. Saha, A. Ganguli, K.H. Kim, C.A. Kim, H.J. Hah, S.K. Kim, G.O. Hwang, G.C. Chung, B. Choi, M. Alamgir, Embedded fiber-optic sensing for accurate internal monitoring of cell state in advanced battery management systems part 1: Cell embedding method and performance, *J. Power Sources.* 341 (2017) 466–473. <https://doi.org/10.1016/j.jpowsour.2016.11.104>.
- [129] L. Zdravkova, Fiber Optic Sensor for In-Situ State-of-Charge Monitoring for Lithium-Ion

- Batteries, University of Waterloo, 2015. <https://uwspace.uwaterloo.ca/handle/10012/9059> (accessed August 4, 2020).
- [130] J.E. Fischer, J.M. Bloch, C.C. Shieh, M.E. Preil, K. Jelley, Reflectivity spectra and dielectric function of stage-1 donor intercalation compounds of graphite, *Phys. Rev. B.* 31 (1985) 4773–4783. <https://doi.org/10.1103/PhysRevB.31.4773>.
- [131] S.J. Harris, A. Timmons, D.R. Baker, C. Monroe, Direct *in situ* measurements of Li transport in Li-ion battery negative electrodes, *Chem. Phys. Lett.* 485 (2010) 265–274. <https://doi.org/10.1016/j.cplett.2009.12.033>.
- [132] Y.-D. Su, Y. Preger, H. Burroughs, C. Sun, P. Ohodnicki, Fiber Optic Sensing Technologies for Battery Management Systems and Energy Storage Applications, *Sensors.* 21 (2021) 1397. <https://doi.org/10.3390/s21041397>.
- [133] J. Fleming, T. Amietszajew, E. McTurk, D. Greenwood, R. Bhagat, Development and evaluation of in-situ instrumentation for cylindrical Li-ion cells using fibre optic sensors, *HardwareX.* 3 (2018) 100–109. <https://doi.org/10.1016/J.OHX.2018.04.001>.
- [134] M. Nascimento, S. Novais, M.S. Ding, M.S. Ferreira, S. Koch, S. Passerini, J.L. Pinto, Internal strain and temperature discrimination with optical fiber hybrid sensors in Li-ion batteries, *J. Power Sources.* 410–411 (2019) 1–9. <https://doi.org/10.1016/j.jpowsour.2018.10.096>.
- [135] M. Nascimento, M.S. Ferreira, J.L. Pinto, Temperature fiber sensing of Li-ion batteries under different environmental and operating conditions, *Appl. Therm. Eng.* 149 (2019) 1236–1243. <https://doi.org/10.1016/j.applthermaleng.2018.12.135>.
- [136] A. Nedjalkov, J. Meyer, A. Gräfenstein, B. Schramm, M. Angelmahr, J. Schwenzel, W. Schade, Refractive Index Measurement of Lithium Ion Battery Electrolyte with Etched Surface Cladding Waveguide Bragg Gratings and Cell Electrode State Monitoring by Optical Strain Sensors, *Batteries.* 5 (2019) 30. <https://doi.org/10.3390/batteries5010030>.
- [137] L.W. Sommer, P. Kiesel, A. Ganguli, A. Lochbaum, B. Saha, J. Schwartz, C.J. Bae, M. Alamgir, A. Raghavan, Fast and slow ion diffusion processes in lithium ion pouch cells during cycling observed with fiber optic strain sensors, *J. Power Sources.* 296 (2015) 46–52. <https://doi.org/10.1016/j.jpowsour.2015.07.025>.
- [138] L.W. Sommer, A. Raghavan, P. Kiesel, B. Saha, J. Schwartz, A. Lochbaum, A. Ganguli, C.-J. Bae, M. Alamgir, Monitoring of Intercalation Stages in Lithium-Ion Cells over Charge-Discharge Cycles with Fiber Optic Sensors, *J. Electrochem. Soc.* 162 (2015) A2664–A2669. <https://doi.org/10.1149/2.0361514jes>.
- [139] J. Huang, L. Albero Blanquer, J. Bonafino, E.R. Logan, D. Alves Dalla Corte, C. Delacourt, B.M. Gallant, S.T. Boles, J.R. Dahn, H.Y. Tam, J.M. Tarascon, Operando decoding of chemical and thermal events in commercial Na(Li)-ion cells via optical sensors, *Nat. Energy.* (2020) 1–10. <https://doi.org/10.1038/s41560-020-0665-y>.
- [140] A. Ganguli, B. Saha, A. Raghavan, P. Kiesel, K. Arakaki, A. Schuh, J. Schwartz, A. Hegyi, L.W. Sommer, A. Lochbaum, S. Sahu, M. Alamgir, Embedded fiber-optic sensing for accurate internal monitoring of cell state in advanced battery management systems part 2: Internal cell signals and utility for state estimation, *J. Power Sources.* 341 (2017) 474–482. <https://doi.org/10.1016/j.jpowsour.2016.11.103>.
- [141] Y.J. Rao, In-fibre Bragg grating sensors, *Meas. Sci. Technol.* 8 (1997) 355–375. <https://doi.org/10.1088/0957-0233/8/4/002>.
- [142] C. Caucheteur, T. Guo, J. Albert, Review of plasmonic fiber optic biochemical sensors: improving

- the limit of detection, *Anal. Bioanal. Chem.* 407 (2015) 3883–3897. <https://doi.org/10.1007/s00216-014-8411-6>.
- [143] G. Han, J. Yan, Z. Guo, D. Greenwood, J. Marco, Y. Yu, A review on various optical fibre sensing methods for batteries, *Renew. Sustain. Energy Rev.* 150 (2021). <https://doi.org/10.1016/J.RSER.2021.111514>.
- [144] P. Larkin, *Infrared and Raman spectroscopy: principles and spectral interpretation*, 2017. [https://books.google.co.uk/books?hl=en&lr=&id=bMgpDwAAQBAJ&oi=fnd&pg=PP1&dq=Peter+J.+Larkin,+in+Infrared+and+Raman+Spectroscopy+\(Second+Edition\),+2018&ots=\\_qDsvbUsjA&sig=r\\_WUhrLmBFh-4AjoI6LR0odJ\\_sl](https://books.google.co.uk/books?hl=en&lr=&id=bMgpDwAAQBAJ&oi=fnd&pg=PP1&dq=Peter+J.+Larkin,+in+Infrared+and+Raman+Spectroscopy+(Second+Edition),+2018&ots=_qDsvbUsjA&sig=r_WUhrLmBFh-4AjoI6LR0odJ_sl) (accessed September 17, 2020).
- [145] PerkinElmer, *The Effects of Varying Force and Contact on ATR Spectra*, 2012. [https://www.perkinelmer.com/lab-solutions/resources/docs/TCH\\_010127\\_01\\_ATR.pdf](https://www.perkinelmer.com/lab-solutions/resources/docs/TCH_010127_01_ATR.pdf) (accessed September 17, 2020).
- [146] J. Hedman, D. Nilebo, E. Larsson Langhammer, F. Björefors, Fibre Optic Sensor for Characterisation of Lithium-Ion Batteries, *ChemSusChem.* 13 (2020) 5731–5739. <https://doi.org/10.1002/cssc.202001709>.
- [147] J. Hedman, F. Björefors, Fiber Optic Monitoring of Composite Lithium Iron Phosphate Cathodes in Pouch Cell Batteries, *ACS Appl. Energy Mater.* 5 (2022) 870–881. <https://doi.org/10.1021/acsaem.1c03304>.
- [148] A. Ghannoum, P. Nieva, A. Yu, A. Khajepour, Development of Embedded Fiber-Optic Evanescent Wave Sensors for Optical Characterization of Graphite Anodes in Lithium-Ion Batteries, *ACS Appl. Mater. Interfaces.* 9 (2017) 41284–41290. <https://doi.org/10.1021/acsami.7b13464>.
- [149] A.R. Ghannoum, P. Nieva, Graphite lithiation and capacity fade monitoring of lithium ion batteries using optical fibers, *J. Energy Storage.* 28 (2020) 101233. <https://doi.org/10.1016/j.est.2020.101233>.
- [150] A. Ghannoum, R.C. Norris, K. Iyer, L. Zdravkova, A. Yu, P. Nieva, Optical Characterization of Commercial Lithiated Graphite Battery Electrodes and *in situ* Fiber Optic Evanescent Wave Spectroscopy, *ACS Appl. Mater. Interfaces.* 8 (2016) 18763–18769. <https://doi.org/10.1021/acsami.6b03638>.
- [151] J. Hedman, R. Mogensen, R. Younesi, F. Björefors, Fiber Optical Detection of Lithium Plating at Graphite Anodes, *Adv. Mater. Interfaces.* 10 (2023) 2201665. <https://doi.org/10.1002/ADMI.202201665>.
- [152] Y.-D. Su, Y. Preger, H. Burroughs, C. Sun, P. Ohodnicki, Fiber Optic Sensing Technologies for Battery Management Systems and Energy Storage Applications, *Sensors.* 21 (2021) 1397. <https://doi.org/10.3390/s21041397>.
- [153] N.A. Padilla, M.T. Rea, M. Foy, S.P. Upadhyay, K.A. Desrochers, T. Derus, K.A. Knapper, N.H. Hunter, S. Wood, D.A. Hinton, A.C. Cavell, A.G. Masias, R.H. Goldsmith, Tracking lithium ions via widefield fluorescence microscopy for battery diagnostics, *ACS Sensors.* 2 (2017) 903–908. [https://doi.org/10.1021/ACSENSORS.7B00087/SUPPL\\_FILE/SE7B00087\\_SI\\_002.AVI](https://doi.org/10.1021/ACSENSORS.7B00087/SUPPL_FILE/SE7B00087_SI_002.AVI).
- [154] E. Vergori, Y. Yu, Monitoring of Li-ion cells with distributed fibre optic sensors, in: *Procedia Struct. Integr.*, Elsevier B.V., 2019: pp. 233–239. <https://doi.org/10.1016/j.prostr.2020.02.020>.
- [155] J. Huang, S.T. Boles, J.M. Tarascon, Sensing as the key to battery lifetime and sustainability, *Nat. Sustain.* 5 (2022) 194–204. <https://doi.org/10.1038/s41893-022-00859-y>.

- [156] A. Rogers, Distributed optical-fibre sensing, *Meas. Sci. Technol.* 10 (1999) R75. <https://doi.org/10.1088/0957-0233/10/8/201>.
- [157] V. Chabot, Y. Miron, M. Grandbois, P.G. Charette, Long range surface plasmon resonance for increased sensitivity in living cell biosensing through greater probing depth, *Sensors Actuators, B Chem.* 174 (2012) 94–101. <https://doi.org/10.1016/j.snb.2012.08.028>.
- [158] U. Künzelmann, H. Schumacher, Characterization of surface processes during oxide CMP by *in situ* FTIR spectroscopy, in: *Adv. Chem. Mech. Planarization*, Elsevier Inc., 2016: pp. 1–396. <https://doi.org/10.1016/B978-0-08-100165-3.00014-0>.
- [159] A. Lanzarotta, Approximating the detection limit of an infrared spectroscopic imaging microscope operating in an Attenuated Total Reflection (ATR) modality: Theoretical and empirical results for an instrument using a linear array detector and a 1.5 millimeter germanium hemisphere internal reflection element, *Appl. Spectrosc.* 69 (2015) 205–214. <https://doi.org/10.1366/14-07538>.
- [160] J. Jatschka, A. Dathe, A. Csáki, W. Fritzsche, O. Stranik, Propagating and localized surface plasmon resonance sensing - A critical comparison based on measurements and theory, *Sens. Bio-Sensing Res.* 7 (2016) 62–70. <https://doi.org/10.1016/j.sbsr.2016.01.003>.
- [161] S. Qian, X. Chen, S. Jiang, Q. Sun, X. Chen, J. Lu, Y. Geng, M. Duan, X. Li, X. Li, S. Liu, S. Liu, Plasmonic fiber-optic sensing system for *in situ* monitoring the capacitance and temperature of supercapacitors, *Opt. Express*, Vol. 30, Issue 15, Pp. 27322-27332. 30 (2022) 27322–27332. <https://doi.org/10.1364/OE.462189>.
- [162] R. Wang, H. Zhang, Q. Liu, F. Liu, X. Han, X. Liu, K. Li, G. Xiao, J. Albert, X. Lu, T. Guo, Operando monitoring of ion activities in aqueous batteries with plasmonic fiber-optic sensors, *Nat. Commun.* 13 (2022) 547. <https://doi.org/10.1038/s41467-022-28267-y>.
- [163] A. Ganguli, B. Saha, A. Raghavan, P. Kiesel, K. Arakaki, A. Schuh, J. Schwartz, A. Hegyi, L.W. Sommer, A. Lochbaum, S. Sahu, M. Alamgir, Embedded fiber-optic sensing for accurate internal monitoring of cell state in advanced battery management systems part 2: Internal cell signals and utility for state estimation, *J. Power Sources.* 341 (2017) 474–482. <https://doi.org/10.1016/j.jpowsour.2016.11.103>.
- [164] K. Berger, J.P. Schögl, R.J. Baumgartner, Digital battery passports to enable circular and sustainable value chains: Conceptualization and use cases, *J. Clean. Prod.* 353 (2022) 131492. <https://doi.org/10.1016/j.jclepro.2022.131492>.
- [165] J. Catton, S.B. Walker, P. McInnis, M. Fowler, R. Fraser, S.B. Young, B. Gaffney, Comparative safety risk and the use of repurposed EV batteries for stationary energy storage, 2017 5th IEEE Int. Conf. Smart Energy Grid Eng. SEGE 2017. (2017) 200–209. <https://doi.org/10.1109/SEGE.2017.8052799>.
- [166] Battery Passport, (n.d.). <https://www.globalbattery.org/battery-passport/> (accessed February 9, 2023).
- [167] S.J. An, J. Li, Y. Sheng, C. Daniel, D.L. Wood III, Long-Term Lithium-Ion Battery Performance Improvement via Ultraviolet Light Treatment of the Graphite Anode, *J. Electrochem. Soc.* 163 (2016) A2866–A2875. <https://doi.org/10.1149/2.0171614jes>.
- [168] A. Dmitriev, Nanoplasmonic sensors, (2012).
- [169] C. Sundvall, E. Langhammer, I. Löfgren, A. Holmer, D. Westerlund, Operando Nanoplasmonic sensing – a means of improving battery control – WP2 Report- ACES Project, 2021.

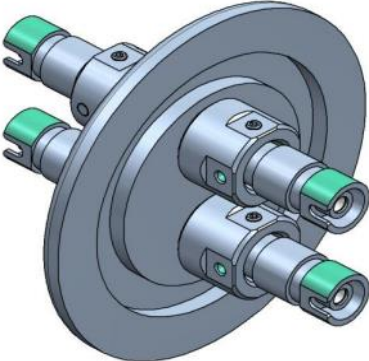
- [170] Y. Liu, Y. Ma, One-Dimensional Plasmonic Sensors, *Front. Phys.* 8 (2020) 312. <https://doi.org/10.3389/fphy.2020.00312>.
- [171] Z. Ahmed, A.J. Roberts, T. Amietszajew, Ti-Based Reference Electrodes for Inline Implementation into Lithium-Ion Pouch Cells, *Energy Technol.* 9 (2021) 2100602. <https://doi.org/10.1002/ente.202100602>.
- [172] S. Wang, J. Zhang, O. Gharbi, V. Vivier, M. Gao, M.E. Orazem, Electrochemical impedance spectroscopy, *Nat. Rev. Methods Prim.* 1 (2021). <https://doi.org/10.1038/S43586-021-00039-W>.
- [173] T. Waldmann, M. Wilka, M. Kasper, M. Fleischhammer, M. Wohlfahrt-Mehrens, Temperature dependent ageing mechanisms in Lithium-ion batteries – A Post-Mortem study, *J. Power Sources.* 262 (2014) 129–135. <https://doi.org/10.1016/J.JPOWSOUR.2014.03.112>.
- [174] Y. Leng, Materials characterization: Introduction to microscopic and spectroscopic methods: Second edition, *Mater. Charact. Introd. to Microsc. Spectrosc. Methods Second Ed.* (2013) 1–376. <https://doi.org/10.1002/9783527670772>.
- [175] H.F. Li, J.K. Gao, S.L. Zhang, Effect of Overdischarge on Swelling and Recharge Performance of Lithium Ion Cells, *Chinese J. Chem.* 26 (2008) 1585–1588. <https://doi.org/10.1002/CJOC.200890286>.
- [176] C. Wenge, B. Arendarski, S. Balischewski, M. Hallmann, M. Nilsson, I. Löfgren, Multi-functional use of battery storage in micro-grid- WP4- ACES Project, 2021.
- [177] C. Xu, A.J. Merryweather, S.S. Pandurangi, Z. Lun, D.S. Hall, V.S. Deshpande, N.A. Fleck, C. Schnedermann, A. Rao, C.P. Grey, Operando visualization of kinetically induced lithium heterogeneities in single-particle layered Ni-rich cathodes, *Joule.* 0 (2022). <https://doi.org/10.1016/J.JOULE.2022.09.008>.
- [178] B. Gulsoy, T.A. Vincent, J.E.H. Sansom, J. Marco, In-situ temperature monitoring of a lithium-ion battery using an embedded thermocouple for smart battery applications, *J. Energy Storage.* 54 (2022) 105260. <https://doi.org/10.1016/J.EST.2022.105260>.
- [179] J. Hemmerling, J. Schäfer, T. Jung, T. Kreher, M. Ströbel, C. Gassmann, J. Günther, A. Fill, K.P. Birke, Investigation of internal gas pressure and internal temperature of cylindrical Li-ion cells to study thermodynamical and mechanical properties of hard case battery cells, *J. Energy Storage.* 59 (2023) 106444. <https://doi.org/10.1016/J.EST.2022.106444>.
- [180] J. Kim, S. Park, S. Hwang, W.-S. Yoon, Principles and Applications of Galvanostatic Intermittent Titration Technique for Lithium-ion Batteries, *J. Electrochem. Sci. Technol.* (2021). <https://doi.org/10.33961/jecst.2021.00836>.
- [181] T.S. Pathan, M. Rashid, M. Walker, W.D. Widanage, E. Kendrick, Active formation of Li-ion batteries and its effect on cycle life, *JPhys Energy.* 1 (2019). <https://doi.org/10.1088/2515-7655/ab2e92>.
- [182] I. Landa-Medrano, A. Eguia-Barrio, S. Sananes-Israel, S. Lijó-Pando, I. Boyano, F. Alcaide, I. Urdampilleta, I. de Meatza, *In situ* Analysis of NMC|graphite Li-ion Batteries by Means of Complementary Electrochemical Methods, *J. Electrochem. Soc.* 167 (2020) 090528. <https://doi.org/10.1149/1945-7111/ab8b99>.
- [183] K. Fröhlich, I. Abrahams, M. Jahn, Determining phase transitions of layered oxides via electrochemical and crystallographic analysis, *Sci. Technol. Adv. Mater.* 21 (2020) 653–660. <https://doi.org/10.1080/14686996.2020.1814116>.

- [184] K.M. Shaju, G. V. Subba Rao, B.V.R. Chowdari, Performance of layered  $\text{Li}(\text{Ni}_{1/3}\text{Co}_{1/3}\text{Mn}_{1/3})\text{O}_2$  as cathode for Li-ion batteries, *Electrochim. Acta.* 48 (2002) 145–151. [https://doi.org/10.1016/S0013-4686\(02\)00593-5](https://doi.org/10.1016/S0013-4686(02)00593-5).
- [185] C. Gardner, E. Langhammer, W. Du, D.J.L. Brett, P.R. Shearing, A.J. Roberts, T. Amietszajew, In-Situ Li-ion Pouch Cell Diagnostics Utilising Plasmonic Based Optical Fibre Sensors, *Sensors.* 22 (2022) 738. <https://doi.org/10.3390/s22030738>.
- [186] S.C. Yin, Y.H. Rho, I. Swainson, L.F. Nazar, X-ray/neutron diffraction and electrochemical studies of lithium De/Re-intercalation in  $\text{Li}_{1-x}\text{Co}_{1/3}\text{Ni}_{1/3}\text{Mn}_{1/3}\text{O}_2$  ( $x = 0 \rightarrow 1$ ), *Chem. Mater.* 18 (2006) 1901–1910. <https://doi.org/10.1021/cm0511769>.
- [187] M. Nascimento, S. Novais, C. Leitão, M.F. Domingues, N. Alberto, P. Antunes, J.L. Pinto, Lithium batteries temperature and strain fiber monitoring, in: 24th Int. Conf. Opt. Fibre Sensors, SPIE, 2015: p. 96347V. <https://doi.org/10.1117/12.2195218>.
- [188] Y. Yu, E. Vergori, F. Maddar, Y. Guo, D. Greenwood, J. Marco, Real-time monitoring of internal structural deformation and thermal events in lithium-ion cell via embedded distributed optical fibre, *J. Power Sources.* 521 (2022) 230957. <https://doi.org/10.1016/j.jpowsour.2021.230957>.

## 8. Appendices

### 8.1. Appendix A- Specification and order of glovebox optical pass through

Order for optical pass through for glovebox, this part was customized designed as per the specifications provided to the supplier to meet the requirements of this project. This unit enables the optical equipment sensors to be used inside the glovebox, enabling their use in electrolyte testing and open cell based experiments.

#	Description	Required quantity	Unit price (EUR)	Total line price (EUR)
10	<p><b><u>2-Ch Fiber Optic Adapter Feedthrough</u></b></p> <p><b>Interface: FC/PC (Female, wide key, SS 304L)</b></p> <p><b>Fiber: MM 100/110/125 Polyimide, NA 0.28, 400-2400nm, Silica/Silica, Optran WF</b></p> <p><b>Flange: KF 40 (SS 304L)</b></p>  <p><b>Vacuum compatible</b> <b>Include double vacuum packaging</b></p>	1+	730	730

## 8.2. Appendix B- Formation step settings

Step 0 is just a 10 second rest, to activate the equipment and software before starting the experiment.

The settings for the formation cycles steps 1 and 2 respectively are shown below.

<input type="checkbox"/> Turn to OCV between techniques	
0	1
0	1
0	2
0	2

<p>① Set <math>I</math> to <math>I_s = 70.000</math> mA vs. &lt;None&gt;</p> <p>for at most <math>t_1 = 30</math> h 0 mn 0.000 0 s</p> <p>Limit <math>E_{we} &gt; E_M = 4.200</math> V</p> <p>Record every <math>dE_1 = 10.0</math> mV</p> <p>or <math>dt_1 = 10.000 0</math> s</p> <hr/> <p>Hold <math>E_M</math> for <math>t_M = 4</math> h 0 mn 0.000 0 s</p> <p>Limit <math> I  &lt; I_m = 14.000</math> mA</p> <p>or <math> dI/dt  &lt; dI/dt_f = 0.000</math> mA/s</p> <p>Record every <math>dQ = 10.000</math> mA.h</p> <p>or <math>dt_q = 120.000 0</math> s</p> <hr/> <p>Limit <math> \Delta Q  &gt; \Delta Q_M = 0.000</math> mA.h</p> <p><math>\Leftrightarrow \Delta x_M = 0.000</math></p> <p><math> \Delta SoC  &gt; \text{pass}</math> %</p> <hr/> <p>E Range = 0 V; 5 V</p> <p><i>Resolution = 100 <math>\mu</math>V</i></p> <p>I Range = 100 mA</p> <p>Bandwidth = 4</p>	<p>① Set <math>I</math> to <math>I_s = -70.000</math> mA vs. &lt;None&gt;</p> <p>for at most <math>t_1 = 30</math> h 0 mn 0.000 0 s</p> <p>Limit <math>E_{we} &lt; E_M = 2.500</math> V</p> <p>Record every <math>dE_1 = 10.0</math> mV</p> <p>or <math>dt_1 = 10.000 0</math> s</p> <hr/> <p>Hold <math>E_M</math> for <math>t_M = 0</math> h 0 mn 0.000 0 s</p> <p>Limit <math> I  &lt; I_m = 0.000</math> mA</p> <p>or <math> dI/dt  &lt; dI/dt_f = 0.000</math> mA/s</p> <p>Record every <math>dQ = 1.000</math> A.h</p> <p>or <math>dt_q = 120.000 0</math> s</p> <hr/> <p>Limit <math> \Delta Q  &gt; \Delta Q_M = 0.000</math> mA.h</p> <p><math>\Leftrightarrow \Delta x_M = 0.000</math></p> <p><math> \Delta SoC  &gt; \text{pass}</math> %</p> <hr/> <p>E Range = 0 V; 5 V</p> <p><i>Resolution = 100 <math>\mu</math>V</i></p> <p>I Range = 100 mA</p> <p>Bandwidth = 4</p>
<p>② Rest for <math>t_R = 1</math> h 0 mn 0.000 0 s</p> <p>Limit <math> dE_{we}/dt  &lt; dE_R/dt = 0.0</math> mV/h</p> <p>Record every <math>dE_R = 10.0</math> mV</p> <p>or <math>dt_R = 120.000 0</math> s</p> <p><i>(If <math>t_R = 0</math> or <math> \Delta Q  &gt; \Delta Q_M</math> go to ④)</i></p>	<p>② Rest for <math>t_R = 1</math> h 0 mn 0.000 0 s</p> <p>Limit <math> dE_{we}/dt  &lt; dE_R/dt = 0.0</math> mV/h</p> <p>Record every <math>dE_R = 10.0</math> mV</p> <p>or <math>dt_R = 120.000 0</math> s</p> <p><i>(If <math>t_R = 0</math> or <math> \Delta Q  &gt; \Delta Q_M</math> go to ④)</i></p>
<p>③ If <math>E_{we} &lt; E_L = \text{pass}</math> V go to ①</p>	<p>③ If <math>E_{we} &gt; E_L = \text{pass}</math> V go to ①</p>
<p>④ Go back to seq. <math>N_s' = 0</math> (9999 ends technique)</p> <p>for <math>n_c = 0</math> time(s) (0 for next sequence)</p>	<p>④ Go back to seq. <math>N_s' = 1</math> (9999 ends technique)</p> <p>for <math>n_c = 1</math> time(s) (0 for next sequence)</p>

### 8.3. Appendix C- Galvanostatic cycling with constant voltage step settings

Examples of constant current with constant voltage cycling settings. Step 0 is a 10 second rest. Top two images are C/5 steps 1 and 2, bottom two images are C/3 steps 1 and 2.

0 1 2

① Set I to  $I_s = 280.000$  mA vs. <None>  
 for at most  $t_1 = 8$  h 0 mn 0.000 0 s  
 Limit  $E_{cell} > E_M = 4.200$  V  
 Record every  $dE_1 = 10.0$  mV  
 or  $dt_1 = 10.000 0$  s  
 Hold  $E_M$  for  $t_M = 2$  h 0 mn 0.000 0 s  
 Limit  $|I| < I_m = 70.000$  mA  
 or  $|dI/dt| < dI/dt_f = 0.000$  mA/s  
 Record every  $dQ = 10.000$  mA.h  
 or  $dt_q = 10.000 0$  s  
 Limit  $|\Delta Q| > \Delta Q_M = 0.000$  mA.h  
 $\Leftrightarrow \Delta x_M = 0.000$   
 $\Delta SoC1 > pass$  %  
 E Range = 0 V; 5 V  
 Resolution = 100  $\mu$ V  
 I Range = 1 A  
 Bandwidth = 4

② Rest for  $t_R = 1$  h 0 mn 0.000 0 s  
 Limit  $|dE_{cell}/dt| < dE_R/dt = 0.0$  mV/h  
 Record every  $dE_R = 10.0$  mV  
 or  $dt_R = 10.000 0$  s  
 (If  $t_R = 0$  or  $|\Delta Q| > \Delta Q_M$  go to ④)

③ If  $E_{cell} < E_L = pass$  V go to ①

④ Go back to seq.  $N_s^* = 0$  (9999 ends technique)  
 for  $n_c = 0$  time(s) (0 for next sequence)

0 1 2

① Set I to  $I_s = -280.000$  mA vs. <None>  
 for at most  $t_1 = 8$  h 0 mn 0.000 0 s  
 Limit  $E_{cell} < E_M = 2.500$  V  
 Record every  $dE_1 = 10.0$  mV  
 or  $dt_1 = 10.000 0$  s  
 Hold  $E_M$  for  $t_M = 0$  h 0 mn 0.000 0 s  
 Limit  $|I| < I_m = 70.000$  mA  
 or  $|dI/dt| < dI/dt_f = 0.000$  mA/s  
 Record every  $dQ = 10.000$  mA.h  
 or  $dt_q = 10.000 0$  s  
 Limit  $|\Delta Q| > \Delta Q_M = 0.000$  mA.h  
 $\Leftrightarrow \Delta x_M = 0.000$   
 $\Delta SoC1 > pass$  %  
 E Range = 0 V; 5 V  
 Resolution = 100  $\mu$ V  
 I Range = 1 A  
 Bandwidth = 4

② Rest for  $t_R = 1$  h 0 mn 0.000 0 s  
 Limit  $|dE_{cell}/dt| < dE_R/dt = 0.0$  mV/h  
 Record every  $dE_R = 10.0$  mV  
 or  $dt_R = 10.000 0$  s  
 (If  $t_R = 0$  or  $|\Delta Q| > \Delta Q_M$  go to ④)

③ If  $E_{cell} > E_L = pass$  V go to ①

④ Go back to seq.  $N_s^* = 1$  (9999 ends technique)  
 for  $n_c = 9$  time(s) (0 for next sequence)

0 1 2

① Set C/N with  $N = 3.00$  and  $I > 0$  ( $I = 466.667$  mA)  
 for at most  $t_1 = 8$  h 0 mn 0.000 0 s  
 Limit  $E_{cell} > E_M = 4.200$  V  
 Record every  $dE_1 = 10.0$  mV  
 or  $dt_1 = 10.000 0$  s  
 Hold  $E_M$  for  $t_M = 2$  h 0 mn 0.000 0 s  
 Limit  $|I| < I_m = 70.000$  mA  
 or  $|dI/dt| < dI/dt_f = 0.000$  mA/s  
 Record every  $dQ = 10.000$  mA.h  
 or  $dt_q = 10.000 0$  s  
 Limit  $|\Delta Q| > \Delta Q_M = 0.000$  mA.h  
 $\Leftrightarrow \Delta x_M = 0.000$   
 $\Delta SoC1 > pass$  %  
 E Range = 0 V; 5 V  
 Resolution = 100  $\mu$ V  
 I Range = 5 A  
 Bandwidth = 4

② Rest for  $t_R = 1$  h 0 mn 0.000 0 s  
 Limit  $|dE_{cell}/dt| < dE_R/dt = 0.0$  mV/h  
 Record every  $dE_R = 10.0$  mV  
 or  $dt_R = 10.000 0$  s  
 (If  $t_R = 0$  or  $|\Delta Q| > \Delta Q_M$  go to ④)

③ If  $E_{cell} < E_L = pass$  V go to ①

④ Go back to seq.  $N_s^* = 0$  (9999 ends technique)  
 for  $n_c = 0$  time(s) (0 for next sequence)

0 1 2

① Set C/N with  $N = 3.00$  and  $I < 0$  ( $I = -466.667$  mA)  
 for at most  $t_1 = 8$  h 0 mn 0.000 0 s  
 Limit  $E_{cell} < E_M = 2.500$  V  
 Record every  $dE_1 = 10.0$  mV  
 or  $dt_1 = 10.000 0$  s  
 Hold  $E_M$  for  $t_M = 0$  h 0 mn 0.000 0 s  
 Limit  $|I| < I_m = 70.000$  mA  
 or  $|dI/dt| < dI/dt_f = 0.000$  mA/s  
 Record every  $dQ = 10.000$  mA.h  
 or  $dt_q = 10.000 0$  s  
 Limit  $|\Delta Q| > \Delta Q_M = 0.000$  mA.h  
 $\Leftrightarrow \Delta x_M = 0.000$   
 $\Delta SoC1 > pass$  %  
 E Range = 0 V; 5 V  
 Resolution = 100  $\mu$ V  
 I Range = 5 A  
 Bandwidth = 4

② Rest for  $t_R = 1$  h 0 mn 0.000 0 s  
 Limit  $|dE_{cell}/dt| < dE_R/dt = 0.0$  mV/h  
 Record every  $dE_R = 10.0$  mV  
 or  $dt_R = 10.000 0$  s  
 (If  $t_R = 0$  or  $|\Delta Q| > \Delta Q_M$  go to ④)

③ If  $E_{cell} > E_L = pass$  V go to ①

④ Go back to seq.  $N_s^* = 1$  (9999 ends technique)  
 for  $n_c = 4$  time(s) (0 for next sequence)

## 8.4. Appendix D- Galvanostatic Intermittent Titration Technique test settings

Step 0 is a 10 second rest, the settings for steps 1 and 2 of the GITT test are shown below.

0	1	2
<p>① Set I to <math>I_s = 240.000</math> mA vs. &lt;None&gt;</p> <p>for at most <math>t_1 = 0</math> h 15 mn 0.000 0 s</p> <p>Limit <math>E_{we} &gt; E_M = 4.200</math> V</p> <p>Record every <math>dE_1 = 10.0</math> mV</p> <p>or <math>dt_1 = 10.000 0</math> s</p> <hr/> <p>Hold <math>E_M</math> for <math>t_M = 0</math> h 0 mn 0.000 0 s</p> <p>Limit <math> I  &lt; I_m = 0.000</math> mA</p> <p>or <math> dI/dt  &lt; dI/dt_f = 0.000</math> mA/s</p> <p>Record every <math>dQ = 1.000</math> A.h</p> <p>or <math>dt_q = 120.000 0</math> s</p> <hr/> <p>Limit <math> \Delta Q  &gt; \Delta Q_M = 0.000</math> mA.h</p> <p><math>\Leftrightarrow \Delta x_M = 0.000</math></p> <p><math> \Delta SoCl  &gt; \text{pass}</math> %</p> <hr/> <p>E Range = 0 V; 5 V Resolution = 100 <math>\mu</math>V</p> <p>I Range = 1 A</p> <p>Bandwidth = 4</p>	<p>① Set I to <math>I_s = .240.000</math> mA vs. &lt;None&gt;</p> <p>for at most <math>t_1 = 0</math> h 15 mn 0.000 0 s</p> <p>Limit <math>E_{we} &lt; E_M = 2.500</math> V</p> <p>Record every <math>dE_1 = 10.0</math> mV</p> <p>or <math>dt_1 = 10.000 0</math> s</p> <hr/> <p>Hold <math>E_M</math> for <math>t_M = 0</math> h 0 mn 0.000 0 s</p> <p>Limit <math> I  &lt; I_m = 0.000</math> mA</p> <p>or <math> dI/dt  &lt; dI/dt_f = 0.000</math> mA/s</p> <p>Record every <math>dQ = 1.000</math> A.h</p> <p>or <math>dt_q = 120.000 0</math> s</p> <hr/> <p>Limit <math> \Delta Q  &gt; \Delta Q_M = 0.000</math> mA.h</p> <p><math>\Leftrightarrow \Delta x_M = 0.000</math></p> <p><math> \Delta SoCl  &gt; \text{pass}</math> %</p> <hr/> <p>E Range = 0 V; 5 V Resolution = 100 <math>\mu</math>V</p> <p>I Range = 1 A</p> <p>Bandwidth = 4</p>	
<p>② Rest for <math>t_R = 0</math> h 45 mn 0.000 0 s</p> <p>Limit <math> dE_{we}/dt  &lt; dE_R/dt = 0.0</math> mV/h</p> <p>Record every <math>dE_R = 10.0</math> mV</p> <p>or <math>dt_R = 10.000 0</math> s</p> <p><i>(if <math>t_R = 0</math> or <math> \Delta Q  &gt; \Delta Q_M</math> go to ④)</i></p>	<p>② Rest for <math>t_R = 0</math> h 45 mn 0.000 0 s</p> <p>Limit <math> dE_{we}/dt  &lt; dE_R/dt = 0.0</math> mV/h</p> <p>Record every <math>dE_R = 10.0</math> mV</p> <p>or <math>dt_R = 10.000 0</math> s</p> <p><i>(if <math>t_R = 0</math> or <math> \Delta Q  &gt; \Delta Q_M</math> go to ④)</i></p>	
<p>③ If <math>E_{we} &lt; E_L = \text{pass}</math> V go to ①</p>	<p>③ If <math>E_{we} &gt; E_L = \text{pass}</math> V go to ①</p>	
<p>④ Go back to seq. <math>N_s' = 1</math> (9999 ends technique)</p> <p>for <math>n_c = 23</math> time(s) (0 for next sequence)</p>	<p>④ Go back to seq. <math>N_s' = 2</math> (9999 ends technique)</p> <p>for <math>n_c = 23</math> time(s) (0 for next sequence)</p>	

## 8.5. Appendix E- Cyclic Voltammetry test settings

The cyclic voltammetry test settings are shown below. The settings on the left are for the CV test carried out at a scan rate of  $0.1\text{mVs}^{-1}$ , the settings on the right are the test carried out at a scan rate of  $0.05\text{mVs}^{-1}$ .

Turn to OCV between techniques  $\mu\text{I}$

Set  $E_{\text{We}}$  to  $E_i = 0.000$  V vs.  $E_{\text{oc}}$

Scan  $E_{\text{We}}$  with  $dE/dt = 0.100$  mV/s  
to vertex potential  $E_1 = 4.200$  V vs. Ref

Reverse scan to vertex  $E_2 = 2.500$  V vs. Ref

Repeat  $n_c = 2$  time(s)

Measure  $\langle I \rangle$  over the last 50 % of the step duration

Record  $\langle I \rangle$  averaged over  $N = 10$  voltage steps

E Range = 0 V; 5 V  
*Resolution = 100  $\mu\text{V}$*

I Range = Auto

Bandwidth = 4

End scan to  $E_f = 0.000$  V vs.  $E_{\text{oc}}$

Force  $E_1 / E_2$  (dE/dt  $\sim 100 \mu\text{V} / 1 \text{ s}$ )  
(dEN  $\sim 1.0 \text{ mV}$ )  
(3400 points per cycle)

Turn to OCV between techniques  $\mu\text{I}$

Set  $E_{\text{We}}$  to  $E_i = 0.000$  V vs.  $E_{\text{oc}}$

Scan  $E_{\text{We}}$  with  $dE/dt = 0.050$  mV/s  
to vertex potential  $E_1 = 4.200$  V vs. Ref

Reverse scan to vertex  $E_2 = 2.500$  V vs. Ref

Repeat  $n_c = 2$  time(s)

Measure  $\langle I \rangle$  over the last 50 % of the step duration

Record  $\langle I \rangle$  averaged over  $N = 10$  voltage steps

E Range = 0 V; 5 V  
*Resolution = 100  $\mu\text{V}$*

I Range = Auto

Bandwidth = 4

End scan to  $E_f = 0.000$  V vs.  $E_{\text{oc}}$

Force  $E_1 / E_2$  (dE/dt  $\sim 100 \mu\text{V} / 2 \text{ s}$ )  
(dEN  $\sim 1.0 \text{ mV}$ )  
(3400 points per cycle)

## 8.6. Appendix F- Electrochemical Impedance Spectroscopy test settings

EIS test settings, set on BioLogic EC-Lab software. 42 frequencies, average result taken from 3 measures per frequency.

Excitation signal mode: Single sine

Set  $I$  to  $I_s$  = 0.000 mA vs. <None>

for  $t_{I_s}$  = 0 h 0 mn 0.000 s

Record every  $dE$  = 0.000 mV and  $dt$  = 0.000 s

Scan from  $f_i$  = 100.000 kHz to  $f_f$  = 10.000 mHz with  $N_d$  = 6 points per decade in Logarithmic spacing

amplitude  $I_a$  = 70.000 mA

wait for  $p_w$  = 0.10 period before each frequency

average  $N_a$  = 3 measure(s) per frequency

drift correction

Repeat  $n_c$  = 0 time(s)

E Range = -10 V; 10 V  
*Resolution = 305.18  $\mu$ V*

I Range = 1 A

Bandwidth = 4 (~ 16mn30s / scan)

EIS test frequencies (Hz)	
0.010 000	38.491 591
0.014 816	57.029 238
0.021 951	84.494 663
0.032 523	125.187 505
0.048 187	185.478 122
0.071 393	274.804 853
0.105 777	407.151 561
0.156 719	603.236 778
0.232 195	893.757 128
0.344 021	1 324.192 809
0.509 703	1 961.927 397
0.755 177	2 906.796 567
1.118 872	4 306.717 108
1.657 724	6 380.842 902
2.456 088	9 453.872 897
3.638 946	14 006.881 869
5.391 472	20 752.631 418
7.988 018	30 747.150 920
11.835 068	45 555.056 160
17.534 866	67 494.485 819
25.979 702	100 000.000 000

## 8.7. Appendix G- Urban Profile discharge cycle

Time (s)	Current (A)				
0	-0.259	840	-0.195	1700	-0.233
20	-0.189	860	-0.203	1720	-0.203
40	-0.240	880	-0.194	1740	-0.203
60	-0.240	900	-0.179	1760	-0.203
80	-0.205	920	-0.173	1780	-0.203
100	-0.190	940	-0.173	1800	-0.203
120	-0.227	960	-0.173	1820	-0.209
140	-0.244	980	-0.173	1840	-0.221
160	-0.227	1000	-0.173	1860	-0.209
180	-0.201	1020	-0.173	1880	-0.197
200	-0.226	1040	-0.173	1900	-0.179
220	-0.234	1060	-0.173	1920	-0.194
240	-0.234	1080	-0.173	1940	-0.199
260	-0.200	1100	-0.173	1960	-0.180
280	-0.191	1120	-0.173	1980	-0.248
300	-0.190	1140	-0.173	2000	-0.256
320	-0.187	1160	-0.173	2020	-0.227
340	-0.201	1180	-0.173	2040	-0.251
360	-0.202	1200	-0.173	2060	-0.243
380	-0.209	1220	-0.198	2080	-0.236
400	-0.209	1240	-0.217	2100	-0.230
420	-0.203	1260	-0.237	2120	-0.212
440	-0.210	1280	-0.257	2140	-0.211
460	-0.243	1300	-0.270	2160	-0.197
480	-0.225	1320	-0.273	2180	-0.182
500	-0.240	1340	-0.225	2200	-0.173
520	-0.218	1360	-0.233	2220	-0.173
540	-0.213	1380	-0.250	2240	-0.173
560	-0.198	1400	-0.251	2260	-0.173
580	-0.194	1420	-0.261	2280	-0.173
600	-0.189	1440	-0.230	2300	-0.173
620	-0.177	1460	-0.235	2320	-0.185
640	-0.198	1480	-0.238	2340	-0.208
660	-0.217	1500	-0.223	2360	-0.227
680	-0.257	1520	-0.235	2380	-0.246
700	-0.265	1540	-0.243	2400	-0.266
720	-0.205	1560	-0.251	2420	-0.230
740	-0.192	1580	-0.206	2440	-0.240
760	-0.181	1600	-0.218	2460	-0.234
780	-0.203	1620	-0.195	2480	-0.214
800	-0.200	1640	-0.183	2500	-0.277
820	-0.222	1660	-0.212	2520	-0.264
		1680	-0.249	2540	-0.243

2560	-0.198
2580	-0.188
2600	-0.178
2620	-0.173
2640	-0.177
2660	-0.189
2680	-0.268
2700	-0.266
2720	-0.253
2740	-0.238
2760	-0.225
2780	-0.210
2800	-0.196
2820	-0.181
2840	-0.173
2860	-0.173
2880	-0.173
2900	-0.173
2920	-0.173
2940	-0.173
2960	-0.173
2980	-0.173
3000	-0.173
3020	-0.173
3040	-0.173
3060	-0.173
3080	-0.173
3100	-0.173
3120	-0.173
3140	-0.173
3160	-0.173
3180	-0.173
3200	-0.173
3220	-0.192
3240	-0.212
3260	-0.231
3280	-0.251
3300	-0.271
3320	-0.232
3340	-0.243
3360	-0.253
3380	-0.255
3400	-0.255
3420	-0.247
3440	-0.226
3460	-0.232

3480	-0.270
3500	-0.218
3520	-0.231
3540	-0.233
3560	-0.197
3580	-0.209
3600	-0.209
3620	-0.190
3640	-0.184
3660	-0.220
3680	-0.203
3700	-0.178
3720	-0.196
3740	-0.196
3760	-0.189
3780	-0.201
3800	-0.201
3820	-0.201
3840	-0.201
3860	-0.201
3880	-0.189
3900	-0.207
3920	-0.207
3940	-0.220
3960	-0.184
3980	-0.189
4000	-0.201
4020	-0.201
4040	-0.189
4060	-0.189
4080	-0.195
4100	-0.199
4120	-0.222
4140	-0.237
4160	-0.242
4180	-0.251
4200	-0.259
4220	-0.241
4240	-0.245
4260	-0.230
4280	-0.212
4300	-0.203
4320	-0.190
4340	-0.177
4360	-0.173
4380	-0.173

4400	-0.173
4420	-0.173
4440	-0.173
4460	-0.173
4480	-0.173
4500	-0.173
4520	-0.173
4540	-0.173
4560	-0.173
4580	-0.173
4600	-0.173
4620	-0.173
4640	-0.173
4660	-0.173
4680	-0.173
4700	-0.173
4720	-0.173
4740	-0.173
4760	-0.173
4780	-0.173
4800	-0.173
4820	-0.189
4840	-0.203
4860	-0.215
4880	-0.233
4900	-0.245
4920	-0.254
4940	-0.193
4960	-0.205
4980	-0.273
5000	-0.220
5020	-0.211
5040	-0.189
5060	-0.173
5080	-0.181
5100	-0.181
5120	-0.179
5140	-0.181
5160	-0.234
5180	-0.212
5200	-0.180
5220	-0.187
5240	-0.188
5260	-0.193
5280	-0.212
5300	-0.246

5320	-0.254
5340	-0.245
5360	-0.193
5380	-0.178
5400	-0.181
5420	-0.203
5440	-0.228
5460	-0.213
5480	-0.196
5500	-0.180
5520	-0.237
5540	-0.252
5560	-0.249
5580	-0.248
5600	-0.227
5620	-0.203
5640	-0.200
5660	-0.192
5680	-0.173
5700	-0.183
5720	-0.195
5740	-0.192
5760	-0.183
5780	-0.183
5800	-0.187
5820	-0.208
5840	-0.209
5860	-0.193
5880	-0.173
5900	-0.178
5920	-0.192
5940	-0.205
5960	-0.214
5980	-0.189
6000	-0.173
6020	-0.206
6040	-0.216
6060	-0.227
6080	-0.244
6100	-0.226
6120	-0.218
6140	-0.208
6160	-0.209
6180	-0.210
6200	-0.195
6220	-0.184

6240	-0.189
6260	-0.189
6280	-0.199
6300	-0.215
6320	-0.173
6340	-0.177
6360	-0.173
6380	-0.208
6400	-0.219
6420	-0.215
6440	-0.205
6460	-0.200
6480	-0.189
6500	-0.176
6520	-0.181
6540	-0.198
6560	-0.209
6580	-0.220
6600	-0.221
6620	-0.228
6640	-0.218
6660	-0.208
6680	-0.186
6700	-0.173
6720	-0.228
6740	-0.226
6760	-0.267
6780	-0.254
6800	-0.240
6820	-0.226
6840	-0.212
6860	-0.197
6880	-0.183
6900	-0.173
6920	-0.173
6940	-0.173
6960	-0.173
6980	-0.173
7000	-0.173
7020	-0.173
7040	-0.173
7060	-0.173
7080	-0.173
7100	-0.173
7120	-0.173
7140	-0.173

7160	-0.173
7180	-0.173
7200	-0.173
7220	-0.173
7240	-0.173
7260	-0.173
7280	-0.173
7300	-0.173
7320	-0.173
7340	-0.173
7360	-0.173
7380	-0.173
7400	-0.173
7420	-0.173
7440	-0.173
7460	-0.173
7480	-0.173
7500	-0.173
7520	-0.173
7540	-0.173
7560	-0.173
7580	-0.173
7600	-0.173
7620	-0.173
7640	-0.173
7660	-0.173
7680	-0.192
7700	-0.212
7720	-0.231
7740	-0.251
7760	-0.271
7780	-0.232
7800	-0.273
7820	-0.271
7840	-0.253
7860	-0.215
7880	-0.185
7900	-0.182
7920	-0.173
7940	-0.200
7960	-0.196
7980	-0.196
8000	-0.205
8020	-0.253
8040	-0.185
8060	-0.248

8080	-0.205
8100	-0.257
8120	-0.209
8140	-0.178
8160	-0.209
8180	-0.197
8200	-0.229
8220	-0.266
8240	-0.227
8260	-0.245
8280	-0.264
8300	-0.269
8320	-0.269
8340	-0.273
8360	-0.256
8380	-0.232
8400	-0.250
8420	-0.246
8440	-0.257
8460	-0.233
8480	-0.272
8500	-0.236
8520	-0.228
8540	-0.212
8560	-0.220
8580	-0.211
8600	-0.227
8620	-0.227
8640	-0.227
8660	-0.227
8680	-0.243
8700	-0.243
8720	-0.269
8740	-0.226
8760	-0.227
8780	-0.267
8800	-0.277
8820	-0.230
8840	-0.272
8860	-0.228
8880	-0.238
8900	-0.253
8920	-0.251
8940	-0.234
8960	-0.226
8980	-0.261

9000	-0.242
9020	-0.223
9040	-0.250
9060	-0.269
9080	-0.226
9100	-0.232
9120	-0.273
9140	-0.233
9160	-0.275
9180	-0.229
9200	-0.268
9220	-0.258
9240	-0.238
9260	-0.257
9280	-0.257
9300	-0.257
9320	-0.257
9340	-0.257
9360	-0.248
9380	-0.228
9400	-0.227
9420	-0.188
9440	-0.205
9460	-0.213
9480	-0.230
9500	-0.220
9520	-0.238
9540	-0.275
9560	-0.257
9580	-0.258
9600	-0.249
9620	-0.221
9640	-0.211
9660	-0.210
9680	-0.209
9700	-0.199
9720	-0.269
9740	-0.207
9760	-0.233
9780	-0.224
9800	-0.223
9820	-0.249
9840	-0.258
9860	-0.268
9880	-0.225
9900	-0.231

9920	-0.232
9940	-0.233
9960	-0.253
9980	-0.236
10000	-0.273
10020	-0.233
10040	-0.255
10060	-0.236
10080	-0.198
10100	-0.187
10120	-0.264
10140	-0.259
10160	-0.189
10180	-0.240
10200	-0.240
10220	-0.205
10240	-0.190
10260	-0.227
10280	-0.244
10300	-0.227
10320	-0.201
10340	-0.226
10360	-0.234
10380	-0.234
10400	-0.200
10420	-0.191
10440	-0.190
10460	-0.187
10480	-0.201
10500	-0.202
10520	-0.209
10540	-0.209
10560	-0.203
10580	-0.210
10600	-0.243
10620	-0.225
10640	-0.240
10660	-0.218
10680	-0.213
10700	-0.198
10720	-0.194
10740	-0.189
10760	-0.177
10780	-0.198
10800	-0.217
10820	-0.257

10840	-0.265
10860	-0.205
10880	-0.192
10900	-0.181
10920	-0.203
10940	-0.200
10960	-0.222
10980	-0.195
11000	-0.203
11020	-0.194
11040	-0.179
11060	-0.173
11080	-0.173
11100	-0.173
11120	-0.173
11140	-0.173
11160	-0.173
11180	-0.173
11200	-0.173
11220	-0.173
11240	-0.173
11260	-0.173
11280	-0.173
11300	-0.173
11320	-0.173
11340	-0.173
11360	-0.198
11380	-0.217
11400	-0.237
11420	-0.257
11440	-0.270
11460	-0.273
11480	-0.225
11500	-0.233
11520	-0.250
11540	-0.251
11560	-0.261
11580	-0.230
11600	-0.235
11620	-0.238
11640	-0.223
11660	-0.235
11680	-0.243
11700	-0.251
11720	-0.206
11740	-0.218

11760	-0.195
11780	-0.183
11800	-0.212
11820	-0.249
11840	-0.233
11860	-0.203
11880	-0.203
11900	-0.203
11920	-0.203
11940	-0.203
11960	-0.209
11980	-0.221
12000	-0.209
12020	-0.197
12040	-0.179
12060	-0.194
12080	-0.199
12100	-0.180
12120	-0.248
12140	-0.256
12160	-0.227
12180	-0.251
12200	-0.243
12220	-0.236
12240	-0.230
12260	-0.212
12280	-0.211
12300	-0.197
12320	-0.182
12340	-0.173
12360	-0.173
12380	-0.173
12400	-0.173
12420	-0.173
12440	-0.173
12460	-0.185
12480	-0.208
12500	-0.227
12520	-0.246
12540	-0.266
12560	-0.230
12580	-0.240
12600	-0.234
12620	-0.214
12640	-0.277
12660	-0.264

12680	-0.243
12700	-0.198
12720	-0.188
12740	-0.178
12760	-0.173
12780	-0.177
12800	-0.189
12820	-0.268
12840	-0.266
12860	-0.253
12880	-0.238
12900	-0.225
12920	-0.210
12940	-0.196
12960	-0.181
12980	-0.173
13000	-0.173
13020	-0.173
13040	-0.173
13060	-0.173
13080	-0.173
13100	-0.173
13120	-0.173
13140	-0.173
13160	-0.173
13180	-0.173
13200	-0.173
13220	-0.173
13240	-0.173
13260	-0.173
13280	-0.173
13300	-0.173
13320	-0.173
13340	-0.173
13360	-0.192
13380	-0.212
13400	-0.231
13420	-0.251
13440	-0.271
13460	-0.232
13480	-0.243
13500	-0.253
13520	-0.255
13540	-0.255
13560	-0.247
13580	-0.226

13600	-0.232
13620	-0.270
13640	-0.218
13660	-0.231
13680	-0.233
13700	-0.197
13720	-0.209
13740	-0.209
13760	-0.190
13780	-0.184
13800	-0.220
13820	-0.203
13840	-0.178
13860	-0.196
13880	-0.196
13900	-0.189
13920	-0.201
13940	-0.201
13960	-0.201
13980	-0.201
14000	-0.201
14020	-0.189
14040	-0.207
14060	-0.207
14080	-0.220
14100	-0.184
14120	-0.189
14140	-0.201
14160	-0.201
14180	-0.189
14200	-0.189
14220	-0.195
14240	-0.199
14260	-0.222
14280	-0.237
14300	-0.242
14320	-0.251
14340	-0.259
14360	-0.241
14380	-0.245
14400	-0.230
14420	-0.212
14440	-0.203
14460	-0.190

14480	-0.177
14500	-0.173
14520	-0.173
14540	-0.173
14560	-0.173
14580	-0.173
14600	-0.173
14620	-0.173
14640	-0.188
14660	-0.193
14680	-0.186
14700	-0.204
14720	-0.194
14740	-0.193
14760	-0.205
14780	-0.228
14800	-0.233
14820	-0.231
14840	-0.223
14860	-0.220
14880	-0.215
14900	-0.221
14920	-0.224
14940	-0.218
14960	-0.215
14980	-0.204
15000	-0.192
15020	-0.188
15040	-0.188
15060	-0.188
15080	-0.188
15100	-0.188
15120	-0.214
15140	-0.197
15160	-0.197
15180	-0.173
15200	-0.173
15220	-0.179
15240	-0.188
15260	-0.188
15280	-0.182
15300	-0.205
15320	-0.258
15340	-0.245

15360	-0.230
15380	-0.216
15400	-0.202
15420	-0.188
15440	-0.173
15460	-0.173
15480	-0.173
15500	-0.173
15520	-0.173
15540	-0.173
15560	-0.173
15580	-0.173
15600	-0.173
15620	-0.173
15640	-0.173
15660	-0.173
15680	-0.173
15700	-0.173
15720	-0.173
15740	-0.173
15760	-0.173
15780	-0.192
15800	-0.212
15820	-0.231
15840	-0.245
15860	-0.218
15880	-0.217
15900	-0.209
15920	-0.181
15940	-0.181
15960	-0.196
15980	-0.187
16000	-0.181
16020	-0.173
16040	-0.178
16060	-0.178
16080	-0.173
16100	-0.192
16120	-0.184
16140	-0.178
16160	-0.173
16180	-0.178

**Total discharge of 0.94Ah over approximately 4 hours 50 minutes, maximum discharge of 0.275A.**

## 8.8. Appendix H- Forced lithium plating at room temperature settings

Example of settings used to try to force lithium plating at 25°C. Step 0 is a 10 second rest period, steps 1 and 2 from a 2100mA charge (1.5C) with CV step and 70mA discharge cycle are shown below.

Step	0	1	2
1	<p>Set <math>I</math> to <math>I_s = 2100.000</math> mA vs. &lt;None&gt;</p> <p>for at most <math>t_1 = 1</math> h 0 mn 0.000 0 s</p> <p>Limit <math>E_{we} &gt; E_M = 4.200</math> V</p> <p>Record every <math>dE_1 = 10.0</math> mV</p> <p>or <math>dt_1 = 10.000 0</math> s</p> <hr/> <p>Hold <math>E_M</math> for <math>t_M = 4</math> h 0 mn 0.000 0 s</p> <p>Limit <math> I  &lt; I_m = 70.000</math> mA</p> <p>or <math> dI/dt  &lt; dI/dt_f = 0.000</math> mA/s</p> <p>Record every <math>dQ = 10.000</math> mA.h</p> <p>or <math>dt_q = 120.000 0</math> s</p> <hr/> <p>Limit <math> \Delta Q  &gt; \Delta Q_M = 0.000</math> mA.h</p> <p><math>\Leftrightarrow \Delta x_M = 0.000</math></p> <p><math> \Delta SoC  &gt; \text{pass}</math> %</p> <hr/> <p>E Range = 0 V; 5 V</p> <p>Resolution = 100 <math>\mu</math>V</p> <p>I Range = 5 A</p> <p>Bandwidth = 4</p>	<p>Set <math>I</math> to <math>I_s = -70.000</math> mA vs. &lt;None&gt;</p> <p>for at most <math>t_1 = 30</math> h 0 mn 0.000 0 s</p> <p>Limit <math>E_{we} &lt; E_M = 2.500</math> V</p> <p>Record every <math>dE_1 = 10.0</math> mV</p> <p>or <math>dt_1 = 10.000 0</math> s</p> <hr/> <p>Hold <math>E_M</math> for <math>t_M = 0</math> h 0 mn 0.000 0 s</p> <p>Limit <math> I  &lt; I_m = 0.000</math> mA</p> <p>or <math> dI/dt  &lt; dI/dt_f = 0.000</math> mA/s</p> <p>Record every <math>dQ = 1.000</math> A.h</p> <p>or <math>dt_q = 120.000 0</math> s</p> <hr/> <p>Limit <math> \Delta Q  &gt; \Delta Q_M = 0.000</math> mA.h</p> <p><math>\Leftrightarrow \Delta x_M = 0.000</math></p> <p><math> \Delta SoC  &gt; \text{pass}</math> %</p> <hr/> <p>E Range = 0 V; 5 V</p> <p>Resolution = 100 <math>\mu</math>V</p> <p>I Range = 100 mA</p> <p>Bandwidth = 4</p>	
2	<p>Rest for <math>t_R = 1</math> h 0 mn 0.000 0 s</p> <p>Limit <math> dE_{we}/dt  &lt; dE_R/dt = 0.0</math> mV/h</p> <p>Record every <math>dE_R = 10.0</math> mV</p> <p>or <math>dt_R = 120.000 0</math> s</p> <p><i>(If <math>t_R = 0</math> or <math> \Delta Q  &gt; \Delta Q_M</math> go to 4)</i></p>	<p>Rest for <math>t_R = 1</math> h 0 mn 0.000 0 s</p> <p>Limit <math> dE_{we}/dt  &lt; dE_R/dt = 0.0</math> mV/h</p> <p>Record every <math>dE_R = 10.0</math> mV</p> <p>or <math>dt_R = 120.000 0</math> s</p> <p><i>(If <math>t_R = 0</math> or <math> \Delta Q  &gt; \Delta Q_M</math> go to 4)</i></p>	
3	<p>If <math>E_{we} &lt; E_L = \text{pass}</math> V go to 1</p>	<p>If <math>E_{we} &gt; E_L = \text{pass}</math> V go to 1</p>	
4	<p>Go back to seq. <math>N_s = 0</math> (9999 ends technique)</p> <p>for <math>n_c = 0</math> time(s) (0 for next sequence)</p>	<p>Go back to seq. <math>N_s = 1</math> (9999 ends technique)</p> <p>for <math>n_c = 1</math> time(s) (0 for next sequence)</p>	

## 8.9. Appendix I- Forced lithium plating on reference cells at 0°C

Cell cycling of C/40 charge with D/20 discharge (top two images steps 1 and 2) for reference, followed by C/2 charge then D/20 discharge (bottom two images steps 1 and 2), at 0°C.

**Step 1: Charge (C/40)**

- Set I to  $I_s = 35.000$  mA vs. <None>
- for at most  $t_1 = 60$  h 0 mn 0.000 0 s
- Limit  $E_{cell} > E_M = 4.200$  V
- Record every  $dE_1 = 10.0$  mV
- or  $dt_1 = 10.000 0$  s
- Hold  $E_M$  for  $t_M = 0$  h 0 mn 0.000 0 s
- Limit  $|I| < I_M = 70.000$  mA
- or  $|dI/dt| < dI/dt_f = 0.000$  mA/s
- Record every  $dQ = 10.000$  mA.h
- or  $dt_q = 10.000 0$  s
- Limit  $|\Delta Q| > \Delta Q_M = 0.000$  mA.h
- $\Delta x_M = 0.000$
- $|\Delta SoC| > \text{pass}$  %
- E Range = 0 V; 5 V Resolution = 100  $\mu$ V
- I Range = 5 A
- Bandwidth = 4

**Step 2: Rest**

- Rest for  $t_R = 0$  h 0 mn 0.000 0 s
- Limit  $|dE_{cell}/dt| < dE_R/dt = 0.0$  mV/h
- Record every  $dE_R = 10.0$  mV
- or  $dt_R = 10.000 0$  s
- (If  $t_R = 0$  or  $|\Delta Q| > \Delta Q_M$  go to ④)

**Step 3: Limit**

- If  $E_{cell} < E_L = \text{pass}$  V go to ①

**Step 4: End of Sequence**

- Go back to seq.  $N_s^* = 0$  (9999 ends technique)
- for  $n_c = 0$  time(s) (0 for next sequence)

**Step 1: Charge (C/2)**

- Set I to  $I_s = -70.000$  mA vs. <None>
- for at most  $t_1 = 30$  h 0 mn 0.000 0 s
- Limit  $E_{cell} < E_M = 2.500$  V
- Record every  $dE_1 = 10.0$  mV
- or  $dt_1 = 10.000 0$  s
- Hold  $E_M$  for  $t_M = 0$  h 0 mn 0.000 0 s
- Limit  $|I| < I_M = 70.000$  mA
- or  $|dI/dt| < dI/dt_f = 0.000$  mA/s
- Record every  $dQ = 10.000$  mA.h
- or  $dt_q = 10.000 0$  s
- Limit  $|\Delta Q| > \Delta Q_M = 0.000$  mA.h
- $\Delta x_M = 0.000$
- $|\Delta SoC| > \text{pass}$  %
- E Range = 0 V; 5 V Resolution = 100  $\mu$ V
- I Range = 5 A
- Bandwidth = 4

**Step 2: Rest**

- Rest for  $t_R = 1$  h 0 mn 0.000 0 s
- Limit  $|dE_{cell}/dt| < dE_R/dt = 0.0$  mV/h
- Record every  $dE_R = 10.0$  mV
- or  $dt_R = 10.000 0$  s
- (If  $t_R = 0$  or  $|\Delta Q| > \Delta Q_M$  go to ④)

**Step 3: Limit**

- If  $E_{cell} > E_L = \text{pass}$  V go to ①

**Step 4: End of Sequence**

- Go back to seq.  $N_s^* = 1$  (9999 ends technique)
- for  $n_c = 2$  time(s) (0 for next sequence)

**Step 1: Charge (C/40)**

- Set I to  $I_s = 700.000$  mA vs. <None>
- for at most  $t_1 = 2$  h 20 mn 0.000 0 s
- Limit  $E_{cell} > E_M = 4.200$  V
- Record every  $dE_1 = 10.0$  mV
- or  $dt_1 = 10.000 0$  s
- Hold  $E_M$  for  $t_M = 0$  h 0 mn 0.000 0 s
- Limit  $|I| < I_M = 140.000$  mA
- or  $|dI/dt| < dI/dt_f = 0.000$  mA/s
- Record every  $dQ = 10.000$  mA.h
- or  $dt_q = 10.000 0$  s
- Limit  $|\Delta Q| > \Delta Q_M = 0.000$  mA.h
- $\Delta x_M = 0.000$
- $|\Delta SoC| > \text{pass}$  %
- E Range = 0 V; 5 V Resolution = 100  $\mu$ V
- I Range = 5 A
- Bandwidth = 4

**Step 2: Rest**

- Rest for  $t_R = 0$  h 0 mn 0.000 0 s
- Limit  $|dE_{cell}/dt| < dE_R/dt = 0.0$  mV/h
- Record every  $dE_R = 10.0$  mV
- or  $dt_R = 10.000 0$  s
- (If  $t_R = 0$  or  $|\Delta Q| > \Delta Q_M$  go to ④)

**Step 3: Limit**

- If  $E_{cell} < E_L = \text{pass}$  V go to ①

**Step 4: End of Sequence**

- Go back to seq.  $N_s^* = 0$  (9999 ends technique)
- for  $n_c = 0$  time(s) (0 for next sequence)

**Step 1: Charge (C/2)**

- Set I to  $I_s = -70.000$  mA vs. <None>
- for at most  $t_1 = 30$  h 0 mn 0.000 0 s
- Limit  $E_{cell} < E_M = 2.500$  V
- Record every  $dE_1 = 10.0$  mV
- or  $dt_1 = 10.000 0$  s
- Hold  $E_M$  for  $t_M = 0$  h 0 mn 0.000 0 s
- Limit  $|I| < I_M = 70.000$  mA
- or  $|dI/dt| < dI/dt_f = 0.000$  mA/s
- Record every  $dQ = 10.000$  mA.h
- or  $dt_q = 10.000 0$  s
- Limit  $|\Delta Q| > \Delta Q_M = 0.000$  mA.h
- $\Delta x_M = 0.000$
- $|\Delta SoC| > \text{pass}$  %
- E Range = 0 V; 5 V Resolution = 100  $\mu$ V
- I Range = 5 A
- Bandwidth = 4

**Step 2: Rest**

- Rest for  $t_R = 1$  h 0 mn 0.000 0 s
- Limit  $|dE_{cell}/dt| < dE_R/dt = 0.0$  mV/h
- Record every  $dE_R = 10.0$  mV
- or  $dt_R = 10.000 0$  s
- (If  $t_R = 0$  or  $|\Delta Q| > \Delta Q_M$  go to ④)

**Step 3: Limit**

- If  $E_{cell} > E_L = \text{pass}$  V go to ①

**Step 4: End of Sequence**

- Go back to seq.  $N_s^* = 1$  (9999 ends technique)
- for  $n_c = 4$  time(s) (0 for next sequence)

## 8.10. Appendix J- Forced lithium plating on cells in copper jigs at 0°C

Top two images C/10 charge D/20 discharge, bottom two images 3C charge and D/20 discharge.

**Parameters Settings**

1 - GCPL6  
2 - GCPL6

① Set  $I$  to  $I_s = 140.000$  mA vs. <None>  
for at most  $t_1 = 12$  h 0 mn 0.000 0 s  
Limit  $E_{cell} > E_M = 4.200$  V  
Record every  $dE_1 = 10.0$  mV  
or  $dt_1 = 10.000$  0 s

Hold  $E_M$  for  $t_M = 0$  h 0 mn 0.000 0 s  
Limit  $|I| < I_m = 70.000$  mA  
or  $|dI/dt| < dI/dt_f = 0.000$  mA/s  
Record every  $dQ = 10.000$  mA.h  
or  $dt_q = 10.000$  0 s

Limit  $|\Delta Q| > \Delta Q_M = 0.000$  mA.h  
<=>  $\Delta x_M = 0.000$   
 $|\Delta SoCl| >$  pass %

E Range = 0V; 5V  
Resolution = 100  $\mu V$   
I Range = 5 A  
Bandwidth = 4

② Rest for  $t_R = 0$  h 0 mn 0.000 0 s  
Limit  $|dE_{cell}/dt| < dE_R/dt = 0.0$  mV/h  
Record every  $dE_R = 10.0$  mV  
or  $dt_R = 10.000$  0 s  
(If  $t_R = 0$  or  $|\Delta Q| > \Delta Q_M$  go to ④)

③ If  $E_{cell} < E_L =$  pass V go to ①

④ Go back to seq.  $N_s' = 0$  (9999 ends technique)  
for  $n_c = 0$  time(s) (0 for next sequence)

**Parameters Settings**

1 - GCPL6  
2 - GCPL6

① Set  $I$  to  $I_s = -70.000$  mA vs. <None>  
for at most  $t_1 = 30$  h 0 mn 0.000 0 s  
Limit  $E_{cell} < E_M = 2.500$  V  
Record every  $dE_1 = 10.0$  mV  
or  $dt_1 = 10.000$  0 s

Hold  $E_M$  for  $t_M = 0$  h 0 mn 0.000 0 s  
Limit  $|I| < I_m = 70.000$  mA  
or  $|dI/dt| < dI/dt_f = 0.000$  mA/s  
Record every  $dQ = 10.000$  mA.h  
or  $dt_q = 10.000$  0 s

Limit  $|\Delta Q| > \Delta Q_M = 0.000$  mA.h  
<=>  $\Delta x_M = 0.000$   
 $|\Delta SoCl| >$  pass %

E Range = 0V; 5V  
Resolution = 100  $\mu V$   
I Range = 5 A  
Bandwidth = 4

② Rest for  $t_R = 1$  h 0 mn 0.000 0 s  
Limit  $|dE_{cell}/dt| < dE_R/dt = 0.0$  mV/h  
Record every  $dE_R = 10.0$  mV  
or  $dt_R = 10.000$  0 s  
(If  $t_R = 0$  or  $|\Delta Q| > \Delta Q_M$  go to ④)

③ If  $E_{cell} > E_L =$  pass V go to ①

④ Go back to seq.  $N_s' = 1$  (9999 ends technique)  
for  $n_c = 2$  time(s) (0 for next sequence)

**Parameters Settings**

1 - GCPL6  
2 - GCPL6

① Set  $I$  to  $I_s = 4200.000$  mA vs. <None>  
for at most  $t_1 = 0$  h 30 mn 0.000 0 s  
Limit  $E_{cell} > E_M = 4.200$  V  
Record every  $dE_1 = 10.0$  mV  
or  $dt_1 = 10.000$  0 s

Hold  $E_M$  for  $t_M = 0$  h 0 mn 0.000 0 s  
Limit  $|I| < I_m = 0.000$  mA  
or  $|dI/dt| < dI/dt_f = 0.000$  mA/s  
Record every  $dQ = 1.000$  mA.h  
or  $dt_q = 120.000$  0 s

Limit  $|\Delta Q| > \Delta Q_M = 0.000$  mA.h  
<=>  $\Delta x_M = 0.000$   
 $|\Delta SoCl| >$  pass %

E Range = 0V; 5V  
Resolution = 100  $\mu V$   
I Range = 5 A  
Bandwidth = 4

② Rest for  $t_R = 0$  h 0 mn 0.000 0 s  
Limit  $|dE_{cell}/dt| < dE_R/dt = 0.0$  mV/h  
Record every  $dE_R = 10.0$  mV  
or  $dt_R = 10.000$  0 s  
(If  $t_R = 0$  or  $|\Delta Q| > \Delta Q_M$  go to ④)

③ If  $E_{cell} < E_L =$  pass V go to ①

④ Go back to seq.  $N_s' = 0$  (9999 ends technique)  
for  $n_c = 0$  time(s) (0 for next sequence)

**Parameters Settings**

1 - GCPL6  
2 - GCPL6

① Set  $I$  to  $I_s = -70.000$  mA vs. <None>  
for at most  $t_1 = 30$  h 0 mn 0.000 0 s  
Limit  $E_{cell} < E_M = 2.500$  V  
Record every  $dE_1 = 10.0$  mV  
or  $dt_1 = 10.000$  0 s

Hold  $E_M$  for  $t_M = 0$  h 0 mn 0.000 0 s  
Limit  $|I| < I_m = 0.000$  mA  
or  $|dI/dt| < dI/dt_f = 0.000$  mA/s  
Record every  $dQ = 1.000$  mA.h  
or  $dt_q = 120.000$  0 s

Limit  $|\Delta Q| > \Delta Q_M = 0.000$  mA.h  
<=>  $\Delta x_M = 0.000$   
 $|\Delta SoCl| >$  pass %

E Range = 0V; 5V  
Resolution = 100  $\mu V$   
I Range = 5 A  
Bandwidth = 4

② Rest for  $t_R = 1$  h 0 mn 0.000 0 s  
Limit  $|dE_{cell}/dt| < dE_R/dt = 0.0$  mV/h  
Record every  $dE_R = 10.0$  mV  
or  $dt_R = 10.000$  0 s  
(If  $t_R = 0$  or  $|\Delta Q| > \Delta Q_M$  go to ④)

③ If  $E_{cell} > E_L =$  pass V go to ①

④ Go back to seq.  $N_s' = 1$  (9999 ends technique)  
for  $n_c = 2$  time(s) (0 for next sequence)

## 8.11. Appendix K- Typical cell safety settings

The screenshot displays the 'Safety/Adv. Settings' window of an electrochemical workstation. The interface is organized into several functional panels:

- Devices:** Shows a single device 'VMP3 - 128'.
- Experiment:** Shows the current experiment as '1 - GCPL6'.
- Safety Limits:** Configured for a duration  $t > 10.0$  ms. The settings include:
  - Ecell max: 4.300 00 V
  - Ecell min: 2.400 00 V
  - I<sub>lim</sub>: 0.000 00 mA
  - I<sub>Q-Qol</sub>: 0.000 00 mA.h
  - Analog IN1: max, 0.000 00 V
  - Analog IN2: max, 0.000 00 V
  - Estack slave max: 0.000 00 V
  - Estack slave min: 0.000 00 V
  - Do not start on E overload
- Record:**
  - Ece/V
  - P/W
  - Analog IN1/V
  - Analog IN2/V
  - [Record external devices on Analog IN#](#)
  - Files
- Electrode Connections:**
  - Modify on disconnected cells only!
  - standard
  - Schematic diagram showing WE/CA2 (ref1), RE/ref2, and CE/CA1 (ref3) connections with associated potentials  $E_{we}$ ,  $E_{ce}$  and current  $I$ .
  - Default
- Data Process:**
  - Online text export [Configure](#)
  - Filter [Edit](#)
  - Smooth on 0 points
  - Create one data file per loop (linked techniques only)
  - Cycles definition:
    - Charge/Discharge
    - Discharge/Charge

## 8.12. Appendix L- Battery cell information

<b>Battery Cell Composition</b>		
Setup	Cell type	Full cell
	Cell format	Pouch cell
	Cathode	NMC111 (10 layers, coated area 33.22cm <sup>2</sup> per electrode face)
	Anode	Graphite (11 layers, same coated area as above with 1 or 2mm overlap)
Cathode (composition percentages by mass)	Active material and loading	94% NMC111 , theoretical loading of 277.9 mAh/g
	Additive	3% Carbon black (C65)
	Binder	3% Polyvinylidene Fluoride (PVdF)
	Electrolyte	1M LiPF6 in EC/EMC (3/7 v/v) +2wt%VC
	Current Collector	Aluminium
	Thickness and mass	Thickness 116um (current collector 21um) Mass 1.0749g for 33.22 cm <sup>2</sup> (current collector 0.0052 g/cm <sup>2</sup> )
Anode (composition percentages by mass)	Host material	Graphite 94%
	Additive	C65 (carbon black) 3%
	Binder	1.5% Carboxymethyl Cellulose (CMC)
		1.5% Styrene-Butadiene Rubber (SBR)
	Thickness and mass	Thickness 108um (current collector 9um) Mass 0.8133g for 35.0 cm <sup>2</sup> (current collector 0.0084 g/cm <sup>2</sup> )

<b>Capacity</b>	
Theoretical capacity of 277.9mAh/g* cathode mass of 9.02g * 0.94 active material / total cell mass of 38 grams= 62.0mAh/g for cell	
Initial capacity (mAh/g)	62.0mAh/g
Capacity achieved (mAh/g)	1300mAh @ C/20 on cycle 1 → 1300mAh/ 38 grams = 34.2 mAh/g
Number of cycles tested	150
Capacity retention	89.5%
Testing temperature	25°C

<b>Characterisation carried out on cell</b>
Charge/ discharge tests
GITT
Incremental Capacity Analysis
Cyclic Voltammetry
Rate capability
EIS
SEM and EDX
X-ray Characterisation (CT scanning)

### 8.13. Appendix M- Copyright approvals for 3<sup>rd</sup> party figures utilised

The following figures have been reproduced from external sources, the copyright permissions obtained to do so are detailed here. Any party wishing to reproduce these figures should seek permission from the publisher of the original source.

<b>Figure</b>	<b>Source</b>	<b>Copyright obtained</b>
Figure 2-1	Reference 13	Reuse is authorised, provided the source of the document is acknowledged and the original meaning is not distorted.
Figure 2-2	Reference 22	Creative Commons 4.0 License
Figure 2-4	Reference 29	Creative Commons 4.0 License
Figure 2-5	Reference 51	Permission to reproduce obtained
Figure 2-6	Reference 62	Permission to reproduce obtained
Figure 2-7	Reference 64	Permission to reproduce obtained
Figure 2-8	Reference 68	Creative Commons 4.0 License
Figure 2-9	Reference 78	Creative Commons 4.0 License
Figure 2-10	Reference 67	Creative Commons 4.0 License
Figure 2-12	Reference 105	Creative Commons 4.0 License
Figure 2-15	Reference 118	Creative Commons 4.0 License
Figure 2-16	Reference 142	Permission to reproduce obtained
Figure 2-17	Reference 127	Permission to reproduce obtained
Figure 2-18	Reference 142	Permission to reproduce obtained
Figure 2-20	Reference 18	Creative Commons 4.0 License